A measurement of hadron production cross-sections for the
simulation of accelerator neutrino beams and
a search for muon neutrino to electron neutrino oscillations
in the $\Delta m^2 \sim 1 \, eV^2$ region

David W. Schmitz

Submitted in partial fulfillment of the
requirements for the degree
of Doctor of Philosophy
in the Graduate School of Arts and Sciences

COLUMBIA UNIVERSITY

2008

ABSTRACT

A measurement of hadron production cross-sections for the
simulation of accelerator neutrino beams and
a search for muon neutrino to electron neutrino oscillations
in the $\Delta m^2 \sim 1 \, eV^2$ region

David W. Schmitz

This dissertation presents measurements from two different high energy physics experiments with a very strong connection: the Hadron Production (HARP) experiment located at CERN in Geneva, Switzerland, and the Mini Booster Neutrino Experiment (Mini-BooNE) located at Fermilab in Batavia, Illinois.

First, charged pion and proton production is measured at the HARP experiment for two experimental configurations relevant to two contemporary accelerator-based neutrino beams. Double-differential cross-sections for π^+, π^- and proton production are presented for proton+beryllium collisions at 8.9 GeV/c and proton+aluminum collisions at 12.9 GeV/c. These data have been used in the predictions of neutrino fluxes by the K2K experiment in Japan and the MiniBooNE and SciBooNE experiments at Fermilab.

Second, a search for evidence of muon neutrino to electron neutrino oscillations at MiniBooNE is presented. MiniBooNE was designed to search for evidence of $\nu_\mu \rightarrow \nu_e$ oscillations consistent with a mass-squared splitting near 1 eV^2. Evidence of such an oscillation was reported by the LSND collaboration in the 1990s but has not been confirmed by other experiments. A method which combines the electron neutrino candidate sample with the high statistics muon neutrino candidate sample to define a single χ^2 statistic is developed. A complete description of experimental uncertainties is contained within a correlated error matrix which includes correlations between the two samples. This correlation reduces the uncertainty on the prediction of the smaller statistics electron sample and improves MiniBooNE's sensitivity to oscillations. Analysis of the MiniBooNE electron candidate data reveals no evidence of direct $\nu_\mu \rightarrow \nu_e$ oscillations consistent with this interpretation of the LSND data.

Contents

8   A Search for $\nu_\mu \to \nu_e$ Oscillations at MiniBooNE   195

List of Figures

List of Tables

Acknowledgments

It is truly humbling to sit here and reflect on the many people who have helped to make the completion of this dissertation possible. And it is my very distinct pleasure to extend my sincere gratitude to each and every one of them. I entered graduate school more than seven years ago under very trying circumstances, and I have relied heavily over that time on the many incredible relationships, both personal and professional, that I have had the good fortune of developing with all of you – and you have never let me down. For that I am eternally grateful. Thank you.

In particular, I would like to thank my advisor, Janet Conrad, who is such a strong advocate for all of her students and who has always believed in me – allowing me to believe in myself. Your enthusiasm and limitless energy for what we do is contagious, your ability and desire to communicate it is enviable, and your keen eye for the bigger picture and the possibilities for the future is inspiring. Finally, you have afforded me every opportunity along this journey, and for that I sincerely thank you.

I wish to extend my sincere appreciation to the rest of the Columbia neutrino group. First, to Professor Mike Shaevitz who has so often provided critical insight and guidance when struggling with complicated analysis problems. You also reminded me that, every once in a while, a scientist should actually look at their data! The numbers just might tell you something.

Over the years, I have had the privilege of overlapping with many students in the group as well. Jocelyn Monroe and Michel Sorel, who were here when I arrived, did so much to help me get started and provided great examples of how one does things in this business. It was a pleasure to work with both of you and, best of all, along the way we became friends. I wish to sincerely thank Alexis Agular-Arévalo. Working with you

in the final months before box opening was a whirlwind of sleep-deprived excitement! But we stuck it out and, together, we developed a successful analysis. More recently, I have shared office space and countless hours of engaging, in-depth conversation with Kendall Mahn. Your willingness to talk things out and help me to develop ideas has been invaluable, particularly down the stretch. Thank you.

I want to offer my sincere thanks to the entire MiniBooNE collaboration. Your dedication to the success of this experiment and countless suggestions and advice for my own analysis have made this work possible. I learned a tremendous amount from observing and participating in this enormous effort. In particular, I thank our spirited spokespersons of then: Bill Louis and Janet Conrad, and now: Steve Brice and Richard Van de Water for your leadership and enthusiasm.

So many others come to mind as well. To Jen Raaf, my former office mate, car pool partner, neighbor, Hyperbole's best ever first mate, and dear friend, thank you for all the fun and all the laughs. The tenth floor has missed you very much. And thank you Teppei Katori for being about the most fun office mate anyone ever had; your hard work coupled with your excitement and curiosity for new things and new people is truly inspiring.

The four months leading up to the publication of MiniBooNE's first oscillation results in April 2007 were absolutely insane. I don't know how it is possible to think back with such fondness on something so painful! Oh wait, yes I do: Steve Brice and Chris Polly. Steve, I have no idea how you coordinated the entire analysis effort, performed many critical components of it yourself, all while mentoring several students, particularly myself, on how to accomplish our own pieces – but you did, and I am amazed and forever indebted. Cheers to you, my friend.

Chris, as plainly stated as possible, working with you has been an absolute privilege. The combination of your patience and willingness to listen with your diverse expertise and insightful advice has been a benefit to every student on the tenth floor, of which I am no exception, but perhaps the best example. The integrity with which you approach everything that you do, including science, is something that I will always strive to emulate. Thank you for the example that you have set for all of us. Finally, and most importantly, thank you for your friendship. I expect that it will long outlast the Booster Neutrino Ex-

periments. Our next 10:30 meeting is definitely on me.

Thank you to Sam Zeller for your constant encouragement and thoughtful advice. Thanks also for your careful read of several chapters of this thesis which were greatly improved by your comments. And thank you for your friendship and, of course, the wild MiniBooNE holiday parties!

As much as I learned working on MiniBooNE, it is my friends and colleagues at HARP who first taught me the difficult and important lesson of turning raw data into a useful physics measurement. Thank you to the entire HARP collaboration, including our spokespersons, Jaap Panman and Gabriella Catanesi. Jaap, thank you for your strong leadership during the challenging times leading up to our first publications.

To my fellow MiniBooNE/HARPsters, Geoff Mills and Linda Coney, thank you for the countless useful discussions over the years concerning the cross-section analysis. Of course, we had an awful lot of fun during several trips to Geneva and Valencia and Los Alamos in the process. A beautiful hike on a glacier and a few dozen dinners at Pizza D'oro (I and II) come immediately to mind! Thank you both very much.

To our analysis coordinator and my friend, Juan Jose Gomez Cadenas, thank you for your mentorship to a young graduate student, for your unwavering confidence in me, and for your kindness and friendship. To me, you exemplify the combination of scientific excellence and artistic passion to which we should all aspire. And to all my dear friends from the Valencia group: Michel, Anselmo, Pau, Justo, Joan, Ana, Elena and others, thank you for your friendship and your hospitality during my fantastic visits to your beautiful city.

When I first arrived in New York City in the autumn of 2001, I relied heavily on the support of many friends both in and out of the physics department. To my long time dear friend Kyle Maude, I never would have made it past the first semester without you, Katie. Thank you. To the group of amazing friends who carried me on their backs through the first two years of graduate school and were always there for me whenever I needed them: Christina, Erik, Alex, Andy and Alex (the bird), Segev and Maggie, Yashar, Amanda, all, thank you so very much. I am forever indebted to you for your support and your friendship, which will last a lifetime.

Similarly, here in Chicago, I have been so fortunate to know so many wonderful people. To Shane and Amy for taking about 6 seconds to decide to go along with my crazy idea to buy a sailboat, thank you. Five sailing seasons later, it is still one of the best decisions I've ever made, and the opportunity to build our friendship is no small part of that feeling.

There are far too many to name here, but thank you to all of my dear friends in Chicago. And thank you to "Team Grafton", where the term includes much more than the players, but all of my extended family from my second home in the city – you know who you are. And especially to you, Matt. I think of "Team Grafton" as a club started way back at your first card game three years ago which has continued to grow right up to the beers shared after yesterday's softball practice. It has been a tremendous amount of fun and an important part of my time here.

And, of course, thank you, Erika. Thank you for your infinite support and understanding through the darkest days of dissertation writing. Thank you for enduring hours of obsessive, incoherent babble about details of its contents that no one in the world could possibly follow! Thank you for celebrating the crossing of every minor hurdle with me along the way. Oh, and the Rosinator (shocking, that failed spell check) wishes to thank you for covering so generously for her horribly neglectful owner.

Finally, it is my privilege and my honor to thank my entire, incredible family. Everyone, from New York to Chicago, from Fermilab to Lake Michigan, has had the same reaction upon meeting you, "Wow, Dave, you weren't kidding. They really *are* wonderful!". Thank you all for your strong support and even your dedicated interest in the neutrino!

Above all, I wish to express my deeply felt appreciation for my amazing parents, Len and Pat Schmitz. You have given me every opportunity at every stage of my life, you have so often put my needs ahead of your own so that I might be successful, and you have set an example for Melissa and me that every young person should be so lucky to have had. I can never repay you for all that you have given me or all that you have taught me, but it is to you that I dedicate this dissertation – a sort of physical manifestation of all the opportunities which you have provided me that one can hold in the palms of their hands. Thank you Mom and Dad.

for my parents.
who have given me everything.

and for Shannon.
whose memory continues to inspire.
I did it, Shan. . . I did it.

Part I

Introduction

Chapter 1

Neutrinos and Oscillations

I have done a terrible thing. I have postulated a particle that cannot be detected.

- W. Pauli, 1931

We are happy to inform you that we have definitely detected neutrinos from fission fragments by observing inverse beta decay of protons.

- F. Reines and C. Cowen, 1956

Thanks for the message. Everything comes to him who knows how to wait.

- W. Pauli, 1956

1.1 Introduction

It took a quarter of a century for physicists to achieve the impossible and detect Pauli's chargeless, massless, weakly interacting particle, but suddenly the field of experimental neutrino physics was born. Since Reines and Cowen's monumental achievement, neutrino physics has become one of the most active fields of research in particle physics. Much of the focus in recent years has been on neutrino masses, originally considered to be identically zero, and the resulting phenomenon of neutrino mixing.

It was the process of nuclear beta decay which led Pauli to postulate the neutrino's existence. It was known that an element could change its place on the periodic table via the emission of an electron

$$(A, Z) = (A, Z + 1) + e^- , \tag{1.1}$$

but a series of experiments showed that the electron is emitted with a continuous energy spectrum, which is inconsistent with a 2-body decay of a nucleon at rest. The implied nonconservation of energy led Pauli to suggest a "desperate way out". He postulated that an unseen neutral particle was also being emitted in the decay and carrying away the missing energy. Many believed the electron and this new "neutron", as Pauli first called it, were part of the nucleus and were simply ejected in the process of beta decay.

In 1934, Enrico Fermi placed this new particle into his theoretical framework of the weak force [1] and gave it the name we use today, "neutrino". In Fermi's theory the interaction was assumed to occur at a single space-time point with the neutron[1] emitting a proton, electron and neutrino (actually what we now know is the electron antineutrino):

$$n \rightarrow p + e^- + \bar{\nu}_e \tag{1.2}$$

and was formulated as a vector×vector current interaction based on analogy to electrodynamics. The approach enabled H. Bethe and R. Peierls to calculate the rate of the inverse process [2]:

$$\bar{\nu}_e + p \rightarrow n + e^+ \tag{1.3}$$

and suddenly a process by which to detect the neutrino was discovered. This is the approach F. Reines and C. Cowen used to detect electron antineutrinos produced at the Savannah River nuclear power reactor in South Carolina [3] leading to their 1956 telegram to Pauli which opened this chapter.

Soon afterward, a major breakthrough in the understanding of the weak force arrived when T.D. Lee and C.N. Yang suggested that the weak force may violate parity [4]. Then, in 1957, C.S. Wu et al. experimentally confirmed that parity is, in fact, *maximally* violated by weak interactions [5]. This led to the very successful (V-A) formulation of the weak interaction by R. Feynman and M. Gell-Mann as well as by E.C.G. Sudarshan and R.E. Marshak in 1958 [6]. In the theory, the weak interaction is described by equal amounts of vector and axial vector coupling which effectively picks out the left-handed helicity

---

[1]The actual neutron had been discovered by J. Chadwick in 1932.

component ($H \equiv \vec{p} \cdot \vec{S}/|\vec{p}|$ where $\vec{p}$ and $\vec{S}$ are the momentum and spin of the particle, respectively) of the massless neutrino and incorporates the observed parity violation.

Another surprise came in 1962 when L. Lederman, M. Schwartz, J. Steinberger and collaborators discovered a second type of neutrino [51] distinct from the one which participated in the reactions 1.2 and 1.3. Their experiment was the first to use the accelerator-based neutrino beam method and led to the discovery of the muon neutrino. The tau neutrino, predicted to exist after the discovery of the tau charged lepton, would have to wait until 2000 to be observed experimentally [52]. However long before the ν_τ was directly detected, leptons were now thought to be grouped in families with lepton flavor (L_e, L_μ, L_τ) being a conserved quantity. The development of this family structure was an important step and led to the formation of the fermion doublets introduced below.

1.2   Neutrinos in the Standard Model

The Standard Model of weak and electromagnetic interactions is based on the spontaneously broken gauge symmetry $SU(2)_L \otimes U(1)_Y$ and was first proposed in 1967 by S. Weinberg [8] and A. Salam [9]. In relativistic quantum mechanics, the spin $\frac{1}{2}$ fermions of mass m are described by the Dirac equation:

$$(i\hbar\gamma^\mu\partial_\mu - mc)\psi = 0 \tag{1.4}$$

where γ^μ are the Dirac matrices [7] and ψ is the 4 component spinor field. Building from the (V-A) theory of weak interactions, it is the left and right chiral projections of the spin $\frac{1}{2}$ particle fields which participate in interactions in electroweak unification theory:

$$\psi = \psi_L + \psi_R = \left(\frac{1-\gamma^5}{2}\right)\psi + \left(\frac{1+\gamma^5}{2}\right)\psi . \tag{1.5}$$

Because neutrinos interact only weakly and are presumed massless in the model, the right handed neutrino states are not included in the Standard Model. The twelve known fermions [135] (ignoring their antiparticles) are then written as six left-handed weak isospin doublets and nine right-handed singlets:

$$\begin{pmatrix} e \\ \nu_e \end{pmatrix}_L \quad \begin{pmatrix} \mu \\ \nu_\mu \end{pmatrix}_L \quad \begin{pmatrix} \tau \\ \nu_\tau \end{pmatrix}_L \qquad e_R \quad \mu_R \quad \tau_R$$
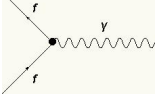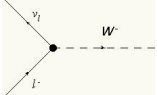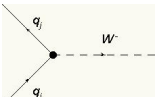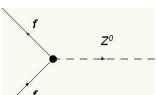
Interaction vertex		Dirac spinors	Chiral spinors
QED fermions		$ig_e \overline{f}\gamma_\mu f$	$ig_e \left(\overline{f}_L\gamma_\mu f_L + \overline{f}_R\gamma_\mu f_R \right)$
CC leptons		$\dfrac{-ig_w}{\sqrt{2}}\overline{\nu}\gamma_\mu \left(\dfrac{1-\gamma^5}{2} \right)\ell$	$\dfrac{-ig_w}{\sqrt{2}}\overline{\nu}_L\gamma_\mu \ell_L$
CC quarks		$\dfrac{-ig_w}{\sqrt{2}}\overline{q_j}\gamma_\mu \left(\dfrac{1-\gamma^5}{2} \right)q_i\, U^{CKM}_{ij}$	$\dfrac{-ig_w}{\sqrt{2}}\overline{q_j}_L\gamma_\mu q_{i\,L}\, U^{CKM}_{ij}$
NC fermions		$\dfrac{-ig_z}{2}\overline{f}\gamma_\mu \left(c_V - c_A\gamma^5 \right) f$	$\dfrac{-ig_z}{2}\overline{\nu}_L\gamma_\mu \nu_L \quad$ for ν

Table 1.1: Feynman rules for basic electroweak interaction vertices written in terms of Dirac spinors and their projections ψ_L and ψ_R [7].

$$\begin{pmatrix} u \\ d' \end{pmatrix}_L \quad \begin{pmatrix} c \\ s' \end{pmatrix}_L \quad \begin{pmatrix} t \\ b' \end{pmatrix}_L \qquad u_R \quad d_R \quad c_R \quad s_R \quad t_R \quad b_R$$

which allows a very symmetric formulation of the rates for electromagnetic and weak interactions. This is illustrated in Table 1.1 where the basic vertex factors of electroweak interactions are written using both Dirac spinors and the ψ_L, ψ_R projections defined in Eq. 1.5.

The vertex factors in Table 1.1 reveal several important features. First, the photon is seen to couple to left and right-handed states equally, as expected for the electromagnetic interaction. The CC weak interactions, however, have the familiar (V-A) form which picks out ψ_L. NC weak interactions depend on the fermion involved, but for neutrinos with $c_V = c_A = 1/2$, only ν_L is involved.

The CC interaction of quarks additionally includes a matrix, U^{CKM}, the Cabibbo-Kobayashi-Maskawa mixing matrix, which describes the mathematical relationship between the quark states of definite mass (d, s, b) and of definite weak flavor (d', s', b'). An equivalent matrix for leptons which relates the observable weak states $(\nu_e, \nu_\mu, \nu_\tau)$ to neutrino mass states (ν_1, ν_2, ν_3) is noticeably absent in this formalism.

Finally, a mechanism for generating particle masses is needed. Not only is particle mass an experimental reality that a theory must deal with, but it is the masses of the gauge bosons $W^{\pm}$ and Z^0 which make the weak force extremely short range ($\sim 10^{-18}$ m) compared to the infinite reach of the electromagnetic interaction governed by the massless photon. Masses are generated in the Standard Model through spontaneous symmetry breaking via the Higgs mechanism [10]. In the model, a complex doublet of scalar fields is introduced [11]:

$$\phi \equiv \begin{pmatrix} \phi^+ \\ \phi^0 \end{pmatrix} \tag{1.6}$$

which leads to additional Yukawa interaction terms in the Standard Model Lagrangian for each lepton family[2]

$$-\mathcal{L}_{\text{Yukawa}} = \sum_{\alpha=e,\mu,\tau} G_\alpha \left[\bar{\nu}_L \phi^+ \ell_R + \bar{\ell}_L \phi^0 \ell_R \right] + \text{h.c.} \tag{1.7}$$

where G_α are new dimensionless coupling constants and the flavor subscript on ν_α and ℓ_α have been left off for clarity.

After spontaneous symmetry breaking, the vacuum expectation values of the Higgs field become $\langle \phi^+ \rangle = 0$ and $\langle \phi^0 \rangle = v/\sqrt{2}$ where $v \simeq 246$ GeV, leaving the neutrinos massless while giving the charged leptons each a Dirac mass term,

$$-\mathcal{L}_D = \sum_{\ell_\alpha=e,\mu,\tau} (m_D^\ell)\, \bar{\ell}_L \ell_R + \text{h.c.} \tag{1.8}$$

with a unique parameter $m_D^\ell = G_\ell \cdot v/\sqrt{2}$ for each lepton. Currently, the coupling strengths G_ℓ are not determined by the theory and can only be measured experimentally.

1.3 Adding neutrino masses to the Standard Model

Perhaps the most obvious way to add neutrino masses to the Standard Model would be to add the chirally right-handed neutrino field ν_R to the model which would automatically create Dirac mass terms for each neutrino, ν, analogous to Eq. 1.8 for the charged

---

[2]Similar terms exist for the quarks, but we restrict ourselves to the leptons here since ultimately we are interested in neutrino masses.

leptons [12]

$$-\mathcal{L}_D = \sum_\nu (m_D^\nu) \, \overline{\nu}_L \nu_R + \text{h.c.} \tag{1.9}$$

where we have intentionally left off any subscript labeling the neutrinos in anticipation of the results of the next section.

Because neutrinos are neutral particles, a different kind of mass term, known as the Majorana mass term, can also be constructed out of ν_L alone or ν_R alone

$$-\mathcal{L}_{M_L} = \sum_\nu \frac{m_L^\nu}{2} \, \overline{(\nu_L)^c} \, \nu_L + \text{h.c.} \qquad - \mathcal{L}_{M_R} = \sum_\nu \frac{m_R^\nu}{2} \, \overline{(\nu_R)^c} \, \nu_R + \text{h.c.} \tag{1.10}$$

where $m_{L,R}^\nu$ are parameters with units of mass and $(\nu)^c = C(\overline{\nu})^T$ where C is the charge conjugation operator. The Majorana mass terms, therefore, involve converting a neutrino into its antiparticle which would be forbidden for other fermions due to violation of charge conservation. Whether Majorana mass terms exist for neutrinos is a matter for experiment to decide. If neutrinos are determined to be their own antiparticles, then the terms almost certainly exist. If the Dirac terms are shown to not exist and neutrinos have mass, then the Majorana terms become necessary to provide it.

1.4 Adding neutrino mixing to the Standard Model

Because neutrinos interact only via the weak force, it is not the mass states that one can directly access experimentally. Instead we know the weak flavor $\nu_\alpha = (\nu_e, \nu_\mu, \nu_\tau, \dots)$ of the neutrino through identification of the charged lepton partner $\ell_\alpha = (e, \mu, \tau, \dots)$ observed in a CC weak interaction $(\nu_\alpha A \to \ell_\alpha A')$:

$$-\mathcal{L}_{CC} = \sum_{\alpha=e,\mu,\tau} \frac{g}{\sqrt{2}} \left(\overline{\nu}_L \gamma_\mu \ell_L W_\mu^+ + \overline{\ell}_L \gamma_\mu \nu_L W_\mu^- \right) \tag{1.11}$$

where again we leave off the flavor subscripts for clarity.

However, a neutrino's propagation through space (for example, from its production to its detection) is dictated by the free Hamiltonian whose eigenstates are states of definite mass $\nu_i = (\nu_1, \nu_2, \nu_3, \dots)$ and whose time evolution is described by the Schrödinger

equation[3]

$$i\frac{\partial}{\partial t}|\nu_i(t)\rangle = E_i |\nu_i(t)\rangle$$
$$= \left(\sqrt{m_i^2 + p_i^2}\right)|\nu_i(t)\rangle \simeq \left(p_i + \frac{m_i^2}{2p_i}\right)|\nu_i(t)\rangle \approx \left(E_i + \frac{m_i^2}{2E_i}\right)|\nu_i(t)\rangle \qquad (1.12)$$

where, in the last steps, we have used the expectation that $m_i \ll p_i$ and thus $p_i \approx E_i$ for any reasonable neutrino energy used in an experiment[4]. The trivial solution to Eq. 1.12 is then simply:

$$|\nu_i(t)\rangle = e^{-i\left(E_i + m_i^2/2E_i\right)t}|\nu_i(0)\rangle \ . \qquad (1.13)$$

Next, we must introduce a description of how the weak eigenstates $|\nu_\alpha\rangle$, which partic-ipate in the interaction, relate to the mass eigenstates $|\nu_i\rangle$, which propagate through space. We introduce a unitary mixing matrix U such that

$$|\nu_i\rangle = \sum_\alpha U_{\alpha i} |\nu_\alpha\rangle$$
$$|\nu_\alpha\rangle = \sum_i U_{\alpha i}^* |\nu_i\rangle \qquad (1.14)$$

which implies that a neutrino produced as a flavor eigenstate $|\nu_\alpha\rangle$ is the quantum mechan-ical superposition of mass eigenstates with amplitudes determined by the elements of U. The mass eigenstates which contribute coherently to an experimental beam are those with a common energy [13] so Eq. 1.13 implies that each mass state propagates with a unique complex phase that depends on m_i^2. Also, because the neutrino is ultra-relativistic, we can consider the propagation distance instead of the time, $L \approx t$ (for $c = 1$). Hence, a neutrino produced as weak eigenstate α is, at distance L:

$$|\nu_\alpha(L)\rangle = \sum_i U_{\alpha i}^* e^{-i(m_i^2/2E)L} \qquad (1.15)$$

Therefore, the probability of producing a neutrino as weak eigenstate α and detecting

---

[3]We will use natural units throughout this section where $\hbar = c = 1$.
[4]For $m \leq 1$ eV and $E \sim 1$ GeV, $\gamma \geq 10^9$

weak eigenstate β at a distance L is given by:

$$P(\nu_\alpha \to \nu_\beta) = |\langle \nu_\beta | \nu_\alpha(L) \rangle|^2 = \left| \sum_i U^*_{\alpha i} e^{-i(m_i^2 L/2E)} U_{\beta i} \right|^2$$

$$= \delta_{\alpha\beta} - 4 \sum_{i>j} \Re \left(U^*_{\alpha i} U_{\beta i} U_{\alpha j} U^*_{\beta j} \right) \sin^2 \left(\Delta m_{ij}^2 \frac{L}{4E} \right) \tag{1.16}$$

$$+ 2 \sum_{i>j} \Im \left(U^*_{\alpha i} U_{\beta i} U_{\alpha j} U^*_{\beta j} \right) \sin \left(\Delta m_{ij}^2 \frac{L}{2E} \right)$$

where $\Delta m_{ij}^2 \equiv m_j^2 - m_i^2$ is the difference in the squared masses of eigenstates ν_j and ν_i. The sinusoidal form of the transmutation probability has earned this effect the name "neutrino oscillations". There are several things to note about the phenomenon of neutrino oscillations as described by Eq. 1.16

- If neutrinos do not have degenerate masses so that all $\Delta m^2 = 0$, then Eq. 1.16 reduces to $\delta_{\alpha\beta}$ and neutrinos cannot change flavor through oscillations. On the other hand, if neutrinos are found to oscillate, then it indicates that one or more neutrino masses are necessarily non-zero and not identical.

- If the neutrino mixing matrix is diagonal, such that mass eigenstates do not mix, then Eq. 1.16 again reduces to $\delta_{\alpha\beta}$ and flavor changing through oscillations cannot occur.

- To determine the oscillation probability of antineutrinos, one must replace the mixing matrix with its complex conjugate matrix changing the sign of the third term to $(-)$. Because $\bar{\nu}_\alpha \to \bar{\nu}_\beta$ is the CP mirror image of $\nu_\alpha \to \nu_\beta$, evidence that $P(\nu_\alpha \to \nu_\beta) \neq P(\bar{\nu}_\alpha \to \bar{\nu}_\beta)$ would be evidence of CP violation in the lepton sector.

- Oscillations are only sensitive to mass differences and thus cannot determine the absolute masses of neutrinos. However, it may be possible to determine the sign of Δm^2 by comparing neutrino and antineutrino oscillation probabilities for neutrinos passing through dense matter [39].

- Including the missing powers of $\hbar$ and c and converting m, L, and E to useful experimental units, the arguments of the trigonometric functions in Eq. 1.16 become,

respectively:

$$\sin^2 \left(1.267 \frac{\Delta m^2 (\text{eV}^2) L (\text{km})}{E(\text{GeV})} \right) , \qquad \sin \left(2.534 \frac{\Delta m^2 (\text{eV}^2) L (\text{km})}{E(\text{GeV})} \right) \quad (1.17)$$

- The parameters L and E determine the values of Δm^2 for which oscillations may be observed by an experiment. If $(1.267 \Delta m^2 L / E) \ll 1$ then the effect will be negligible. Effects of oscillations are largest for values of $(1.267 \Delta m^2 L / E)$ of $\mathcal{O}(1)$.

1.4.1   Quasi-two neutrino oscillation formula

In an experiment designed to look for effects of neutrino oscillations, if the produced eigenstate $|\nu_\alpha\rangle$ couples strongly to only two mass eigenstates OR if the various Δm^2 are sufficiently different and the ratio L/E is such that the the effect of one is dominant over the others, then the oscillation probability can be greatly simplified. This is referred to as the "quasi-two neutrino oscillation formula".

For a system with only two weak eigenstates and two mass eigenstates Eq. 1.14 can be expanded to read

$$\left| \begin{array}{c} \nu_\alpha \\ \nu_\beta \end{array} \right\rangle = \left(\begin{array}{cc} \cos\theta & \sin\theta \\ -\sin\theta & \cos\theta \end{array} \right) \left| \begin{array}{c} \nu_i \\ \nu_j \end{array} \right\rangle \qquad (1.18)$$

where the angle θ describes the level of mixing. The oscillation probability Eq. 1.16 then greatly simplifies to

$$P(\nu_\alpha \rightarrow \nu_\beta) = \delta_{\alpha\beta} - 4 \left(U_{\alpha i}^* U_{\beta i} U_{\alpha j} U_{\beta j}^* \right) \sin^2 \left(1.267 \frac{\Delta m_{ij}^2 L}{E} \right) \quad (2\,\nu \text{ oscillations}) \quad (1.19)$$

There are two ways to observe the effects of the neutrino flavor oscillations given by Eq. 1.19. The first is to observe, in a beam of ν_α, the appearance of neutrinos of flavor ν_β. This is referred to as an "appearance" measurement and the probability is given by:

$$P(\nu_\alpha \rightarrow \nu_\beta) = \sin^2 (2\theta) \sin^2 \left(1.267 \frac{\Delta m_{ij}^2 L}{E} \right) \qquad (\nu_\beta \text{ appearance}) \quad (1.20)$$

Second, one can begin with a known flux of ν_α and observe fewer ν_α at a different location than were originally in the neutrino beam. This is known as a "disappearance" measurement and the probability is given by:

$$P(\nu_\alpha \rightarrow \nu_\alpha) = 1 - \sin^2 (2\theta) \sin^2 \left(1.267 \frac{\Delta m_{ij}^2 L}{E} \right) \qquad (\nu_\alpha \text{ disappearance}) \quad (1.21)$$

In both formulas, we have made use of the trigonometric identity $2 \sin\theta \cos\theta = \sin(2\theta)$. Most neutrino oscillation measurements to date have interpreted their data using one of these formulas, so we will refer them often.

1.4.2   Three neutrino mixing matrix

If one assumes the three known, weakly interacting neutrino eigenstates, $\nu_\alpha = (\nu_e, \nu_\mu, \nu_\tau)$, are superpositions of three mass eigenstates, $\nu_i = (\nu_1, \nu_2, \nu_3)$, then the mixing is described by a 3×3 unitary mixing matrix.

The nine elements of the neutrino matrix can be expressed as functions of three angles, θ_{12}, θ_{23} and θ_{13}, describing the levels of mixing between the mass states and a Dirac CP-invariance violating phase[5], δ. There are many possible parameterizations, but a common choice is the form used for the U^{CKM} matrix [135] in the quark sector where weak–mass eigenstate mixing dates back to 1973 [14]. The 3×3 neutrino mixing matrix is known as the Maki-Nakagawa-Sakata-Pontecorvo matrix:

$$U^{MNSP} = \begin{pmatrix} c_{12}c_{13} & s_{12}c_{13} & s_{13}e^{-i\delta} \\ -s_{12}c_{23} - c_{12}s_{23}s_{13}e^{i\delta} & c_{12}c_{23} - s_{12}s_{23}s_{13}e^{i\delta} & s_{23}c_{13} \\ s_{12}s_{23} - c_{12}c_{23}s_{13}e^{i\delta} & -c_{12}s_{23} - s_{12}c_{23}s_{13}e^{i\delta} & c_{23}c_{13} \end{pmatrix} \quad (1.22)$$

where $c_{ij} \equiv \cos\theta_{ij}$ and $s_{ij} \equiv \sin\theta_{ij}$. It is extremely instructive to factorize the matrix into three factors, separating the various mixing terms:

$$U^{MNSP} = \begin{pmatrix} 1 & 0 & 0 \\ 0 & \cos(\theta_{23}) & \sin(\theta_{23}) \\ 0 & -\sin(\theta_{23}) & \cos(\theta_{23}) \end{pmatrix} \times \begin{pmatrix} \cos(\theta_{13}) & 0 & \sin(\theta_{13})e^{-i\delta} \\ 0 & 1 & 0 \\ -\sin(\theta_{13})e^{i\delta} & 0 & \cos(\theta_{13}) \end{pmatrix}$$
$$\times \begin{pmatrix} \cos(\theta_{12}) & \sin(\theta_{12}) & 0 \\ -\sin(\theta_{12}) & \cos(\theta_{12}) & 0 \\ 0 & 0 & 1 \end{pmatrix} \quad (1.23)$$

---

[5]Possible additional Majorana CP violating phases, $\alpha_{1,2}$, are ignored in our treatment as they have no effect on oscillation probabilities. See [13].

1.5 The experimental evidence for neutrino oscillations

There is compelling evidence from an impressive variety of experiments that the phenomenon described in the previous section occurs in nature and thus that neutrinos are not massless. When possible, a given experiment is designed to probe just one of the matrices of Eq. 1.23 and its corresponding mass-squared splitting, although, in general, there will be dependencies on the other sectors [40]. We discuss each in turn.

1.5.1 The $(\Delta m^2_{12}, \theta_{12})$ sector

Evidence of neutrino oscillations consistent with a mass-squared splitting near 8×10^{-5} eV^2 has been seen using both neutrinos naturally produced in the core of the sun and electron antineutrinos produced in the fission process at nuclear power reactors.

1.5.1.1 Neutrinos from the sun - SNO

The first evidence of neutrino oscillations came as a surprise in 1968 when R. Davis Jr. and collaborators first attempted to detect neutrinos produced inside the core of the sun [15, 16] and found about 1/3 of the event rate predicted by the Standard Solar Model (SSM) of J. Bahcall [17]. The nuclear processes in the sun produce only electron neutrinos and Davis' detector located in the Homestake Gold Mine in South Dakota could only detect electron neutrinos. Eventually it was proposed that the measured deficit could be due to oscillations from $\nu_e \rightarrow \nu_\mu, \nu_\tau$ which could not be seen in the Homestake detector.

Many solar neutrino experiments followed [18, 19, 20, 21, 22] measuring flux ratios $\phi^{\text{obs}}/\phi^{SSM}$ ranging from 0.3–0.6. The different experiments, however, were sensitive to solar ν_e energies ranging from $\sim$200 keV to 7 MeV. The energy dependent solar neutrino flux measurements, all inconsistent with the theoretical prediction, became known as the "solar neutrino problem". The favored solution was known as the Mikheyev-Smirnov-Wolfenstein (MSW) [23] large mixing angle (LMA) solution which carefully accounts for the effects of dense solar matter in the propagation of neutrino eigenstates.

The definitive experimental statement about the solar neutrino problem came in 2001 from the Sudbury Neutrino Observatory (SNO) [24] which used the deuterium in heavy
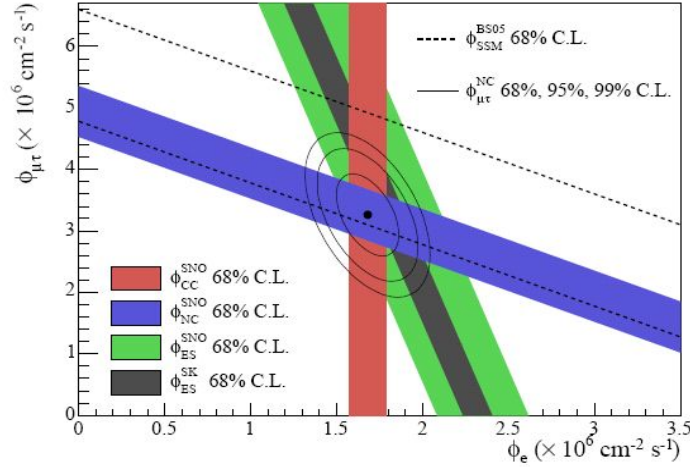
Figure 1.1: Flux of muon and tau neutrinos versus flux of electron neutrinos at SNO. The colored bands correspond to the measured fluxes for CC (red), NC (blue), and ES (green) interactions. The Standard Solar Model expectation for the NC flux is shown by the band between the dashed lines. The gray band corresponds to an ES measurement made at Super-Kamiokande and is in good agreement with SNO data. The point is the best fit for $\phi_{\mu\tau}$ and ϕ_e with the 68%, 95% and 99% C.L. contours indicated. Plot taken from [24].

water as a target for solar neutrinos. The major advantage of SNO is the ability to see charged-current (CC) as well as neutral-current (NC) and elastic-scattering (ES) neutrino interactions:

$$\nu_e + d \;\;\rightarrow\;\; p + p + e^- \quad \text{(CC)}$$

$$\nu_\alpha + d \;\;\rightarrow\;\; p + n + \nu_\alpha \quad \text{(NC)}$$

$$\nu_\alpha + e^- \rightarrow \nu_\alpha + e^- \quad \text{(ES)}$$
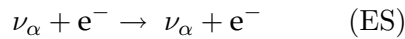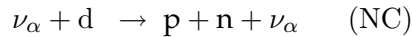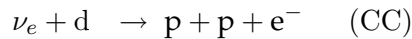
Because of the low neutrino energies, the CC reaction is sensitive to only the ν_e flux while the NC and ES reactions sample the total active (ν_e,ν_μ,ν_τ) flux. The SNO results are summarized in Figure 1.1. The plot shows the measured ν_μ,ν_τ combined flux versus the ν_e flux. The red band is the CC measurement (ν_e only) where the width represents the 1σ uncertainty. The slopes of the blue (NC) and green (ES) are determined by the relative sensitivity to the ν_e and non-ν_e components of these interactions. The total solar neutrino
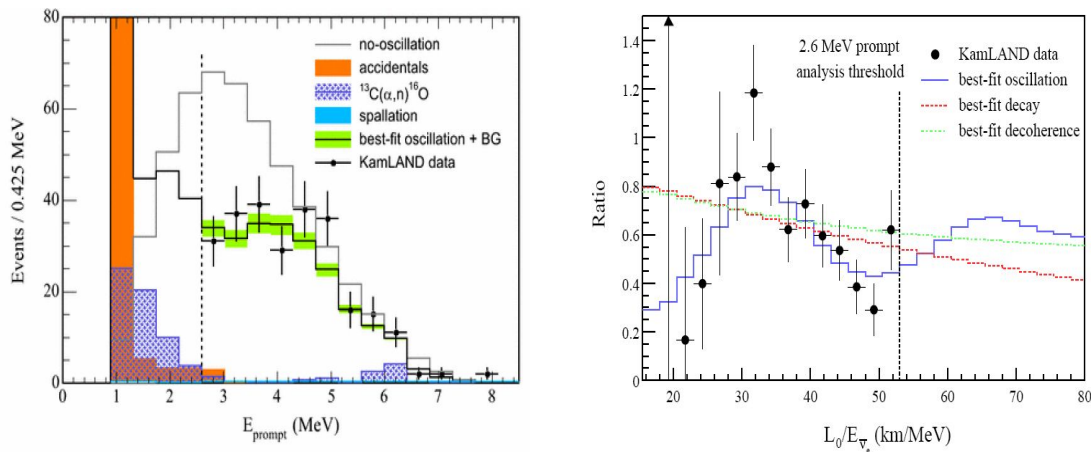
Figure 1.2: Summary of KamLAND $\overline{\nu}_e$ disappearance results. The left panel shows the energy distribution of events for the no oscillations hypothesis compared to data. The right panel shows the $N_{\mathrm{data}}/N_{\mathrm{no-osc}}$ ratio as a function of L_ν/E_ν where $L_\nu = 180$ km is the average neutrino distance determined from simulation and E_ν is the reconstructed $\overline{\nu}_e$ energy. The blue histogram shows the best fit for an oscillation hypothesis using Eq. 1.21. Plot taken from [25].

flux measured using the NC events is in excellent agreement with the prediction of the Standard Solar Model, but the ν_e component is shown to be only $\sim 34\%$ of the total. The sun is not energetic enough to produce muons or taus, yet SNO measures a non-zero ν_μ, ν_τ flux at over 5σ. This is strong evidence that the ν_e's produced in the sun have oscillated into other active flavors. Global analysis of the solar neutrino data under the MSW LMA hypothesis shows that the data are consistent with $\nu_e \rightarrow \nu_\mu, \nu_\tau$ oscillations specified by a mixing angle $\theta_{\mathrm{solar}} \sim 34°$ and mass-squared splitting $\Delta m_{\mathrm{solar}}^2 \sim 7 \times 10^{-5}$ eV^2 [40].

1.5.1.2   Neutrinos from nuclear power reactors - KamLAND

Equally compelling is the complimentary measurement made by the KamLAND experiment in Japan [25]. KamLAND looked for the disappearance of $\overline{\nu}_e$'s produced in nuclear power reactors across Japan. The average distance $L = 180$ km and the average neutrino energy is a few MeV, giving KamLAND a sensitivity to mass-squared differences of order $\Delta m^2 \geq 1/(1.267 * 180\mathrm{km}/0.005\mathrm{GeV}) \sim 10^{-5}$ eV^2. KamLAND detects electron an-

tineutrinos by the same inverse beta decay reaction that Reines and Cowen first used to discover the neutrino, $\bar{\nu}_e + \mathrm{p} \to \mathrm{n} + \mathrm{e}^+$. By measuring the energy of the emitted positron, KamLAND can estimate the $\bar{\nu}_e$ energy for each event. Their results are shown in Figure 1.2. In the left panel, the thin black histogram shows their expected event rate as a function of measured energy in the absence of $\bar{\nu}_e$ oscillations and the points show the measured rate; a clear energy-dependent deficit is seen. The right panel shows the ratio of $\mathrm{N_{data}}/\mathrm{N_{no-osc}}$ as a function of the average neutrino path length $L = 180$ km divided by the reconstructed neutrino energy, or L_ν/E_ν. The oscillatory pattern of the $\bar{\nu}_e$ deficit is clear. The solid blue histogram is the result of a fit to a neutrino disappearance hypothesis (Eq. 1.21).

The allowed combinations of oscillation parameters at different C.L. for the solar experiments and KamLAND are compared in the left panel of Figure 1.3. A combined analysis of data from KamLAND and solar neutrino experiments, shown in the right panel, yields [25]:

$$\Delta m^2_{12} = 7.9^{+0.6}_{-0.5} \times 10^{-5} \text{ eV}^2$$

$$\theta_{12} = 32.3^{+3.0}_{-2.4} \text{ deg.}$$

1.5.2 The $(\mathbf{\Delta m^2_{23}}, \theta_{23})$ sector

Evidence of neutrino oscillations consistent with a mass-squared splitting near 2.5×10^{-3} eV^2 has been seen using both neutrinos naturally produced by cosmic rays hitting the upper atmosphere and using muon neutrino beams produced at particle accelerators.

1.5.2.1 Neutrinos from the atmosphere - Super-Kamiokande

Following the solar neutrino results, the second evidence for neutrino oscillations again came quite unexpectedly. The Kamiokande detector in Japan was constructed in 1983 to search for nucleon decay, however, it ultimately detected the oscillation of neutrinos produced in the Earth's atmosphere.

Cosmic rays interacting with nitrogen and oxygen in the upper atmosphere produce secondary pions and kaons whose subsequent decay chains produce both electron and
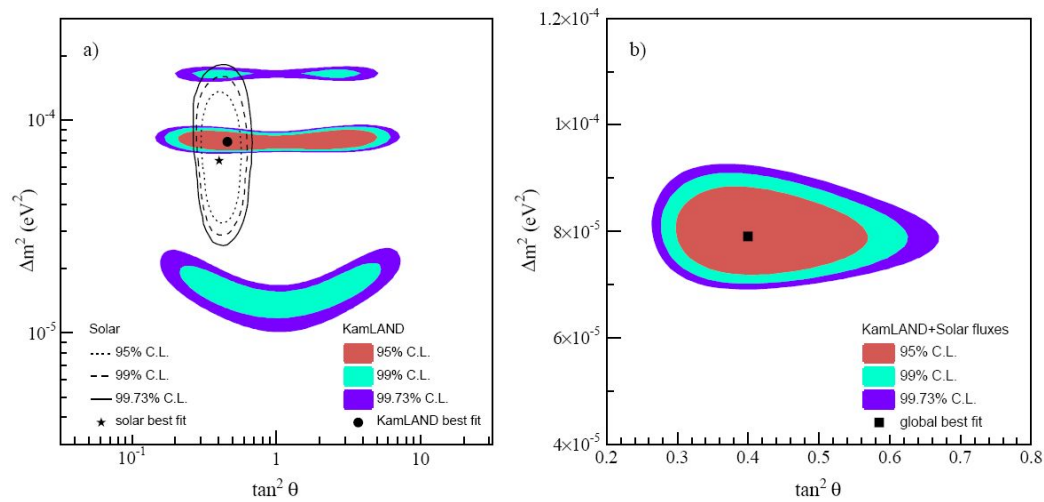
Figure 1.3: Allowed $(\Delta m^2_{\text{solar}}, \tan^2 \theta_{\text{solar}})$ oscillation parameter combinations for a combination of solar neutrino data compared to the KamLAND reactor neutrino data. The right panel is a global analysis of solar and reactor data providing the best determination of Δm^2 and $\tan^2 \theta$. Plot taken from [25].

muon neutrinos. From $\pi \rightarrow \mu \nu_\mu$ and $\mu \rightarrow e \nu_\mu \nu_e$ the ratio of muon to electron flavor neutrinos is expected to be approximately 2:1. Observations at Kamiokande [26] and the IMB [27] detector in the US indicated a ν_μ / ν_e ratio about 60% of that expected. Other early atmospheric neutrino experiments reported ratios ranging from 0.5–1.0. This surprising result soon became known as the "atmospheric neutrino problem".

This time, the definitive experimental statement would come from the Super-Kamiokande experiment. The Super-Kamiokande detector (the successor of Kamiokande) is an underground 50 kton water Cherenkov detector lined with photomultiplier tubes to detect light produced by charged particles in the tank. Taking advantage of high statistics samples of atmospheric ν_μ induced CC events and the ability to determine the direction of the incoming neutrino, Super-K was able to bin their data into many energy and zenith angle bins and detect a deficit of upward going muons consistent with oscillations [28].

The clearest way to view the effects of ν_μ disappearance at Super-K came in a later L/E analysis of ν_μ events [29]. Atmospheric muon neutrinos in the range $E_\nu \sim 1$–10 GeV are detected through the charged-current interaction $\nu_\mu + \text{n} \rightarrow \text{p} + \mu^- + X$ where the
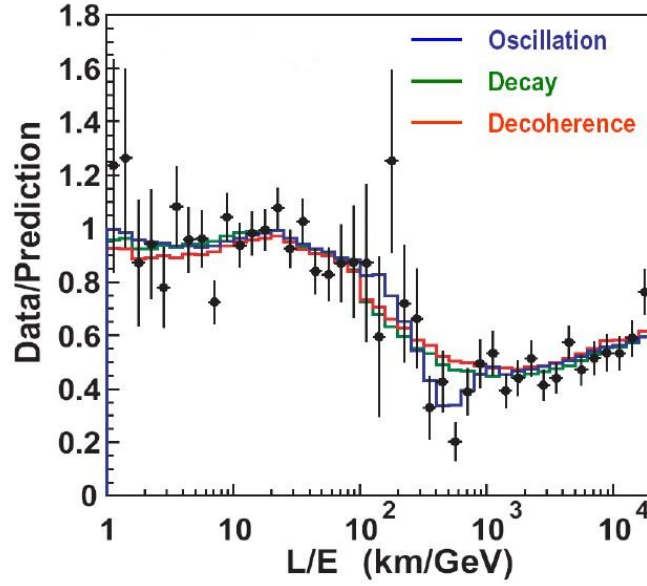
Figure 1.4: Ratio of measured ν_μ events to the number predicted in the absence of oscillations versus the reconstructed ratio L_ν/E_ν in Super-Kamiokande. Plot taken from [29].

final-state muon produces a sharp ring of Cherenkov light identifying it as a muon. From the total energy deposited in the photo tubes, the incident neutrino energy is able to be reconstructed.

The path lengths of atmospheric neutrinos at Super-Kamiokande are in the range $L_\nu \sim 10$–10^4 km where the shortest distances correspond to neutrinos produced directly above the detector and the longest are those that travel through the diameter of the Earth before intercepting the Super-K detector. The path length is estimated from the reconstructed direction of the incident neutrino and assuming it was produced in the upper atmosphere at an average height of 15 km. These ranges of L_ν and E_ν make Super-K sensitive to oscillation effects corresponding to mass-squared differences ranging from $\Delta m^2 \sim 1/(1.267 * 10^4 \text{km}/1\text{GeV})$ to $1/(1.267 * 10\text{km}/10\text{GeV}) \sim 10^{-4}$ to 1 eV^2.

Figure 1.4 shows the ratio of measured ν_μ events to the number predicted in the absence of oscillations versus the reconstructed ratio L_ν/E_ν in Super-K. The oscillatory behavior of the ν_μ deficit is clear. The blue histogram is a fit to the ν_μ disappearance hypothesis as in Eq. 1.21. The other curves are fits to other possible phenomena and are strongly

disfavored. The data are consistent with $\nu_\mu \to \nu_\tau$ oscillations[6] specified by a mixing angle $\theta_{\mathrm{atm}} \sim 45°$ and mass-squared splitting $\Delta m^2_{\mathrm{atm}} \sim 2.4 \times 10^{-3}$ eV^2.

1.5.2.2 Accelerator based neutrino beams - K2K & MINOS

The neutrino oscillation experiments K2K and MINOS both use the accelerator-based neutrino beam method to be described in the next chapter. The bottom line is the generation of a very pure (>90%) beam of ν_μ with a broad energy distribution peaked in the range $E_\nu \sim 1\text{–}10$ GeV, depending on the exact experimental configuration.

Both experiments look for ν_μ disappearance using a two detector approach. A near detector located ~ 1 km from the neutrino source is used to normalize the expected event rate in the absence of oscillations at a far detector several hundred kilometers distant. An energy dependent deficit in the predicted ν_μ rate is thus evidence for the same $\nu_\mu \to \nu_\tau$ oscillations as seen in atmospheric neutrinos.

K2K used the 12 GeV proton synchrotron at KEK to produce a neutrino beam peaked at 1.3 GeV directed at the Super-Kamiokande detector 250 km away which served as a far detector. For the ν_μ disappearance search, K2K observed 112 fully-contained events in Super-K while $158.1^{+9.2}_{-8.6}$ events were predicted based on data in their near detectors [31]. Using a smaller sample (58) of charged-current quasi-elastic events, they were able to observe an energy dependence to the discrepancy consistent with an oscillation hypothesis.

The most precise measurement to date of the Δm^2 that dictates the $\nu_\mu \to \nu_\tau$ oscillation comes from the MINOS experiment at Fermilab [32]. MINOS uses the NuMI (Neutrinos from the Main Injector) neutrino beam produced by 120 GeV protons from the Main Injector. Two functionally identical detectors comprised of alternating iron and scintillator planes are used: a 1 kton near detector at Fermilab and a 5.4 kton far detector located 735 km away in the Soudan Mine in northern Minnesota. In the configuration used in the oscillation analysis, the ν_μ beam peaks near 3 GeV, making MINOS most sensitive to oscillations of order $\Delta m^2 = 1/(1.267 * 735\mathrm{km}/3\mathrm{GeV}) \sim 3 \times 10^{-3}$ eV^2.

MINOS' results [33] (updated since [32] using $2.5{\times}10^{20}$ proton on target (POT) of data)

---

[6]Oscillations to ν_e are disfavored by the fact that ν_e event rates agree well with prediction at Super-K and no evidence of $\bar{\nu}_e$ disappearance was seen by the CHOOZ reactor experiment.
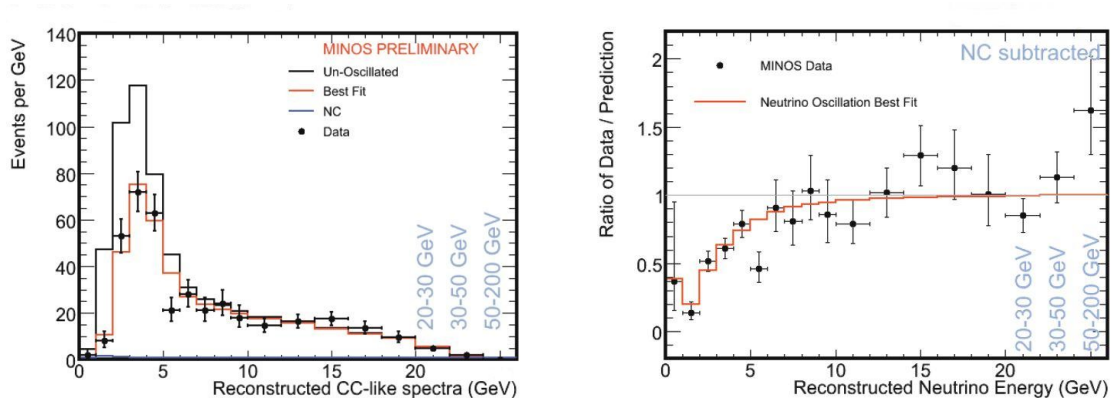
Figure 1.5: MINOS ν_μ disappearance results based on 2.5×10^{20} POT of data. The left panel shows the measured ν_μ event rate as a function of reconstructed neutrino energy compared to the prediction in the absence of oscillations. The right panel shows the data/simulation ratio. Plots taken from [33].

are shown in Figure 1.5. The disappearance of ν_μ is clear, and the oscillation hypothesis fits the spectral distortion well with a mixing angle $\theta_{\mathrm{MINOS}} \sim 45°$ and mass-squared splitting $\Delta m_{\mathrm{MINOS}}^2 \sim 2.38 \times 10^{-3}$ eV^2.

The allowed combinations of oscillation parameters at different C.L. for the atmospheric neutrino data at Super-K and the K2K/MINOS data are compared in Figure 1.6. No combined analysis of just atmospheric, K2K and MINOS data in a simple two neutrino oscillation scenario is currently available, but it is clear that MINOS provides the best constraint on the value of Δm^2 while the mixing angle is better constrained by the Super-K data:

$$\Delta m_{23}^2 \sim \Delta m_{\mathrm{MINOS}}^2 = 2.38^{+0.20}_{-0.16} \times 10^{-3} \text{ eV}^2$$

$$\theta_{23} \quad \sim \quad \theta_{\mathrm{atm}} \quad = 45^{+0.0}_{-8.2} \text{ deg.}$$

Note that the atmospheric and accelerator experiments cannot determine the sign of Δm_{23}^2, but only it's absolute value. This means we do not yet know the hierarchy of the mass states which we call ν_1, ν_2 and ν_3. The possible arrangements are shown in Figure 1.8 with the nearly degenerate pair (ν_1, ν_2) either above or below ν_3.[7]

---

[7]We do know that ν_2 is heavier than ν_1 because of the MSW LMA mechanism that accounts for solar
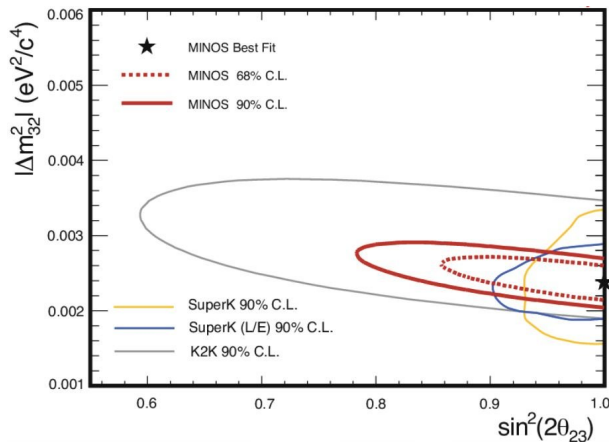
Figure 1.6: Allowed $(\Delta m_{\text{atm}}^2, \sin^2(2\theta_{\text{atm}}))$ oscillation parameter combinations for atmospheric neutrino data using the two Super-Kamiokande analyses [28, 29] compared to the K2K [31] and MINOS [33] data. Plot taken from [33].

1.5.3   The $(\mathbf{\Delta m_{13}^2}, \theta_{13})$ sector

The final Δm^2 (in a three neutrino model) is not a new independent parameter in the mixing formalism but is determined from

$$\Delta m_{13}^2 = \Delta m_{12}^2 + \Delta m_{23}^2 \,, \tag{1.24}$$

and given that $\Delta m_{12}^2 \sim \frac{1}{30}\Delta m_{23}^2$ and $\delta(\Delta_{23}^2) \sim \frac{1}{12}\Delta m_{23}^2$, to a good approximation $\Delta m_{13}^2 = \Delta m_{23}^2$.

The third mixing θ_{13}, however, has no such dependence on the known parameters and must be determined experimentally. No evidence of this third mixing has yet been detected; the strongest constraint on its value comes from the CHOOZ reactor experiment [34, 35] in France. CHOOZ searched for the disappearance of $\overline{\nu}_e$ produced at the Chooz nuclear power station ($E_\nu \sim 3$ MeV) over a baseline of approximately 1 km. No significant deviation from prediction was found, as shown in the left panels of Figure 1.7, so a limit on the value of $\sin^2(2\theta_{13})$ with a strong dependence on the value of Δm_{13}^2 is set (right panel). From Figure 1.7, near the best fit value of $\Delta m_{13}^2 = \Delta m_{23}^2 = 2.38 \times 10^{-3}$ eV^2, the CHOOZ limit corresponds to θ_{13} below $\approx 11.5°$ at 90% C.L..

---

neutrino oscillations.
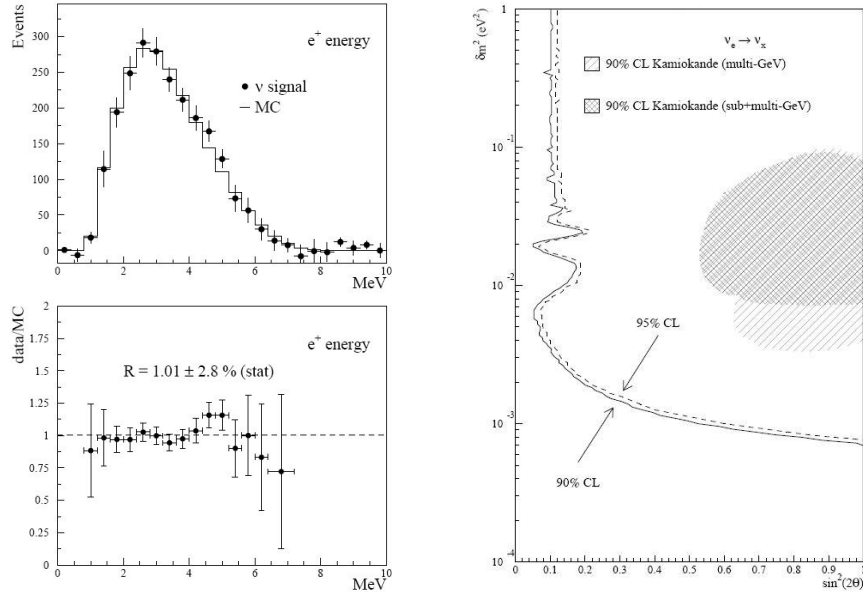
Figure 1.7: Final results of the CHOOZ experiment. The left panels show the measured and predicted positron energy spectra (from $\overline{\nu}_e + p \rightarrow n + e^+$) and the data/MC ratio on the bottom which is consistent with 1.0 within uncertainties. The right panel shows the limit on $\sin^2(2\theta_{13})$ that is set based on these data.

The search for θ_{13} represents an important component of the world's current neutrino physics research program. Next generation reactor experiments searching for $\overline{\nu}_e$ disappearance include the Double Chooz [36] experiment at the site of the former CHOOZ experiment and the Daya Bay [37] experiment in China. Both experiments combine high reactor power, multiple detectors to cancel systematics, and careful calibration to improve the sensitivity to $\sin^2(2\theta_{13})$ below 0.01 or $\theta_{13} < 3°$.

A second category of planned next generation experiments are long baseline (LBL) accelerator based neutrino beam experiments which will search for evidence of θ_{13} through $\nu_\mu \rightarrow \nu_e$ transitions at the Δm_{13}^2 scale, in particular the T2K [38] experiment in Japan and the NOνA [39] experiment at Fermilab in the US. The expression for the $P(\nu_\mu \rightarrow \nu_e)$ oscillation probability is quite complicated [38, 39, 40] and involves all three mixing angles, mass-squared splittings, the CP parameter δ and matter effects caused by passing the neutrino beam through the Earth's crust. This is both a significant complication and an

advantage - with sufficiently intense beams and statistics in both neutrinos and antineutrinos one can access the CP violation in the lepton sector as well as determine the sign of Δm_{13}^2.

1.5.4 Three neutrino oscillation summary

The oscillations first discovered in neutrinos from the sun and the atmosphere have now been verified with terrestrial sources and measured with significant accuracy. Figure 1.8 provides a schematic summary of the parameters that we now know or wish to know. The two mass splittings which have been measured, Δm_{12}^2 and Δm_{23}^2, are depicted, however, as mentioned, we do not know the sign of Δm_{23}^2 so both the "normal" (left) and "inverted" (right) hierarchies are still possible. The colored bars represent the amount of each flavor eigenstate which make up the mass eigenstates. The size of the tiny sliver of purple in the ν_3 state is determined by the value of θ_{13} and so could still be zero. Also, the absolute mass scale, given by m_{lightest}^2, is still unknown.

The data of the various experiments to date have all been analyzed using the simplified two neutrino formulas given by Eq. 1.20 and 1.21. In reality, however, there are subdominant effects and correlations between the three mixing and two mass-squared parameters. Global 3-ν fits of all oscillation data have been performed by various authors [40, 41] and only their results will be summarized here.

Figure 1.9 shows the results of T. Schwetz et al. [42]. The final KamLAND results (Figure 1.2) and updated MINOS results (Figure 1.5) have been included in their analysis. The best fit parameter values are given below. The uncertainties given correspond to 3σ ranges.

$$\Delta m_{12}^2 \;=\; 7.6^{+0.7}_{-0.5} \times 10^{-5} \text{ eV}^2$$

$$\left|\Delta m_{23}^2\right| \;=\; 2.4^{+0.4}_{-0.4} \times 10^{-3} \text{ eV}^2$$

$$\theta_{12} \;=\; 34.4^{+4.8}_{-3.7} \text{ deg.}$$

$$\theta_{23} \;=\; 45^{+9.9}_{-9.3} \text{ deg.}$$

$$\theta_{13} \;\leq\; 12.9 \text{ deg.}$$

$$\delta_{\text{CP}} \;=\; \in [0, 360] \text{ deg.}$$
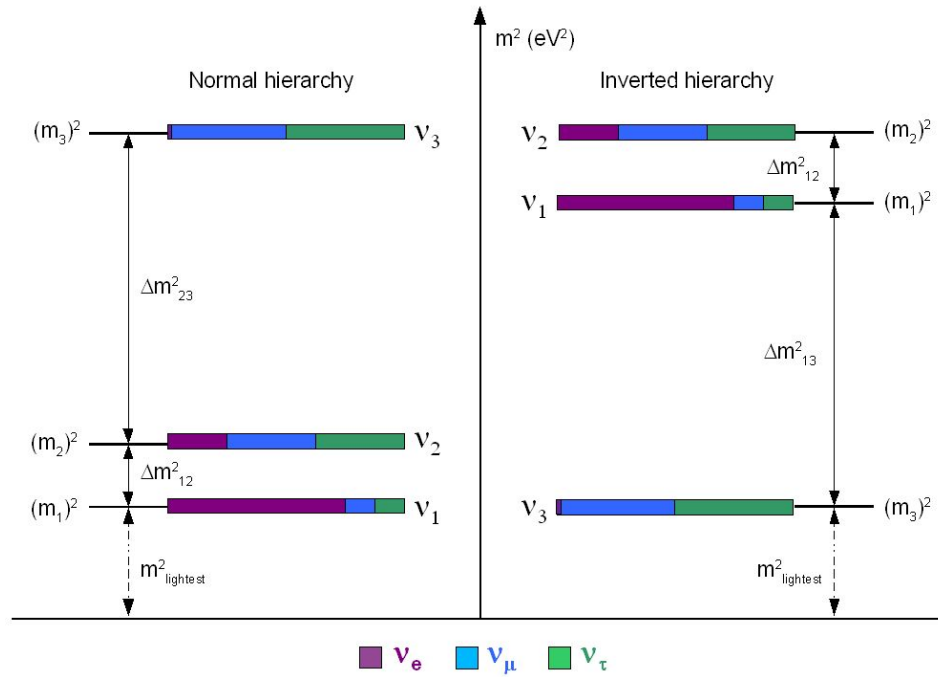
Figure 1.8: Schematic summary of the neutrino mixing parameters in a model with three active neutrinos. The vertical axis is mass-squared and the bars represent mass eigenstates ν_1, ν_2 and ν_3. The colored sections represent the fractions of ν_e, ν_μ and ν_τ comprising each mass eigenstate. We do not yet know if the mass hierarchy is "normal" (left) or "inverted" (right).
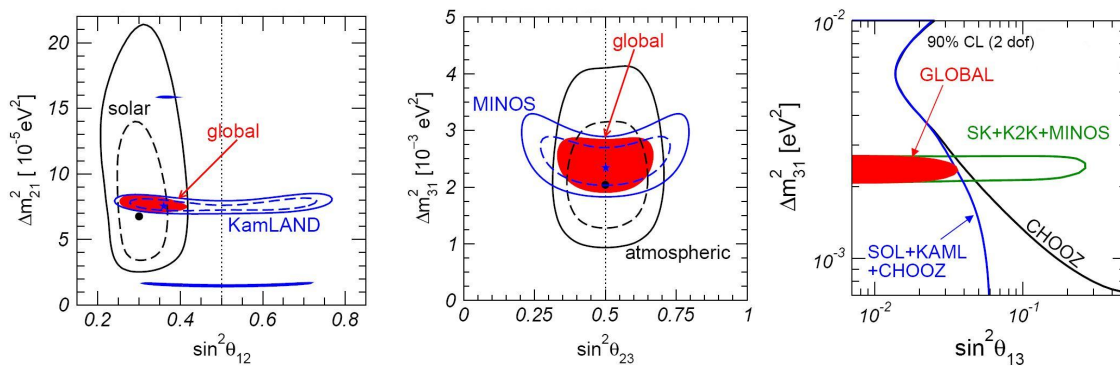
Figure 1.9: Status of 3-ν mixing model parameters in a global fit to all oscillation data including solar neutrinos, atmospheric neutrinos, reactor experiments and accelerator based experiments. Plots taken from [41].

Note that the results of the global analysis are consistent with the simple 2-ν interpretations used to determine $(\Delta m_{12}^2, \theta_{12})$ and $(\Delta m_{23}^2, \theta_{23})$ in Sections 1.5.1 and 1.5.2. This is simply the statement that the experimental uncertainties are still larger than the subdominant effects. In the next generation of experiments, however, this should no longer be the case.

1.5.5 The LSND oscillation signal

Several neutrino experiments have searched for neutrino oscillations consistent with a mass-squared splitting significantly above Δm_{12}^2 and Δm_{23}^2. These searches are typically performed using neutrinos produced at reactors or accelerators over distances $L_\nu \sim$ 10–1000 m with sensitivities to $\Delta m^2 > 10^{-2}$ eV^2. Only one such experiment has reported a positive oscillation result, the Liquid Scintillator Neutrino Detector (LSND) [43, 44] performed at Los Alamos National Laboratory in the 1990's. The LSND experiment and analysis are discussed in detail in Section 5.1 as direct motivation for the design of Mini-BooNE, so here we simply present the results and their implications for neutrino physics.

LSND searched for the appearance of $\overline{\nu}_e$ in a beam of $\overline{\nu}_\mu$ and discovered an excess of $87.9 \pm 22.4 \pm 6.0$ $\overline{\nu}_e$ events above expected backgrounds. Using the 2-ν appearance
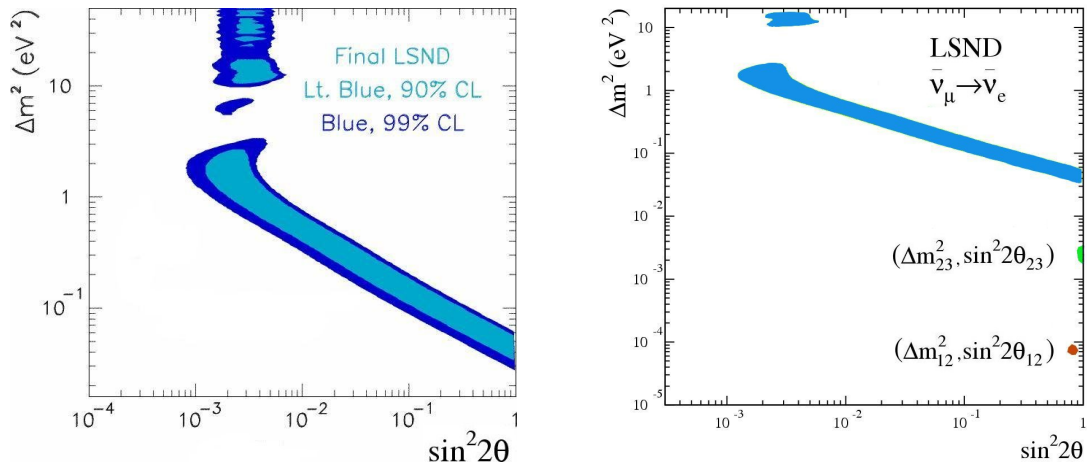
Figure 1.10: Allowed combinations of oscillation parameters based on the excess of $\bar{\nu}_e$'s seen by the LSND experiment at Los Alamos National Laboratory. The 90% and 99% C.L. allowed regions are shown in the left panel. The right panel compares the 90% C.L. allowed region from LSND to the oscillation parameters discussed in the previous sections.

probability of Eq. 1.20 to interpret the results, the allowed combinations of $(\Delta m^2, \sin^2(2\theta))$ are shown in Figure 1.10. The best fit combination, $(1.2\,\text{eV}^2, 0.003)$, corresponds to an oscillation probability $P(\bar{\nu}_\mu \to \bar{\nu}_e) \sim 0.3\%$. The right panel compares the LSND oscillation result to the two oscillation results already discussed in Sections 1.5.1 and 1.5.2.

While neutrino oscillations may now seem like familiar phenomena, the LSND result is remarkable for the following reason. It is clear from Figure 1.10 that, for the allowed sets of parameters, $\Delta m^2_{\text{LSND}} \neq \Delta m^2_{12} + \Delta m^2_{23}$. Therefore, the LSND result cannot be accommodated by the extension to the Standard Model already introduced with three weakly interacting, massive neutrinos, and implies the introduction of additional neutrino mass eigenstates.

This is difficult to reconcile, however, with the precision electroweak measurements on the Z boson resonance performed at the Large Electron-Positron collider (LEP) at CERN [45]. The total width of the Z is the sum of the partial widths to the various fermion decay channels:

$$\Gamma_{\text{Z}} = \Gamma_{ee} + \Gamma_{\mu\mu} + \Gamma_{\tau\tau} + \Gamma_{\text{had}} + \Gamma_{\text{inv}} \tag{1.25}$$
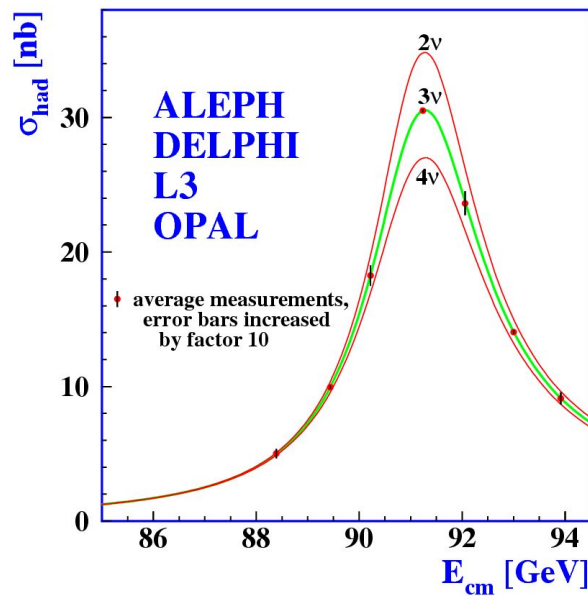
Figure 1.11: Measurements of the hadron production cross-section around the Z resonance at four experiments at LEP. The curves are predicted cross-sections for an invisible decay contribution coming from 2, 3 and 4 light neutrino species with negligible mass. Plot taken from [45].

where $\Gamma_{\mathrm{had}} = \sum_{q \neq t} \Gamma_{q\bar{q}}$ is a sum over all quark-antiquark pairs excluding the top quark, since the Z boson cannot decay into the more massive top, and $\Gamma_{\mathrm{inv}} = N_\nu(\Gamma_{\nu\bar{\nu}})$ is the decay to undetected (hence, invisible) light neutrino pairs. Figure 1.11 shows the measured hadron production cross-section around the Z resonance at four experiments at LEP compared to the Standard Model predictions for an invisible decay comprised of 2,3 and 4 neutrino families. The result is a stringent limit on there being 3 light, weakly interacting neutrino species.

A further extension to the Standard Model is, therefore, required to incorporate the third, independent Δm^2 reported by LSND. A common model includes the addition of one or more neutrino mass eigenstates, but which are mostly non-weakly interacting, or "sterile" [46, 47], as depicted in Figure 1.12. The oscillation signal at LSND is then interpreted as a coupling with the small component of active flavors in the fourth mass eigenstate.
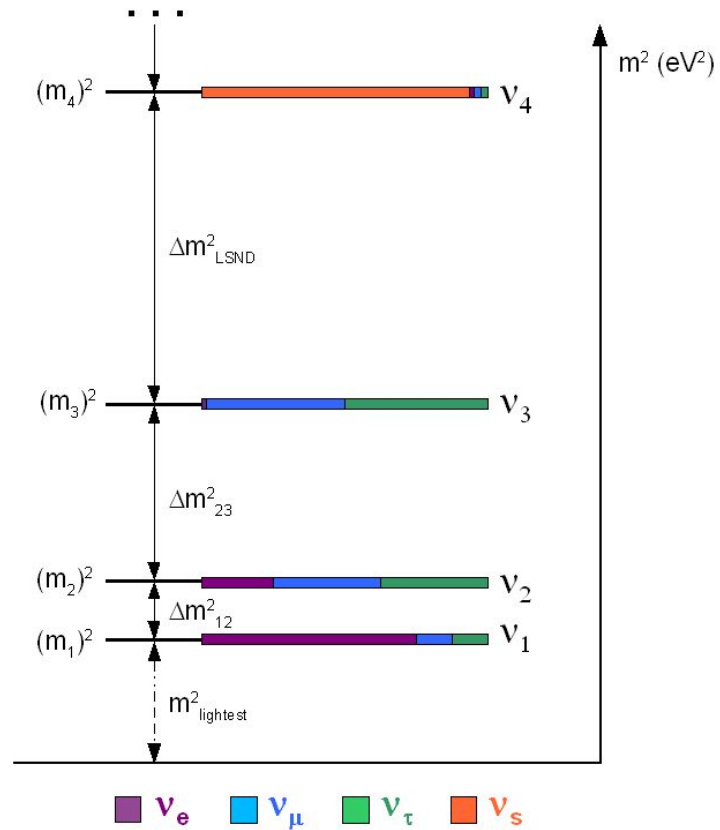
Figure 1.12: Possible mass hierarchy of neutrino masses with 3 active neutrinos and 1 sterile neutrino. Sterile neutrino models are not limited to one additional state, but often include 2 or 3 additional sterile neutrinos [46, 47].

Clearly, the implications for the Standard Model of a third, independent mass-squared splitting in the neutrino sector are enormous and potentially very exciting. The LSND result, however, lacks the strong confirmation of other experiments which the other oscillation measurements have enjoyed. It is the main goal of the Mini Booster Neutrino Experiment (MiniBooNE) at Fermilab to directly test the oscillation interpretation of the LSND data. Part III of this thesis will present the results of such a search.

Chapter 2

Accelerator-based Neutrino Beams

Neutrino physics was initially explored using natural sources (sun, atmosphere, cosmos) or nuclear power reactors which are an isotropic source of antielectron neutrinos only. The challenge of creating a directional beam of neutrinos using an accelerator earned a Nobel Prize for Lederman, Schwartz and Steinberger in 1988 for "the neutrino beam method and the demonstration of the doublet structure of the leptons through the discovery of the muon neutrino". In this Chapter, we will describe the basics of creating a neutrino beam using an accelerator and highlight the role played by hadronic interactions in the final prediction of neutrino spectra.

2.1   Overview of a conventional accelerator neutrino beam

The generation of an accelerator based neutrino beam begins with a primary proton beam impinged upon a nuclear target to produce secondary pions and kaons. Space is provided to allow these mesons to decay-in-flight into a tertiary beam of muons and neutrinos followed by a large mass of dense material to act as a beam absorber. Hadrons are quickly absorbed by nuclear interactions and muons suffer ionization loss. Only the neutrinos pass through without interacting. Downstream of the absorber one constructs physics detectors capable of seeing the rare interactions of neutrinos with the detector mass. Unique to neutrino experiments, the low interaction cross-section of neutrinos al-
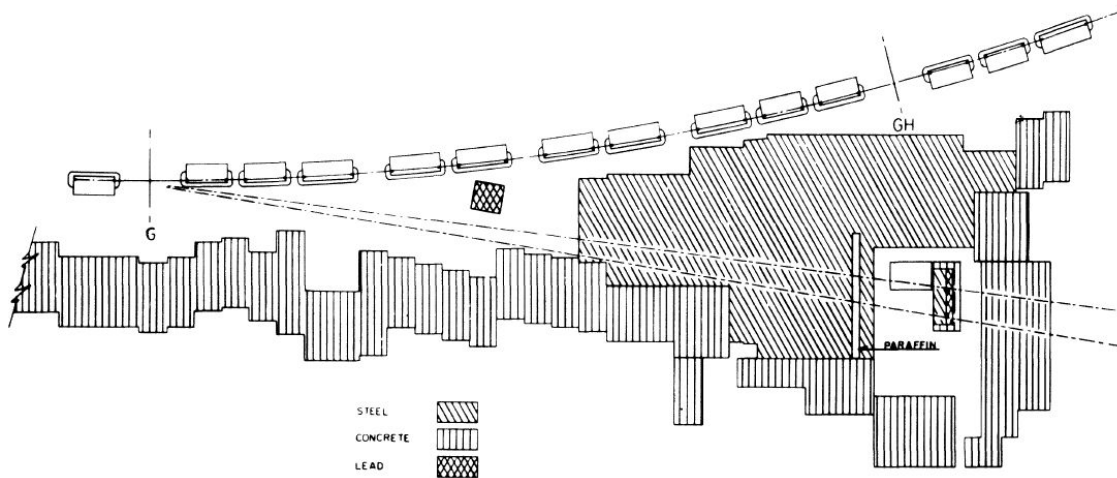
Figure 2.1: Plan view of the first accelerator neutrino beam experiment of Lederman *et al*. A beryllium target was placed in the synchrotron ring near the point labeled 'G'. A 10-ton aluminum spark chamber was placed behind 13.5 m of steel shielding and 7.5° off the proton beam axis. Plot taken from [51].

lows for multiple detectors to sit in the same beam with a negligible effect on the flux at the more distant detectors.

Figure 2.1 shows the first neutrino beam experiment of Lederman, *et al*. Protons from the AGS at Brookhaven National Laboratory struck a beryllium target placed in a straight section of the ring. The neutrino detector was placed behind steel shielding and was 7.5° off-axis with respect to the proton beam direction at the target. A neutrino beam created in this way is predominately muon neutrinos due to the favored decays of charged pions ($\pi^{\pm} \rightarrow \mu^{\pm}\nu_{\mu}(\overline{\nu}_{\mu})$, BR = 99.988%) and kaons ($K^{\pm} \rightarrow \mu^{\pm}\nu_{\mu}(\overline{\nu}_{\mu})$, BR = 63.4%) to muon flavors. The contamination of ν_e ($\overline{\nu}_e$) from K and μ decays tends to be small, of $\mathcal{O}(1\%)$. In fact, taking advantage of the high purity of neutrinos created in combination with a muon, this experiment was used to determine that the muon neutrino and electron neutrino are, in fact, unique particles [51].

While the basic principle has remained the same for over 40 years, some technological advances have increased the intensity and improved the purity of the resulting beams. Contemporary experiments extract proton bunches from the synchrotron and into a dedi-
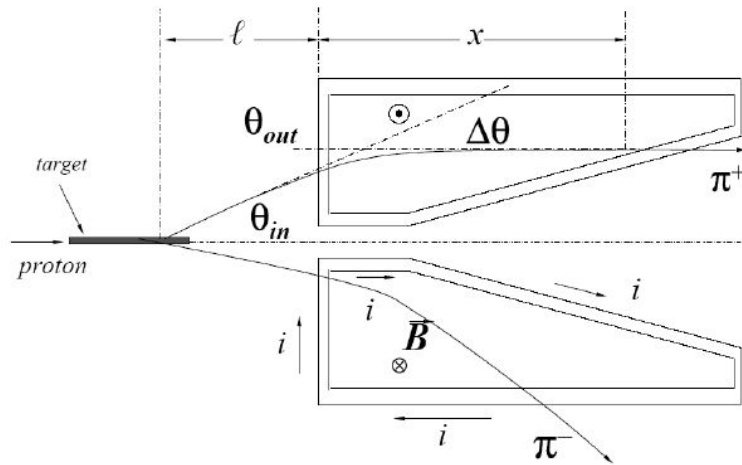
Figure 2.2: Schematic drawing of a generic horn focusing device used in neutrino beams. A typical trajectory of a π^+ and a π^- are shown (for neutrino mode running). Plot taken from [53].

cated beamline. This maximizes the efficiency for proton+target collisions and allows the neutrino experiments to be placed along the proton beam axis where meson production is maximal and symmetric.

Aligning the experiment along the beam axis also facilitates the introduction of focusing. A major enhancement of neutrino fluxes has been achieved through the addition of magnetic focusing systems, called horns, in the neutrino beam design. The neutrinos themselves, of course, cannot be focused by magnetic fields, but only their charged π and K parents. However, the daughter neutrinos are highly boosted in the laboratory frame for typical parent meson energies of $\mathcal{O}(1\,\text{GeV})$ so the neutrino direction is highly correlated with the meson direction in the lab and focusing the parent mesons acts to focus the neutrino beam.

Figure 2.2 is a schematic diagram of a generic focusing system. Focusing horns are roughly cylindrical devices made of two axially-symmetric conductors. Current is passed through the inner conductor and returns via the outer conductor, creating a toroidal magnetic field between the two shells which falls off with radius and can be well estimated by

the familiar expression for an infinitely long conductor,

$$B_\phi(r) = \frac{\mu_0 I}{2\pi r}, \quad B_r = B_z = 0 \tag{2.1}$$

where μ_0 is the magnetic permeability of air, I is the horn current and r is the perpendicular distance from the axis of the horn. The resulting $q(\vec{v} \times \vec{B})$ force on charged particles in the field will act to focus particles of one sign and defocus particles of the other, thus increasing the desired flux while reducing the antiparticle background. By changing the direction of the current in the horn one can create a predominately ν_μ (neutrino mode) or $\overline{\nu}_\mu$ (antineutrino mode) beam.

Using the approximation that the field strength is constant along the path of the particle (constant r), the angular deflection, $\Delta\theta$, that results is proportional to the strength of the field and the amount of field the particle traverses and inversely proportional to the particle's momentum,

$$\Delta\theta = \frac{Bx}{p} = \frac{\mu_0 I}{2\pi r} \frac{x}{p} \tag{2.2}$$

where x is the path length of the particle through the field region and p is the particle's momentum. The goal of any horn design is to cancel the incoming particle angle, θ_{in}, with the deflection caused by the magnetic field such that $\theta_{\text{out}} = \theta_{\text{in}} - \Delta\theta = 0$. The tapered end of the inner conductor in Figure 2.2 acts to increase x for larger values of the starting angle, θ_{in}, thus increasing $\Delta\theta$ to compensate. Horn design has become significantly more complicated than this simple example over the years and sophisticated Monte Carlo techniques are typically used to optimize the exact shape of the inner conductor which account for the full pion kinematic spectrum and the precise locations of currents through the horn materials. Nonetheless, this simple description provides an adequate framework for understanding basic horn design.

To illustrate the effect of a horn focusing system, Figure 2.3 compares ν_μ and $\overline{\nu}_\mu$ fluxes at the MiniBooNE detector for the case of no focusing system with that of using the Booster Neutrino Beam magnetic horn in neutrino mode. The increase in the ν_μ flux is more than a factor of 7 at 1.25 GeV and larger than 5 throughout the peak of the spectrum. The $\overline{\nu}_\mu$ background is reduced by the defocusing of negative pions by as much as
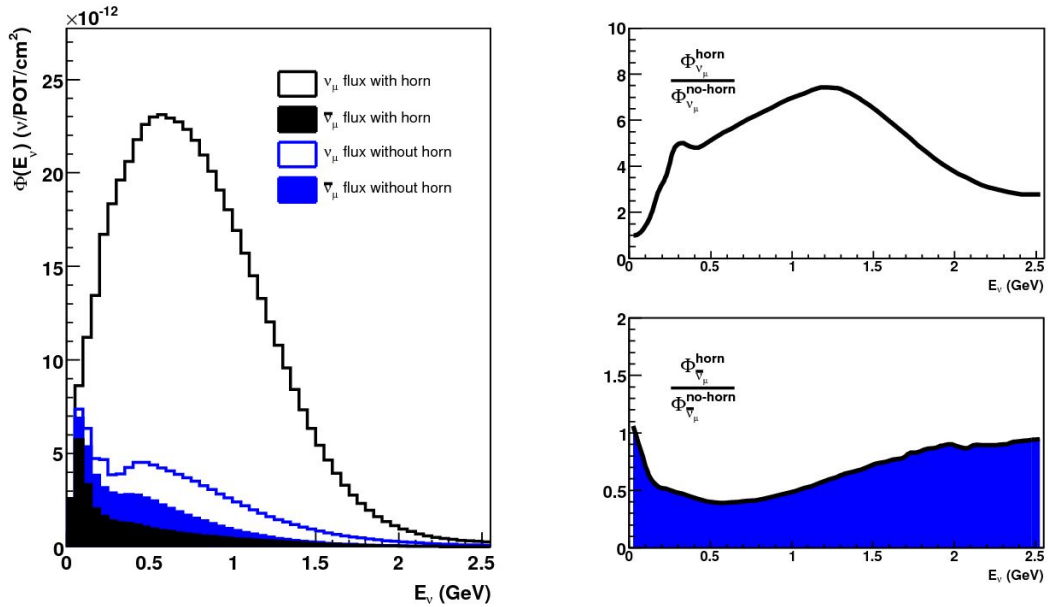
Figure 2.3: Comparison of neutrino fluxes with and without use of the magnetic focusing horn at MiniBooNE. The left panel shows the predicted fluxes of ν_μ and $\overline{\nu}_\mu$. The "with horn" curves correspond to running in neutrino mode. The ratios of with-horn to without-horn are shown on the right for ν_μ (top) and $\overline{\nu}_\mu$ (bottom).

60% at 600 MeV. Integrated across the neutrino energy range from 0–2.5 GeV the ν_μ flux is increased 4.93 times by the use of the focusing system while the $\overline{\nu}_\mu$ flux is reduced by 45%.

Predictably, the horn alters significantly the pion phase space which is relevant to the production of the neutrino flux in the detector. Figure 2.4 shows the effect. With no focusing (left panel) only very forward (small θ) π^+ contribute to the forward neutrino flux. With focusing (right panel) the pions which contribute most to the flux are slightly lower energy and produced at larger angles, $\theta \geq 50$ mrad.

Finally, we point out that a very comprehensive and up-to-date summary of the science and technology of accelerator neutrino beams has recently been provided by S. Kopp [53] and the interested reader is strongly encouraged to look there for more information.
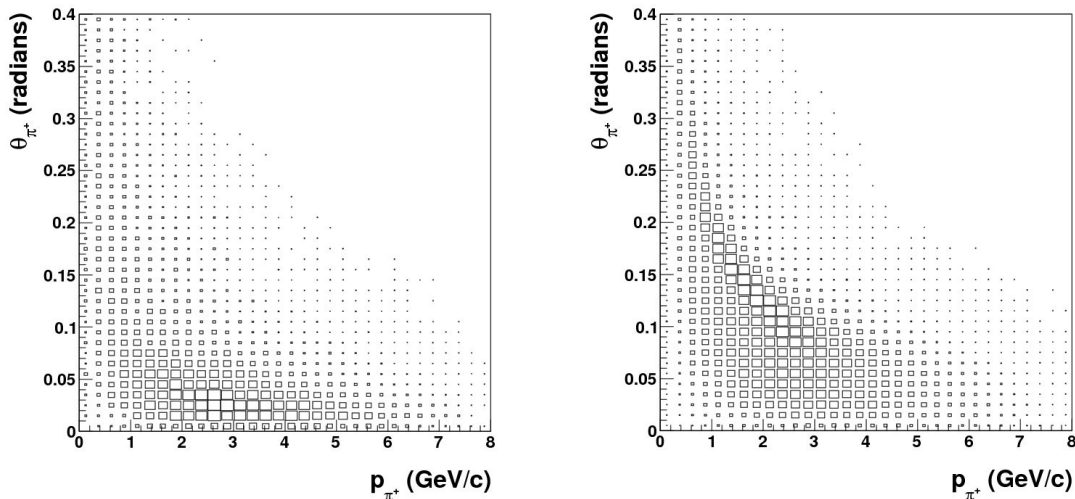
Figure 2.4: Kinematic distributions of pions (at production) which contribute to the ν_μ flux in the MiniBooNE detector via $\text{p} + \text{Be} \rightarrow \pi^+ \rightarrow \nu_\mu$ with no focusing (left) and with focusing (right).

2.2 The importance of hadronic interactions

To better motivate the measurement to be presented in the following chapters we now look in some detail at the impact of the hadronic interaction models used in the simulation of accelerator-based neutrino beams. A typical simulation of an accelerator neutrino beam begins with inclusive, double-differential production cross-sections for p, n, π^+,π^-,K^+,K^- and K^0 produced in the collisions of incident protons on a nuclear target. The major source of uncertainty in the accurate prediction of neutrino fluxes is the production of these primary hadrons. A secondary effect arises from the reinteractions and absorption that can take place in thicker nuclear targets. Further, the use of focusing systems means that a larger region of π and K phase space is relevant to the flux predictions. In this section we will explore the importance of correctly modeling these hadronic interactions and define the range over which they are important. As with horn focusing in the previous section, we will use the Booster Neutrino Beamline as an illustrative example.

Figure 2.5, taken from [53], provides a starting point for assessing the relative importance of the primary and secondary hadronic interactions. The plots show the fraction of
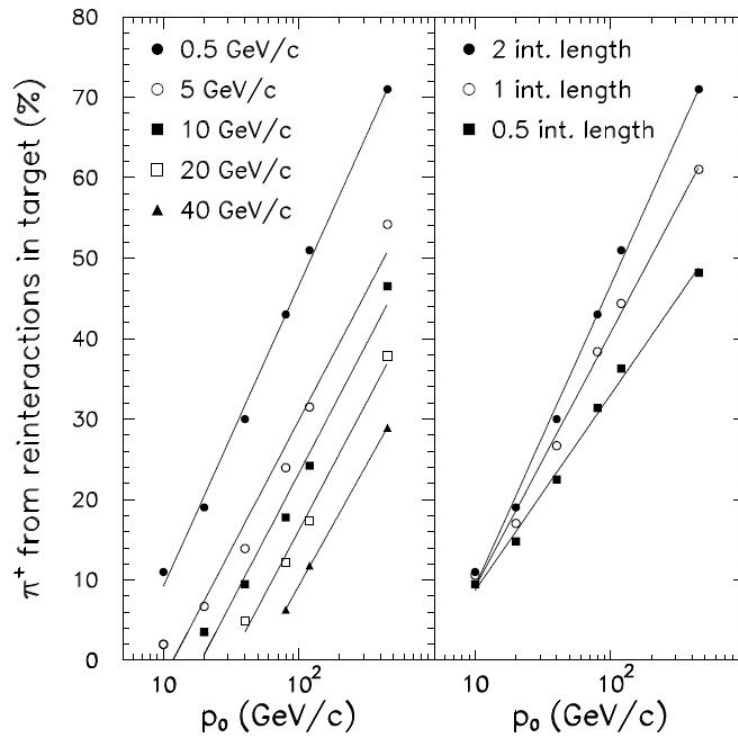
Figure 2.5: Fluka calculations of the fraction of π^+ escaping a thick graphite target which are tertiary particles as a function of incident proton momentum, p_0. The target cross-sectional area is $6.4 \times 15\text{mm}^2$. The left panel shows the tertiary fraction for a 2.0 interaction length target for π^+ with longitudinal momentum, $p_z > 0.5, 5.0$, etc.. The right panel shows the total tertiary fraction for targets of different lengths, $0.5\lambda, 1.0\lambda, 2.0\lambda$. Plot taken from [53].

π^+ escaping a thick carbon target which are tertiary particles created in interactions other than primary p+C interactions as a function of primary proton beam momentum, p_0. The fraction will depend on specific features of a particular beamline including the target material and geometry, but the plot is still very instructive. The fraction of tertiary π^+ rises sharply with the proton momentum and reaches roughly 50% for the NuMI configuration of a 120 GeV/c beam and a 2.0λ carbon target. At lower proton energies, such as that of the Booster at 8.9 GeV/c, the fraction of π^+ which are tertiary has dropped to 10%. This indicates that secondary interactions will be generally less important in the Booster Neutrino Beamline than for Neutrinos from the Main Injector.

To better quantify the impact of variations in models of hadronic interactions one can use the MiniBooNE Geant4 beam Monte Carlo. The Monte Carlo will be described in some detail in Chapter 5 and has been thoroughly presented in [94] and [69]. For this discussion it suffices to know that the interactions of p+Be at 8.9 GeV/c are handled separately from all other hadronic interactions in the simulation, including p+Be at other momenta, $\pi^\pm$+Be, K$^\pm$+Be, p+Al, $\pi^\pm$+Al, K$^\pm$+Al, etc. This modular construction facilitates the changing of models for primary and secondary interactions separately.

2.2.1 Primary hadronic interactions

Primary interactions refer specifically to the interactions of incident beam protons with target nuclei (p+Be at 8.9 GeV/c) with the most relevant result being the inelastic production of secondary pions and kaons. The multiplicity and kinematics of the produced mesons can be generated by available built-in Geant4 physics models or by inputing externally produced double-differential inclusive cross-sections for π, K production. Figure 2.6 compares the π^+, π^- and K$^+$ spectra exiting the MiniBooNE beryllium target (71 cm long $\times$ 1.0 cm diameter) when four different models are used to simulate primary interactions. MARS (v15) [121] was used to create double-differential cross-section tables while G4 LHEP, the "Low Energy Parameterization Driven Model" [124] based on the Geant3.21 GHEISHA package, G4 Bertini, the "Bertini Intranuclear Cascade Model" [123] and G4 Binary, the "Binary Cascade Model" [122] are built-in Geant4 physics packages. The comparison is striking with differences larger than a factor of 2 in pion production and still larger in kaon production. The relevant comparison, however, is in the resulting neutrino fluxes and is shown in Figure 2.7. The left panel shows the resulting ν_μ flux predictions in neutrinos per proton on target per cm^2 of detector surface area for the four different primary hadronic interaction models. All other components of the Mini-BooNE beam Monte Carlo are held fixed for these comparisons. One clearly sees that a naive choice of available hadronic interaction models is not acceptable. Just the four models shown would imply a flux uncertainty of order 50–100%. Production data is clearly needed to motivate a choice between available models or to facilitate the generation of a new one.
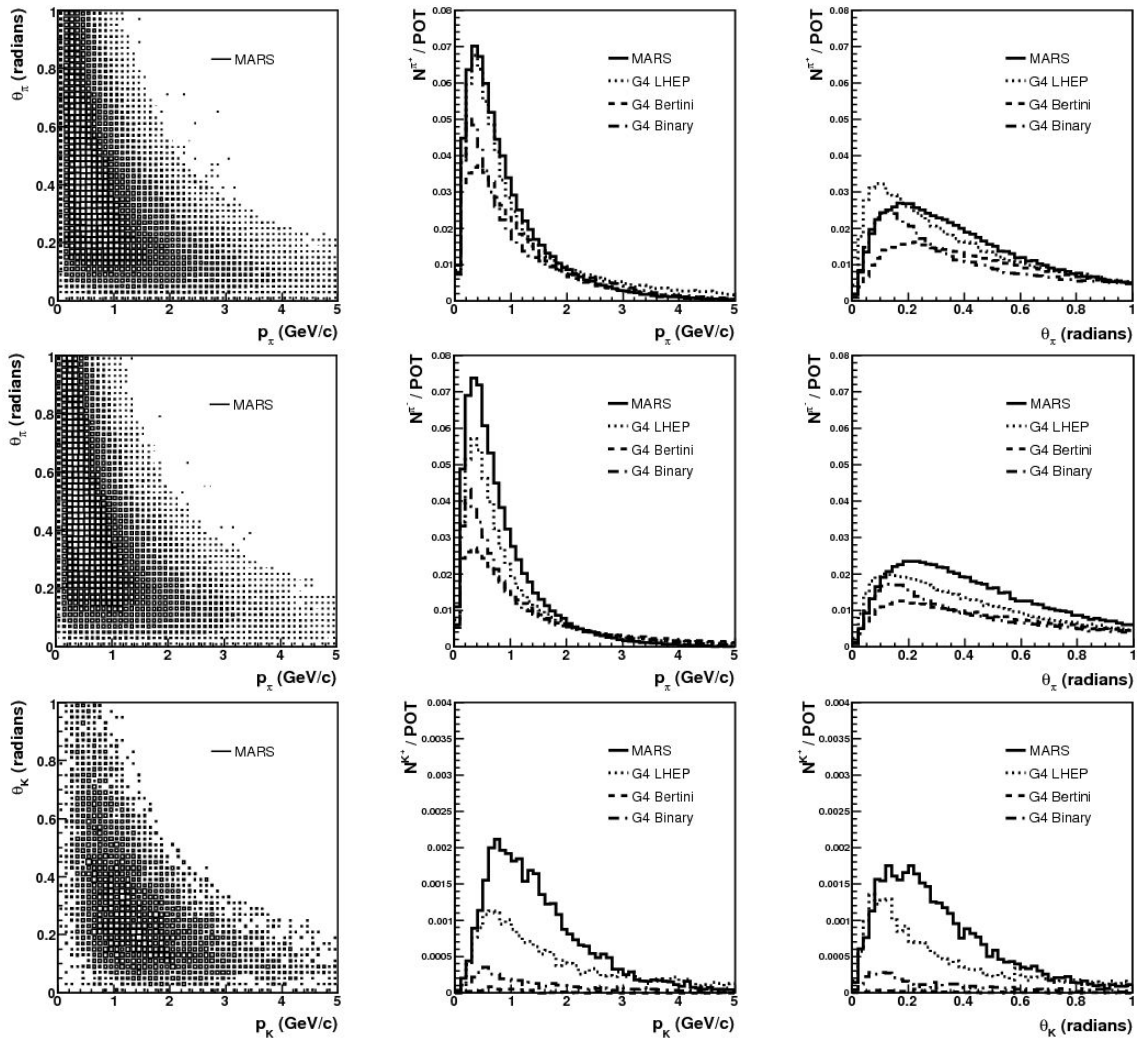
Figure 2.6: Spectra of π^+ (top), π^- (middle) and K^+ (bottom) generated in collisions of 8.9 GeV/c protons with a 1.7λ beryllium target 1.0 cm in diameter according to four different Monte Carlo hadronic interaction generators (see text). The 2-dimensional (p, θ) distributions shown on the left for one of the generators are intended as a guide to understanding the other two panels only. The middle panels compare the total π^+ momentum distributions integrated over angles up to 1 radian. The right panels compare the polar angle distributions integrated over momenta values up to 5 GeV/c. Note the vertical scale on the K^+ panels are reduced by 20x with respect to the $\pi^\pm$ panels.
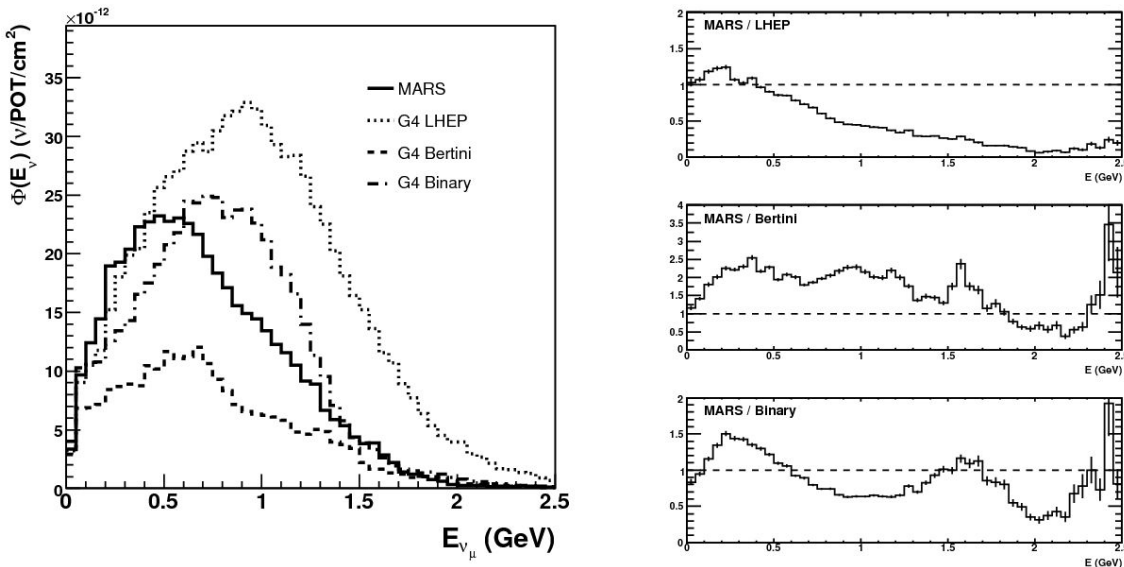
Figure 2.7: Comparison of generated ν_μ fluxes at the MiniBooNE detector for four different hadronic interaction Monte Carlos (see text) used for the production of hadrons in primary interactions of p+Be at 8.9 GeV/c.

2.2.2   Secondary hadronic interactions

Secondary interactions refer to all hadronic interactions in the beamline that are *not* incident beam protons with target nuclei at 8.9 GeV/c. The analogous comparison was made to quantify the effect of these secondary interactions on the neutrino flux prediction at MiniBooNE. Figure 2.8 shows the resulting ν_μ fluxes when the LHEP, Bertini Cascade and Binary Cascade models are used to simulate secondary hadronic interactions. All other components of the MiniBooNE beam Monte Carlo, including the simulation of primary p+Be interactions, are held fixed for these comparisons. We see in Figure 2.8 that the resulting variation in the predicted neutrino flux is much smaller than when the same models were used for primary interactions. Across most of the relevant neutrino energies the differences between the three models is $\leq$ 10% with a slight increase at the highest and lowest energies. This study indicates that an improved understanding of the effects of secondary interactions in the beamline is important but clearly a second order effect compared to primary production in p+Be collisions at 8.9 GeV/c.
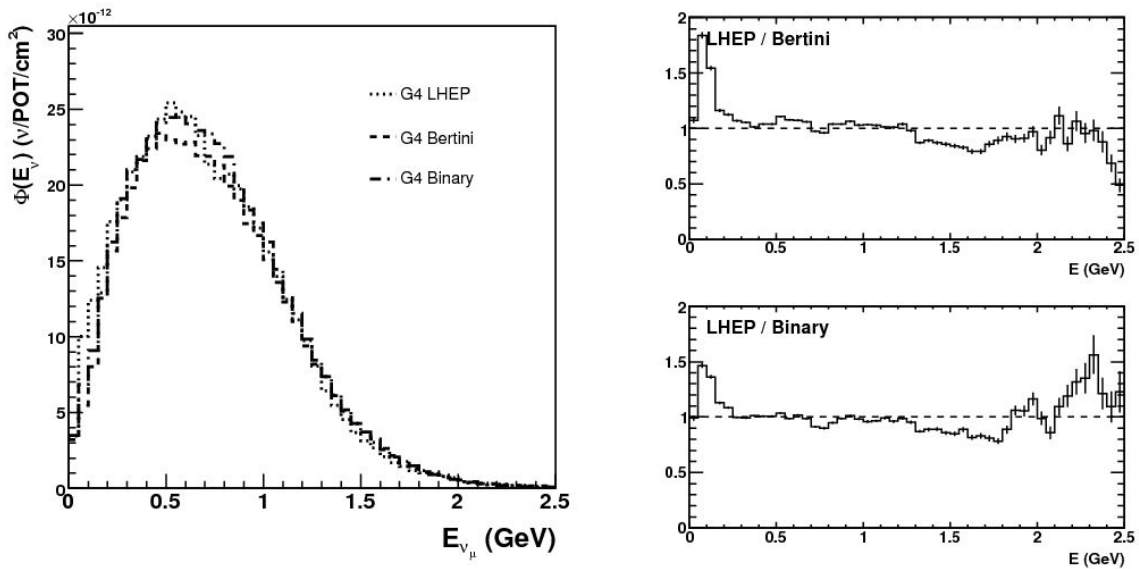
Figure 2.8: Comparison of generated ν_μ fluxes at the MiniBooNE detector for three different hadronic interaction Monte Carlos (see text) used for the interactions of all hadrons *except* primary interactions of p+Be at 8.9 GeV/c.

The best way to reduce both primary and secondary production uncertainties is by making dedicated hadron production measurements with an identically matched beam and target configuration.

2.3 Typical parameters of accelerator neutrino beams

Since the original demonstration of the neutrino beam in 1962 many accelerator neutrino beamlines have been constructed around the world. There are five beamlines which have run since 2000 or are currently being constructed; they include two in Japan at KEK and JPARC, two in the United States at Fermilab, the BNB and NuMI beams, and one in Europe at the CERN SPS.

In this chapter we have used the Booster Neutrino Beamline at Fermilab and the Mini-BooNE detector to illustrate the effects of focusing systems and to demonstrate the importance of accurate simulations of hadronic interactions within the beamline. However, each accelerator based neutrino beam has its own configuration with unique sensitivi-

ties to hadronic uncertainties. They do share some basic characteristics, however, which determine the relevant range of hadron measurements:

- Primary proton energies range from $\sim$ 10–500 GeV. The large range indicates that multiple hadron production experiments are likely needed. The mean number of pions produced per incident proton, $\langle n_\pi \rangle$, scales approximately linearly with incident proton momentum [53].

- Nuclear targets tend to be lighter elements (Be, C, Al,...) due to the difficulty of dissipating heat build-up in high-Z targets. Secondary interaction rates are also reduced in lower Z targets.

- Targets are thick (1–2 interaction lengths) to increase proton reaction rates, but secondary interactions become non-negligible. The importance of secondary interactions also increases with incident proton momentum (See Figure 2.5 and [53]).

- The relevant meson production off the target is typically forward, but can extend out to $\sim$ 20 degrees (350 mrad) in the lab frame due to focusing systems.

- Measurements of π^+, π^-, K^+, K^- and K^0 production are needed to fully understand $\nu_\mu, \overline{\nu}_\mu, \nu_e$ and $\overline{\nu}_e$ fluxes.

The specific combinations of incident proton beam energy and nuclear target for the world's neutrino beams are represented in Figure 2.9. Several modern hadron production experiments have been built in recent years to measure the secondary production for these beamlines including the Hadron Production (HARP) [54] experiment at CERN, the NA49 [99] experiment also at CERN and the Main Injector Particle Production (MIPP) [98] experiment at Fermilab. The MIPP and NA49 experiments are well suited to measure production at higher proton energies while the HARP experiment collected data for $E_p \leq 15$ GeV. In the following chapters we will present a measurement of the hadronic production cross-sections needed by the two lower energy beamlines, the FNAL Booster neutrino beam and the KEK neutrino beam in Japan.
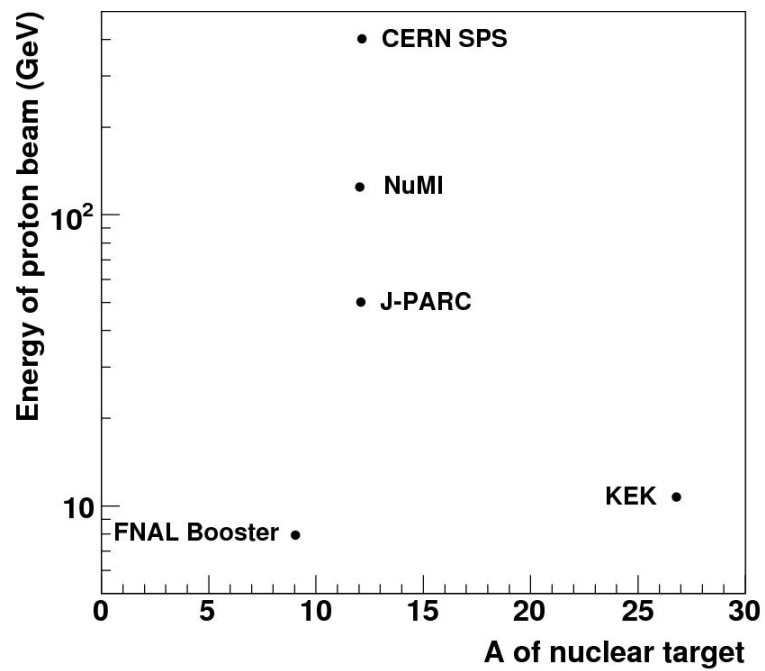
Figure 2.9: The incident proton energy and nuclear target atomic mass for the world's five accelerator neutrino beams.

Part II

HARP

Chapter 3

The HARP (PS214) Experiment at CERN

The HARP (Hadron Production) experiment, located in the T9 beam of the Proton Synchrotron at CERN, took data in 2001 and 2002. HARP is a high statistics, large angular acceptance spectrometer experiment for measuring production rates of secondary hadrons in the interactions of protons and charged pions with nuclei. Incident beam momenta in the data set range from 1.5 GeV/c to 15 GeV/c and the nuclear targets vary from hydrogen to lead. In this chapter, we describe the experimental apparatus, explore its calibration and quantify its performance.

3.1 Motivations for the HARP experiment

Precise measurements of secondary yields in hadron-nucleus collisions in the few GeV/c region are relevant to several areas of particle physics, particularly experimental neutrino physics.

The first proposed [54] goal of the HARP experiment is to contribute to optimization studies in the design of a future Neutrino Factory [49]. The front end of a Neutrino Factory would include a high intensity proton beam focused onto a high Z nuclear target for the

copious production of secondary charged pions. These pions are allowed to decay and the resulting muons must be cooled and guided into an accelerator channel. An optimized design of this complicated system (including the choice of incident proton beam momentum and target material) requires precise knowledge of the phase space distribution of the charged pions created in proton-target collisions [59].

The observation of ν_μ disappearance in neutrinos produced in the atmosphere provides a second motivation for the HARP experiment. The largest systematic in the determination of oscillation parameters from atmospheric neutrino data arises from an incomplete model of the interactions of protons and pions with nitrogen and oxygen in the Earth's atmosphere [28]. HARP has collected data with a solid carbon target (carbon has the atomic mass nearest to that of nitrogen and oxygen), as well as with nitrogen and oxygen cryogenic targets.

Third, the data recorded by HARP can have a broad impact on the improvement of models used in the simulation of hadronic interactions in this energy range. There are several hadronic interaction simulation packages which claim some validity in the energy range represented by the HARP data set, including MARS15 [121], the Binary cascade model [122], the Bertini intra-nuclear cascade model [123], the Quark-Gluon String CHIPS (QGSC) model and the Quark-Gluon String Precompound (QGSP) model. Differences between the models' predictions can be resolved and deficiencies in the models can be revealed by a detailed comparison of their predictions to a data set like that available from HARP.

Finally, measurements made at HARP can have a direct impact on the detailed understanding of the neutrino fluxes of several accelerator-based neutrino experiments, including the K2K experiment in Japan and MiniBooNE and SciBooNE at Fermilab. The K2K muon neutrino beam is created by decaying pions produced in collisions of 12.9 GeV/c protons from the KEK PS with an aluminum target. The Booster Neutrino Beam, used by MiniBooNE and SciBooNE, begins when 8.9 GeV/c protons from the Fermilab Booster are impinged upon a beryllium target. HARP recorded millions of events with these exact beam energies and target materials using both thin and thick targets. The quantitative impact of these data on the flux predictions and oscillation measurements of these exper-

iments is discussed in Appendix C.

3.2   Glossary of particles and kinematic variables at HARP

Before describing the HARP experiment in detail or presenting physics results, it is useful to explicitly state a few important definitions. Figures 3.1 and 3.2 show schematic drawings of the HARP detector and beamline for reference.

- *Primary beam particles* from the T9 beam are guided in from the left in both figures and collided with a nuclear target sitting inside the volume of the TPC.

- *Secondary particles* are created in *primary interactions* of beam particles with target nuclei. When measuring production cross-sections one is interested in these secondaries only. Hadrons created in interactions other than primary beam particles with target nuclei are a background to the measurement.

- *Tertiary particles* are those created when secondary particles decay or inelastically interact downstream of the target in air or detector materials and are not to be included in the measured cross-section.

- In the HARP coordinate system the center of the target is located at $(x,y,z) = (0,0,0)$.

- The z-axis is oriented along the primary beam direction, $+x$ is to the left and $+y$ is up.

- Given azimuthal symmetry in hadron production, all physics results are presented in polar coordinates (p, θ) where p is the total momentum of the particle and θ is the angle with respect to the primary beam direction (approximately equal to the z-axis).

- Given the rectangular geometry of the dipole and drift chambers, $\theta_x = \tan^{-1}(p_x/p_z)$ and $\theta_y = \tan^{-1}(p_y/p_z)$ are useful variables for viewing the detector in x,y-plane coordinates. They are related to the standard polar angle by $\theta = \tan^{-1}(\sqrt{\tan^2 \theta_x + \tan^2 \theta_y})$.
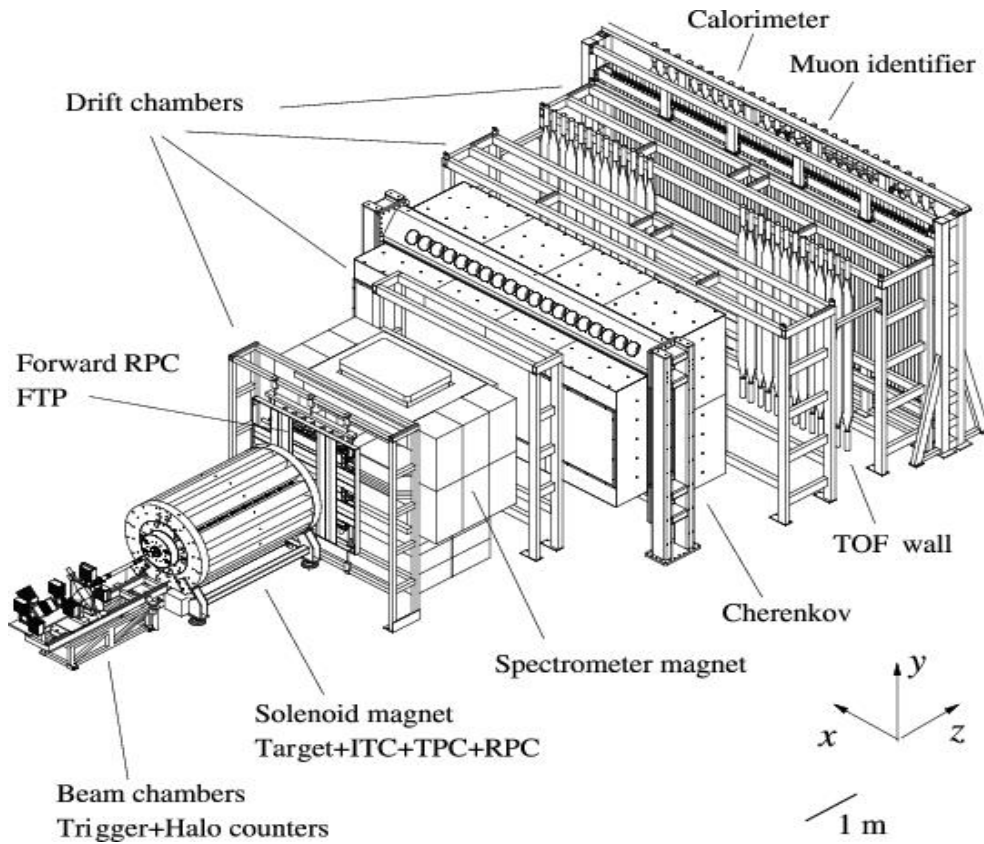
Figure 3.1: Schematic drawing of the HARP spectrometer at CERN. The large angle track-ing and PID system consists of a time projection chamber (TPC) and resistive plate cham-bers (RPC). The forward angle tracking and PID system is made up of five drift chambers (NDCs) with a spectrometer magnet, a Cherenkov (CHE) detector, time-of-flight scintilla-tor wall (TOFW), electromagnetic calorimeter (ECAL) and a muon identifier.
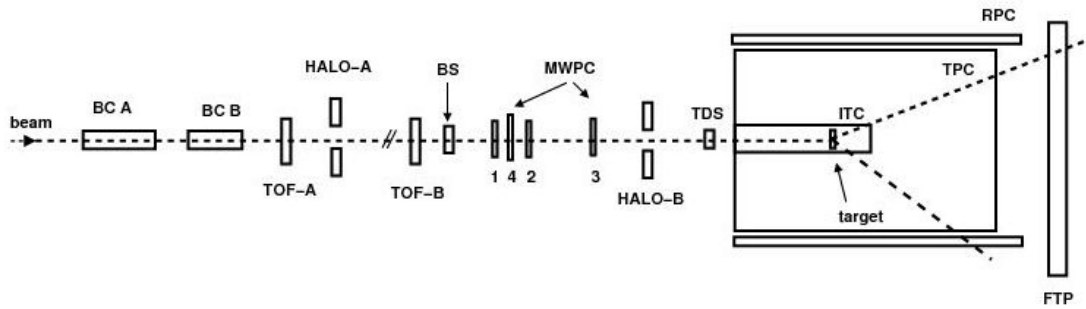
Figure 3.2: Schematic drawing of the HARP beamline showing the relative locations of the tracking (MWPC), triggering (BS,TDS,HALO-A,HALO-B) and particle identification (BCA,BCB,TOFA,TOFB) detectors. The locations of the target and ITC trigger inside the TPC volume and the FTP downstream of the TPC are also shown.

3.3   Description of the HARP experimental apparatus

The HARP experimental apparatus [55] is effectively divided into four subsystems:

- a primary beamline with tracking and particle identification (PID) instrumentation upstream of the nuclear target

- a set of triggering devices for recording different types of events

- a large angle/low momentum tracking and PID system surrounding the nuclear target

- a small angle/high momentum tracking and PID system downstream of the nuclear target

The T9 beamline is created by momentum selecting charged particles created in collisions of 28 GeV kinetic energy protons from the CERN PS with a fixed target. Either positive or negative particles can be selected with momenta between 1.5 GeV/c and 15 GeV/c. The momentum resolution of the T9 beam is about 0.24% in the momentum range used [57]. Figure 3.2 shows the relative positions of all beam detectors and trigger elements of the HARP primary beam.
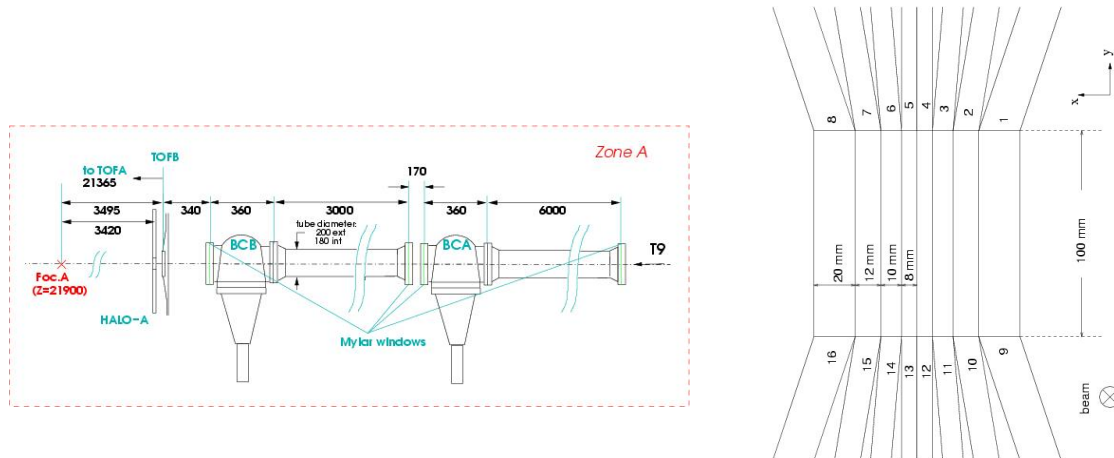
Figure 3.3: HARP beam particle identification detectors.   There are two threshold Cherenkov detectors with adjustable gas pressures (left) and two identical scintillator panels (right) for making time-of-flight measurements over a 21.4 m baseline.

Beam particle tracking is performed with a set of four multi-wire proportional chambers (MWPCs) located just upstream of the target area. The position and direction of incoming beam particles are measured with an accuracy of $\sim$ 1 mm and $\sim$ 0.2 mrad, respectively [57]. These chambers are aligned with the nominal HARP coordinate system and the downstream detectors have been carefully aligned with the beam chambers.

The incoming beam for the HARP experiment is of mixed composition, necessitating a beamline particle identification system. The PID system is comprised of two threshold Cherenkov detectors (BCA and BCB) as well as two scintillator planes (TOFA and TOFB) used to measure particle times-of-flight across a 21.4 m baseline. The Cherenkov gas volumes are 6 m and 3 m for BCA and BCB, respectively, and are filled with nitrogen gas. The pressure is adjustable allowing the thresholds to be controlled as the beam momentum is changed. The Cherenkov light produced is read out via a single photo-multiplier tube attached to each detector. The tagging efficiency for pions and electrons is nearly 100%. TOFA and TOFB are identical counters comprised of eight 5 mm thick scintillator slabs oriented vertically as shown in Figure 3.3 each read out by two Hamamatsu H1949 PMTs. The varying widths were selected to roughly equalize the rates for the eight strips.

The trigger system is comprised of scintillator planes in the T9 beamline to trigger on the presence of an incoming beam particle, as well as planes surrounding the nuclear target to trigger on hadrons emanating from the target volume. The Beam Scintillator (BS) is the start of the triggering logic for each event and in combination with a hit in TOFB is the minimum requirement for the lowest level trigger. Additionally, the BS provides the reference time for all ADC gates in other sub-detectors. The BS is comprised of a single scintillator slab 5 mm in thickness and with an 80 mm $\times$ 80 mm sensitive area perpendicular to the beam axis which is read out by a single Philips XP2020 photo-multiplier tube (PMT). Two HALO counters (HALO-A and HALO-B) are scintillator slabs with a central hole and are used to veto events where the beam particle is accompanied by a second particle in the halo of the beam.

The Target Defining Scintillator (TDS) is a circular scintillator volume 20 mm in diameter and read out by four Hamamatsu R1635P 3/8 inch PMTs. The efficiency to record at least one hit when a beam particle passes through the TDS is $> 99.9\%$ and its location as near as possible to the upstream end of the target volume nearly guarantees its correlation with a beam particle striking the target.

There are two downstream trigger counters (see Figure 3.4), one for the large angle spectrometer and one for the forward angle system. The Inner Trigger Counter (ITC) is a cylindrical tube mounted inside the TPC field cage and provides a trigger for the large angle system. Six layers of scintillator fibers are read out by 24 Hamamatsu R1635P 3/8 inch tubes resulting in a trigger efficiency $> 99\%$. The forward angle system is triggered by the Forward Trigger Plane (FTP). The FTP is comprised of two orthogonal planes of seven scintillator slabs each with a total area of 1240 mm $\times$ 1400 mm. Light is read out on both ends of each slab by Hamamatsu R2490 fine-mesh tubes. The FTP plane is located just downstream of the TPC volume as shown in Figure 3.1 and triggers on forward tracks with an efficiency $> 99.8\%$. A 60 mm diameter hole has been cut out along the beam axis to allow non-interacting beam particles to pass without triggering the FTP.

The tracking and identification of particles beyond the target region consists of separate large angle and forward angle systems. Tracking in the angular region beyond $\sim 20°$ is achieved by a 3972 channel time projection chamber (TPC) built specifically for the
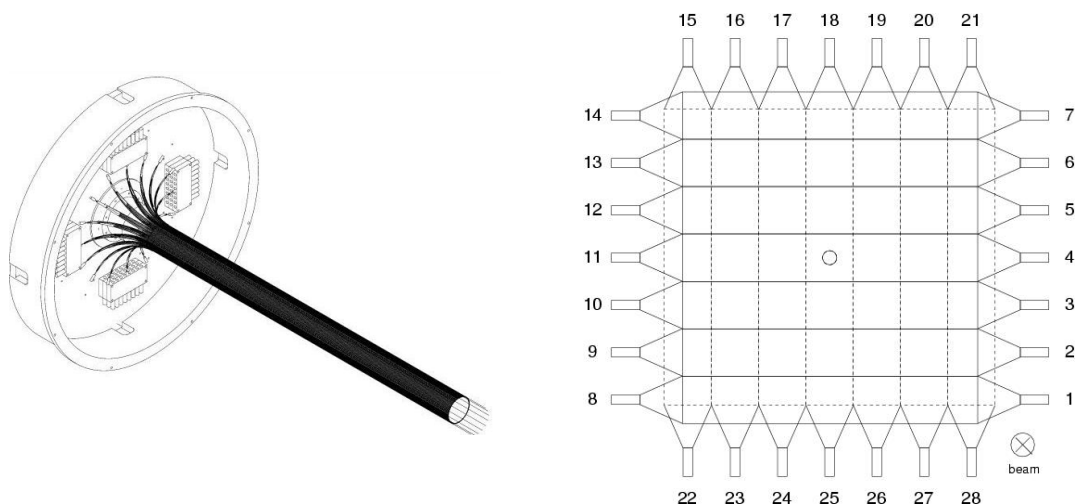
Figure 3.4: HARP downstream trigger counters. The left panel shows the Inner Trigger Counter (ITC) which surrounds the target volume inside of the TPC. The right panel is a schematic drawing of the 14 scintillator slabs of the Forward Trigger Plane (FTP) which sit downstream of the TPC and triggers on forward going particles.

HARP experiment. The TPC sits inside a 0.7 T solenoidal field enabling momentum reconstruction of tracks. Particle identification is primarily done using a dE/dx measurement provided by the TPC and is supplemented by a time-of-flight measurement given by resistive plate chambers which surround the TPC volume. The TPC and RPCs have been described in detail elsewhere [55] and will not be repeated here. The cross-sections which will be presented as part of this dissertation have been measured using only the forward spectrometer of the HARP detector. The relevant meson production for the creation of traditional accelerator-based neutrino beams is forward (0–0.30 rad) and at large momenta (0.5–6 GeV/c). These ranges are best covered by the forward tracking system and PID detectors.

In the forward detector, tracking is performed by five drift chamber modules previously used by the NOMAD experiment [50] (for this reason they are referred to in what follows as the NOMAD drift chambers, or NDC1–5). The five chambers are arranged in three planes perpendicular to the beam axis as shown in Figure 3.1 (the fourth plane shown was never instrumented). Sandwiched between NDC1 and NDC2 is a large aper-

ture dipole magnet ($x \times y \times z$ = 2.41 m $\times$ 0.88 m $\times$ 1.72 m). The magnetic field is not homogeneous with a maximum B_y = 0.5 T at the center of the field region. The field of the spectrometer magnet was mapped using Hall probes and this map has been used in the reconstruction program.

The chambers all consist of four modules each containing three planes of wires making a possible 12 hits per chamber. This implies that a short 3D segment for determining the direction of the track can be reconstructed at each chamber position. The three sense wire planes are oriented at $0°$, $+5°$ and $-5°$ with respect to the vertical axis. A detailed description of the electronics, alignment procedure and the spatial resolution of reconstructed points can all be found in [55]. Below, we will focus only on higher level features of the drift chamber system such as the track reconstruction efficiency and the resolution and absolute scale of track momentum measurements.

Particle identification in the forward spectrometer is performed using a Cherenkov detector (CHE) and a time-of-flight system that includes the beam TOF counters in combination with a scintillator wall (TOFW) downstream of the third drift chamber plane. An electromagnetic calorimeter (ECAL) beyond the TOFW distinguishes electrons from hadrons, but has only been used in this analysis to reject electrons when quantifying the response of the other PID detectors.

The Cherenkov detector is located just downstream of NDC2 and the spectrometer magnet (Figure 3.1). The detector volume is filled with perfluorobutane (C_4F_{10}) whose high refractive index allows it to be operated at atmospheric pressures. The total volume of the Cherenkov vessel is about 31 m^3 with a 6 m $\times$ 3 m cross-section along the beam direction. Photons are collected by two rows of nineteen EMI 9356-KA 8-inch photomultiplier tubes, one mounted above and one below the gas chamber with the tube faces pointing away from the incoming beam. Two large cylindrical mirrors deflect the photons backward at about $135°$ upward or downward to the two rows of tubes. Signals in the PMTs are clustered together to give a total number of photo-electrons and a reconstructed position in the $x - y$ plane. This hit position can then be matched to reconstructed particle tracks from the drift chamber information.
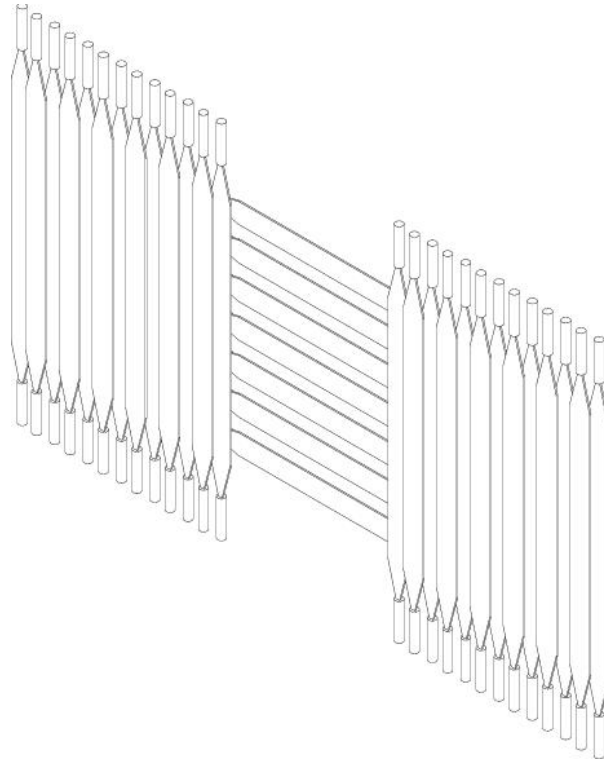
Figure 3.5: Layout of the 39 scintillator slabs that comprise the TOFW at the HARP experiment.

The TOFW is made up of 39 BC-408 bars from Bicron, 2.5 cm thick and 21 cm wide. Two lengths are used, 250 cm and 180 cm, and each slab is read out on both ends by Philips XP2020 photo-multiplier tubes. The TOFW is locateded $\sim$ 10 m downstream of the nuclear target and the configuration of the scintillator slabs is shown in Figure 3.5. The slabs overlap by 2.5 cm to ensure full coverage, and the total active area is $\sim$ 6.5 m $\times$ 2.5 m. The vertical position in the outside slabs and the horizontal position in the central slabs can be determined from the time difference of the hits in the PMTs at either end of the counter. The position in the other dimension can only be determined to within the width of the scintillator slabs, 21 cm. As with the CHE, the $x - y$ position of a hit in the TOFW can be used to associate a time measurement with a reconstructed particle track.

3.4 Calibration and performance of the HARP sub-detectors

This section will concentrate on the performance of the various subsystems of the HARP beamline and forward angle spectrometer. Primary beam particle identification and secondary track reconstruction, momentum resolution and PID will be described for the relevant particles in the relevant regions of phase space. Chapter 4 will then focus on using the detector with the demonstrated performance to extract the production cross-sections of pions and protons for two different beam and target configurations.

3.4.1 Primary particle identification in the T9 beamline

3.4.1.1 Beam Cherenkov detectors

The beam Cherenkov counters require no post data-taking calibration beyond inspection of the hit distributions and determination of a cut value to select the desired particle type. The gas pressures can be adjusted for different beam momentum settings to select $e^\pm$ only, $e^\pm$ and $\pi^\pm$, or even $e^\pm$, $\pi^\pm$ and $K^\pm$. Additional flexibility is provided by the existence of two counters which can be adjusted separately. The two counters should be configured to best compliment the discrimination power of the TOF system. Below 3 GeV/c, for example, the TOF can completely separate the heavier particles, so the beam Cherenkovs are set to select electrons only. At momenta above ~ 8 GeV/c, the TOF can no longer separate pions and protons, so the gas pressures are set to radiate for $\pi^\pm$. Figure 3.6 demonstrates the performance of the beam Cherenkov PID system for an 8.9 GeV/c beam.

3.4.1.2 Beam time-of-flight system

The beam time-of-flight system (BTOF) is a critical system even for high momentum beam settings where there is no discrimination power for identifying beam particles. Timing information from TOFA, TOFB and the TDS is used to extrapolate and estimate an arrival time of the beam particle at the nuclear target. This time, t_0, is the start time for the time-of-flight measurements made by the TOFW. Without this t_0 a TOF measurement
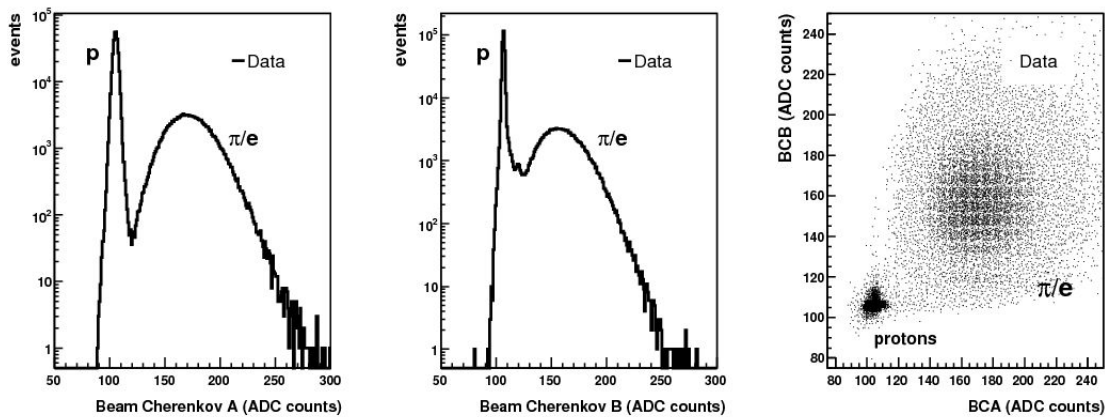
Figure 3.6: Beam Cherenkov distributions for an 8.9 GeV/c beam. Protons are clearly visible at the ADC pedestal values. Pions and electrons can be selected with nearly 100% efficiency by requiring an ADC count above pedestal in both BCA and BCB.

of particles created in the target cannot be made. Also, since the resolution of the downstream TOF measurement is given by $\sigma_{\mathrm{TOF}} = \sqrt{\sigma_{\mathrm{TOFW}}^2 + \sigma_{t_0}^2}$, a well calibrated BTOF system is important for both primary and secondary PID.

Calibration of the beam time-of-flight detectors   The BTOF detectors are, in many ways, small versions of the ~ 16 m^2 TOFW downstream. The TOFW, TOFA and TOFB are all made up of thin scintillator bars instrumented with a PMT at each end for which an ADC and TDC count is recorded. The calibration methods for the two detector systems, therefore, are similar. Calibration of the TOFW has been maintained through a combination of dedicated cosmic ray runs, a laser system and beam particles. Calibration of the BTOF system was performed using beam particles only. For a detailed description of the calibration of the TOFW see [62].

Several effects must be considered for the proper calibration of plastic scintillation counters being used for precise timing measurements.

- non-linear time-to-digital converter (TDC) performance

- time slewing due to varying signal amplitudes which are read from analog-to-digital converter (ADC) channels

- light propagation time and hardware delays unique to each PMT channel in the TOF
  system

The intrinsic resolution (without calibration) of a time-of-flight measurement using the
BTOF system at HARP, $\Delta t = t_{\text{TOFB}} - t_{\text{TOFA}}$, is ~ 260 ps. After applying the calibrations
described here the timing resolution is improved to better than 160 ps, demonstrating the
importance of such corrections. The final resolution on the determination of t_0 will be
~ 70 ps.

PMT signals are split and carried to the ADC and TDC electronics. The expected per-
formance of the 37 TDC channels (TOFA(16), TOFB(16) ,TDS(4) and BS(1)) is 35 ps/count.
A more accurate time estimation is achieved, however, by considering the non-linear devi-
ations from this specification for each of 4096 TDC bins for all 37 channels. The conversion
factors have been measured off-line for all BTOF channels, and Figure 3.7 shows values
of Δt per TDC bin for one representative channel (TOFA ch. 1). A Gaussian fit to the last
3096 values of Δt reveals a mean conversion factor of 37.0 ps with a width of 1.0 ps. The
average conversion factors range from 35.3 ps to 37.6 ps for the 37 TDC channels.

With the TDC reading converted to a time value, one must next consider pulse-height
effects. The time measurement will depend on the amount of charge created in the photo-
multiplier tube. Events generating less charge, or, equivalently, a lower ADC count, will
record later times due to the longer rise time for the pulse to cross the hardware thresh-
old. This effect has proved significant in all three BTOF detectors, TOFA/B and the TDS.
Figure 3.8 shows converted TDC readings as a function of ADC counts for a characteristic
channel (TOFB ch. 5) as a scatter plot and a profile histogram. 8.9 GeV/c protons were
selected using the beam Cherenkov detectors to generate the distribution. The profile
histogram has been fit to an expansion in $1/\sqrt{\text{ADC}}$ to three terms,

$$f(\text{ADC}) = p_0 + p_1 \frac{1}{\sqrt{\text{ADC}}} + p_2 \frac{1}{\text{ADC}} + p_3 \frac{1}{\text{ADC}^{3/2}} \tag{3.1}$$

and the four parameters extracted (the constant, p_0, is discarded). A parameterization has
been generated for each channel and is used to apply a timing correction to all converted
TDC counts. Figure 3.8 shows that this pulse-height correction can be as large as 1.5 ns
for low ADC values.
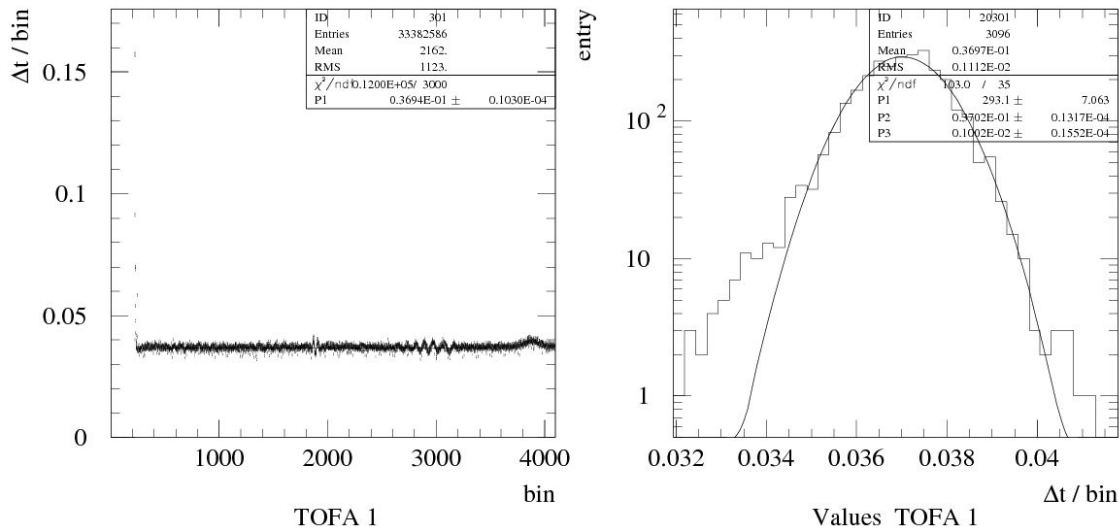
Figure 3.7: Non-linear TDC-to-time conversion for TDC channel 1 in TOFA. The left panel shows the measured Δt/bin for each of 4096 bins in the TDC. In the right panel the last 3096 Δt/bin values are histogramed and fit to a Gaussian function with $\bar{\mu} = 37.0$ ps and $\sigma = 1.0$ ps.
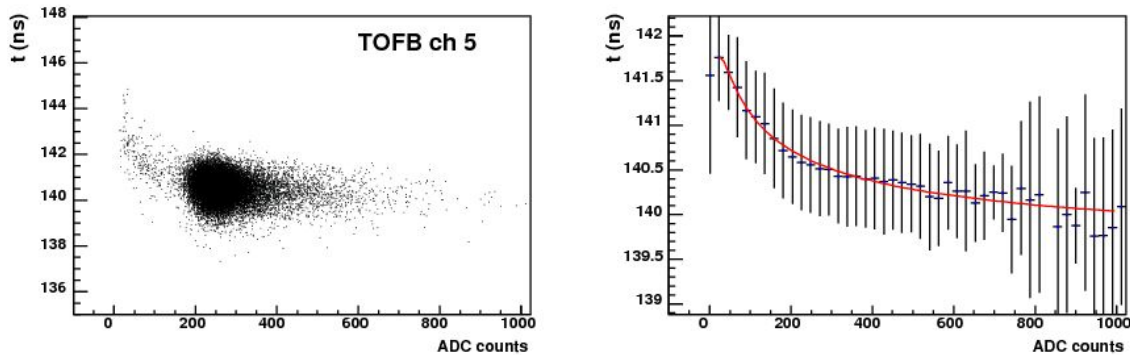
Figure 3.8: Reconstructed time as a function of pulse-height (ADC count) for TDC channel 5 in TOFB. The right panel is a profile histogram of the scatter plot on the left. A parameterization (see text) has been fit to the profile histogram to extract the pulse-height correction. Similar fits were performed for all 37 BTOF system channels.
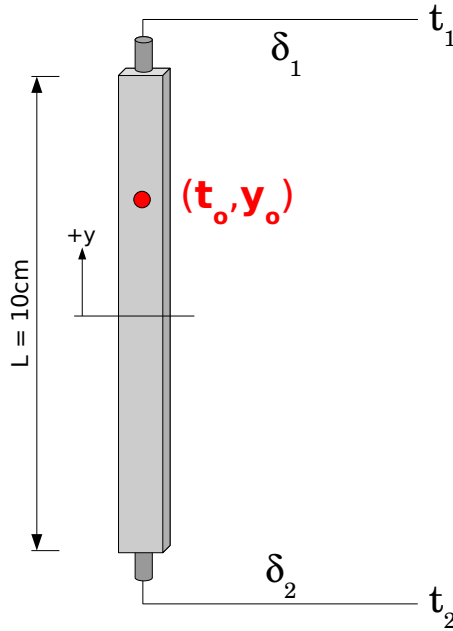
Figure 3.9: Schematic diagram of a scintillator strip in TOFA/B with a photo-multiplier tube read out from each end.

Before one can measure a meaningful time-of-flight between any pair of detectors, the 37 channels of the BTOF system must be brought into a common time reference-frame. This requires the determination of the 37 unique signal delays in each circuit due to the hardware components - mostly the signal cables connecting PMTs to the ADC/TDC hardware. Figure 3.9 is a schematic depiction of a typical scintillator in TOFA/B. The strips are 10 cm in length and the width varies across the eight slabs from 8–20 cm (see Figure 3.3).

If a particle strikes the scintillator at known time t_0 and vertical position y_0 then the corrected (TDC-to-time converted and pulse-height corrected) times in the two PMT channels, t_1 and t_2, are given by

$$t_1 = t_0 + \frac{\mathrm{L}/2 - y_0}{v_{\mathrm{eff}}} + \delta_1 - t_{\mathrm{ref}}, \qquad t_2 = t_0 + \frac{\mathrm{L}/2 + y_0}{v_{\mathrm{eff}}} + \delta_2 - t_{\mathrm{ref}} \qquad (3.2)$$

where t_0 is the true time the particle passes the detector (NOT target arrival time in this case), L = 10 cm is the total length of the scintillator strips in TOFA/B, y_0 is the vertical

position of the particle as it passes the detector, $v_{eff} \sim 0.57c$ is the effective velocity of light in the scintillators, δ_1 and δ_2 are the delays in the top and bottom channels, respectively and t_{ref} is a global time reference signal. The sums and differences of these two quantities are used to determine the delays for the two channels.

$$\Delta T = \frac{t_2 + t_1}{2} = t_0 + \frac{L}{2v_{eff}} + D - t_{ref} \tag{3.3}$$

$$\Delta t = \frac{t_2 - t_1}{2} = \frac{y_0}{v_{eff}} + \frac{d}{2} \tag{3.4}$$

where $D = (\delta_2 + \delta_1)/2$ and $d = \delta_2 - \delta_1$. The sum of the delays, D, can be immediately determined from the timing information; the y position of the hit has canceled out of the equation. The difference, however, requires knowledge of the y position of the beam particle as it passes each detector. The MWPC tracks have been used to extrapolate to the TOFB detector and this position is used in the delay calculation. TOFA is upstream of several quadrupole magnets, making the extrapolation impossible, so the middle of the detector must be assumed. The bias introduced is small, however, of the order $y_0/v_{eff} \approx$ 1.0 cm/0.6c ~ 0.05 ns.

As when calculating the pulse-height corrections above, applying strong cuts to the beam Cherenkov signals provides pure samples of particles of known β to be used for calibration purposes. The beam momentum setting, particle mass and path length (as determined from the MWPC track) are used to calculate the expected t_0 at the given detector. Here t = 0 is defined at z = 0, so the times are, by convention, negative, as the detectors are all upstream of the target. Knowing t_0, the channel delays δ_1 and δ_2 can be calculated from equations 3.3 and 3.4.

All calibration parameters except the non-linear TDC conversion numbers had to be generated for each experimental configuration in the HARP data set (beam momentum and target) after it was determined that the running configurations were not sufficiently constant beyond a time period of weeks. Currently, calibrations for 68 configurations are incorporated into the HARP analysis tools and are used by the collaboration for all official analysis.

Beam time-of-flight system performance Applying the non-linear TDC-to-time conversion, the parameterized pulse-height correction and the channel delay offsets, the reconstructed time, t, for any PMT channel, $j = 1\text{--}37$, is given by

$$t_j = \sum_{i=0}^{\text{TDC}} (\Delta t_i)_j - f_j(\text{ADC}, p_1, p_2, p_3) - \delta_j \tag{3.5}$$

where i is used to sum over TDC bins up to the recorded TDC value. Combining the reconstructed times in a pair of PMT channels on a single scintillator strip and solving Eq. 3.3 for t_0 one can reconstruct the time the beam particle passed that detector. A reconstruction package has been incorporated into the HARP analysis tools to apply the available calibrations and reconstruct the higher lever quantities t_{TOFA}, t_{TOFB} and t_{TDS} as well as the t_0 to be described in the following section.

Figure 3.10 demonstrates the BTOF reconstruction using this calibration for a 3.0 GeV/c and a 5.0 GeV/c beam. At 3.0 GeV/c kaons are separable from pions and electrons at about 3.9σ and pions and protons are easily distinguished at over 13σ. At 5.0 GeV/c pions and protons are still separable at nearly 5σ. Beyond 5.0 GeV/c the BTOF system is not used for beam particle identification.

Calculating t_0 Above 5.0 GeV/c beam momentum nearly all ability to identify beam particles by time-of-flight alone is lost. However, a well calibrated system remains important as TOFA, TOFB, and the TDS detectors are used to determine an arrival time of a beam particle at the target (z=0 in this analysis). This t_0 then serves as a start time for subsequent secondary particle time-of-flight measurements. The time-of-flight resolution for secondaries is, therefore, determined by the beam detectors as well as the TOF wall.

In calculating the t_0 for an event it was noted that the uncertainty in the beam momentum is small compared to that in the timing measurements made with the three beam detectors. Therefore, one uses the β of a beam particle based on the T9 momentum setting and the particle's mass to propagate the times forward to z = 0 m instead of using the beam detectors to measure a velocity. This method allows three separate calculations of t_0 (from three separate detectors), reducing the error significantly. Additionally, it becomes possible to calculate a t_0 value even in the case where only one beam detector registers a
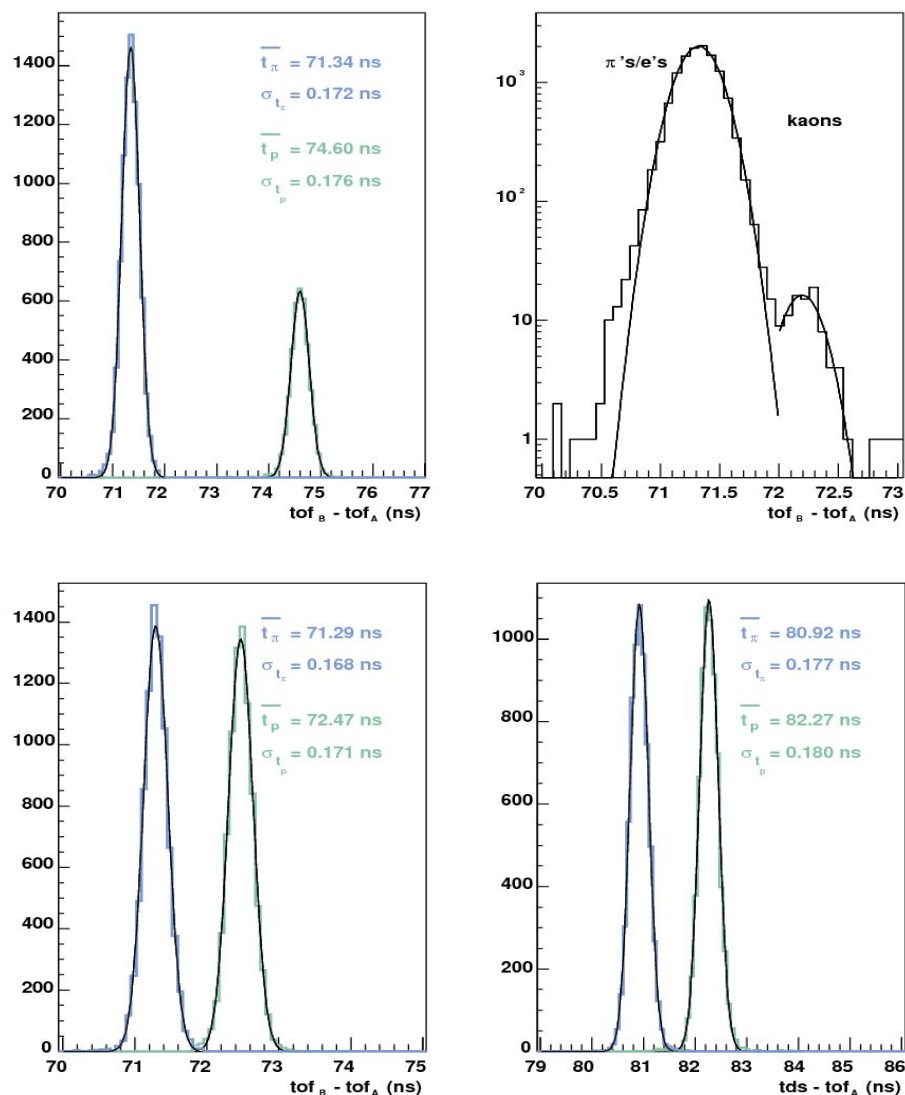
Figure 3.10: Beam time-of-flight measurements for two different beam momenta after calibration. The top two panels show TOFB-TOFA measurements for a 3.0 GeV/c beam at two different zoom levels; the second plot shows a clear kaon peak separate from the pions and electrons at about 3.9σ, and these are separated from protons at over 13σ. The bottom two panels show the TOFB-TOFA and TDS-TOFA reconstructions for a 5 GeV/c beam. The pion and proton peaks are separated at about 4.9σ.

Run #	Momentum	σ_A (ps)	σ_B (ps)	σ_{TDS} (ps)	σ_{t_0}
19130	1.5 GeV/c	109.5	136.7	138.2	72.7 ps
14180	3.0 GeV/c	114.4	130.9	135.8	72.8 ps
14425	5.0 GeV/c	108.3	130.8	141.7	71.9 ps
17900	8.9 GeV/c	115.4	116.7	138.5	70.6 ps
18263	12.9 GeV/c	108.2	118.0	128.4	67.8 ps

Table 3.1: Beam time-of-flight and t_0 resolutions for five different runs and beam momenta.

hit for an event, increasing the efficiency of attaining a t_0 value to $> 99\%$.

The drawback to this method is that particle identification is required to choose the correct mass for determining β. In order to retain as much information as possible and allow for later adjustments, a t_0 value is calculated and stored based on four different particle type assumptions: proton, pion, kaon, and electron.

$$t_0^\alpha = \frac{1}{N} \sum_{i=1}^{N} \left(t_i + \frac{d_i}{\beta^\alpha c} \right) \tag{3.6}$$

where α is the particle type (p, π, K, or e), t_i is the time measured by the ith detector, d_i is the path length of the particle from detector i to z = 0, and $\beta^\alpha c = pc/\sqrt{p^2 + m_\alpha^2}$ is the velocity. Assuming that the uncertainty on d_i and the momentum are negligible compared to the time measurements, we see that the t_0 found from Eq. 3.6 is the average of three independent t_0 values each with the uncertainty of the respective time measurement, σ_{t_i}. For a sample whose individual measurements have unique uncertainties the error on the mean can be found from

$$\sigma_{t_0}^2 = \frac{1}{\sum_{i=1}^{N} 1/\sigma_{t_i}^2} \tag{3.7}$$

Table 3.1 lists the t_0 resolutions for five runs in the HARP data set. The average resolution is ~ 70 ps which is almost negligible compared to the resolution of measurements in the TOFW, ~ 160-170 ps.

3.4.2 Secondary track reconstruction using the NDCs and dipole magnet

3.4.2.1 Secondary track reconstruction algorithm

The five drift chambers are used to reconstruct particle trajectory parameters downstream of the target area. The full path is needed to match particles with reconstructed hits in the Cherenkov, TOFW or calorimeter. The directions before and after entering the field area of the dipole magnet are used to determine the particle's momentum.

Due to safety regulations, HARP was forced to use a different chamber gas mixture than the NOMAD experiment before it. The result of changing to a non-flammable mixture (Ar-90%, CO_2-9%, CH_2-1%) was a significant reduction in wire hit efficiency to $\sim 80\%$. A standard reconstruction algorithm which combines triplets of hits (u, x, v) to generate 3D space points was, therefore, not adequate as the 3D point efficiency would go as 0.8^3, or about 50%.

Secondary track reconstruction is performed in several stages. The building, fitting, extrapolation and matching of tracks is all performed by a sophisticated software package called RecPack [63] developed by HARP collaborators and based on the Kalman Filter [64] technique. First, 2D plane segments and 3D track segments are constructed in individual chambers (recall that each chamber is comprised of four modules each with three planes of wires for 12 total wire planes):

- *Plane (2D) segment* - At least three hits out of four in the same projection ($0°$, $+5°$ or $-5°$) compatible with being aligned.

- *Track (3D) segment* - More than one plane segment of different projections whose intersection(s) define a 3D straight line. A track segment can be made from 3 plane segments or 2 plane segments and a single hit which intersects the 3D line defined by the two segments.

Note that this method requires a minimum of seven hits out of twelve wire planes to create a track segment.

Individual chamber segments downstream of the dipole magnet (NDC2–5) are then

combined to form longer, straight line segments[1]. At this point the Kalman Package is capable of extrapolating these long segments to all PID detectors downstream of the dipole (including the TOFW, CHE and ECAL) for hit matching. All possible combinations of track segments and reconstructed PID hits are attempted and matching-χ^2's calculated.

Finally, downstream segments must be matched with a 3D point or segment upstream of the dipole to determine the track momentum. Two independent upstream constraints on the track have been used to make independent momentum measurements of each reconstructed track. The first uses the well defined interaction vertex where the secondary particle was created. The x, y coordinates are provided by the MWPC extrapolation of the primary beam particle to the $z = 0$ plane, or the target center[2]. A matching χ^2 is constructed between the beam particle extrapolation, (x_0, y_0), and the extrapolated position of track segments constructed downstream of the dipole, (x_t, y_t). The algorithm loops over allowed values of the momentum and minimizes this χ^2 to estimate the momentum, p_{v}, of each secondary. Multiple scattering and inhomogeneities in the dipole magnetic field are fully taken into account by the Kalman Filter implementation. An upper cut on this χ^2 has been applied to reduce contamination by tertiary particles which have not emanated from the primary vertex. This cut will account for about a 1% inefficiency in this algorithm.

The second upstream constraint is provided by 3D segments reconstructed in the upstream drift chamber, NDC1. The matching algorithm works similarly to the one just described but matches to the NDC1 segment to estimate each particle's momentum, p_{NDC1}. This algorithm suffers a major disadvantage relative to the one using the event vertex described above. The tracking efficiency is now directly proportional to the segment efficiency of NDC1. The segment efficiency in NDC1 is known to be much lower than the other chambers and, further, suffers from charge saturation caused by the bright beam spot even for modest event rates. This saturation is difficult to simulate or measure and

---

[1]Actually, the Kalman Package does take into account multiple scattering between drift chambers and does not just assume a perfect straight line path.

[2]The 5% nuclear interaction length targets used in these analyses are all $\sim$ 2cm in length, making the center a very good approximation of the actual z coordinate of the interaction vertex.

is a function of event number within a spill from the T9 beamline. For this reason the quantity p_v is used in all physics analysis, but the estimator, p_NDC1, can be used to very accurately measure the efficiency of the vertex algorithm as will be shown.

3.4.2.2   Determination of the track reconstruction efficiency

The following criteria have been applied to select tracks in the forward spectrometer for all physics analyses:

- a successful momentum reconstruction, p_v, using a downstream track segment in NDC modules 2, 3, 4 or 5 and the position of the beam particle at the target as an upstream constraint.

- a reconstructed vertex radius (*i.e.* the distance of the reconstructed track from the z-axis in a plane perpendicular to this axis at $z = 0$) $r \leq 200$ mm

- number of hits in the road around the track in NDC1 ≥ 4 and average χ^2 for these hits with respect to the track in NDC1 ≤ 30

- number of hits in the road around the track in NDC2 ≥ 6

Cuts 2–4 are applied to reduce non-target interaction backgrounds.

The track reconstruction efficiency is defined as the fraction of the total number of particles that fully traverse the fiducial volume of the HARP spectrometer which are tracked with a measured momentum and direction by the algorithm and pass the above cuts. For reasons which will become clear, this is defined as a function of momentum and θ_x and θ_y defined in Sec. 3.2.

$$\varepsilon^\mathrm{track}(p, \theta_x, \theta_y) = \frac{\mathrm{N}^\mathrm{track}(p, \theta_x, \theta_y)}{\mathrm{N}^\mathrm{parts}(p, \theta_x, \theta_y)} \tag{3.8}$$

where $\mathrm{N}^\mathrm{parts}$ is the number of particles passing through the detector and $\mathrm{N}^\mathrm{track}$ is the number which have had a successful track parameter reconstruction. The goal is to determine the efficiency directly from data to avoid any bias introduced by the Monte Carlo simulation of the spectrometer system. This is enabled by taking advantage of the redundancy

of chambers in the downstream region and by the two, independent upstream constraints introduced above.

Next, consider the calculation of the efficiency for the event vertex algorithm. To measure the efficiency from data one must map the efficiency in a reconstructed quantity, such as the momentum estimator, p_{NDC1}. Additional constraints are applied to ensure that the track is a true secondary particle emanating from the nuclear target: $\chi^2_{\mathrm{match-NDC1}} < 10$ and reconstructed vertex (in the $z = 0$ plane) less than 15mm [3]. The efficiency is a statistical calculation determined using large samples of tracks, and since p_{NDC1} is Gaussian distributed around the true momentum, p, with $\sigma_p/p < 10\%$, it can be used to approximate the later for the efficiency calculation. Further, it will be seen that the efficiency is flat at higher momentum, eliminating any tiny bias introduced.

The total tracking efficiency can be expressed as the product of two factors, $\varepsilon^{\mathrm{down}}$, representing the downstream track segment efficiency given that the particle entered the downstream region (without being deflected, absorbed or decaying in the upstream region) and $\varepsilon^{\mathrm{vertex}}$, the efficiency for matching a downstream segment with the event vertex to measure a momentum and direction,

$$\varepsilon^{\mathrm{track}} = \frac{\mathrm{N}^{\mathrm{down}}}{\mathrm{N}^{\mathrm{parts}}} \times \frac{\mathrm{N}^{\mathrm{vertex}}}{\mathrm{N}^{\mathrm{down}}} = \varepsilon^{\mathrm{down}} \times \varepsilon^{\mathrm{vertex}}. \tag{3.9}$$

Further, in the downstream region there are two planes of drift chambers, NDC2 and the *back-plane* made of the combination of NDC3-4-5. A downstream track segment can be made of a segment in NDC2 only, a segment in the back-plane only, or a segment in both which are combined into a longer segment. These independent, but not mutually exclusive probabilities combine to give a total downstream segment efficiency of

$$\varepsilon^{\mathrm{down}} = \varepsilon^{\mathrm{NDC2}} + \varepsilon^{\mathrm{back-plane}} - \varepsilon^{\mathrm{NDC2}} \cdot \varepsilon^{\mathrm{back-plane}}. \tag{3.10}$$

To calculate the segment efficiency of NDC2 one selects tracks from the p_{NDC1} control sample with a segment in the back-plane and then asks if a segment was also reconstructed in NDC2. The efficiency can then be mapped out as a function of the p_{NDC1} reconstructed quantities. This efficiency is the 'true' segment efficiency of NDC2 because it is

---

[3]All of the nuclear targets being analyzed here are 15mm in radius
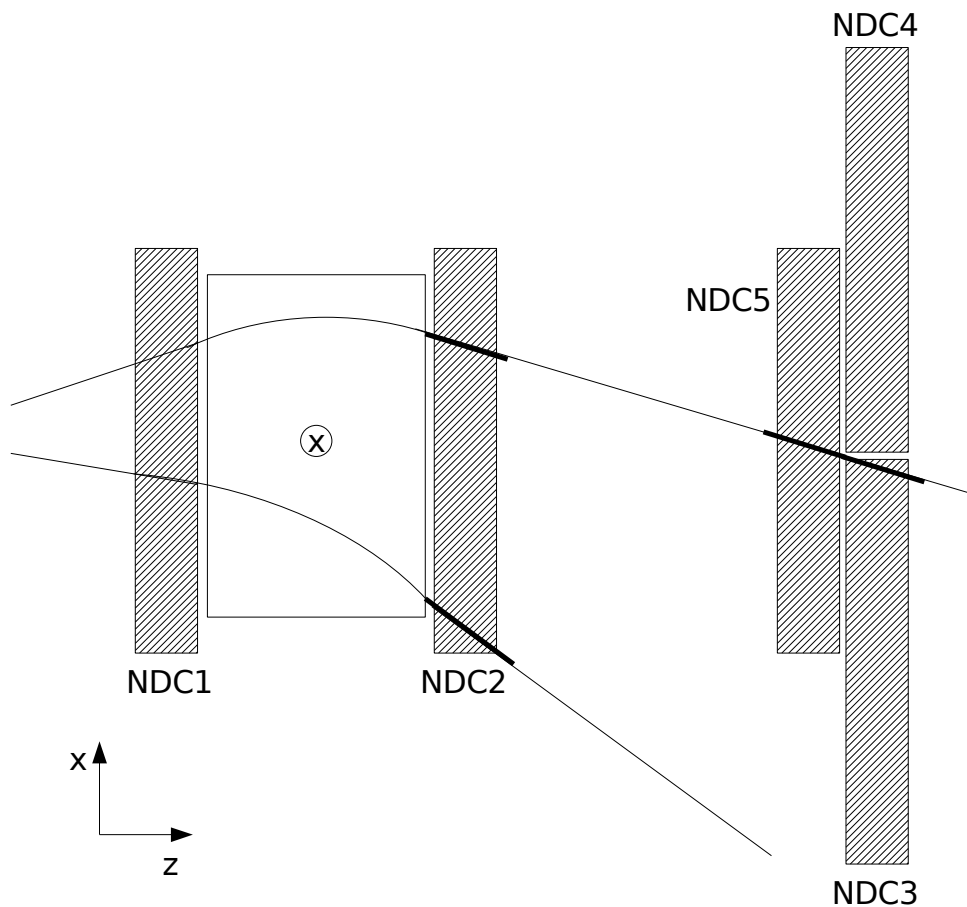
Figure 3.11: Schematic plan view of the HARP forward angle spectrometer system comprised of five drift chambers and a large aperture dipole magnet. Two types of secondary tracks are represented in the diagram (both having negative charge, incidentally). The one at the top of the figure shows how track segments in the back-plane are used to map the segment efficiency of NDC2 and vice versa. The second track illustrates the effect of geometric acceptance for particles at large, positive values of $q \cdot \theta_x$.
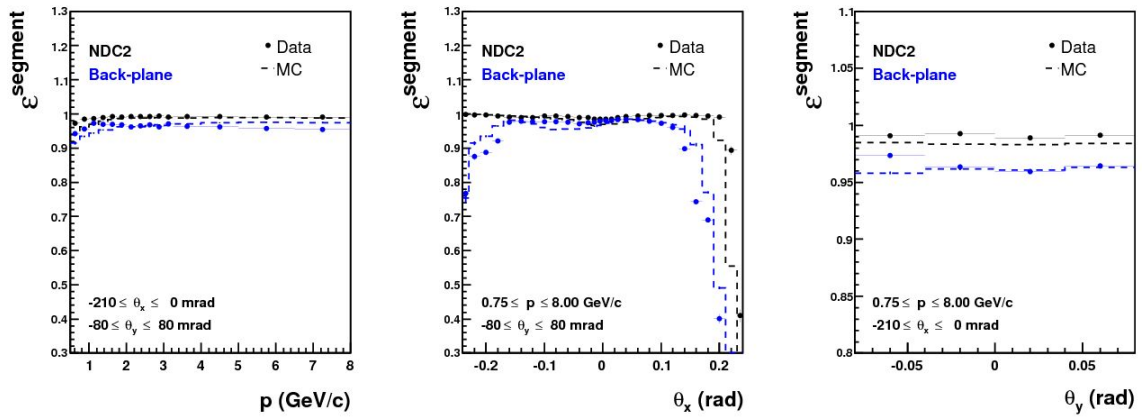
Figure 3.12: Track segment efficiencies for positive particles as a function of particle momentum (left), production angle in the horizontal plane, θ_x (center), and production angle in the vertical plane, θ_y (right). The segment efficiency for NDC2 is shown in black, and that for the 'back-plane' consisting of NDC3-4-5 is shown in blue.

the efficiency of the chamber *given* that a particle passed through its volume. One knows this because the selected tracks created segments in both NDC1 and the back-plane which surround NDC2 (see Figure 3.11). Figure 3.12 shows the average efficiency calculated by this method for both data and Monte Carlo to be $\sim 99\%$.

To determine the segment efficiency of the back-plane one simply asks the opposite question: for tracks which created a track segment in NDC2, how many also created a segment in the back-plane? A signal in the ECAL, downstream of the back plane of chambers, is also required to ensure the track traversed the back plane of chambers. As seen in Figure 3.12 the efficiency of the back-plane is a few percent lower than was calculated for NDC2, but combining them will result in a total downstream efficiency of nearly 100%.

Also clearly visible in Figure 3.12 is the effect of geometric acceptance in the HARP forward spectrometer. The acceptance is both momentum and charge dependent due to the varying amount and direction of bend in the track path that results from passing through the magnetic field region. The dipole bends particles in the horizontal plane and low momentum tracks at large, positive values of $q \cdot \theta_x$ can be bent beyond the reach of the downstream drift chambers. One expects the effect to extend to smaller values of $q \cdot \theta_x$ for

the back-plane because it is further downstream (see Figure 3.11), and this can be seen in the middle panel in Figure 3.12. The small acceptance loss visible at large negative θ_x (for positive particles) are high momentum tracks that are bent only slightly in the magnetic field region and miss the back-plane of chambers on the opposite side. The efficiency for negative particles, which is almost exactly the mirror image of that for positives as a function of θ_x, has been calculated but is not shown in the figures for the sake of clarity.

By combining the efficiencies of the two downstream planes according to equation 3.10, one determines the total downstream segment efficiency, $\varepsilon^{\text{down}}$, shown in the top panel of Figure 3.13. After accounting for geometric acceptance of the spectrometer the downstream segment efficiency is $\sim 100\%$ and does not depend on momentum or opening angle in the vertical plane, θ_y.

The final piece of the track reconstruction efficiency, $\varepsilon^{\text{vertex}}$, is the efficiency of the p_{v} algorithm given that a downstream track segment was constructed. Again, this can be measured by using a sample of p_{NDC1} tracks. The successful p_{NDC1} momentum reconstruction guarantees the existence of a downstream segment allowing us to determine the ratio $N^{\text{vertex}}/N^{\text{down}}$. The result is shown in Figure 3.13. The average efficiency is $\sim 97\%$, most easily seen in the plot as a function of θ_y. The drop in efficiency below $\sim 1.75\,\text{GeV}/c$ is due to the second cut listed above, $r \leq 200$ mm. This cut is necessary to remove a substantial non-target background and maintain a good resolution at low momentum. However, because the efficiency can be measured from the data themselves, the only systematic error contribution will come from the statistical uncertainty in the sample used to generate the correction. For this reason, high momentum data sets ranging from 8–15 GeV/c and using aluminum, beryllium, carbon and tantalum targets have all been combined. Studies have shown that small changes in spectrum and secondary multiplicity have negligible effects on the track reconstruction efficiency as a function of p, θ_x and θ_y.

3.4.2.3   Geometric acceptance correction

To avoid unnecessary complications caused by the momentum dependent acceptance of the spectrometer, most clearly visible in the plot of $\varepsilon^{\text{down}}$ as a function of θ_x, a fiducial volume cut ($-210 \leq \theta_x \leq 0$ mrad for positives and $0 \leq \theta_x \leq 210$ mrad for negatives) will
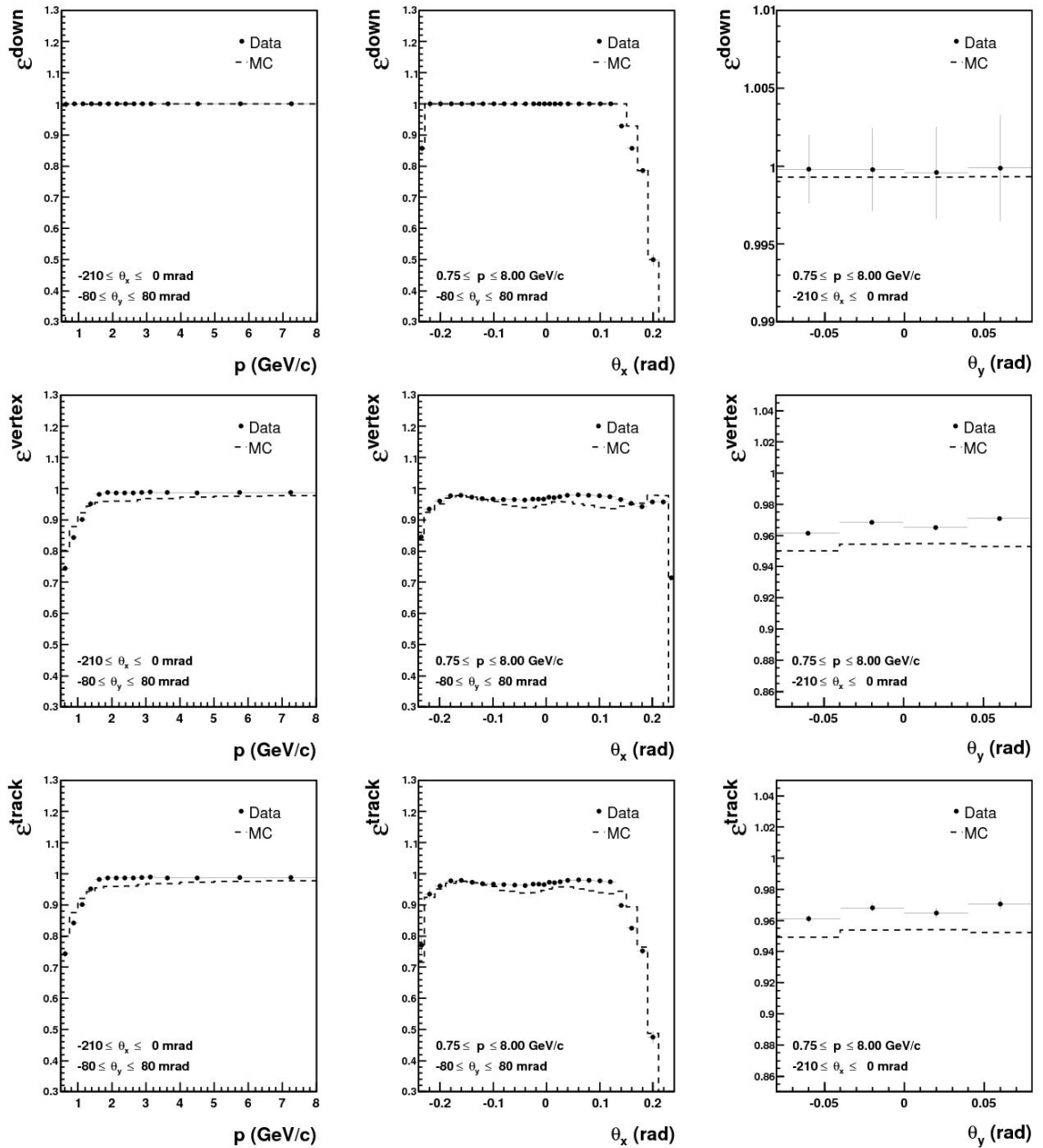
Figure 3.13: The track reconstruction efficiency (bottom row), shown as a function of particle momentum (left), production angle in the horizontal plane, θ_x (center), and production angle in the vertical plane, θ_y (right), is computed by multiplying the downstream segment efficiency (top row) by the vertex matching efficiency (middle row). Each are measured from the data and the Monte Carlo as described in the text. The results from data will be used in the cross-section measurements to be presented.
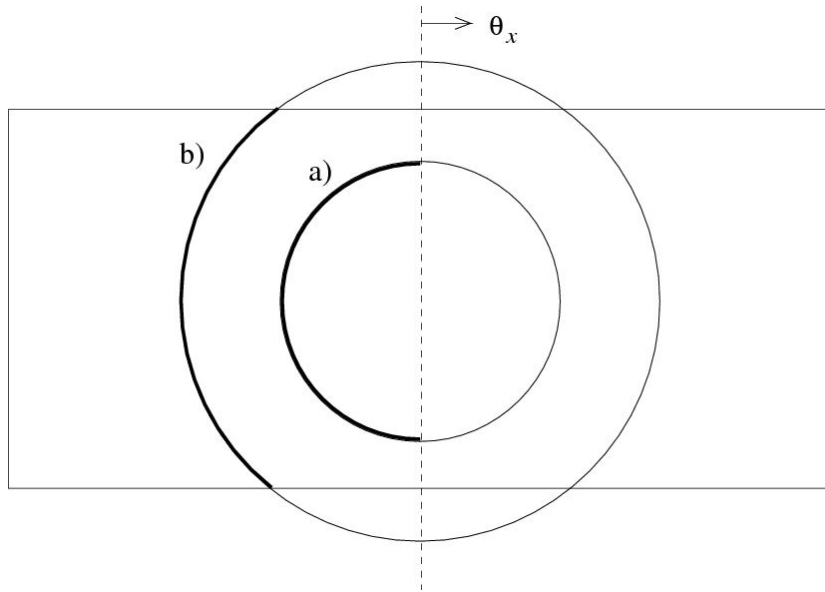
Figure 3.14: Sketch of the forward detector illustrating the two forms of geometric acceptance corrections, a) for $\theta \leq \theta_y^{\mathrm{cut}}$ and b) for $\theta > \theta_y^{\mathrm{cut}}$. The corrections are given by Eq. 3.11.

be applied to all cross-section analyses, thus utilizing only the region where the downstream segment efficiency is $\sim$ 100% and extremely flat. In the vertical direction only tracks with $-80 \leq \theta_y \leq 80$ mrad are selected to avoid drift chamber and magnetic field edge effects.

This restricted fiducial volume definition necessitates a correction. Assuming azimuthal symmetry in hadron production this correction is purely analytical. Inside the θ_y acceptance (± 80 mrad) the correction is a simple factor of 2 since tracks with $\theta_x > (<)$ 0 mrad are not used for positive (negative) tracks. For values of θ above the θ_y cutoff the correction is more complicated and describes the fraction of the circle within the acceptance.

$$
\begin{aligned}
\varepsilon^{\mathrm{acc}}(\theta) &= \frac{1}{2} & \theta \leq \theta_y^{\mathrm{cut}} \\
\varepsilon^{\mathrm{acc}}(\theta) &= \frac{1}{\pi} \cdot \arcsin\left(\frac{\tan(\theta_y^{\mathrm{cut}})}{\tan(\theta)}\right) & \theta > \theta_y^{\mathrm{cut}}
\end{aligned}
\tag{3.11}
$$

Figure 3.14 shows a sketch depicting the two forms of the geometric acceptance and the origins of the correction formulas. All reconstructed tracks are weighted by $1/\varepsilon^{\mathrm{acc}}(\theta)$.

3.4.2.4 Momentum resolution and scale of the p_v algorithm

In the next chapter we will use the Monte Carlo simulation to make corrections associated with the resolution of the momentum reconstruction. Also, the momentum scale will be used to assess a systematic error on the cross-section results. Therefore, it is important to measure the resolution and scale from the data, and for the Monte Carlo and data to be in good agreement.

Several methods were developed by HARP collaborators to measure and map the momentum scale and resolution as a function of p and θ. Parameters of the Monte Carlo simulation were then adjusted to attain adequate agreement with data. Detailed descriptions of these methods have been given previously in [58] and will not be repeated here. The challenge is to isolate a set of tracks in the data sample with a known momentum. Briefly, the three methods are based on empty target data sets, samples of elastic scattering events and using the excellent resolution of the time-of-flight system to determine the momentum.

To give a sense of the resolution and the agreement between data and Monte Carlo Figure 3.15 shows the resolution as a function of momentum for a set of empty target data sets and Monte Carlo samples. In this case the known momentum is the incoming primary T9 beam momentum. Histograms of secondary tracks were fit to a Gaussian function and the fractional resolution, σ_p/p, is plotted as a function of the beam momentum. Incoming pion and proton beams were used for both data and Monte Carlo. There is good agreement between data and Monte Carlo and between different particle types across the full momentum range from 1.5 GeV/c to 15 GeV/c. Below 5 GeV/c, where most of the total production cross-section of π^+ and π^- will be for the data sets being analyzed, the resolution is better than 5% and everywhere better than 10%.

A multiplicative momentum scale correction is applied to all reconstructed tracks in the data to remove a θ_x, θ_y dependence seen in the calibration samples. After this correction, no significant momentum mis-calibration is seen beyond the 2% absolute momentum scale uncertainty estimated using the elastic scattering technique [58]. Also shown in Figure 3.15 is the momentum scale, again computed using empty target data sets. Pion
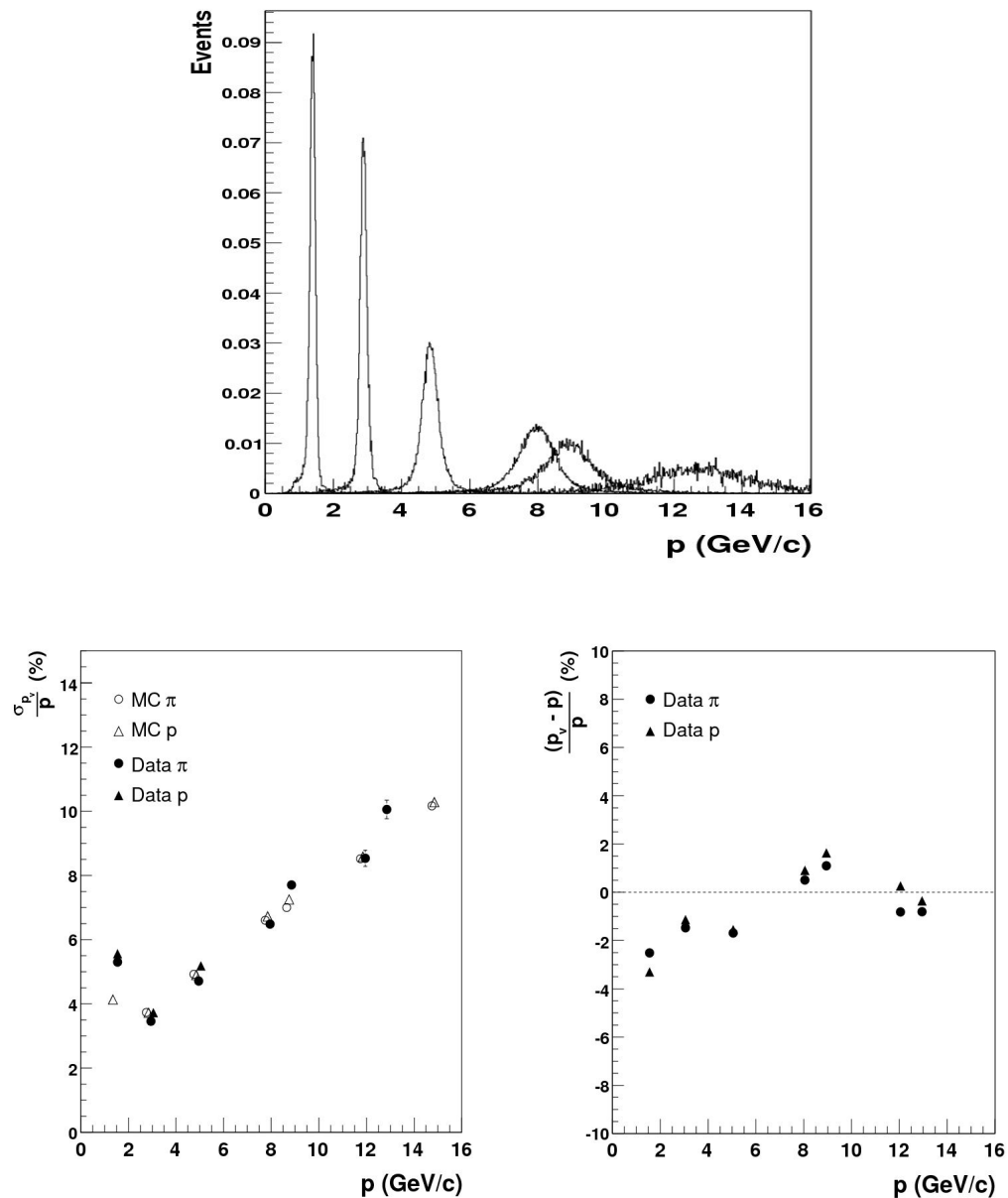
Figure 3.15: The momentum resolution (bottom left) and absolute scale (bottom right) can be measured as a function of momentum by using data sets taken using several well-defined discrete beam momenta and no nuclear target. The top panel shows the unit-area normalized distributions of beam pion data taken at 1.5, 3.0, 5.0, 8.0, 8.9, and 12.9 GeV/c. However, both incident pions (circles) and protons (triangles) are used to measure the resolution and scale for comparison.

Cherenkov gas	C_4F_{10}
index of refraction	1.001415
π threshold	2.6 GeV/c
K threshold	9.3 GeV/c
proton threshold	17.6 GeV/c

Table 3.2: Properties of the radiator gas used in the HARP threshold Cherenkov detector.

and proton beams are compared and no difference is seen. At most momenta the momentum scale is better than 2%. In the cross-section analysis, the minimum ratio of momentum bin width over momentum bin central value will be 8%, four times this value.

3.4.3   Cherenkov detector response

The Cherenkov thresholds of the most relevant charged particles in C_4F_{10} gas at atmospheric pressure are listed in Table 3.2. Below 3 GeV/c the Cherenkov can be used to veto electrons in the sample. Above 3 GeV/c it is a powerful discriminator of pions and protons/kaons.

Figure 3.16 qualitatively demonstrates this discrimination power using a data set with a 12.9 GeV/c π^+ beam on a thin aluminum target. A minimum bias trigger was used and the non-interacting beam pions are clearly visible at high momentum and large number of photo-electrons (N_{pe}). At $p < 2$ GeV/c secondary electrons can be seen clustered at $\sim$ 25–30 N_{pe} and are easily separable from pions at $N_{pe} < 2$. Finally, the Cherenkov threshold for pions at 2.6 GeV/c is clearly visible. Only a small number of protons are represented in this plot, but would show up as a band below 2 N_{pe} out to 17.6 GeV/c.

In the cross-section analysis to be presented, the Cherenkov has been used digitally - that is, the spectral information of the light output as pions go beyond threshold, which is evident in Figure 3.16, is not being used. Instead, we define a signal as an associated hit with greater than 2 photo-electrons; two or less is considered no signal. Based on this definition one must determine the efficiency for pions and protons to have a signal in the
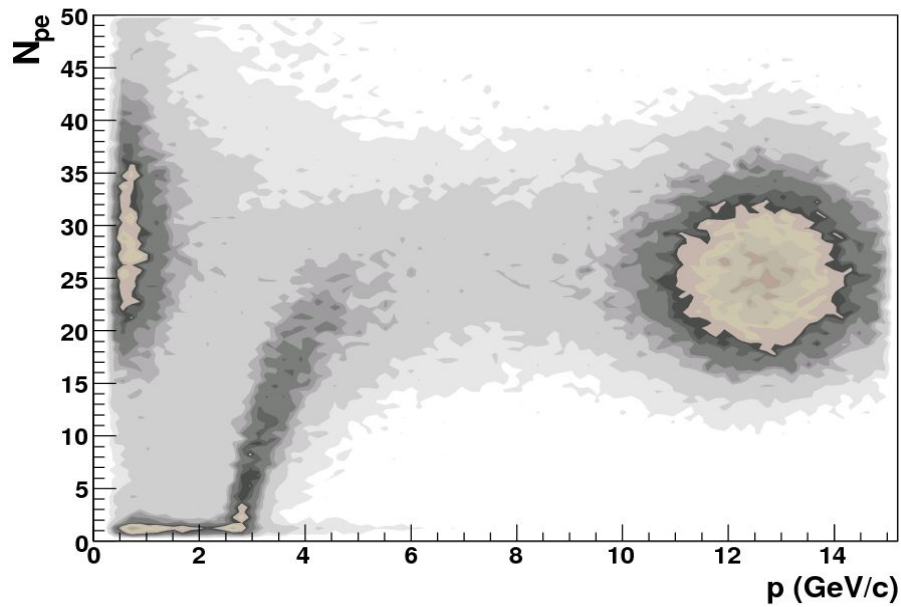
Figure 3.16: Reconstructed number of photo-electrons in the Cherenkov detector as a function of particle momentum for a data set with a 12.9 GeV/c π^+ beam on a thin aluminum target. See the text for an explanation.

Cherenkov as a function of particle momentum. At the time of the first HARP publication [57] the analysis included only a geometric criteria for hit-track matching. A χ^2 was constructed between the positions of all tracks in the plane of the CHE detector ($x_{\text{track}}, y_{\text{track}}$) and the reconstructed position of all Cherenkov hits ($x_{\text{CHE}}, y_{\text{CHE}}$); hits that matched with a sufficient χ^2 were associated with that track. In this approach the reconstruction can associate a single detector hit with multiple tracks. In particular, it was seen that a fraction of protons (as high as 20%) had a non-negligible amount of associated photo-electrons due to light from pions or electrons being wrongly associated with proton tracks. By the time of [58] this problem had been corrected by assigning hits only to the track with which they are best matched. The loss in efficiency for pions and electrons proved to be negligible. Above threshold the Cherenkov is greater than 97% efficient for pions. The small efficiency for protons and pions below threshold is due to remaining false associations with light generated by other particles in the event. This rate is slightly dependent on the experimental configuration - the target material and beam momentum - because

configurations with higher particle multiplicities will have higher rates of false associa-
tions. Because of this one would like to use the Monte Carlo simulation to determine the
Cherenkov efficiency. By using the Monte Carlo one is not limited to the statistical sample
of a particular data set.

However, one still needs to verify the Monte Carlo simulation for the calculation of
the Cherenkov efficiency. One of the largest data sets is with a 12.9 GeV/c proton beam
on a thin aluminum target, so it will be used to compare the Cherenkov efficiency in
data and Monte Carlo. From the Monte Carlo one can use the known particle type to
build the Cherenkov efficiency as a function of momentum. For both the data and the
Monte Carlo one can select a pure sample of pions and protons by making a very tight,
momentum dependent cut on the measured β of all particles. The left panel of Figure 3.17
demonstrates how this is done. The red points are all reconstructed particles in the data
set. The black points are those selected for characterizing the CHE response. The band
that curves down at low momentum is protons, the band that is nearly flat at $\beta = 1.0$
is pions. Kaons can be seen in the middle band and will not be included. Electrons are
rejected using the electromagnetic calorimeter. The middle and right panels of Figure 3.17
show the calculated Cherenkov efficiency for pions (middle) and protons (right) using the
true particle type in the Monte Carlo and the time-of-flight selection technique applied to
both data and Monte Carlo samples. The agreement is within the statistical fluctuations
of the values determined from data. However, since the accidental rates for pions and
protons below 2.5 GeV/c are nearly the same and provide no discrimination power, and
because the threshold region is steep and difficult to simulate, the PID algorithm uses the
Cherenkov to separate pions and protons only above 3.0 GeV/c where the efficiency is flat
and agreement is excellent.

Figure 3.19 shows the expected response for pions and protons in the Cherenkov for
the two data sets for which we will present cross-section measurements - 8.9 GeV/c pro-
tons on a beryllium target and 12.9 GeV/c protons on an aluminum target. Indeed the
high momentum efficiency differs by a few percent as expected.

As mentioned above, the Cherenkov detector is also used to veto electrons below the
pion threshold. Any tracks below 3.0 GeV/c with $N_{pe} > 15$ are rejected as electrons.
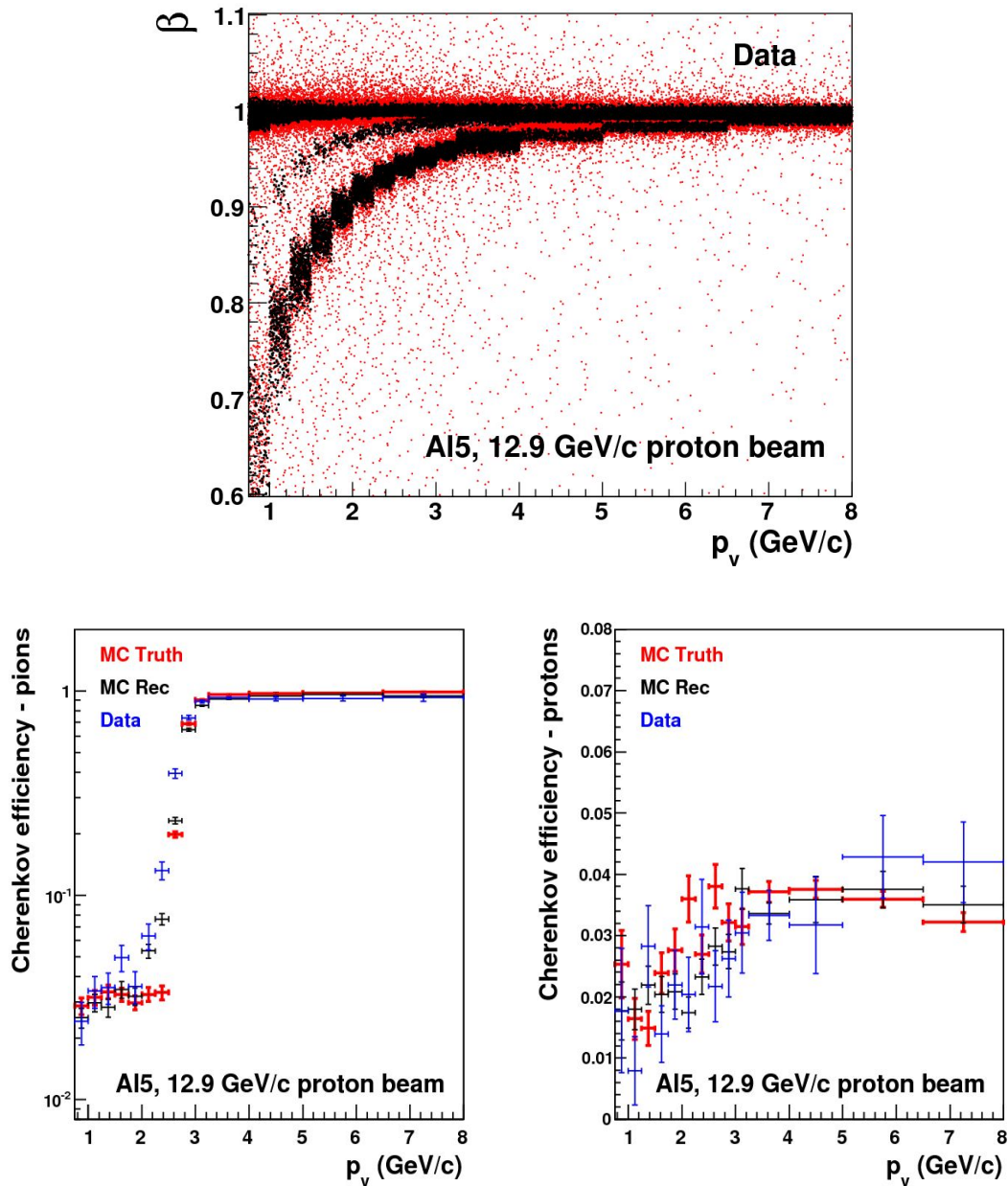
Figure 3.17: Cherenkov response for pions (middle) and protons (right) as measured from data and Monte Carlo for a 12.9 GeV/c proton beam on an aluminum target setting. The points are the efficiencies for a track to have an associated Cherenkov hit with greater than 2 photo-electrons. Samples of protons and pions are selected from the data by making a very tight, momentum dependent cut on the measured β as shown in the left panel.
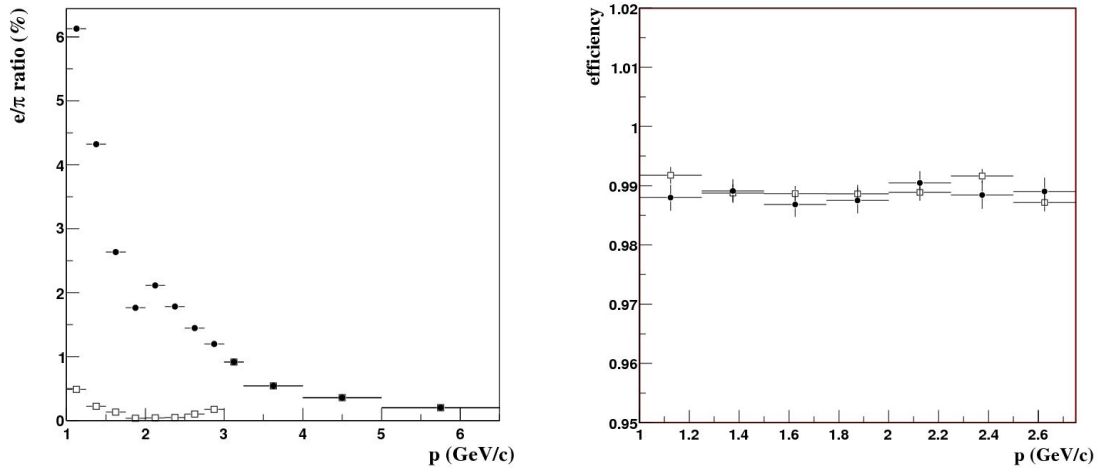
Figure 3.18: The left panel shows the e/π ratio from a Monte Carlo simulation before (solid points) and after (open squares) the application of a 15 photo-electron cut. This cut reduces the electron contamination to 0.5% or less in the region where it is applied. The right panel shows the efficiency for pions (solid points) and protons (open squares) to pass the 15 photo-electron cut below 3 GeV/c, and is $\approx 99\%$ for both. Plots taken from [58].

Figure 3.18 shows the effects of the electron veto cut. A Monte Carlo simulation is used to verify that such a cut reduces the electron contamination to a negligible level, in this case $\leq 0.5\%$. Of course there is a small efficiency loss for pions and protons. This has been carefully measured from data and is found to be $\sim 1\%$ as shown in the right panel of Figure 3.18.

3.4.4 Time-of-flight system performance

The TOF system compliments the CHE by discriminating particle types at momenta below the pion Cherenkov threshold of 3 GeV/c. The time-of-flight of each track from the nuclear target to the TOFW is determined by combining the TOFW and BTOF systems, $t_{\text{tof}} = t_{\text{TOFW}} - t_0$. The path length between these same positions is calculated by the Kalman Filter fitting package. These are then combined to determine the velocity or $\beta = \text{d}/\text{t}c$ of each track.
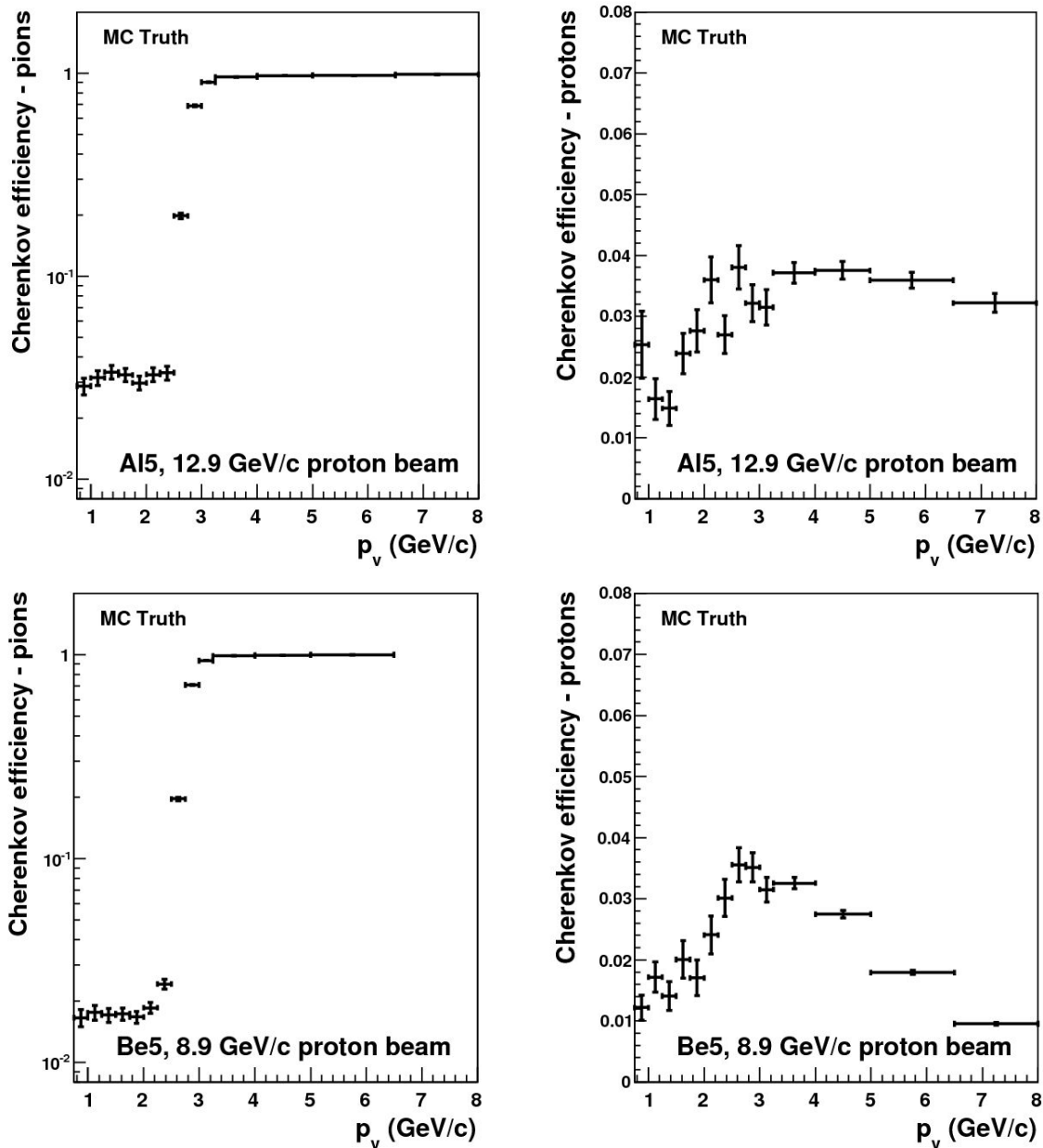
Figure 3.19: Cherenkov response for two different data sets for pions (left) and protons (right). The points are the efficiencies for a track to have an associated Cherenkov hit with greater than 2 photo-electrons. The threshold for pions at around 2.6 GeV/c is clearly visible (note the log scale). The small efficiency for protons and below threshold pions of around 1.5% is due to false associations with light generated by other particles in the event.
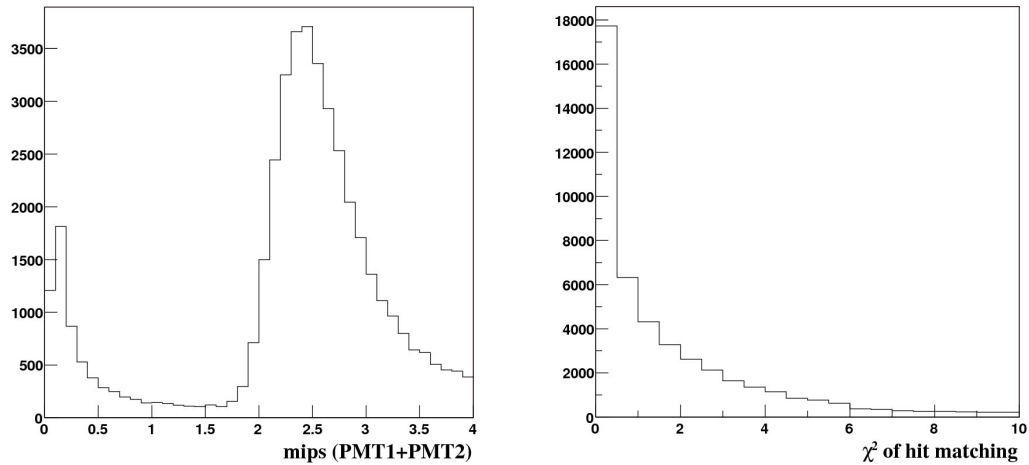
Figure 3.20: TOFW hit reconstructed variables. The left panel shows the distribution of the χ^2 between the extrapolated track position and the reconstructed scintillator hit position. The right panel shows the total reconstructed number of minimum ionizing particles (mips) from the two PMTs on the scintillator volume that was hit. Time-of-flight hits are selected by requiring a $\chi^2 \leq 6$ and number of mips ≥ 1.5 (see the text). Plots taken from [58].

The selection of TOFW hits has been designed to address a significant non-Gaussian component to the TOFW response that was reported in [57]. As with the CHE, the hit selection was previously based entirely on geometric matching between TOFW hits and track parameters. About 10% of the reconstructed β fell greater than 5σ from the mean expectation for pions or protons and could not be used for particle identification. It was discovered that many of these β–outliers were correlated with TOFW hits of particularly low charge indicating they are some form of noise. Figure 3.20 shows a distribution of the reconstructed number of minimum ionizing particles, or mips, from the two PMTs that make up a TOFW hit for a sample of data. The hits piled up at low mip counts are clearly separable from those with two or more reconstructed ionizing particles.

The following TOFW hit selection criteria have been used for the matching of TOFW hits with secondary tracks:

- if the track shares the TOFW hit with another track, it must have the better geometric
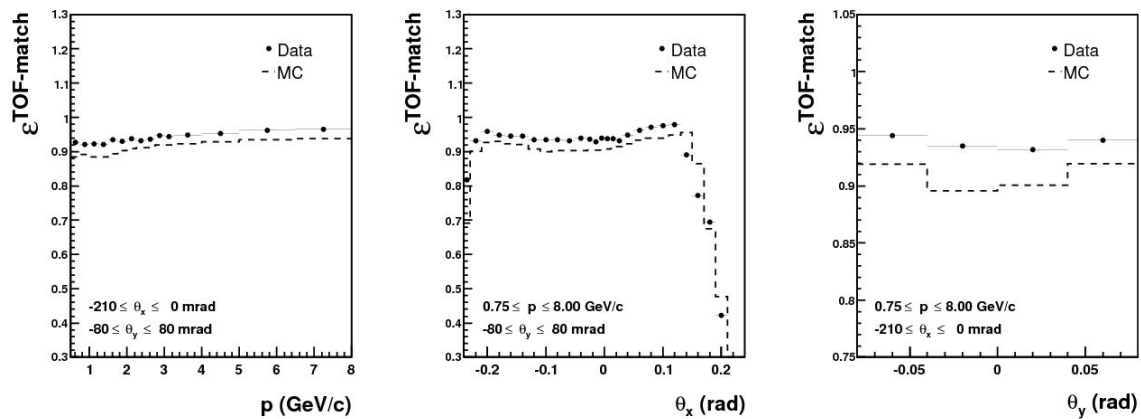
Figure 3.21: TOFW matching efficiency as a function of particle momentum (left) and production angle in the horizontal plane, θ_x (right) as measured from data and Monte Carlo. The effect of geometric acceptance can be seen in the right, θ_x, plot. Note the present analysis is performed using tracks in the range -0.210 rad $\leq \theta_x \leq 0$ rad where the acceptance is flat in momentum.

matching χ^2;

- χ^2 of the geometrical matching between the track and TOFW hit ≤ 6;

- total reconstructed number of minimum ionizing particles (mips) from the two PMTs in a hit ≥ 1.5.

The TOF hit matching efficiency can be measured directly from the data by once again taking advantage of the redundancy of the detectors in HARP and using a sample of reconstructed tracks which leave a signal in the calorimeter (downstream of the scintillator wall) and asking how often a time-of-flight measurement passing selection cuts is found. Figure 3.21 shows the matching efficiency for data and Monte Carlo to be flat in momentum and around 95% in the data.

We may also measure the response function of the TOF system from the data themselves. This is preferable to using the Monte Carlo as it avoids any bias that may be introduced by the simulation of the TOFW. To build the TOF response function one must know the shape of the β distributions as a function of particle momentum for all relevant
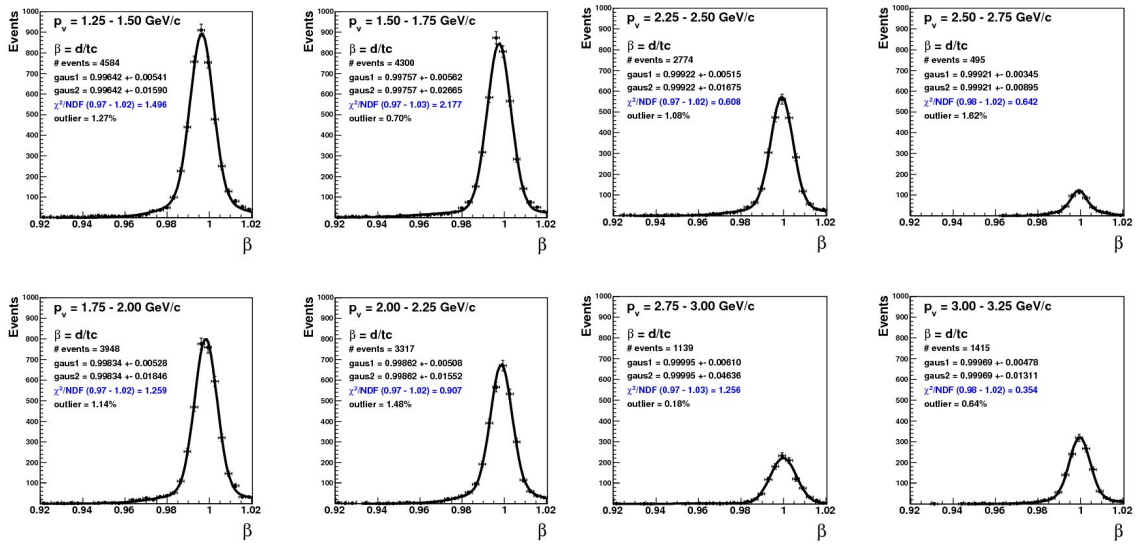
Figure 3.22: Double Gaussian fits to samples of π^- tracks in bins of reconstructed momentum, p_v, from 1.25 GeV/c to 3.25 GeV/c. Fits are perfomed across the full range of momentum but are not shown. From these fits one can extract the mean and width of the time-of-flight system response (in units of $\beta = \mathrm{d}/\mathrm{tc}$) for pions as a function of momentum directly from data. The CHE and ECAL are used to select π^- and reject electrons below 2.5 GeV/c. Above 2.5 GeV/c K$^-$ and antiprotons are rejected using the CHE (although the contamination from antiprotons and K$^-$ is expected to be negligible).

secondary particle types. In Chapter 4 we will only be interested in the β response functions for pions and protons. However, those of electrons and kaons are extracted as part of the procedure.

A sample of pions with only negligible contamination from other species can be obtained by selecting particles of negative charge which have passed an electron veto. Negative pions are used because the number of antiprotons produced at these energies is expected to be negligible and the ratio of K$^-$/π^- is known to be much smaller than the ratio of K$^+$/π^+.[4] Below 2.5 GeV/c negative tracks are required to have no associated Cherenkov hit and be consistent with a hadron in the calorimeter (ECAL). Above 2.5

_____

[4]The double ratio (K$^+$/π^+)/(K$^-$/π^-) is as large as 10 for 8.9 GeV/c protons on beryllium according to some hadron production Monte Carlos [94].
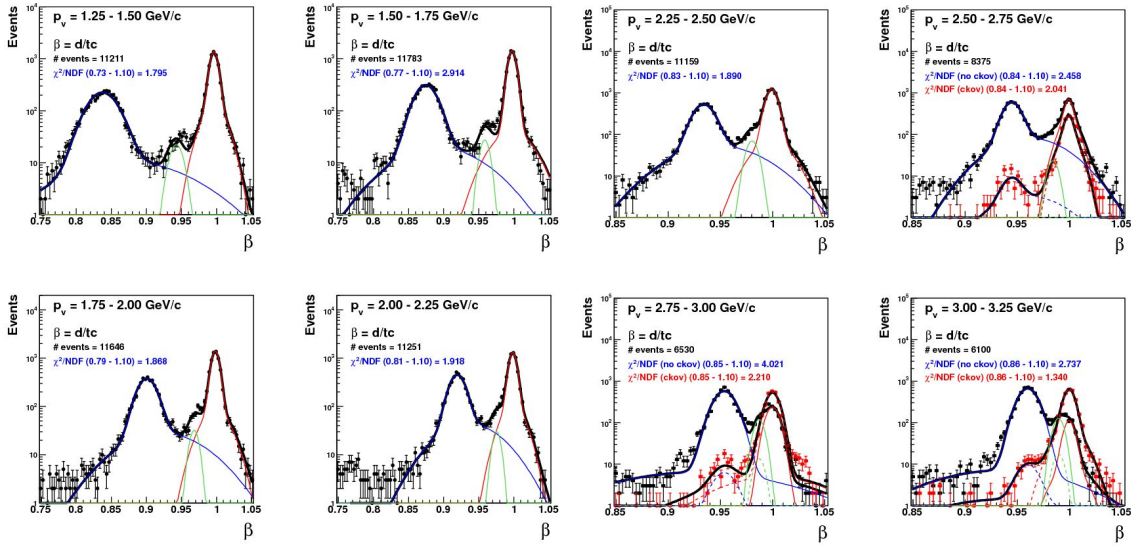
Figure 3.23: Simultaneous fits to proton, kaon and pion tracks in bins of reconstructed momentum, p_v, from 1.25 GeV/c to 3.25 GeV/c. The pion parameters are fixed to those found in fits to π^- samples and one can extract the mean and width of the time-of-flight system response (in units of $\beta = \mathrm{d}/\mathrm{tc}$) for protons and kaons as a function of momentum directly from data. Above the pion Cherenkov threshold, the CHE can be used to better expose the proton peak. For momenta above 2.5 GeV/c both the tracks with 0 associated N_{pe} (black points) and with more than 5 N_{pe} (red points) are shown.

GeV/c they must have a CHE hit $> 5\,N_{pe}$ and again be consistent with a hadron in the ECAL. Note the Cherenkov selection cut used here is much tighter than the selection used in a cross-section analysis of $N_{pe} > 2$. This is done to push the purity of the sample near 100% with a small loss in the statistics available to extract the response function parameters. However, since the time-of-flight does not depend on the target material or beam momentum, several data sets can be combined to greatly increase the statistics of the sample. The selected π^- are separated into bins of momentum and fit with a double Gaussian function to extract $\overline{\beta}$ and σ_β as functions of momentum. Figure 3.22 shows these fits for eight momentum bins between 1.25 GeV/c and 3.25 GeV/c.

The proton and kaon time-of-flight response functions can be obtained by selecting samples of positive tracks and simultaneously fitting the proton, kaon and pion β peaks
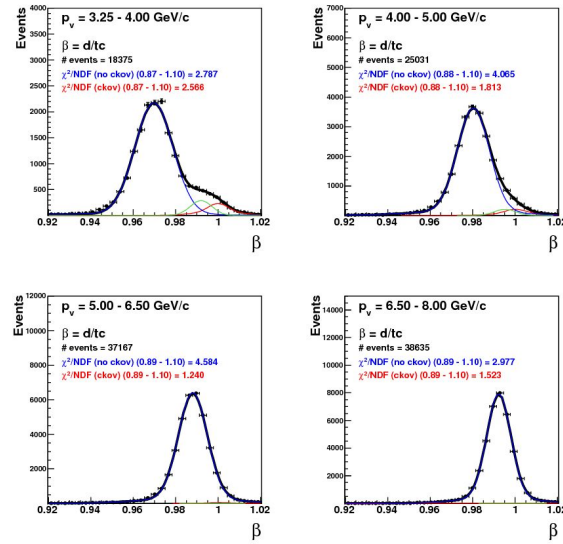
Figure 3.24: Simultaneous fits to proton, kaon and pion tracks in bins of reconstructed momentum, p_v, from 3.25 GeV/c to 8.00 GeV/c for tracks with no associated photo-electrons in the Cherenkov detector.

to Gaussian functions. The mean and width of the pions are fixed to the values found from the negative pions. The Monte Carlo is used to determine initial parameters for protons and kaons, but these are then allowed to float in the fit. Below 2.5 GeV/c the proton and pion peaks are well separated and can be fit simultaneously. Above 2.5 GeV/c the Cherenkov is used to reject 99% of pions to better expose the proton peak for fitting. Figure 3.23 shows examples of these fits above and near this threshold. For momenta above 2.5 GeV/c both tracks with no associated photo-electrons (black points) and with more than 5 photo-electrons (red points) are shown. Interestingly, comparing the two distributions gives a rough estimate of the Cherenkov efficiency - note the ratio of red to black in the proton peak is about 1%, as we saw in the previous section. Figure 3.24 shows examples well above the pion Cherenkov threshold where clean samples of protons can be obtained by selecting only tracks with no associated photo-electrons.

Organizing the information from this multi-step method one obtains the momentum dependent TOF response function for all relevant particle types. The results are summarized in Figure 3.25. The described procedure can be tested by using the Monte Carlo

simulation. Time-of-flight response function parameters are extracted from reconstructed distributions as prescribed and from histograms built using the true particle type available from the simulation. The results of such a test are illustrated on the left in Figure 3.25. No significant bias is seen coming from the method. Therefore, one may safely apply the method to data and obtain the needed time-of-flight response functions for performing particle identification, shown on the right half of Figure 3.25. Below the Cherenkov threshold at 2.6 GeV/c there is excellent pion/proton separation (6.2σ at 2.25–2.5 GeV/c). Above the threshold the time-of-flight system quickly loses its discrimination power (2.2σ at 4–5 GeV/c), but only acts as a supplement to the Cherenkov detector in this range.

As mentioned above, the TOFW hit selection cuts used here were developed to reduce the β–outlier rate of $\sim 10\%$ that affected the initial HARP publication [57]. While the effect is reduced significantly, it has not been eliminated. Figure 3.26 shows the remaining rate of β–outliers with the current hit selection to be 1–3% for pions and protons. Below the pion Cherenkov threshold, one has no useful PID information for these tracks. Therefore, they directly contribute to the PID inefficiency and will be accounted for in the PID efficiency calculation (see Section 4.5).

In the cross-section analysis to be presented we will require a TOF measurement as part of our selection of secondary tracks. Therefore, the efficiency loss due to TOFW hit selection must be combined with the tracking efficiency discussed earlier to form an overall *reconstruction efficiency*,

$$\varepsilon^{\mathrm{recon}} = \varepsilon^{\mathrm{track}} \cdot \varepsilon^{\mathrm{TOFW-match}} \tag{3.12}$$

Figure 3.27 shows the final reconstruction efficiency for positive and negative tracks in the forward spectrometer. The mirror symmetry in the acceptance for tracks of opposite charge is clear in the figures. These efficiencies, measured directly from the data, will be used in all cross-section analyses.
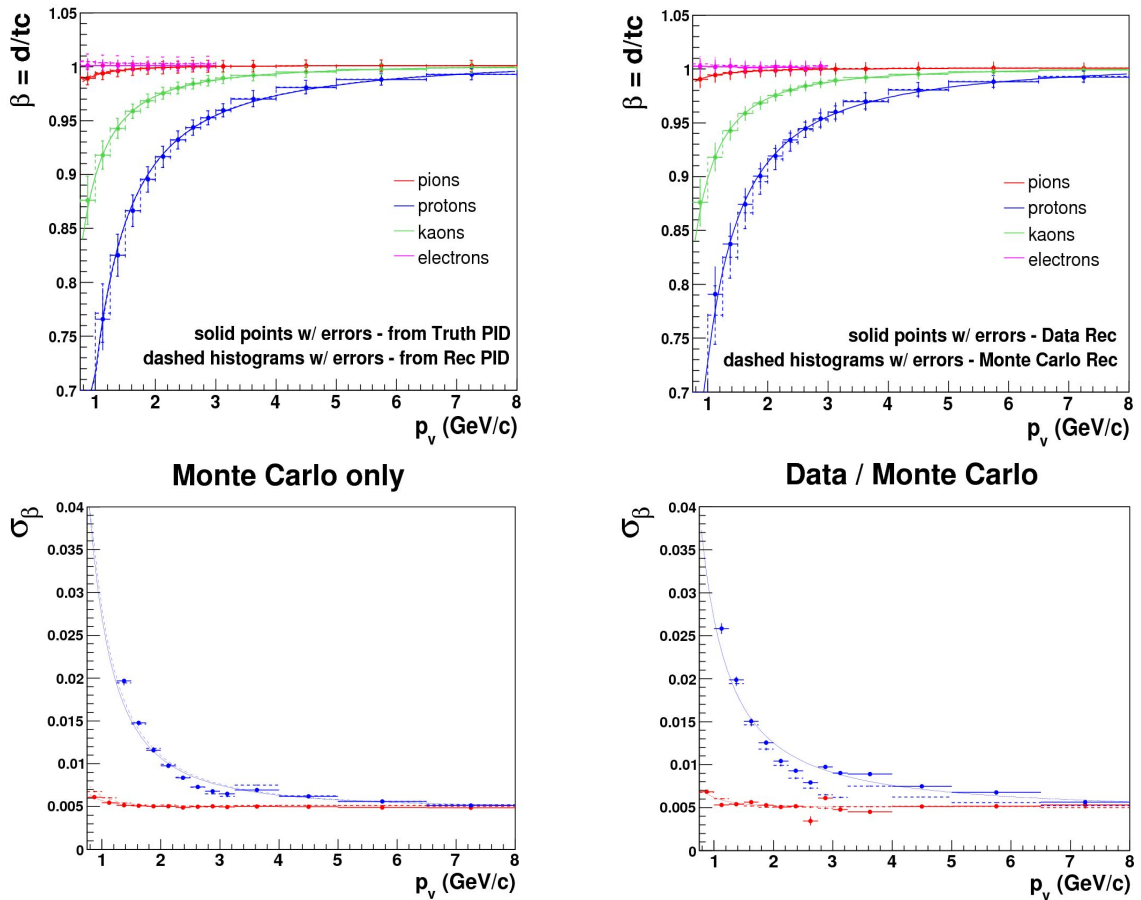
Figure 3.25: Time-of-flight response functions for pions (red), protons (blue), koans (green) and electrons (pink). The top panels show the mean and width of the β distribution as a function of reconstructed momentum. The bottom panels show the widths (same as the error bars in the top panels) for pions and protons only. On the left are the parameters extracted using Monte Carlo truth information to obtain samples of π^+, p, K^+ and e^+ and parameters found from the method described in the text using reconstructed information. No significant bias is seen in the means or widths of the β distributions found from the described method. Therefore, it can be applied to extract the response function directly from data as shown in the right panels and compared to the values found from Monte Carlo.
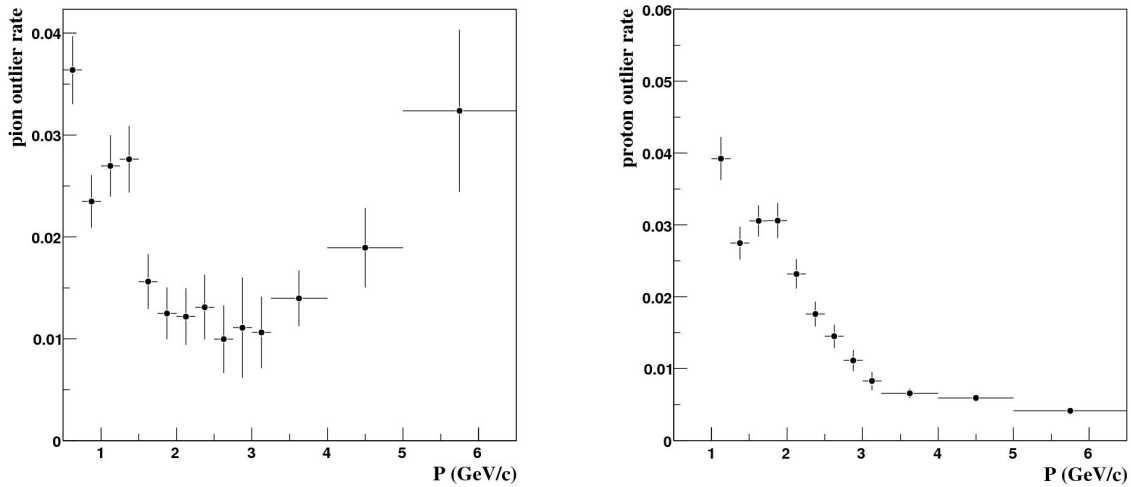
Figure 3.26: β–outlier rates for pions (left) and protons (right). The pion outlier rate has been measured from the data; the proton outlier rate is estimated using the Monte Carlo. Plots taken from [58].
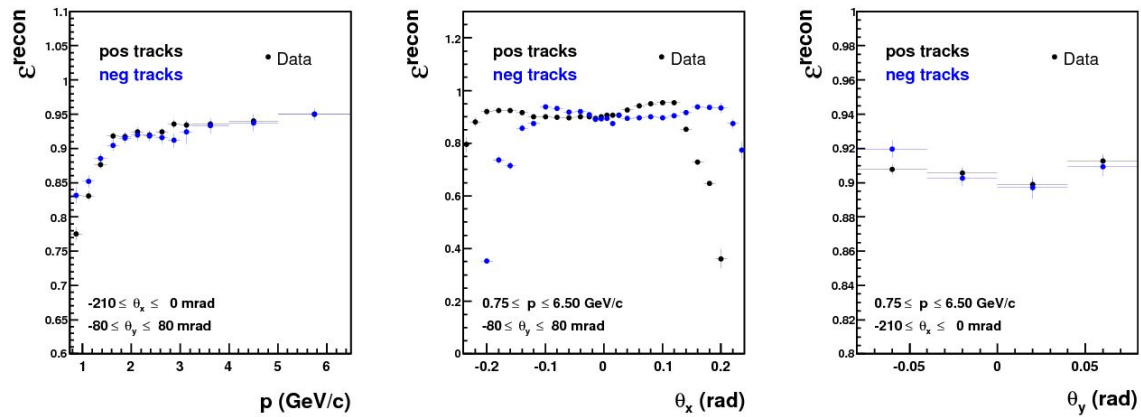
Figure 3.27: Total reconstruction efficiency including track kinematic parameters and time-of-flight measurement for positive (black) and negative (blue) tracks in the forward spectrometer. The effects of geometric acceptance are clearly visible in the plot as a function of θ_x (center). The average reconstruction efficiency for tracks of both charges is around 91%.

Chapter 4

Hadron cross-section measurements at HARP

Armed with the detailed understanding of the efficiency and performance of the HARP experimental apparatus outlined in the previous chapter we now develop an algorithm for the extraction of hadron production cross-sections from the data. We present absolute differential production cross-sections for π^+, π^-, and protons from two beam and target configurations of particular relevance to existing neutrino physics experiments: 8.9 GeV/c protons on beryllium and 12.9 GeV/c protons on aluminum. We also develop a procedure for the estimation of correlated systematic uncertainties associated with these measurements.

4.1 Recipe for a cross-section

The goal of this analysis is to measure the inclusive yield of secondary hadrons (π^+,π^-,p) from proton-nucleus collisions:

$$\mathrm{p} + \mathrm{A} \rightarrow (\pi^+, \pi^-, \mathrm{p}) + X$$

The absolutely normalized double-differential cross-section for this process can be expressed in bins of kinematic variables in the laboratory frame, (p, θ), as

$$\frac{d^2\sigma^\alpha}{dpd\Omega}(p,\theta) = \frac{A}{N_A \cdot \rho \cdot t} \cdot \frac{1}{\Delta p \Delta \Omega} \cdot \frac{1}{N_{pot}} \cdot N^\alpha(p,\theta) \,, \tag{4.1}$$

where:

- $\frac{d^2\sigma^\alpha}{dpd\Omega}$ is the production cross-section of hadron $\alpha = (\pi^+, \pi^-, p)$ in $cm^2/(GeV/c)/sr$ for each (p, θ) bin covered in the analysis.

- $\frac{A}{N_A \cdot \rho}$ is the reciprocal of the number density of target nuclei [1]. A is the atomic mass of the target material, N_A is Avogadro's number and ρ is the density of the target.

- t is the thickness of the nuclear target along the beam direction. The target has a cylindrical shape with a diameter, d $\simeq$ 3.0 cm, and a measured thickness of t = (2.046 $\pm$ 0.002) cm and t = (1.9804 $\pm$ 0.002) cm for the beryllium and aluminum targets, respectively.

- Δp and $\Delta \Omega$ are the bin sizes in momentum and solid angle, respectively.[2]

- N_{pot} is the number of protons on target after event selection cuts (see Section 4.2).

- $N^\alpha(p, \theta)$ is the yield of hadron α in bins of momentum and polar angle in the laboratory frame.

The true hadron yield, $N^\alpha(p, \theta)$, is related to the measured one, $N^{\alpha'}(p', \theta')$, by a set of efficiency corrections and kinematic smearing matrices. In addition, there is a small but non-negligible mis-identification of particle types, predominantly between pions and protons. Both yields must be measured simultaneously in order to correct for migrations. Eq. 4.1 can be generalized to give the inclusive cross-section for a particle of type α,

$$\frac{d^2\sigma^\alpha}{dpd\Omega}(p,\theta) = \frac{A}{N_A \cdot \rho \cdot t} \cdot \frac{1}{\Delta p \Delta \Omega} \cdot \frac{1}{N_{pot}} \cdot M^{-1}_{p\theta\alpha \cdot p'\theta'\alpha'} \cdot N^{\alpha'}(p',\theta') \tag{4.2}$$

where reconstructed quantities are marked with a prime and $M^{-1}_{p\theta\alpha \cdot p'\theta'\alpha'}$ is the inverse of a matrix which fully describes the migrations between bins of generated and reconstructed

---

[1] $1.2349 \cdot 10^{23}$ per cm^3 for beryllium, $0.6004 \cdot 10^{23}$ per cm^3 for aluminum
[2] $\Delta p = p_{max} - p_{min}$; $\Delta \Omega = 2\pi(cos(\theta_{min}) - cos(\theta_{max}))$

quantities, namely: laboratory frame momentum, p, laboratory frame angle, θ, and particle type, α. In practice, the matrix M can be factorized into a set of individual corrections, as will be done here. The reasons for doing this are threefold:

- Not all efficiencies and migrations are functions of all three variables. Particle identification efficiencies and migrations do not depend on the angle, θ, and the tracking efficiency and momentum resolution are the same for pions and protons.

- Using techniques described in Chapter 3 the tracking efficiency and particle identification detector response functions can be determined from the data themselves and do not rely on simulation. Other corrections require using the Monte Carlo simulation.

- Measuring and applying the corrections separately will ease the assessment of systematic errors as will be discussed in Section 4.6.

The form of the corrections can be separated into two basic categories: absolute efficiencies and bin–to–bin migrations between true and reconstructed quantities. In particular, migrations in momentum and in particle identification are carefully considered. The various efficiency corrections can be functions of either reconstructed quantities or true ones and must then be applied at the appropriate point in the analysis. This is important given that some corrections, as mentioned above, are measured from the data themselves where one has only reconstructed quantities.

Particle distributions are built by multiplying a set of correction weights for each reconstructed track and weighting events before they are added to the total yields. In the present analysis, $M^{-1}_{p\theta\alpha\cdot p'\theta'\alpha'}$ has been factorized into the following components:

- $\varepsilon^{\mathrm{recon}}(p', \theta'_x, \theta'_y)$ is the efficiency for the reconstruction of an 'analysis track'. An 'analysis track' is defined to include a momentum measurement from the event vertex constraint, p_{v}, as well as a matched time-of-flight hit passing the criteria outlined in Section 3.4.4 such that $\varepsilon^{\mathrm{recon}} = \varepsilon^{\mathrm{track}} \cdot \varepsilon^{\mathrm{TOFW-match}}$. This efficiency, as measured from data, is shown for positive and negative tracks in Figure 3.27.

- $\varepsilon^{\mathrm{acc}}(\theta')$ is the correction for the geometric acceptance of the spectrometer and is a purely analytical function based on the assumption of azimuthal symmetry in hadron production and the fiducial volume cuts used in the analysis. See Section 3.4.2 and Eq. 3.11 for a full description of the acceptance correction and its dependence on the θ_y fiducial volume cut.

- $M^{-1}_{p \cdot p'}$ is the inverse of a matrix describing the migration between bins of generated and measured momentum, $M_{p' \cdot p}$,

$$\mathbf{N}'(p') = M_{p' \cdot p} \cdot \mathbf{N}(p)$$

  Monte Carlo samples will be used to generate the momentum migration correction. Therefore, it is not necessary to build the matrix M and then invert it. Instead, we build directly the elements of $M^{-1}_{p \cdot p'}$

$$\mathbf{N}(p) = M^{-1}_{p \cdot p'} \cdot \mathbf{N}'(p')$$

  The matrix is normalized across rows of reconstructed momentum (each track has a 100% probability of coming from *some* true momentum value) and the weights are used to 'spread' a single reconstructed track over multiple true momentum bins according to the elements of $M^{-1}_{p \cdot p'}$. In this way, the population in each true bin is comprised of tracks from all reconstructed momentum bins. A separate matrix is generated for each angular bin in the analysis since the momentum resolution can be a function of the track's angle.

$$N(p, \theta') = \sum_{p'} M^{-1}_{pp'}(\theta') \cdot N(p', \theta') \tag{4.3}$$

  This approach avoids difficulties associated with inverting a large smearing matrix as well as potential pathologies in the inverted matrix caused by a loss of information at the kinematic boundaries of the matrix itself. The drawback to this method is that one has some sensitivity to the underlying spectrum in the Monte Carlo used to generate the matrix.

- $M^{-1}_{\theta \cdot \theta'}(p)$ is a unit matrix, implying that angular migrations, which are small, are being neglected.

- $\eta^{\text{absorb}}(p, \theta_x, \theta_y, \alpha)$ is the absorption plus decay rate of secondary particles before reaching the time-of-flight wall. The reconstruction efficiency has been calculated for particles which are known to have traversed the detector; the absorption correction accounts for the fraction of particles which never make it to the downstream detectors. The absorption rate cannot be measured from data and must be determined from a Monte Carlo simulation. The absorption rate is measured as a function of the true momentum of the lost particle.

- $(1 - \eta^{\text{tert}}(p', \theta'_x, \theta'_y, \alpha))$ corrects for the fraction, $\eta^{\text{tert}} = \frac{\text{N}^{\text{rec}-\text{tert}}}{\text{N}^{\text{rec}}}$, of total tracks passing reconstruction cuts, N^{rec}, which are actually tertiary particles, $\text{N}^{\text{rec}-\text{tert}}$. Again the Monte Carlo will be used to estimate this rate, but the tertiary correction is generated as a function of the reconstructed momentum. These tracks emanate from outside the nuclear target and, therefore, are not reconstructed according to the same resolution function as secondary particles and must be subtracted before applying the momentum migration weights.

- $\varepsilon^{\text{e}-\text{veto}}(p, \alpha)$ is the efficiency for particles of type α passing the electron veto cut used to remove electrons from the analysis track sample as described in Section 3.4.3.

- $M^{-1}_{\alpha \cdot \alpha'}(p)$ is the inverse of the particle identification efficiency and migration matrix describing migrations between identified pions and protons,

$$
M_{\alpha' \cdot \alpha} = \begin{pmatrix} M_{\pi\pi} & M_{\pi\text{p}} \\ M_{\text{p}\pi} & M_{\text{pp}} \end{pmatrix}
$$

where $M_{\pi\pi}$ is the pion efficiency, $M_{\pi\text{p}}$ is the proton to pion migration, $M_{\text{p}\pi}$ is the pion to proton migration and M_{pp} is the proton efficiency. In Section 4.5 we will describe the particle identification algorithm and a method for calculating these matrix elements. The PID matrix is the only correction that is not applied as a weight to individual tracks but instead to the final distributions of identified pions and protons. The efficiency component does not create a problem as it is just another multiplicative weight and can be applied at any time. The late application of the migration elements, however, introduces a bias. Fortunately, we will show that the migration

terms are mostly $< 1\%$ and therefore the bias introduced is very small and can be neglected.

Neglecting the PID term, the expanded correction matrix takes the form,

$$
M^{-1}_{p\theta \cdot p'\theta'} = \frac{1}{\varepsilon^{\text{e}-\text{veto}}(p,\alpha)} \cdot \frac{1}{1-\eta^{\text{absorb}}(p,\theta_x,\theta_y,\alpha)}
$$
$$
\cdot M^{-1}_{p\cdot p'}(\theta') \cdot (1-\eta^{\text{tert}}(p',\theta'_x,\theta'_y,\alpha)) \cdot \frac{1}{\varepsilon^{\text{acc}}(\theta')} \cdot \frac{1}{\varepsilon^{\text{recon}}(p',\theta'_x,\theta'_y)}
$$

(4.4)

A final aspect of the analysis is the so-called 'empty target subtraction'. A background arises from beam protons interacting in materials other than the nuclear target (parts of the detector, air, etc.). These events can be subtracted by using data collected without the nuclear target in place where tracks have been selected and identified using the identical algorithm and set of cuts such that $\mathrm{N}^{\alpha'}(p',\theta') \rightarrow \left[\mathrm{N}^{\alpha'}_{\text{target}}(p',\theta') - \mathrm{N}^{\alpha'}_{\text{empty}}(p',\theta')\right]$.

Finally, simultaneously building corrected yields of identified pions and protons, multiplying by the inverse of the PID efficiency and migration matrix, and normalizing the cross-sections with the appropriate physical and kinematic quantities gives the double differential production cross-sections for pions and protons:

$$
\begin{pmatrix} \frac{d^2\sigma^\pi}{dpd\Omega}(p,\theta) \\[2ex] \frac{d^2\sigma^{\text{P}}}{dpd\Omega}(p,\theta) \end{pmatrix} = \frac{A}{\mathrm{N}_A \cdot \rho \cdot t} \cdot \frac{1}{\Delta p \Delta \Omega} \cdot \frac{1}{\mathrm{N}_{\text{pot}}} \cdot M^{-1}_{\alpha \cdot \alpha'}(p) \cdot \begin{pmatrix} M^{-1}_{p\theta \cdot p'\theta'} \left[\mathrm{N}^{\pi'}_{\text{target}}(p',\theta') - \mathrm{N}^{\pi'}_{\text{empty}}(p',\theta')\right] \\[2ex] M^{-1}_{p\theta \cdot p'\theta'} \left[\mathrm{N}^{\text{p}'}_{\text{target}}(p',\theta') - \mathrm{N}^{\text{p}'}_{\text{empty}}(p',\theta')\right] \end{pmatrix} .
$$

(4.5)

4.2 Event selection

The two threshold Cherenkov detectors (BCA and BCB) in the T9 beamline are used to select protons by requiring a value consistent with the pedestal in both detectors. The beam Cherenkov pulse height distributions for the 8.9 GeV/c and 12.9 GeV/c beams are shown in Figure 4.1. Figure 4.2 shows the time-of-flight distributions of those beam tracks identified as protons and pions by the Cherenkov selection in the 8.9 GeV/c beam, and we see that the two time peaks are consistent with the proton and pion hypotheses at this momentum.

Only events with a single reconstructed beam track in the four beam multi-wire proportional chambers (MWPCs) and no signal in the beam halo counters are accepted. This MWPC track is used to determine the impact position and angle of the beam particle on the target. A time measurement in one of three beam timing detectors consistent with a beam particle is also required for determining the arrival time of the proton at the target, t_0, as described in Section 3.4.1. This t_0 is necessary for calculating the time-of-flight of secondary particles.

The full set of criteria for selecting beam protons for this analysis is as follows:

- ADC count less than 120 in both beam Cherenkov A and beam Cherenkov B at 8.9 GeV/c and less than 130 in beam Cherenkov A and less than 125 in beam Cherenkov B at 12.9 GeV/c.

- time measurement(s) in TOFA, TOFB and/or TDS which are needed for calculating the arrival time of the beam proton at the target, t_0

- extrapolated position at the target within a 10 mm radius of the center of the target

- extrapolated angle at the target less than 5 mrad

- no signal in the beam halo counters

At the time of data taking, for data taken with a nuclear target, a downstream trigger in the forward trigger plane (FTP) was required to record the event.[3] The FTP is a double plane of scintillation counters covering the full aperture of the spectrometer magnet except a 60 mm central hole for allowing non-interacting beam particles to pass - which for a 5% interaction length target would otherwise comprise most of the recorded data. The efficiency of the FTP is measured to be $> 99.8\%$.

Using the FTP as an interaction trigger necessitates an additional set of unbiased, prescaled triggers for absolute normalization of the cross-section. Beam protons in the prescale trigger sample (1/64 of the total trigger rate) are subject to exactly the same selection criteria as FTP trigger events allowing the efficiencies of the selections to cancel and

---

[3]Empty target data sets are recored with an unbiased trigger setting since these samples are used to calibrate the experimental apparatus as well as for the empty target subtraction for cross-section measurements.
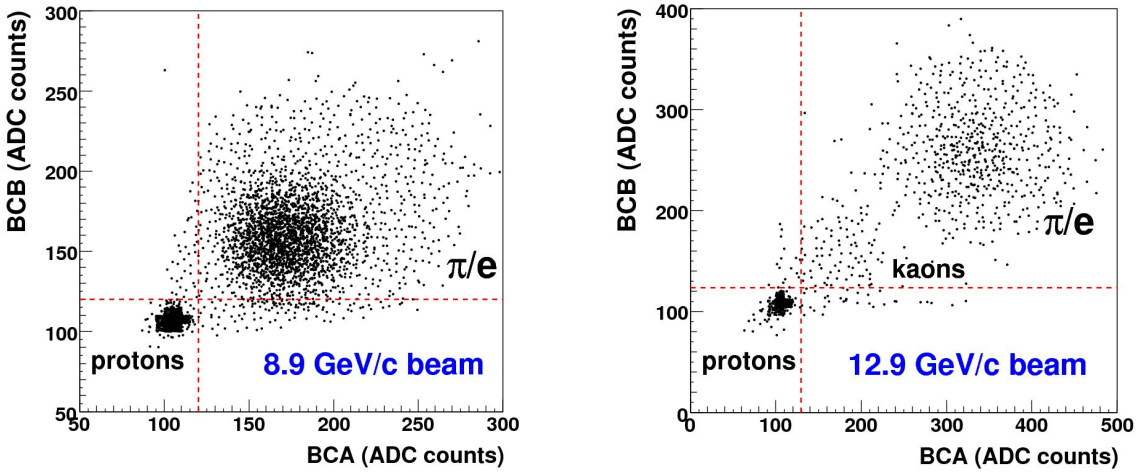
Figure 4.1: Beam Cherenkov pulse height distributions showing the expected correlation between the measurements in BCA and BCB. The cuts used to select protons in the 8.9 GeV/c beam (left) and 12.9 GeV/c beam (right) are shown.
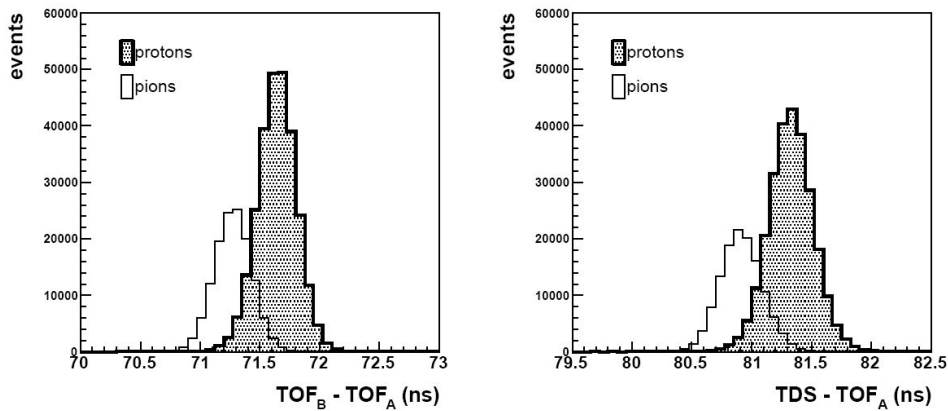
Figure 4.2: Beam time-of-flight distributions for the 8.9 GeV/c beam. The time difference between TOFA and TOFB is shown in the left panel. The right panel is the time difference between TOFA and the TDS. The shaded distributions are for particles identified as protons by the Cherenkov detectors as described in the text. The open histograms are all other beam tracks: pions, electrons and muons from pion decays.

Beam Momentum		8.9 GeV/c		12.9 GeV/c	
Target		**Be 5%**	**Empty**	**Al 5%**	**Empty**
protons on target		13,074,880	1,990,400	16,258,688	4,174,336
total events processed		4,682,911	413,095	4,252,252	674,027
events with accepted beam proton		2,277,657	200,310	3,082,365	478,747
beam proton events with FTP trigger		1,518,683	91,690	1,889,865	197,181
total good tracks in fiducial volume (pos)		132,147	4,584	143,870	7,274
total good tracks in fiducial volume (neg)		21,591	611	46,745	2,311

Table 4.1: Total number of events and number of protons on target as calculated from the prescaled trigger count for the 8.9 GeV/c and 12.9 GeV/c data sets with and without the beryllium or aluminum nuclear targets.

adding no additional systematic uncertainty to the absolute normalization of the result. These unbiased events are used to determine the N_{pot} used in the cross-section formula. The number of protons-on-target is known to better than 1%.

Applying these criteria we are left with the event totals and numbers of protons on target summarized in Table 4.1.

4.3   Secondary track selection

Secondary tracks are selected as described in Section 3.4.2. The selection criteria were optimized to ensure the quality of the momentum reconstruction as well as a clean time-of-flight measurement while maintaining a high reconstruction efficiency. The fiducial volume cuts, also described in Section 3.4.2, eliminate systematic effects that could arise from a complicated geometrical acceptance of tracks as a function of momentum.

Applying these cuts to reconstructed tracks in accepted events we are left with 132,147 positive and 21,591 negative secondary tracks in the beryllium thin target data set and 143,870 positive and 46,745 negative secondary tracks in the aluminum thin target data set as listed in Table 4.1.

4.4   Particle yield corrections

The reconstruction efficiency (Figure 3.27), acceptance correction (Eq. 3.11) and electron-veto efficiency (Figure 3.18) have already been described in Chapter 3. These efficiencies are the same for all data sets. Here we discuss the remaining yield corrections: the absorption rate, the tertiary particle rate and the momentum migration matrix. The PID algorithm and corrections will be covered in the next section.

4.4.1   Secondary particle absorption

The correction for absorption and decay refers to secondary particles created in the nuclear target that never make it to the time-of-flight wall for detection and possible identification. Figure 3.1 shows the location of the time-of-flight scintillator wall just beyond the back plane of drift chamber modules NDC3, NDC4 and NDC5. We use the Monte Carlo simulation to determine the size of the correction and the result is shown in Figure 4.3. Note this is an upward adjustment to the raw yield measured and is implemented as $1/(1 - \eta^{absorb}(p, \theta_x, \theta_y, \alpha))$ in Eq. 4.4. The absorption correction (which includes pion decays) is a function of θ_x and θ_y because it depends on the amount and type of physical material a particle passes through, thus the geometry of the detector. It is a function of α because of the different interaction cross-sections and possible decay rates of hadrons. This correction is separated from the tertiary correction discussed below because it does not depend on event multiplicity, kinematics or other details of the hadron production model used in the simulation, but only the total interaction cross-sections which are known with significantly more certainty.

4.4.2   Tertiary particle subtraction

The tertiary correction refers to the subtraction of reconstructed tracks which are actually reconstructions of tertiary particles, *i.e.* particles produced in inelastic interactions or decays of true secondary particles and not in primary interactions of beam protons with target nuclei (See section 3.2). The tertiary subtraction includes muons created in decays which are falsely identified as pions nearly 100% of the time due to their high β. This
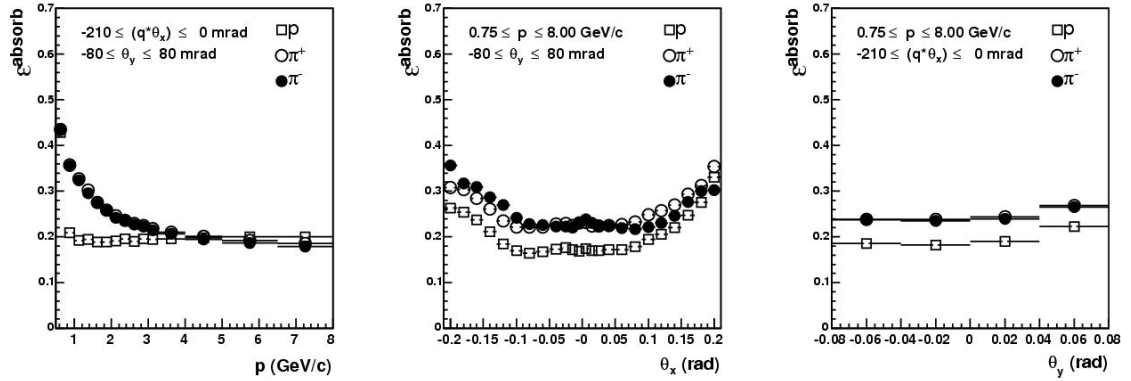
Figure 4.3: Absorption corrections for pions and protons according to Monte Carlo simulation as a function of particle momentum (left), production angle in the horizontal plane, θ_x (center) and production angle in the vertical plane, θ_y (right).

tertiary subtraction is also generated using the Monte Carlo simulation but *is* dependent on the details of the hadron production model used in the simulation. Figure 4.4 shows the tertiary fractions, η^{tert}, for the 8.9 GeV/c proton+beryllium data and the 12.9 GeV/c proton+aluminum data. The correction is significantly smaller than the absorption correction (compare Figures 4.3 and 4.4), but is less certain, so the contribution to the systematic error will be non-negligible.

4.4.3   Momentum migration matrix

The Monte Carlo simulation must be used to generate the momentum migration matrix as well. Three factors contribute to the values of the elements in this matrix: the resolution of the momentum reconstruction, $\sigma_p(p)$, the widths of the momentum bins as a function of momentum, and the underlying true particle spectrum. A unique matrix exists for each angular bin in the analysis since the momentum resolution and particle spectrum vary with angle. In Section 3.4.2 we measured the resolution, $\sigma_p(p)$, in the Monte Carlo and the data and found good agreement at zero angle. Other analyses, described in [58], have demonstrated agreement at non-zero angles, thus justifying the use of the simulation to generate the correction. Finally, using different available hadronic models to build different matrices allows us to quantify this effect on the measured cross-sections.
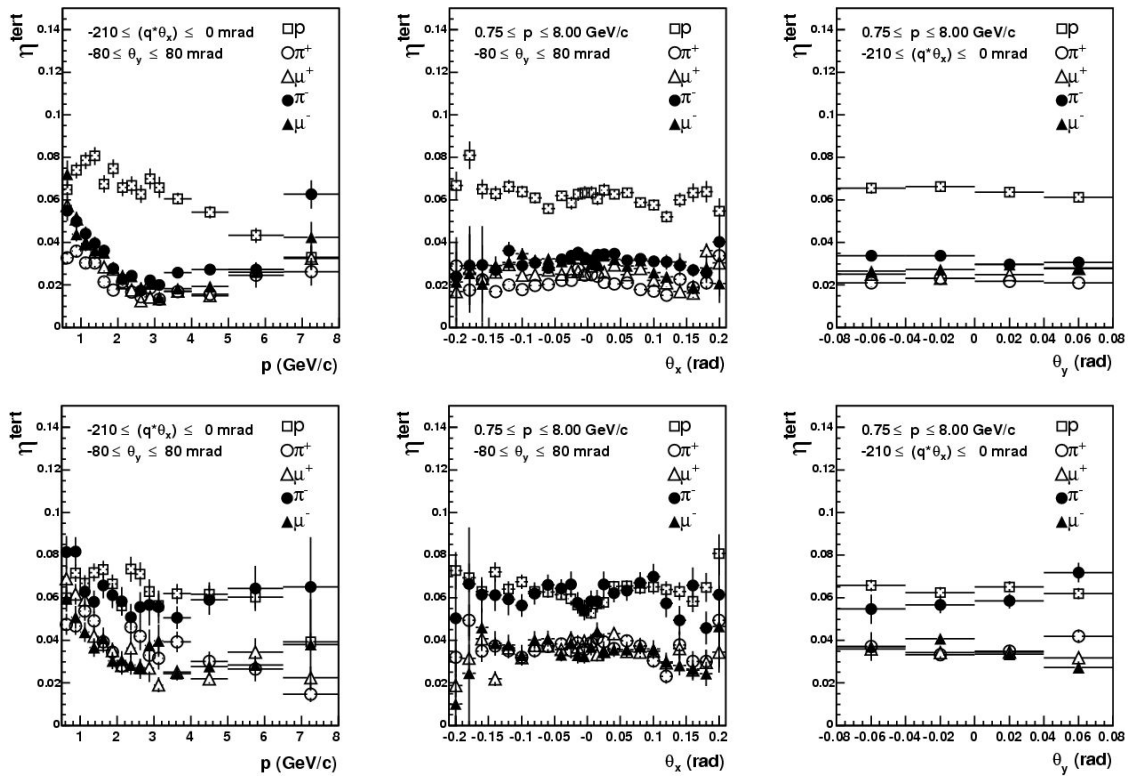
Figure 4.4: Tertiary particle rates for protons, pions and muons (which get identified as pions) according to Monte Carlo simulation for 8.9 GeV/c proton+beryllium data (top row) and 12.9 GeV/c proton+aluminum data (bottom row) as a function of particle momentum (left), production angle in the horizontal plane, θ_x (center) and production angle in the vertical plane, θ_y (right).

Figure 4.5 shows the diagonal elements of migration matrices generated for six angular

bins for the 8.9 GeV/c proton+beryllium data set. The momentum binning of the analysis

was designed to ensure that the diagonal migration remained above $\approx 50\%$ for most bins.

The momentum resolution becomes worse at higher momentum, so above 3.25 GeV/c the

momentum bins have been broadened. Two different hadronic models are compared in

Figure 4.5 to give a sense of the variation caused by this effect. Note that in some large an-

gle, high momentum bins the fluctuations are largely statistical due to poor Monte Carlo

statistics in these regions. The statistical precision of the migration matrices will be con-

sidered in the error analysis for the cross-section results presented below.

4.5   Particle identification algorithm

The cross-section analysis uses particle identification information from the time-of-

flight and Cherenkov PID systems; the discrimination power of time-of-flight below 3

GeV/c and the Cherenkov detector above 3 GeV/c are combined to provide powerful

separation of pions and protons. The calorimeter is presently used only for separating

pions and electrons when characterizing the response of the other detectors (See Sections

3.4.3 and 3.4.4). The resulting efficiency and purity of pion identification in the analysis

region is excellent.

4.5.1   The PID estimator

Particle identification is performed by determining the probability that a given track

is a pion or a proton based on the expected response of the detectors to each particle type

and the measured response for the track. Information from both detectors is combined for

maximum discrimination power using a Bayesian technique,

$$P(\alpha|\beta, \mathrm{N_{pe}}, p, \theta) = \frac{P(\beta, \mathrm{N_{pe}}|\alpha, p, \theta) \cdot P(\alpha|p, \theta)}{\sum\limits_{i=\pi,\mathrm{p},...} P(\beta, \mathrm{N_{pe}}|i, p, \theta) \cdot P(i|p, \theta)} \ . \tag{4.6}$$

where $P(\alpha|\beta, \mathrm{N_{pe}}, p, \theta)$ is the probability that a track with reconstructed velocity β, num-

ber of associated photo-electrons $\mathrm{N_{pe}}$, and momentum and angle p and θ is a particle of

type α. $P(i|p, \theta)$ is the so-called prior probability for each particle type, i, and is a function
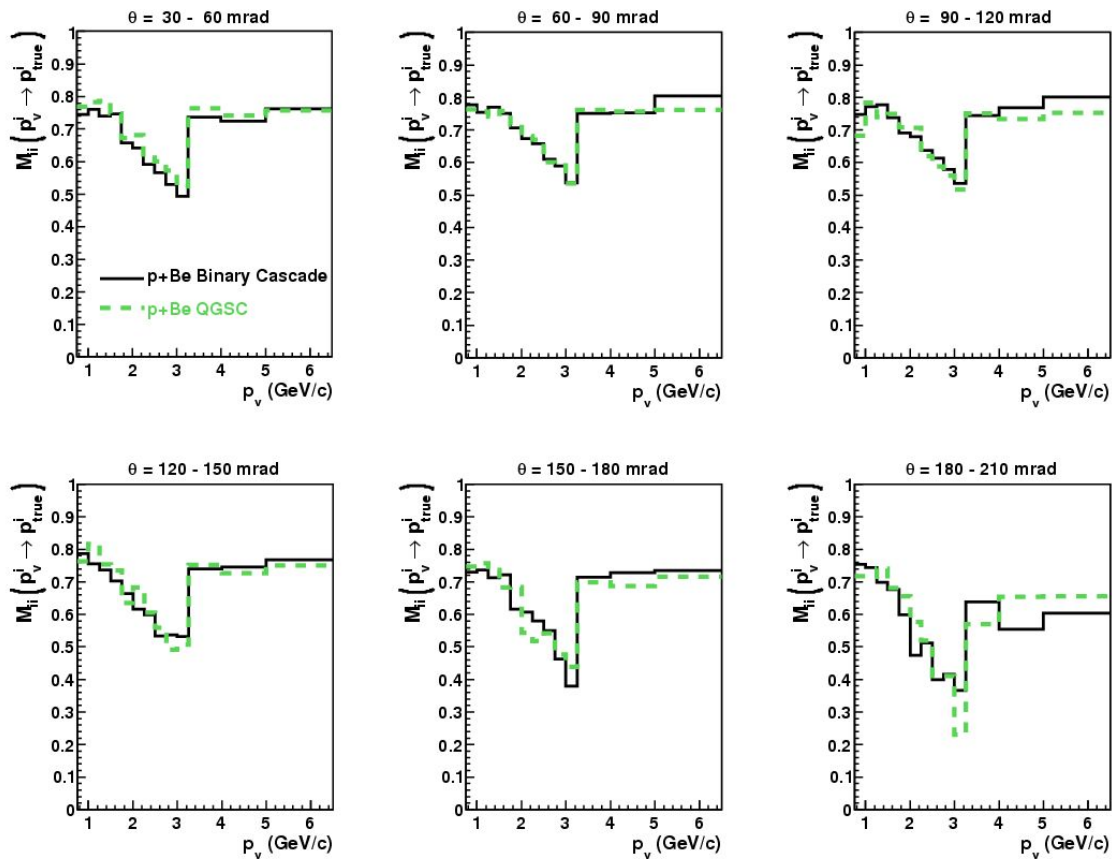
Figure 4.5: Diagonal elements of the momentum migration matrices generated for the 8.9 GeV/c proton+beryllium data set. A matrix is shown for each of the six angular bins to be used in the analysis. The matrix elements are shown for two different hadronic interaction models used in the simulation of proton+beryllium interactions, the Binary cascade model (black solid) and the QGSC model (green dashed).

of p and θ. In the Bayesian approach, the priors represent one's knowledge of the relative particle populations before performing a measurement. Finally, $P(\beta, \mathrm{N_{pe}}|i, p, \theta)$ is the expected response (β and $\mathrm{N_{pe}}$) of the PID detectors for a particle of type i and momentum and angle p, θ.

The following simplifications are applied to Eq. 4.6. First, we will assume no a priori knowledge of the underlying pion/proton spectra; that is, the prior distributions will be flat and equal everywhere, $P(i|p, \theta) = 1$ for all p, θ. This allows the priors to be dropped

from the expression, but the PID estimator no longer has a full probabilistic interpretation and cannot be directly used to estimate the particle yields. One could iterate the probability distributions to determine the yields. Alternatively, one can build the PID estimator for each track independently, and an efficiency and migration must be determined for a given cut on the estimator value, $P_{\text{track}} > P_{\text{cut}}$. We will see that the necessary corrections are small and the systematic uncertainty is negligible compared to other sources, making this approach adequate. Second, we will consider the response functions of the different PID detectors as independent and can therefore factorize the probability into separate terms for the TOFW and CHE. Third, the time-of-flight and Cherenkov detector responses show no angular dependence allowing θ to be removed from the above expression. Finally, we will only consider pions and protons as possible secondary particle types. Monte Carlo simulation indicates other potential backgrounds to be small.

$$P(\alpha|\beta, \text{N}_{\text{pe}}, p) = \frac{P(\beta|\alpha, p) \cdot P(\text{N}_{\text{pe}}|\alpha, p)}{P(\beta, |\pi, p) \cdot P(\text{N}_{\text{pe}}|\pi, p) + P(\beta|\text{p}, p) \cdot P(\text{N}_{\text{pe}}|\text{p}, p)} \, . \tag{4.7}$$

where $P(\alpha|\beta, \text{N}_{\text{pe}}, p)$ is the PID estimator for a track with reconstructed β, N_{pe} and p to be of type α and $P(\beta|\pi(\text{p}), p)$ and $P(\text{N}_{\text{pe}}|\pi(\text{p}), p)$ are the response functions for the TOFW and CHE, respectively, for pions(protons). Methods for measuring these functions from data have been presented in Chapter 3. The TOFW response function has been parameterized as a Gaussian function in bins of reconstructed momentum for both pions and protons,

$$P(\beta|\pi(\text{p}), p) = \frac{1}{\sigma_{\pi,\text{p}}(p)\sqrt{2\pi}} \cdot exp\left(-\frac{1}{2}\left(\frac{\beta - \overline{\beta}_{\pi,\text{p}}(p)}{\sigma_{\pi,\text{p}}(p)}\right)^2\right) \tag{4.8}$$

where the functions $\overline{\beta}_{\pi,\text{p}}(p)$ and $\sigma_{\pi,\text{p}}(p)$ are shown in Figure 3.25. The CHE response function, $P(\text{N}_{\text{pe}}|\pi(\text{p}), p)$, is just the probability that a pion or proton at momentum p will have more than 2 associated photo-electrons. $P(\text{N}_{\text{pe}} > 2|\pi(\text{p}), p)$ is shown in Figure 3.19.

For each reconstructed track, the PID estimator (Eq. 4.7) is evaluated under the pion and proton hypotheses. These are normalized quantities such that $P(\pi) + P(\text{p}) = 1$. A selection cut for both particle types of $P \geq 0.6$ was used to build raw yields of pions and protons. This cut will be shown to yield a very high purity (important for minimizing the bias discussed above) and it eliminates the possibility of identifying a single track as both a pion and a proton (because the estimators have been normalized).

4.5.2 Particle ID efficiency and migration matrix

The PID matrix describes the migrations of true pions and protons into reconstructed particle ID bins for a given PID estimator cut value used to select pions and protons,

$$
\begin{pmatrix} N_\pi \\ N_p \end{pmatrix}_{\text{rec}} = \begin{pmatrix} M_{\pi\pi} & M_{\pi p} \\ M_{p\pi} & M_{pp} \end{pmatrix} \cdot \begin{pmatrix} N_\pi \\ N_p \end{pmatrix}_{\text{true}}
\tag{4.9}
$$

where $M_{\pi\pi}$ is the pion efficiency, $M_{\pi p}$ is the proton to pion migration, $M_{p\pi}$ is the pion to proton migration and M_{pp} is the proton efficiency. A separate matrix is generated for each momentum bin used in the analysis as the PID migrations will vary with secondary momentum. The inverse of these matrices, $M^{-1}_{\alpha \cdot \alpha'}(p)$ are used to unfold the raw yields in Eq. 4.5.

The analytical calculation of these matrix elements is described in detail in [61]. Briefly, the four matrix elements can be expressed as an integral over the possible ranges of β and N_{pe} for values of the PID estimator above the cut value, P_{cut},

$$
M_{\alpha\alpha'} = \int_{P_\alpha > P_{\text{cut}}} d\beta \; dN_{pe} \; P(\beta|\alpha') \; P(N_{pe}|\alpha')
\tag{4.10}
$$

where $P(\beta|\alpha')$ and $P(N_{pe}|\alpha')$ are the TOFW and CHE response functions for a particle of type α'. This expression is good for a given bin of momentum and so the explicit dependence on p has been dropped from Eqs. 4.10 and 4.11. Because the CHE is used digitally, the integral over N_{pe} can be separated into two flat regions corresponding to a CHE signal and no CHE signal. The TOFW part is a Gaussian function and so can be integrated analytically using the Error function.

$$
M_{\alpha\alpha'} = P(N_{pe} \le 2|\alpha') \times \int_{P_\alpha^{N_{pe} \le 2} > P_{\text{cut}}} d\beta \; P(\beta|\alpha') \; +
$$
$$
P(N_{pe} > 2|\alpha') \times \int_{P_\alpha^{N_{pe} > 2} > P_{\text{cut}}} d\beta \; P(\beta|\alpha')
\tag{4.11}
$$

The only remaining task is to solve for the value of β that corresponds to a given value of the PID estimator, P_α, in order to determine the limits of the integrals in Eq. 4.11. These limits are slightly complicated by the existence of the β–outliers introduced in Section 3.4.4, and we will refer the reader to [61] for the final expressions.

The PID efficiency and migration matrix elements depend upon eight parameters of the particle ID detector response functions: the CHE signal efficiencies for pions and protons, $P(\mathrm{N_{pe}}|\pi(\mathrm{p}))$, the TOFW response parameters $\overline{\beta}_{\pi,\mathrm{p}}$ and $\sigma_{\pi,\mathrm{p}}$ and the β–outlier rates for pions and protons. These parameters were extracted from data or Monte Carlo in Chapter 3 with errors. From these parameters and their uncertainties one can calculate the 16 element covariance matrix for the PID efficiency and migration matrix

$$C_{ij}^{kl} = \mathrm{cov}(M_{ij}, M_{kl}) = \frac{\partial M_{ij}}{\partial \lambda_m} \frac{\partial M_{kl}}{\partial \lambda_m} \mathrm{cov}(\lambda_m, \lambda_m) \, , \qquad (4.12)$$

where the λ_m are the 8 parameters that go into the matrix element calculation. Each of the derivatives, $\partial M_{ij}/\partial \lambda_m$, have been explicitly derived in the Appendices of [61].

The final matrix elements and diagonal errors for the 8.9 GeV/c proton+beryllium data and the 12.9 GeV/c proton+aluminum data are shown in Figure 4.6. The four panels are the four matrix elements, $M_{\pi\pi}$, $M_{\pi\mathrm{p}}$, $M_{\mathrm{p}\pi}$ and M_{pp}, each shown as a function of particle momentum. The four elements of a single matrix from Eq. 4.5 would be given by the value from each panel corresponding to a given momentum.

Looking first at the upper left panel we see that pion identification efficiency is $> 95\%$ across the full range of momenta and for both data sets. The proton efficiency (lower right) dips slightly at low momentum due to a larger β–outlier rate for protons at low momentum, but the efficiency is still above 92% except in the first bin. The migrations between pions and protons are small in both data sets. They are negligible ($< 10^{-3}$) below 2.5 GeV/c and grow to the largest value of 3% above 6.5 GeV/c for the aluminum data set only. For the beryllium data set the migrations are no where above 1%.

4.6 Method for the estimation of systematic errors

For the cross-sections to be presented in the next section a systematic error analysis will be performed to estimate the accuracy of the measurements. A contribution to the total uncertainty will be evaluated for each correction applied to the raw yields described in Section 4.1 and correlations between (p, θ) bins will be included, resulting in a full error matrix with N^2 elements where N is the number of (p, θ) bins.
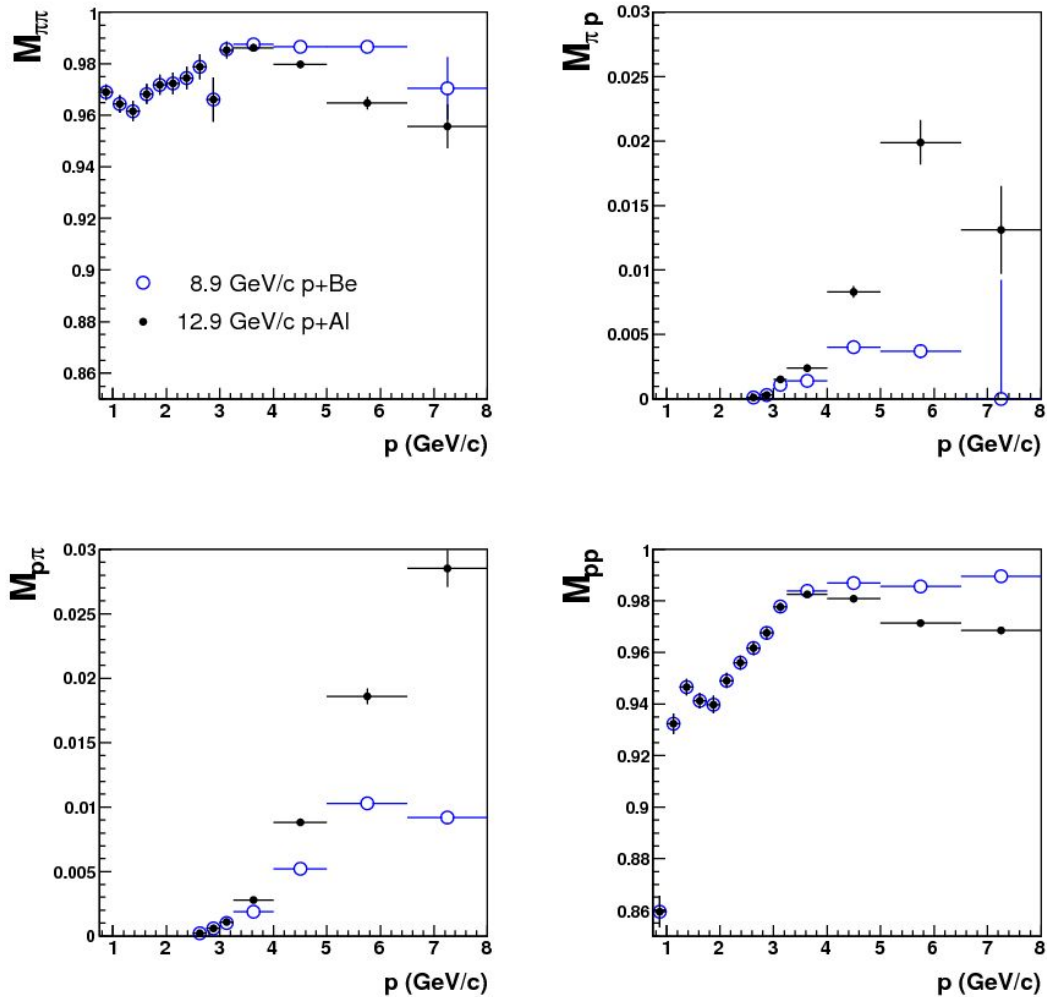
Figure 4.6: Particle ID efficiency and migration matrix elements as a function of momentum. Upper left is the pion identification efficiency, $M_{\pi\pi}$. Upper right is the proton to pion migration, $M_{\pi p}$. Lower left is the pion to proton migration, $M_{p\pi}$. Lower right is the proton identification efficiency, M_{pp}. The blue open circles are the matrix elements calculated for the 8.9 GeV/c proton+beryllium data set. The black points are the elements for the 12.9 GeV/c proton+aluminum data set.

A Monte Carlo technique is used to estimate the uncertainty on the cross-section. First, for each correction applied to the raw yields, an error is estimated on the correction itself. For example, the absorption correction refers to the loss of secondary hadrons due to absorption in detector materials and air up-stream of the time-of-flight wall. The Monte Carlo is used to estimate the rate and it depends mostly on the total interaction cross-sections of pions and protons in carbon. The data used to set these cross-sections in the simulation have uncertainties of order 10%. Therefore, we assume this uncertainty on the correction. To estimate the uncertainty on the cross-section arising from the absorption correction, $N \approx 100$ analyses are performed where only the absorption correction is randomly fluctuated for each analysis with an RMS of 10%. Similarly, N cross-section results are generated for N fluctuations of each source of systematic error. The correlated error matrix for each correction is then built from the N cross-section results,

$$
E_{ij}^m = \frac{1}{N} \sum_{n=1}^{N} \left[\frac{d^2\sigma_{\mathrm{CV}}^\alpha}{dpd\Omega} - \frac{d^2\sigma_{m,n}^\alpha}{dpd\Omega} \right]_i \times \left[\frac{d^2\sigma_{\mathrm{CV}}^\alpha}{dpd\Omega} - \frac{d^2\sigma_{m,n}^\alpha}{dpd\Omega} \right]_j
\tag{4.13}
$$

where i and j label bins of (p, θ), E_{ij}^m is the $(i, j)^{th}$ element of one of the error matrices (labeled m), $d^2\sigma_{\mathrm{CV}}^\alpha/(dpd\Omega)$ is the central value for the double-differential cross-section measurement of particle α and $d^2\sigma_{m,n}^\alpha/(dpd\Omega)$ is the cross-section result from the nth variation of the mth systematic error source.

Note that Eq. 4.13 produces matrix elements in units of $(\mathrm{error})^2$. And while the correlations between kinematic bins are considered for each source of uncertainty, the sources themselves will be assumed to be independent so that the total error matrix is just the sum of the m matrices,

$$
E_{ij} = \sum_m E_{ij}^m \, .
\tag{4.14}
$$

It is often convenient to consider the uncertainty in percentage instead of in cross-section units. In addition, we define the fractional error matrix

$$
E_{ij}^{\mathrm{frac}} = \frac{E_{ij}}{\left[\dfrac{d^2\sigma_{\mathrm{CV}}^\alpha}{dpd\Omega} \right]_i \times \left[\dfrac{d^2\sigma_{\mathrm{CV}}^\alpha}{dpd\Omega} \right]_j}
\tag{4.15}
$$

In total, we will consider 14 sources of systematic uncertainty on the measured cross-sections. These include data statistical errors and Monte Carlo statistical errors in addition

to systematic sources. Below we briefly describe each source of error considered.

i. **Target data statistical uncertainty :** Since statistical errors are uncorrelated the statistical error matrices are purely diagonal. A unique matrix for pions and protons is constructed with $N^{\alpha}_{\text{tracks}}(p, \theta) \times f$ as the diagonal elements. $N^{\alpha}_{\text{tracks}}(p, \theta)$ is the number of reconstructed tracks with momentum p and angle θ identified as particle type α and f is a constant factor that converts the error into cross-section units. The number of tracks, and not the square root of the number of tracks, is used because we want the error matrix to be in units of $(\text{error})^2$.

ii. **Empty target data statistical uncertainty :** As described in Section 4.1 data sets with the same beam momentum but with no nuclear target are used to subtract non-target interaction backgrounds from target data. The subtraction ranges from negligible to about 30%, but the data sets typically correspond to significantly fewer beam protons on target. Therefore, a second statistical error matrix with diagonal elements $N^{\alpha}_{\text{tracks}}(p, \theta) \times f$ is also generated for the empty target data set used. We will see that the effect on the final cross-section can be as large as that coming from the target data statistics.

iii. **Empty target subtraction systematic uncertainty :** For both data sets being analyzed here the nuclear target is 5% of a nuclear interaction length for that material, so the proton beam is attenuated by $\sim 5\%$ for target data. Therefore, a normalization uncertainty of 5% has been estimated for the empty target subtraction in addition to the statistical error considered above. With the level of the subtraction ranging from negligible to 30%, the uncertainty on the final cross-section is typically a few percent.

iv. **Reconstruction efficiency statistical uncertainty :** The reconstruction efficiency has been estimated from the data themselves as described in Section 3.4.2. For this reason the only uncertainty considered on this efficiency is the size of the statistical sample used to calculate it. To decrease this error, many high momentum data sets have been combined including beryllium, aluminum, carbon and tantalum targets with incident proton beams ranging from 8 GeV/c to 15 GeV/c. The reconstruction efficiency

in each (p, θ_x, θ_y) bin is just the ratio of reconstructed tracks, $\mathrm{N^{track}}$, to the total number of particles passing through the detector, $\mathrm{N^{parts}}$, so at each stage binomial errors are assumed, $\sqrt{\mathrm{N^{track}} * (1 - \frac{\mathrm{N^{track}}}{\mathrm{N^{parts}}})}/\mathrm{N^{parts}}$, and propagated through the calculation described.

v. **Absorption correction systematic uncertainty :** As described above, the systematic error on the absorption correction is estimated to be 10% for both pions and protons. The error is implemented as a fully correlated normalization uncertainty on the level of absorption predicted, so the absorption in all (p, θ_x, θ_y) bins shifts up and down together. In this way we determine the maximum excursions on the total integrated cross-section measured.

vi. **Absorption correction Monte Carlo statistical uncertainty :** The absorption correction is estimated from a Monte Carlo simulation. The absorption probability of a particle of type α produced in the nuclear target with kinematics (p, θ_x, θ_y) is determined by the amount and type of material that the individual particle trajectory will pass through before reaching the TOFW. It does not depend on the underlying spectrum of secondaries or incident beam momentum. Therefore, different Monte Carlo samples have been combined to increase the statistical sample in each kinematic bin used to measure the correction and minimize this uncertainty.

vii. **Tertiary subtraction systematic uncertainty :** The tertiary particle reconstruction rate is a more complicated correction than the absorption rate. It does depend on the beam momentum, the shape of the secondary spectrum, and the hadronic production models of hadrons in detector materials at a large range of momenta (from the incident beam momentum down). Fortunately the correction is an order of magnitude smaller than the more certain absorption correction. Most of the material where tertiary particles might be produced in the detector is carbon, so it is the simulation of inelastic interactions of low-energy protons and pions in carbon that become important in generating this correction. Comparisons of low momentum HARP p+C, π^++C and π^-+C data to the hadronic models used in the simulation have verified these models to $\approx$ 50% and we will assume this uncertainty on the calculated tertiary

subtraction.

viii. **Tertiary subtraction Monte Carlo statistical uncertainty :** Because the tertiary rate depends on the specific experimental configuration, different Monte Carlo samples could not be combined to reduce Monte Carlo statistical uncertainties.

ix. **Momentum scale systematic uncertainty :** In Section 3.4.2 we investigated the uncertainty on the absolute scale of the momentum reconstruction. At zero angle it was seen to be $\sim 2\%$ in empty target data samples from 1.5–12.9 GeV/c. In Ref. [58] other methods are used to explore non-zero angles and the conclusion is the same. To assess the impact on the cross-section measurement N measurements are made where the momentum of each track is scaled by the same fraction, $p \to \eta \cdot p$, where the factor, η, is randomly drawn from a Gaussian function with width 0.02 and mean 1.0.

x. **Momentum smearing systematic uncertainty :** Momentum smearing refers to the migration of reconstructed tracks from their true momentum value to a different momentum value due to the finite resolution of the apparatus and the reconstruction algorithm employed. The measured spectrum of secondaries is corrected by using an unsmearing matrix according to Eq. 4.3. As described in Section 4.4 the dominant source of systematic uncertainty in the matrix elements is the choice of hadronic generator used to determine the secondary spectrum. Therefore, to asses the error on the cross-section a matrix is generated for a hadronic interaction model other than the default and compared to the central value cross-section results.

xi. **Momentum smearing Monte Carlo statistical uncertainty :** The statistical uncertainty in the momentum migration matrix can be large since reconstructed tracks are divided into $N^{\theta-\mathrm{bins}} \times N^{p-\mathrm{bins}} \times N^{p-\mathrm{bins}}$ bins. To estimate the effects, each row of the matrix is fluctuated according to a multinomial distribution before being normalized and the cross-section is calculated for N such variations of the matrix.

xii. **Electron-veto efficiency statistical uncertainty :** As with the reconstruction efficiency the uncertainty on the electron-veto efficiency is due only to the statistical error of the sample used to generate the correction.

xiii. **PID efficiency and migration matrix systematic uncertainty :** The 4-element PID efficiency matrix and 16-element covariance matrix are calculated analytically as described in Section 4.5. To determine the impact on the measured cross-section, N analyses are performed where the PID matrix has been fluctuated according to its covariance matrix as described at [136].

Consider the multivariate normal distribution comprised of:

mean values $\mu = (M_{\pi\pi}, M_{\pi p}, M_{p\pi}, M_{pp})$

covariance matrix, Σ.

After finding the Cholesky decomposition of Σ, A, such that $AA^T = \Sigma$, the fluctuated vector can be found from $\mu + AZ$ where Z is a 4-element vector of independently fluctuated standard normal $(\text{mean} = 0, \sigma = 1)$ variates.

xiv. **Overall normalization systematic uncertainty :** A main source of fully correlated normalization uncertainty comes from the proton beam targeting efficiency. A small fraction ($\sim 1\%$) of the protons which pass all event selection cuts in Section 4.2 are deflected and do no collide with the nuclear target. In addition, there are fully correlated contributions to the reconstruction efficiency and particle identification efficiency calculations estimated at another $\sim 1\%$. Uncertainty on the measured thickness of the nuclear target ($\sim 0.1\%$) and the count of the number of protons on target ($\sim 0.2\%$) are negligible. In total we estimate a fully correlated normalization uncertainty on the measured cross-section of 2%.

4.7 Cross-section results

Two data sets have been analyzed according to Eq. 4.5 to extract the double-differential production cross-sections of charged pions and protons: 8.9 GeV/c protons on beryllium and 12.9 GeV/c protons on aluminum. Emphasis has been put on these particular data sets because of their importance to existing neutrino oscillation experiments, namely, MiniBooNE at Fermilab in the US and the K2K experiment in Japan[4].

---

[4]The analysis methods and software tools developed to generate these results have been carefully prepared in a general way to allow their use for the measurement of other useful cross-sections including thick

Cross-section results will be presented for both data sets in the kinematic range from $0.75\,\mathrm{GeV}/c \leq p \leq 8.0\,\mathrm{GeV}/c$ and $0.030\,\mathrm{rad} \leq \theta \leq 0.210\,\mathrm{rad}$. There are 14 momentum bins and 6 angular bins with boundaries defined by:

- $p = [0.75, 1.0, 1.25, 1.5, 1.75, 2.0, 2.25, 2.5, 2.75, 3.0, 3.25, 4.0, 5.0, 6.5, 8.0]\,\mathrm{GeV}/c$

- $\theta = [30, 60, 90, 120, 150, 180, 210]\,\mathrm{mrad}$

Production cross-sections have been measured for protons, π^+ and π^- and a full error matrix with $(14 \times 6)^2 = 7056$ elements has been generated for each. The measured π^+ and π^- production cross-sections from $8.9\,\mathrm{GeV}/c$ proton+beryllium collisions are shown in Figure 4.7 with proton production cross-sections shown in Figure 4.8. The error bars shown are the square-root of the diagonal elements of the error matrices. No graphical representation of the off-diagonal elements is shown. Figures 4.9 and 4.10 show the π^+, π^- and proton production cross-sections for the $12.9\,\mathrm{GeV}/c$ proton+aluminum data. All cross-sections and diagonal errors are tabulated in Appendix A.

Finally, it is important to better quantify the uncertainty on the cross-section measurements. In addition to the total uncertainty, knowing the contributions of the individual error sources provides valuable guidance for future efforts to improve the results. To get an idea of the uncertainty on the cross-section we define the quantity δ_{diff},

$$\delta_{\mathrm{diff}} \equiv \frac{1}{\mathrm{N}} \sum_{i=1}^{\mathrm{N}} \frac{\sqrt{E_{ii}}}{\left[d^2\sigma_{\mathrm{CV}}^{\alpha}/(dpd\Omega)\right]_i} \ . \tag{4.16}$$

where N is the number of (p, θ) bins to be averaged over. E_{ij} is either the total covariance matrix or one of the individual 14 covariance matrices evaluated for the cross-section. δ_{diff} can be interpreted as the average fractional uncertainty on the double-differential cross-section (diagonal errors only). Additionally, we define the quantity δ_{int},

$$\delta_{\mathrm{int}} \equiv \frac{\sqrt{\sum_{ij} (dpd\Omega)_i \, E_{ij} \, (dpd\Omega)_j}}{\sum_i \left(d^2\sigma_{\mathrm{CV}}^{\alpha}\right)_i} \tag{4.17}$$

target (up to 1 interaction length) versions of these settings and data with other nuclear targets from hydrogen to lead. Currently work is being done to expand the software's capabilities to include the measurement of the production cross-section of charged kaons as well.

where $(d^2\sigma_{CV}^\alpha)_i$ is the double-differential cross-section in bin i multiplied by its phase space factor, $(dpd\Omega)_i$. δ_{int} can be interpreted as the uncertainty on the total integrated cross-section within the kinematic region considered.

Both quantities were evaluated for each of the fourteen error sources as well as the total. The results are tabulated in Tables 4.2 and 4.3 for the beryllium and aluminum data, respectively. The average total error on the differential cross-section is <10% for π^+ and protons. The π^- errors are slightly higher at 12–13% due mostly to larger statistical errors from their smaller production rates.

Close inspection of Tables 4.2 and 4.3 reveals that statistical and systematic errors contribute almost equally for the chosen binning. Also, particle identification uncertainties are negligible compared to other sources, so the PID algorithm appears optimized. The largest contributions to the cross-section uncertainty come from the momentum reconstruction and the absorption and tertiary corrections. The track reconstruction algorithm is probably optimal given the spatial resolution of the drift chambers ($\sim 340\ \mu m$) and low chamber hit efficiency. The most likely place to reduce the uncertainty on the cross-section measurement is the absorption and tertiary track corrections. The accuracy of both corrections could be improved by using the increasing wealth of hadron cross-section data available from HARP to improve the hadronic simulation packages used to generate the corrections. However, both of these ideas are sizable projects and beyond the scope of this dissertation.
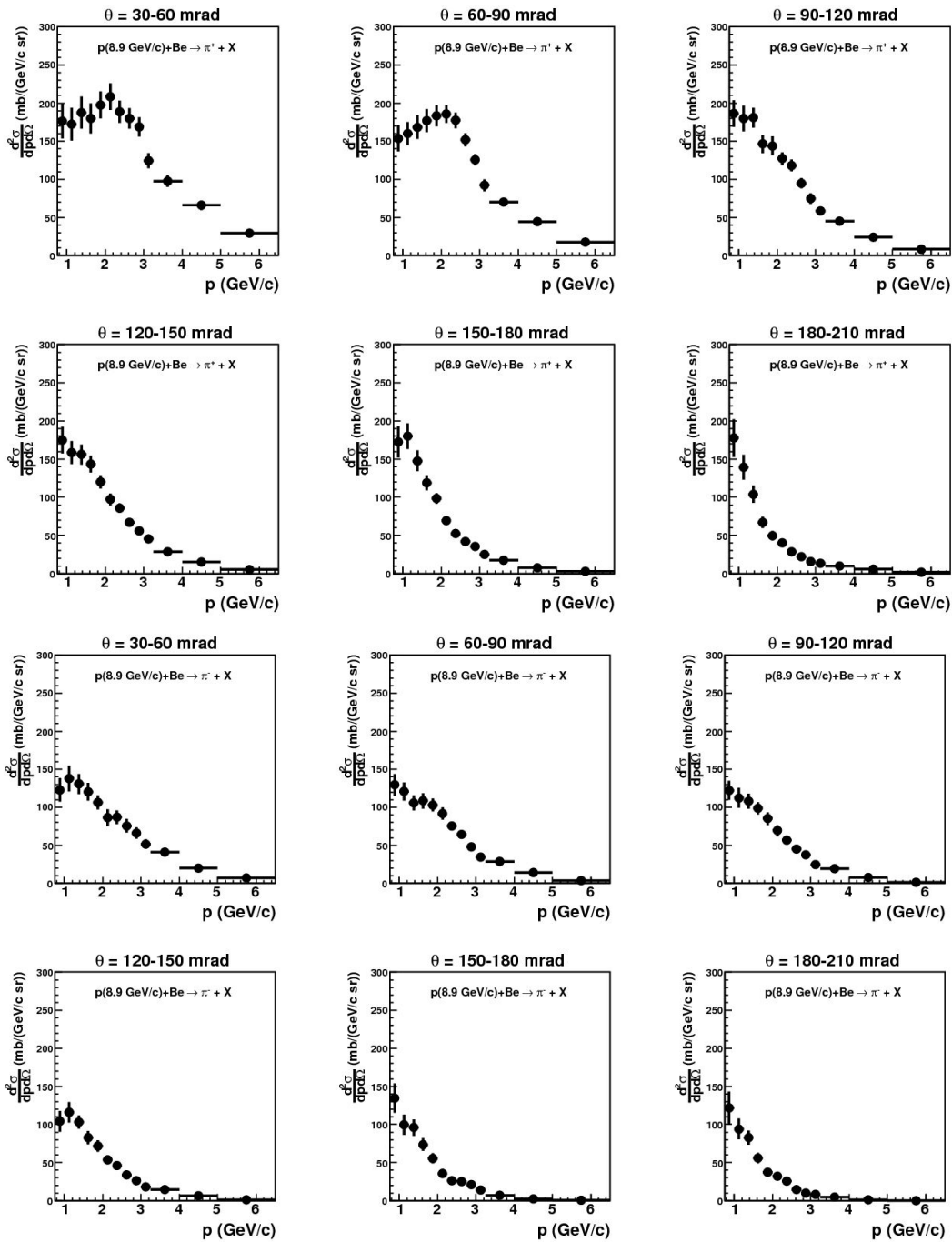
Figure 4.7: Double-differential production cross-sections of π^+ (top two rows) and π^- (bottom two rows) from the interaction of 8.9 GeV/c protons with beryllium. Each panel shows the cross-section as a function of momentum from 0.75 GeV/c to 6.5 GeV/c in a particular angular bin indicated above each plot. The error bars shown are the square-root of the diagonal elements of the total error matrices.
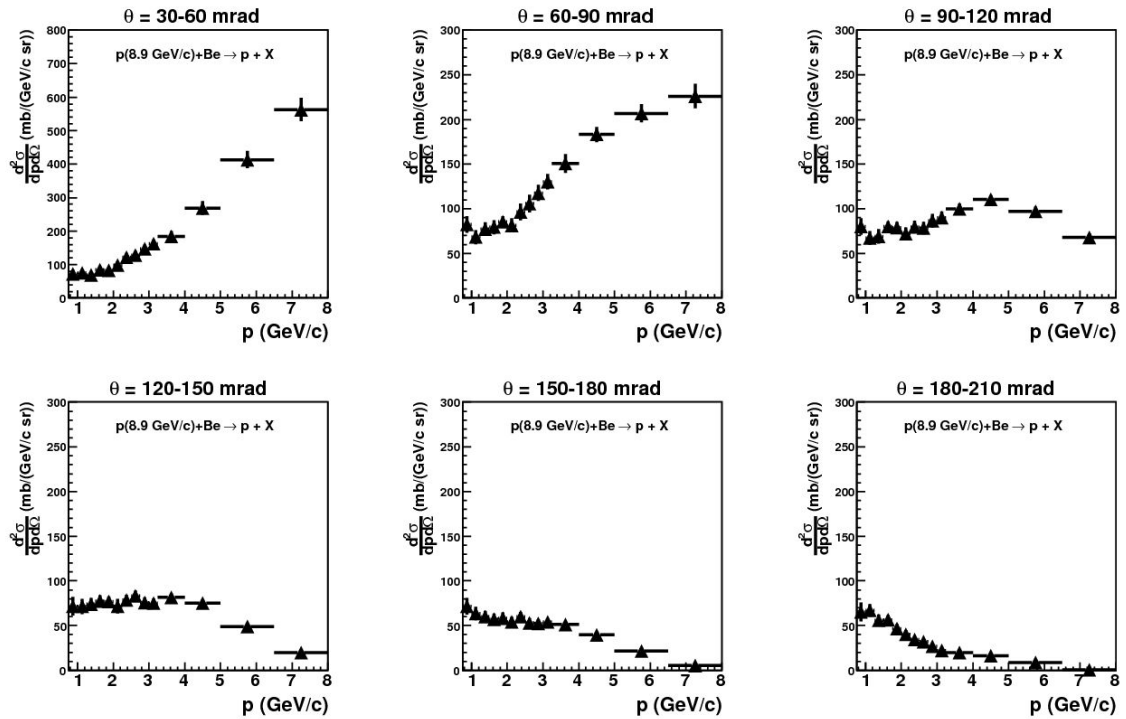
Figure 4.8: Double-differential production cross-sections of protons from the interaction of 8.9 GeV/c protons with beryllium. Each panel shows the cross-section as a function of momentum from 0.75 GeV/c to 8.0 GeV/c in a particular angular bin indicated above each plot. The error bars shown are the square-root of the diagonal elements of the total error matrix.

Data Set	p(8.9GeV/c) + beryllium					
secondary particle	π^+		π^-		proton	
mometum range (GeV/c)	0.75 – 6.5		0.75 – 6.5		0.75 – 8.0	
angular range (rad)	0.03 – 0.21		0.03 – 0.21		0.03 – 0.21	
Error Category	$\delta^{\pi^+}_{\mathrm{diff}}$ (%)	$\delta^{\pi^+}_{\mathrm{int}}$ (%)	$\delta^{\pi^-}_{\mathrm{diff}}$ (%)	$\delta^{\pi^-}_{\mathrm{int}}$ (%)	$\delta^{\mathrm{P}}_{\mathrm{diff}}$ (%)	$\delta^{\mathrm{P}}_{\mathrm{int}}$ (%)
Statistical Errors:						
i. Target statistics	4.8	0.6	7.4	0.8	4.7	0.4
ii. Empty target statistics	4.9	0.6	6.3	0.8	5.1	0.4
Sub-total	**6.9**	**0.8**	**9.7**	**1.1**	**6.9**	**0.6**
Track yield corrections:						
iii. Empty target subtraction	1.5	0.1	2.1	0.2	1.4	0.1
iv. Reconstruction efficiency	1.1	0.5	4.4	1.0	1.2	0.2
v. Pion, proton absorption syst.	3.6	4.2	4.7	5.8	2.6	2.4
vi. Pion, proton absorption stat.	0.4	<0.1	0.4	<0.1	0.4	<0.1
vii. Tertiary subtraction syst.	1.5	1.7	1.1	1.2	2.2	1.6
viii. Tertiary subtraction syst.	0.5	0.1	0.6	0.2	0.7	0.1
Sub-total	**4.4**	**4.6**	**6.9**	**6.0**	**3.9**	**2.9**
Momentum reconstruction:						
ix. Momentum scale	4.0	0.1	2.0	0.1	4.2	1.7
x. Momentum resolution syst.	2.2	0.8	4.6	0.5	2.6	0.7
xi. Momentum resolution stat.	1.4	<0.1	1.9	0.1	1.5	<0.1
Sub-total	**4.8**	**0.8**	**5.4**	**0.5**	**5.2**	**1.8**
Particle Identification:						
xii. Electron veto	0.1	<0.1	0.1	<0.1	0.1	<0.1
xiii. Pion, proton ID correction	0.4	0.4	0.3	0.3	0.3	0.1
Sub-total	**0.4**	**0.4**	**0.3**	**0.3**	**0.3**	**0.1**
Overall normalization:	**2.0**	**2.0**	**2.0**	**2.0**	**2.0**	**2.0**
Total	**9.7**	**5.2**	**13.2**	**6.4**	**9.7**	**4.0**

Table 4.2: Summary of the uncertainties affecting the measured π^+, π^- and proton cross-sections from 8.9 GeV/c proton+beryllium interactions. The average error on the differential cross-section, δ_{diff}, and the error on the total integrated cross-section, δ_{int}, are listed for each of the fourteen error sources described in Section 4.6 as well as the total uncertainty.
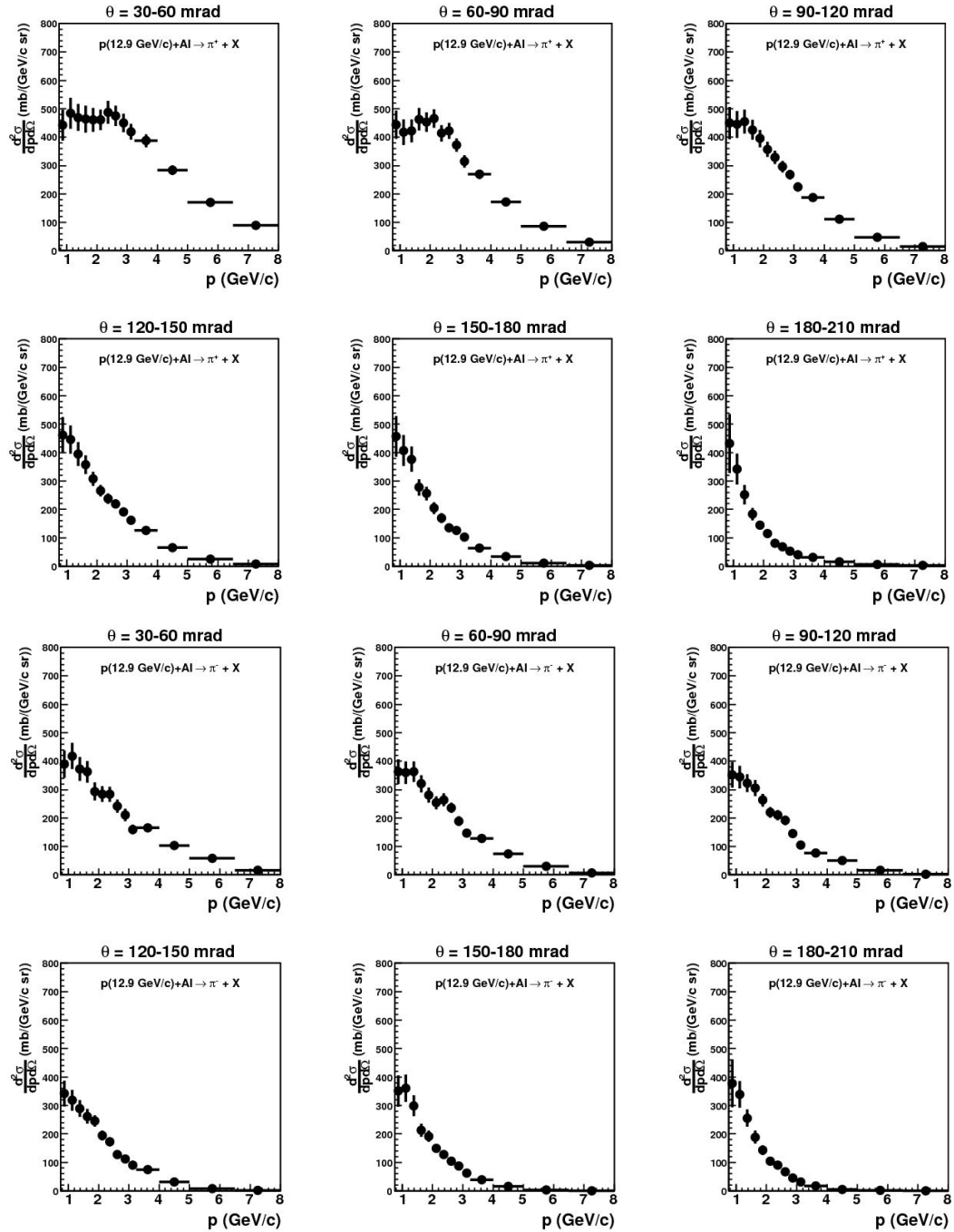
Figure 4.9: Double-differential production cross-sections of π^+ (top two rows) and π^- (bottom two rows) from the interaction of 12.9 GeV/c protons with aluminum. Each panel shows the cross-section as a function of momentum from 0.75 GeV/c to 8.0 GeV/c in a particular angular bin indicated above each plot. The error bars shown are the square-root of the diagonal elements of the total error matrices.
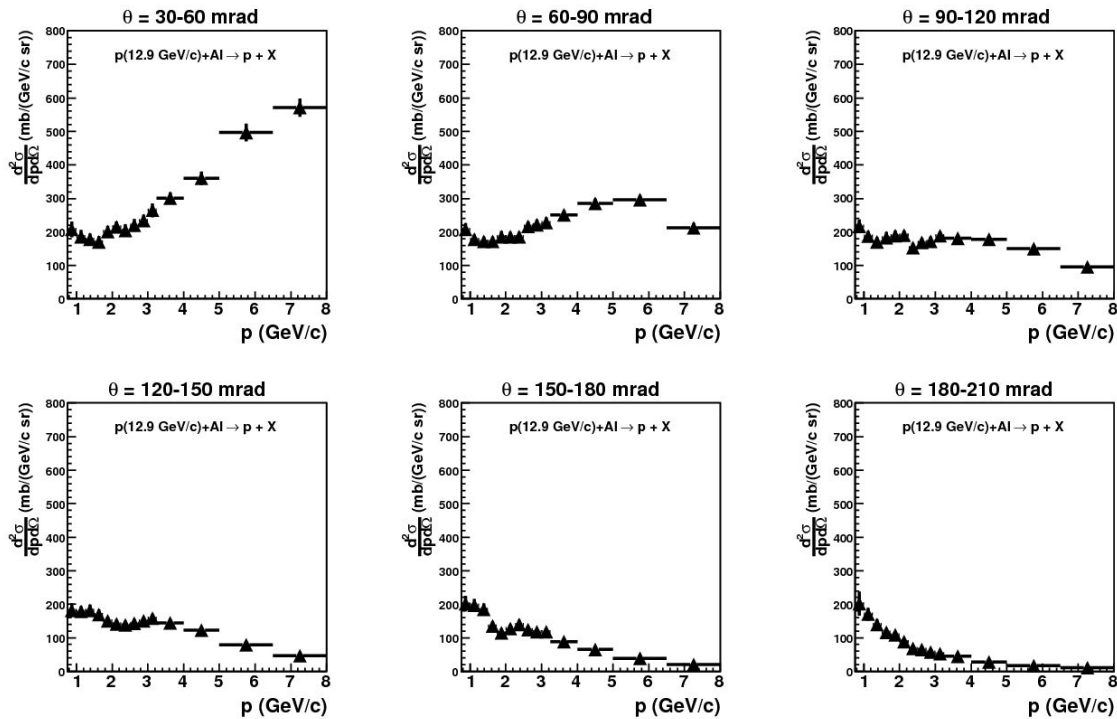
Figure 4.10: Double-differential production cross-sections of protons from the interaction of 12.9 GeV/c protons with aluminum. Each panel shows the cross-section as a function of momentum from 0.75 GeV/c to 8.0 GeV/c in a particular angular bin indicated above each plot. The error bars shown are the square-root of the diagonal elements of the total error matrix.

Data Set	p(12.9GeV/c) + aluminum					
secondary particle	π^+		π^-		proton	
mometum range (GeV/c)	0.75 − 8.0		0.75 − 8.0		0.75 − 8.0	
angular range (rad)	0.03 − 0.21		0.03 − 0.21		0.03 − 0.21	
Error Category	$\delta^{\pi^+}_{\text{diff}}$ (%)	$\delta^{\pi^+}_{\text{int}}$ (%)	$\delta^{\pi^-}_{\text{diff}}$ (%)	$\delta^{\pi^-}_{\text{int}}$ (%)	$\delta^{\text{P}}_{\text{diff}}$ (%)	$\delta^{\text{P}}_{\text{int}}$ (%)
Statistical Errors:						
i. Target statistics	3.7	0.4	5.5	0.5	4.0	0.4
ii. Empty target statistics	3.0	0.3	4.0	0.4	3.1	0.3
Sub-total	**4.8**	**0.5**	**6.8**	**0.6**	**5.1**	**0.5**
Track yield corrections:						
iii. Empty target subtraction	1.0	0.1	1.7	0.1	0.8	0.1
iv. Reconstruction efficiency	1.2	0.7	3.0	1.0	1.2	0.4
v. π, p absorption syst.	5.4	6.1	5.4	6.6	3.9	3.9
vi. π, p absorption stat.	0.4	<0.1	0.4	<0.1	0.4	<0.1
vii. Tertiary subtraction syst.	4.1	4.4	4.9	5.2	3.7	3.3
viii. Tertiary subtraction stat.	1.1	0.2	1.6	0.3	0.7	0.1
Sub-total	**7.0**	**7.6**	**8.2**	**8.5**	**5.6**	**5.1**
Momentum reconstruction:						
ix. Momentum scale	2.4	0.1	3.6	0.4	2.2	0.7
x. Momentum resolution syst.	1.7	0.7	2.5	0.6	1.8	0.1
xi. Momentum resolution stat.	1.9	0.1	3.8	0.1	1.8	<0.1
Sub-total	**3.7**	**0.8**	**5.8**	**0.7**	**3.3**	**0.8**
Particle Identification:						
xii. Electron veto	0.1	<0.1	0.1	<0.1	0.1	<0.1
xiii. π, p ID correction	0.5	0.3	0.5	0.4	0.3	0.2
Sub-total	**0.5**	**0.3**	**0.5**	**0.4**	**0.3**	**0.2**
Overall normalization:	**2.0**	**2.0**	**2.0**	**2.0**	**2.0**	**2.0**
Total	**9.5**	**7.9**	**12.3**	**8.8**	**8.5**	**5.6**

Table 4.3: Summary of the uncertainties affecting the measured π^+, π^- and proton cross-sections from 12.9 GeV/c proton+aluminum interactions. The average error on the differential cross-section, δ_{diff}, and the error on the total integrated cross-section, δ_{int}, are listed for each of the fourteen error sources described in Section 4.6.

Part III

MiniBooNE

Chapter 5

MiniBooNE (E898) at Fermilab

MiniBooNE (The Mini Booster Neutrino Experiment), at Fermilab, was designed to search for the transmutation of muon neutrinos into electron neutrinos consistent with a neutrino oscillation hypothesis. With a mean neutrino energy of ~ 0.7 GeV and a path length of ~ 0.5 km, MiniBooNE is sensitive to oscillations governed by a large mass splitting (relative to the solar and atmospheric results) of order 1 eV^2. MiniBooNE took data in neutrino mode from September 2002 through December 2006 collecting $\sim 5.6 \times 10^{20}$ protons on target before changing to antineutrino mode in January 2007. The oscillation analysis to be presented here is based on the neutrino mode data only. In this chapter, we begin with a detailed description of the LSND result as motivation for the basic MiniBooNE design, and then step through a description of the experiment in greater detail.

5.1 Motivation for MiniBooNE – the LSND experiment

As discussed in Chapter 1, neutrino oscillations in the solar and atmospheric Δm^2 regions are now well established. Evidence for a third mixing at significantly higher Δm^2 was reported by the LSND collaboration but awaits similar confirmation; this serves as the primary goal of the Booster Neutrino Experiment. A brief description of the LSND experiment and its results is instructive to understanding the MiniBooNE design and analysis
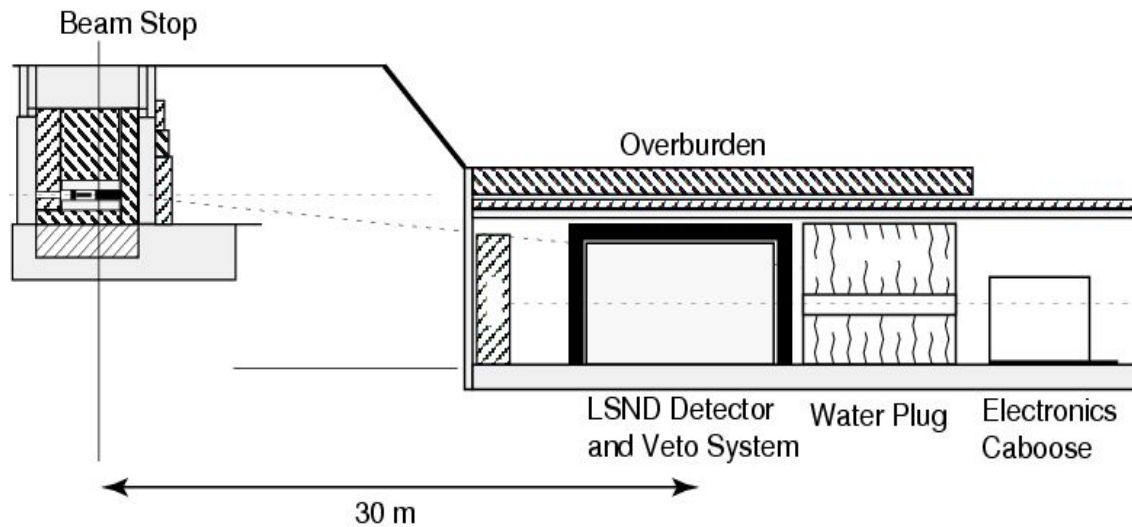
Figure 5.1: Schematic drawing of the LSND experiment at Los Alamos National Laboratory. The 798 MeV proton beam comes in from the left of the figure and collides with a water or high-Z metal target. Secondary pions are stopped in the copper beam stop and decay. The LSND detector is a cylindrical tank 8.3 m long and 5.7 m in diameter filled with liquid scintillator doped mineral oil and the center of the detector sits 30 m downstream of the beam stop. Plot taken from [44].

goals.

The Liquid Scintillator Neutrino Detector experiment [43] was conducted at Los Alamos National Laboratory from 1993 through 1998. A schematic drawing of the experiment is shown in Figure 5.1. The neutrino beam was generated by focusing the high intensity 798 MeV kinetic energy proton beam at the Los Alamos Neutron Science Center (LANSCE) onto a water target (1993–1995) or a dense high-Z nuclear target (1996–1998). A copper beam dump was located downstream of the target and most secondary pions and tertiary muons decayed-at-rest within this beam stop. Only a few percent of the pions could decay-in-flight in the small open space between the targets and the beam dump.

The resulting flux spectra from the two decay modes, decay-in-flight (DIF) and decay-at-rest (DAR), are substantially different. The main oscillation search of LSND was for $\bar{\nu}_\mu \rightarrow \bar{\nu}_e$ oscillations of $\bar{\nu}_\mu$ created in μ^+ DAR. A search for $\nu_\mu \rightarrow \nu_e$ oscillations of ν_μ

created in π^+ DIF was also pursued, and while consistent with the DAR analysis, suffered from very large statistical uncertainties. In the end, both samples were combined to determine the allowed oscillation parameters [44].

The 3-body decay of the muon, $\mu^+ \rightarrow e^+ \nu_e \bar{\nu}_\mu$, with the muon at rest, generates a well known $\bar{\nu}_\mu$ spectrum with an energy cutoff at 52.8 MeV. Further, in the π^+/μ^+ decay chain, no $\bar{\nu}_e$ are produced anywhere. The only beam related sources of $\bar{\nu}_e$ come from DIF of π^- (suppressed $\sim 10^{-4}$ by the low branching fraction for $\pi^- \rightarrow e^+ \bar{\nu}_e$) and DAR of μ^- from π^- DIF. This background is suppressed by the fact that most μ^- will be captured in the beam dump before they can decay. Both sources are further reduced by the low π^- production cross-section and low probability for DIF mentioned above [1].

The LSND detector, capable of detecting both scintillation and Cherenkov light, was a cylindrical tank filled with liquid scintillator doped mineral oil and lined with 1220 8" photo-multiplier tubes. The center of the tank was located 30 meters from the copper beam dump. Evidence for $\bar{\nu}_\mu \rightarrow \bar{\nu}_e$ oscillations was searched for by looking for an excess of inverse beta decay (IBD) events, $\bar{\nu}_e p \rightarrow e^+ n$, indicating an excess of $\bar{\nu}_e$ in the beam. The signature of IBD events is a e^+ followed by a 2.2 MeV γ from the capture of the neutron on a free proton. The key to separating IBD events from other events with an electron/positron[2] is the existence of this correlated gamma-ray. The distance between the positron position and γ position, Δr, the time interval between the positron event and the γ event, Δt, and the reconstructed energy of the γ event must all be consistent with the neutron capture hypothesis. These three quantities were combined to create a likelihood variable, R_γ, for separating correlated from accidental photon events. The R_γ distribution for events passing initial electron/positron cuts is shown in Figure 5.2. The shape of this distribution for data (the black points with error bars) is compared to a Monte Carlo simulation that includes both accidental (green histogram) and correlated (blue histogram) photon events.

For the μ^+ DAR analysis the positron will have a reconstructed energy below 60 MeV due to the kinematic limit on the $\bar{\nu}_\mu$ produced in the decay. Large low energy cosmic ray

---

[1] This also explains why the DIF oscillation analysis suffers from poor statistics.

[2] The LSND detector is not capable of determining the sign of the electron.
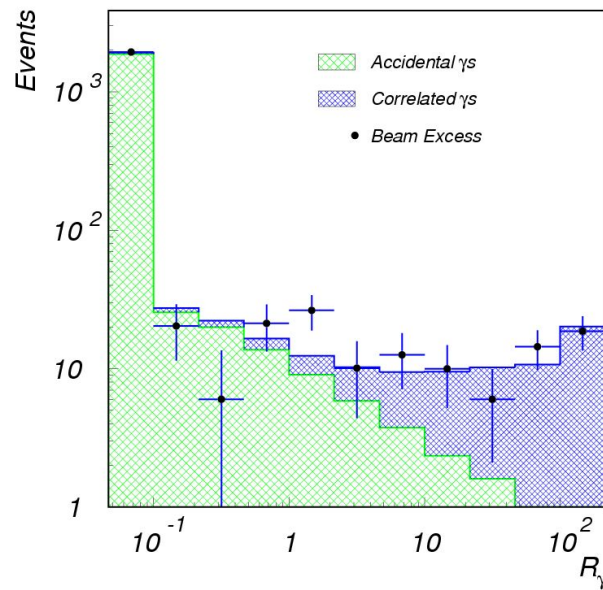
Figure 5.2: The R_γ distribution for events in LSND that satisfy electron/positron selection cuts. Correlated-γs refer to the 2.2 MeV gamma-ray produced when the neutron captures on a free proton in an inverse beta decay event, $\bar{\nu}_e p \rightarrow e^+ n$. Plot taken from [44].

induced backgrounds can be removed with a low energy cut of 20 MeV. The left panel of Figure 5.3 shows the number of reconstructed IBD events with a positron energy in the range $20 < E_e < 60$ MeV compared with the predicted backgrounds and a best fit oscillation hypothesis. The event excess above the predicted backgrounds (shown in red and green) is $32.2 \pm 9.4 \pm 2.3$, where the first error is statistical and the second error is from systematic uncertainties. This sample was isolated by applying a cut in the event identification variable of $R_\gamma > 10$. The significance of the result is increased slightly from 3.2σ to 3.8σ by using a more sophisticated technique of fitting the full R_γ distribution to an accidental-γ and correlated-γ template from the Monte Carlo and extracting the normalizations of the two samples. This is the result shown in Figure 5.2 and reveals a total number of 117.9 ± 22.4 events in the data with a correlated gamma. This is $87.9 \pm 22.4 \pm 6.0$ events more than expected in the absence of oscillations.

For each candidate IBD event the interaction vertex within the tank and neutrino energy can be reconstructed. The distance from the beam dump to the vertex position
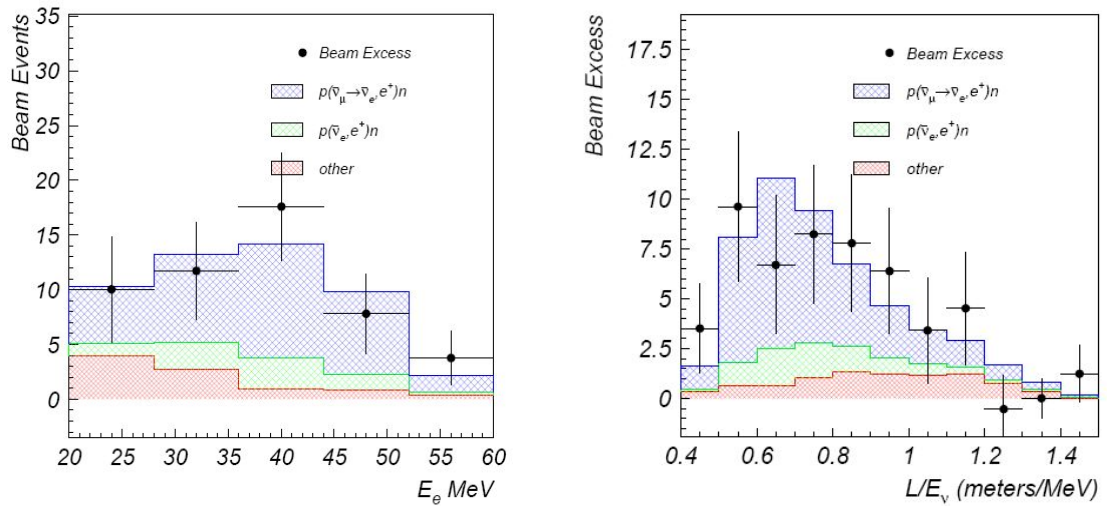
Figure 5.3: The energy (left) and path length to energy ratio (right) for events in LSND identified as inverse beta decay events with $R_\gamma > 10$. A clear excess above predicted backgrounds (green and red histograms) is seen. The blue histogram corresponds to a best fit oscillation hypothesis of $(\Delta m^2, \sin^2(2\theta)) = (1.2 \text{ eV}^2, 0.003)$. Plots taken from [44].

and the neutrino energy are used to create the ratio L_ν/E_ν plotted in the right panel of Figure 5.3 for events with $R_\gamma > 10$. Here one clearly sees the L/E dependence of the excess of $\bar{\nu}_e$ events which peaks at an L/E value of ~ 0.7m/MeV. Assuming the excess is due to $\bar{\nu}_\mu \to \bar{\nu}_e$ oscillations, it implies an average oscillation probability of $(0.264 \pm 0.067 \pm 0.045)\%$. The corresponding allowed values of the oscillation parameters $\sin^2(2\theta)$ and Δm^2 can be determined by fitting the event excess to the two neutrino oscillation formula,

$$P(\bar{\nu}_\mu \to \bar{\nu}_e) = \sin^2(2\theta) \sin^2\left(1.27\Delta m^2 \frac{L_\nu}{E_\nu}\right). \tag{5.1}$$

This fit has been performed with careful consideration of the experiment's statistical and systematic uncertainties [44]. The resulting allowed oscillation parameter combinations at 90% and 99% C.L. are shown in Figure 5.4 with the most probable combination being:

$$(\Delta m^2, \sin^2(2\theta))_{\text{best-fit}} = (1.2 \text{ eV}^2, 0.003).$$
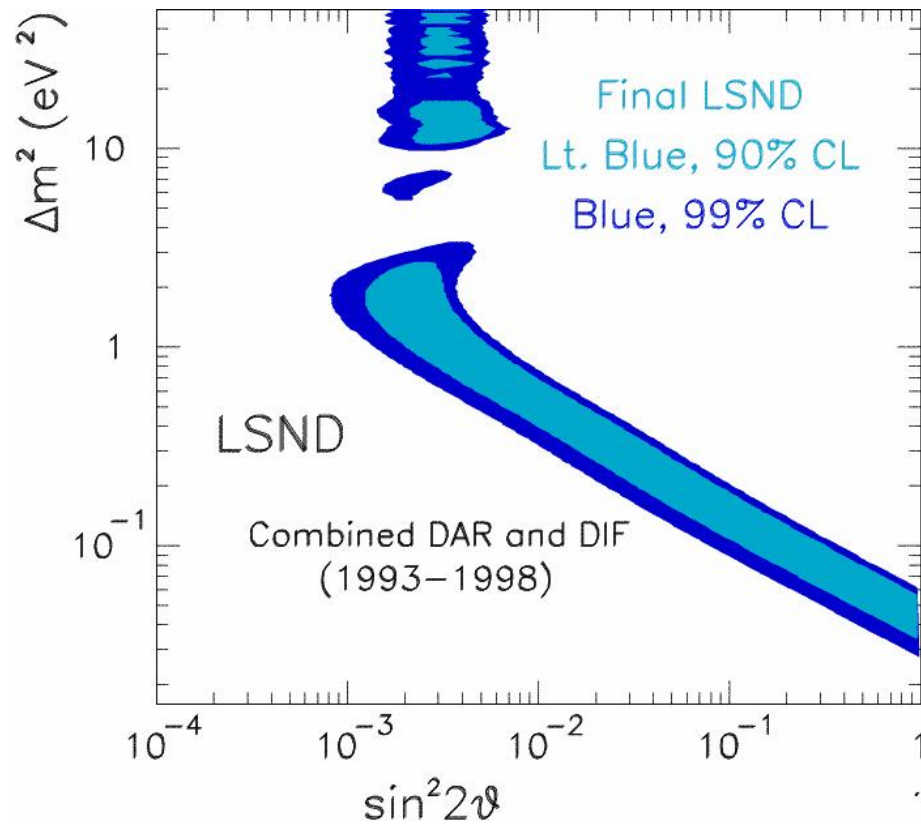
Figure 5.4:   Allowed oscillation parameter $(\Delta m^2, \sin^2(2\theta))$ combinations if the excess of electron neutrino events seen in LSND are assumed to come from oscillations. The $\overline{\nu}_\mu \rightarrow \overline{\nu}_e$ DAR data and the $\nu_\mu \rightarrow \nu_e$ DIF data from all six years of running are included. The best fit point is at $(\Delta m^2, \sin^2(2\theta)) = (1.2 \text{ eV}^2, 0.003)$. Plot taken from [44].

5.2 Overview of MiniBooNE

The primary goal of MiniBooNE is to search for neutrino oscillations in the regions of parameter space allowed by the LSND result and shown in Figure 5.4. Because the oscillation probability remains constant for constant values of the ratio L/E, it is possible to search for the same effect but with a significantly different experimental setup. Evidence consistent with the oscillation hypothesis seen by an experiment of substantially different design would be very strong evidence that the LSND signal is due to $\bar{\nu}_\mu \rightarrow \bar{\nu}_e$ transmutation.

Two key factors dictate the design of such an experiment: the very small probability for oscillation of $\sim 0.26\%$ and the range of values of L/E which determine the region of Δm^2 to which the experiment is sensitive. Simple inspection of Figure 5.3 reveals that the relevant values of L/E lie between ~ 0.4–1.2 m/MeV. The MiniBooNE detector was constructed 541 m from the neutrino source and to a good approximation this is the path length of all neutrinos. Therefore, the relevant neutrino energies are 450–1350 MeV. Because the oscillation probability is expected to be small and it is not feasible at this time to predict flux levels to $< 0.1\%$, MiniBooNE will instead search for evidence of the oscillation in the appearance of electron neutrinos.

The primary experimental aim of the Booster Neutrino Experiment can be very concisely stated:

> **MiniBooNE will search for an excess of electron neutrino events above predicted backgrounds in the energy range $\sim$ 450–1350 MeV. An observed excess of order 0.26% of the muon neutrino flux in this same energy range would be evidence for the neutrino oscillation interpretation of the LSND data.**

Sounds simple enough.

MiniBooNE, therefore, requires a high statistics, broad-band muon neutrino beam with mean energy around 700 MeV and a very small contamination of electron neutrinos. The detector must be capable of distinguishing ν_e events with high efficiency while rejecting $> 99\%$ of ν_μ induced events.
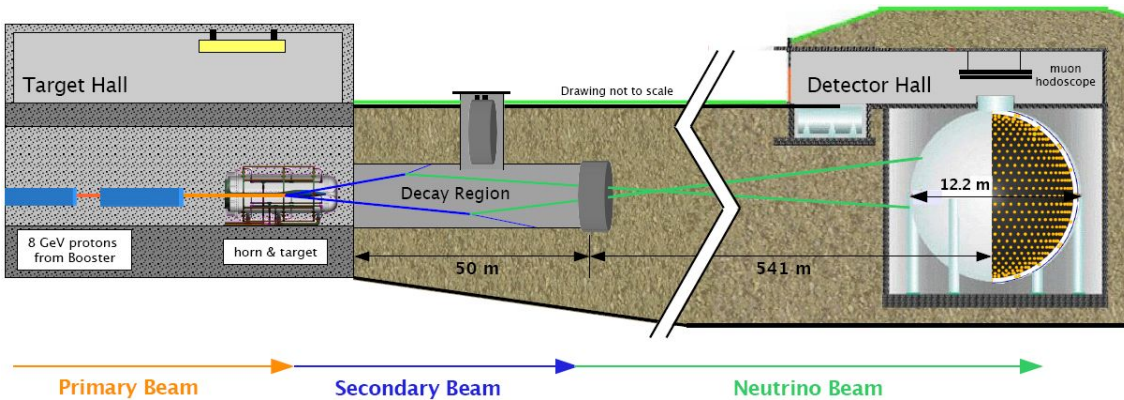
Figure 5.5: Schematic representation of the MiniBooNE beamline and detector. The view is a cross-sectional elevation and the drawing is not to scale.

A schematic representation of the experiment in shown in Figure 5.5. The Booster Neutrino Beamline (BNB) begins with 8 GeV kinetic energy (8.9 GeV/c momentum) protons from the Fermilab Booster which impinge upon a thick beryllium target. Secondary hadrons, mostly charged pions, protons and kaons, are produced in inelastic interactions between incident protons and beryllium nuclei. The target sits along the axis of an aluminum, cylindrical magnetic focusing horn. Large currents pass through the shell of the horn in time with each proton bunch from the Booster and the resulting magnetic field acts to focus/defocus charged secondaries of opposite sign. By reversing the direction of the current one can change the sign selection and thus the content of the resulting neutrino beam.

Focused secondaries enter an open, air-filled decay region 50 m in length where short-lived pions and kaons will decay[3]. The tertiary beam is mostly muons and muon neutrinos from $\pi^{\pm}$ decays. A small contamination of ν_e results from kaon decays, $\pi \rightarrow e\nu_e$, and muons that manage to decay before hitting the end of the decay region. All charged particles that have not decayed will be stopped in an absorber at the end of the 50 m tunnel. Only neutrinos pass through the absorber and ~ 500 m of dirt unaffected and reach the MiniBooNE detector.

---

[3]Steel plates are suspended above the decay tunnel by chains. Lowering these plates shortens the decay region to 25 m which can be useful for studying beam related systematics. See Figure 5.5.

The MiniBooNE detector is a 610 cm radius carbon steel sphere built just below ground level in a concrete cylindrical cavity. The detector is filled with 950,000 liters of mineral oil chosen for its favorable optical properties and stability. The detector is separated into two optically isolated concentric shells. The outer shell is the "veto" region and is instrumented with 240 photomultiplier tubes (PMTs). It is mostly used to reject events caused by cosmic muons passing through the detector. The inner spherical region acts as the neutrino target for the oscillation analysis and the outer wall is instrumented with 1280 PMTs facing inward.

When neutrinos from the Booster Neutrino Beam interact with nucleons within the oil (the oil is essentially a carbon target) charged particles created in the interaction produce both Cherenkov and scintillation light which is detected at the edge of the tank by the photo tubes. Final state particles can be reconstructed and identified by their characteristic light patterns in the detector. From this information sophisticated reconstructions will be used to identify the type of the neutrino that caused the event. In this way we will measure the ν_e content of the beam and search for $\nu_\mu \to \nu_e$ oscillations. Much more about this will be said in coming sections and chapters.

5.3 The Booster Neutrino Beam

Figure 5.6 shows the layout of the 8 GeV extraction line at Fermilab. The Fermilab Booster is a 474 m circumference synchrotron which accelerates protons coming from the LINAC at 400 MeV up to 8 GeV kinetic energy. After being extracted from the Booster ring, proton bunches are directed either into the Main Injector for further acceleration to 120 GeV or into the Booster Neutrino Beamline by a switch magnet near the point labeled A in the figure.

5.3.1 Primary proton beam

A lattice of focusing and defocusing magnets (FODO) and bending dipoles transport proton bunches through the ~ 200 m beamline to the target area located under the MI-12 service building. The position, direction and profile of the primary beam are monitored
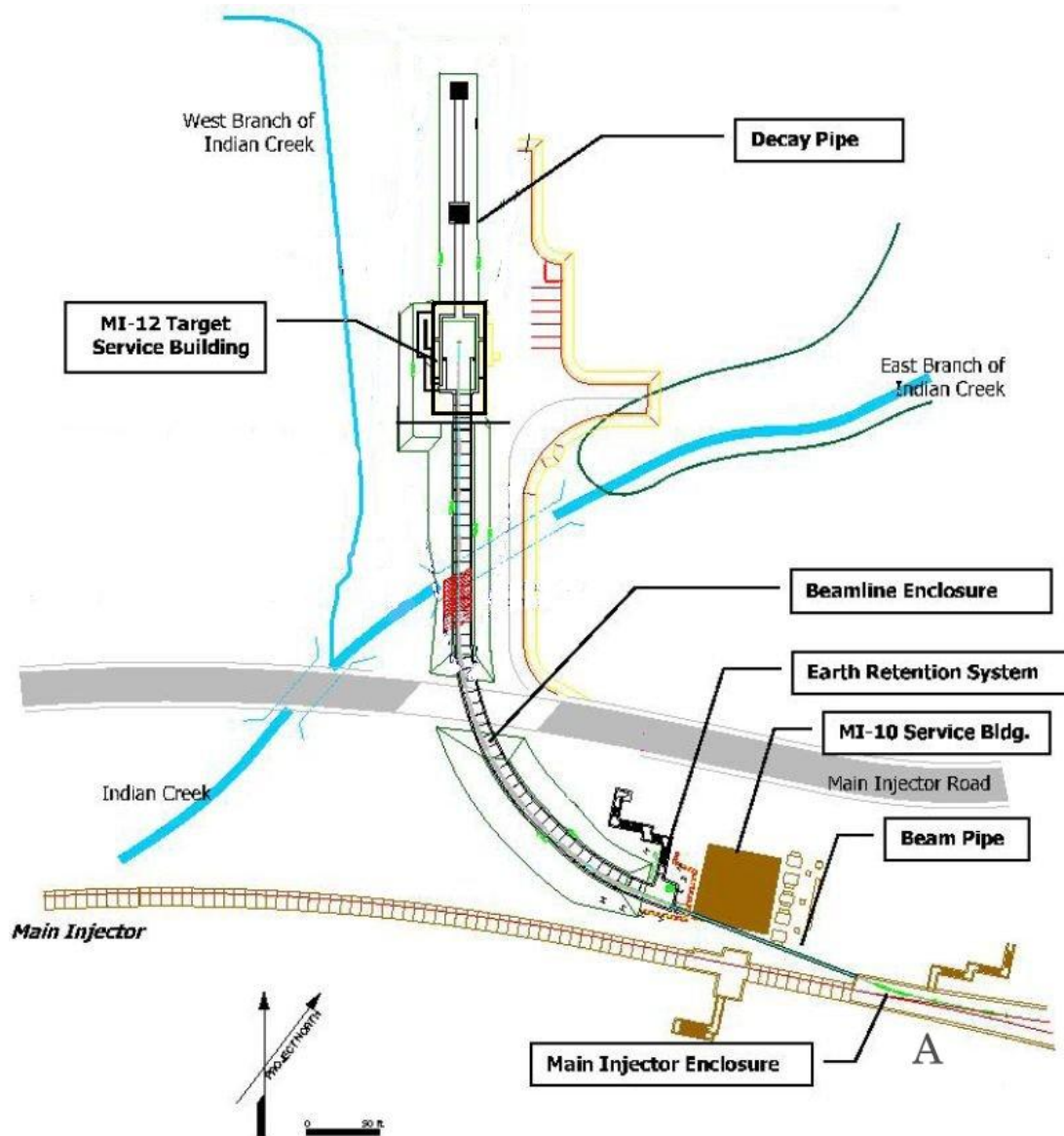
Figure 5.6: Schematic drawing of the Booster Neutrino Beamline including the 8 GeV extraction line, target hall and decay region. Plot taken from [71].

$\overline{x}$	0.0 mm	σ_x	1.51 mm
$\overline{y}$	0.0 mm	σ_y	0.75 mm
$\overline{\theta_x}$	0.0 mrad	σ_{θ_x}	0.66 mrad
$\overline{\theta_y}$	0.0 mrad	σ_{θ_x}	0.40 mrad

Table 5.1: Typical position, size and direction of the 8 GeV primary proton beam 1.0 cm upstream of the face of the beryllium target in the Booster Neutrino Beamline.

in real-time by a set of beam position monitors (BPMs) and multiwires. A final set of focusing magnets are used to ensure that the beam hits the upstream face of the beryllium target with a sufficiently small spread and incident angle. A feedback control system know as Autotune [73] automatically corrects small beam wanderings using the real-time monitoring information. Table 5.1 lists the average parameters of the transverse position and angle profile of the proton bunches just upstream of the target face. The RMS of the beam profile in the horizontal (x) and vertical (y) directions of < 2 mm are well within the experimental requirements determined by the 5 mm radius of the beryllium target.

At design intensity, each proton pulse is 1.6 μs wide and contains $\sim 5 \times 10^{12}$ protons. The design of the horn and power supply system limit the instantaneous proton pulse delivery rate to the BNB to 15 Hz with a maximum of 10 consecutive pulses in a 2 second period (5 Hz average rate). The number of protons in each pulse is measured using two toroids located in the beamline near the target. The toroids are continuously calibrated on a pulse-by-pulse basis and absolutely calibrated twice per year. The measured proton intensity in the two devices agree to within 2%.

Figure 5.7 shows the number of protons delivered to the BNB target since the beamline was commissioned in September, 2002. The gaps in the distribution are due to scheduled accelerator shutdowns. The thick black line tracks the total integrated protons on target since September 2002 and passed the important milestone of 1.0×10^{21} on New Year's Day, 2008!
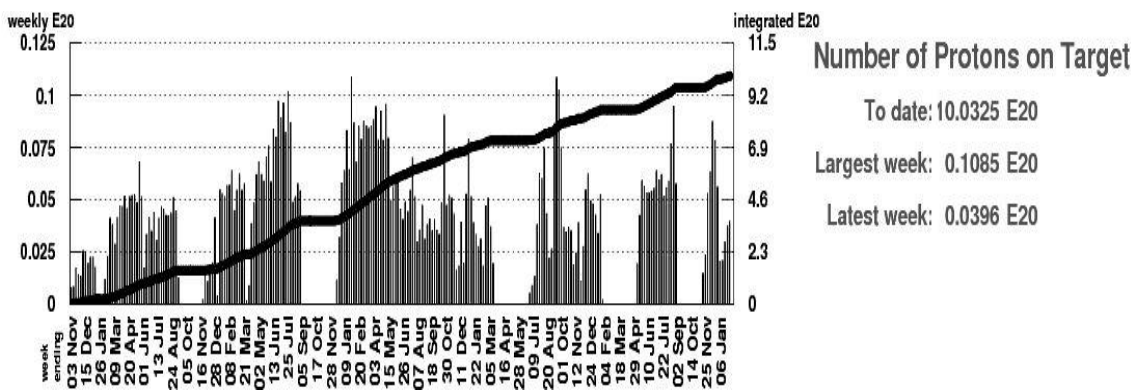
Figure 5.7: Weekly proton delivery rate to the Booster Neutrino Beam since the beamline start-up in September, 2002. The total integrated protons on target is also plotted using the units shown on the right axis. The total POT surpassed 1.0×10^{21} in early January, 2008.

5.3.2   Beryllium target

The beryllium target is comprised of seven 10.2 cm long and 0.48 cm radius cylindrical sections placed end-to-end to make the full 71.1 cm long target. Three "fins", also made from beryllium, are attached to the solid cylindrical cores at 120° intervals. Figure 5.8 details the geometry and assembly of the target. The seven sections, supported by the fins, are housed in a beryllium sleeve 0.9 cm thick with a 1.37 cm inner radius and the full assembly is supported from the upstream end where it is attached to the horn shell and is fully insulated from the aluminum of the horn and, consequently, the horn current.

The target must be cooled due to the $\simeq 600$ W of power that are deposited by the proton beam under standard operating conditions ($\sim 5 \times 10^{12}$ protons per pulse at a 5 Hz average rate). This is achieved by circulating air along the target in the open space between the fins and inside of the beryllium sleeve and out through a set of heat exchangers. A set of temperature and air flow monitors are located throughout the air circulation system, and any abnormal conditions would trigger the stopping of the proton beam. Readings from the monitoring devices indicate an air flow rate of $\simeq 8 \times 10^{-3}$ m^3/s. The temperature of the air coming off the target is $\simeq 120°$ C which is well below the melting temperature

of beryllium (1278° C).

5.3.3   Magnetic focusing horn

The Booster Neutrino Beamline magnetic focusing horn design is based on the general principles introduced in Chapter 2, but was designed to satisfy the specific physics requirements of MiniBooNE by Bartoszek Engineering [138].

The horn sits along the axis of the incident proton beam and is constructed from the aluminum alloy 6061-T6. The inner and outer conductor shapes are shown in the engineering rendering in Figure 5.9. The up-stream half of the inner conductor, which houses the beryllium target, has a radius of 2.2 cm. The down-stream section is made of two conical shaped pieces with minimum radius 2.2 cm and maximum radius 6.54 cm. The outer conductor is a 30.0 cm cylinder connected to the inner conductor at the down-stream end by a half-donut shaped aluminum cap. The shape and size of the horn conducting shell was determined using a sophisticated Monte Carlo simulation to maximize the neutrino flux in the relevant energy range at the MiniBooNE detector. The effect on the MiniBooNE ν_μ flux was shown back in Chapter 2 in Figure 2.3.

The magnetic field is created by a 143 μs half-sinusoid current pulse passed through the outer conductor shell, the half-donut end cap, and back through the inner conductor. The peak current, nominally 170 kA, is timed to coincide with a proton bunch hitting the target. The maximum instantaneous frequency of the horn power supply system is 15 Hz while the requirement to constantly dissipate the heat built up in the target limits the average rate to 5 Hz. The resulting magnetic field per kA of current is shown in the right panel of Figure 5.9 as a function of the distance from the central axis and follows the expected $1/r$ behavior.

Due to the large currents, the aluminum shell must be externally cooled. This is achieved by a closed radioactive water (RAW) system which sprays onto the inner conductor via portholes in the outer conductor shell which are visible in Figures 5.8 and 5.9. To avoid the system of pipes and nozzles being broken apart by large vibrations in the horn, the water system is not rigidly fixed to the shell, but built around it with spray nozzles aligned with the portholes using a spring connection shown in Figure 5.10.
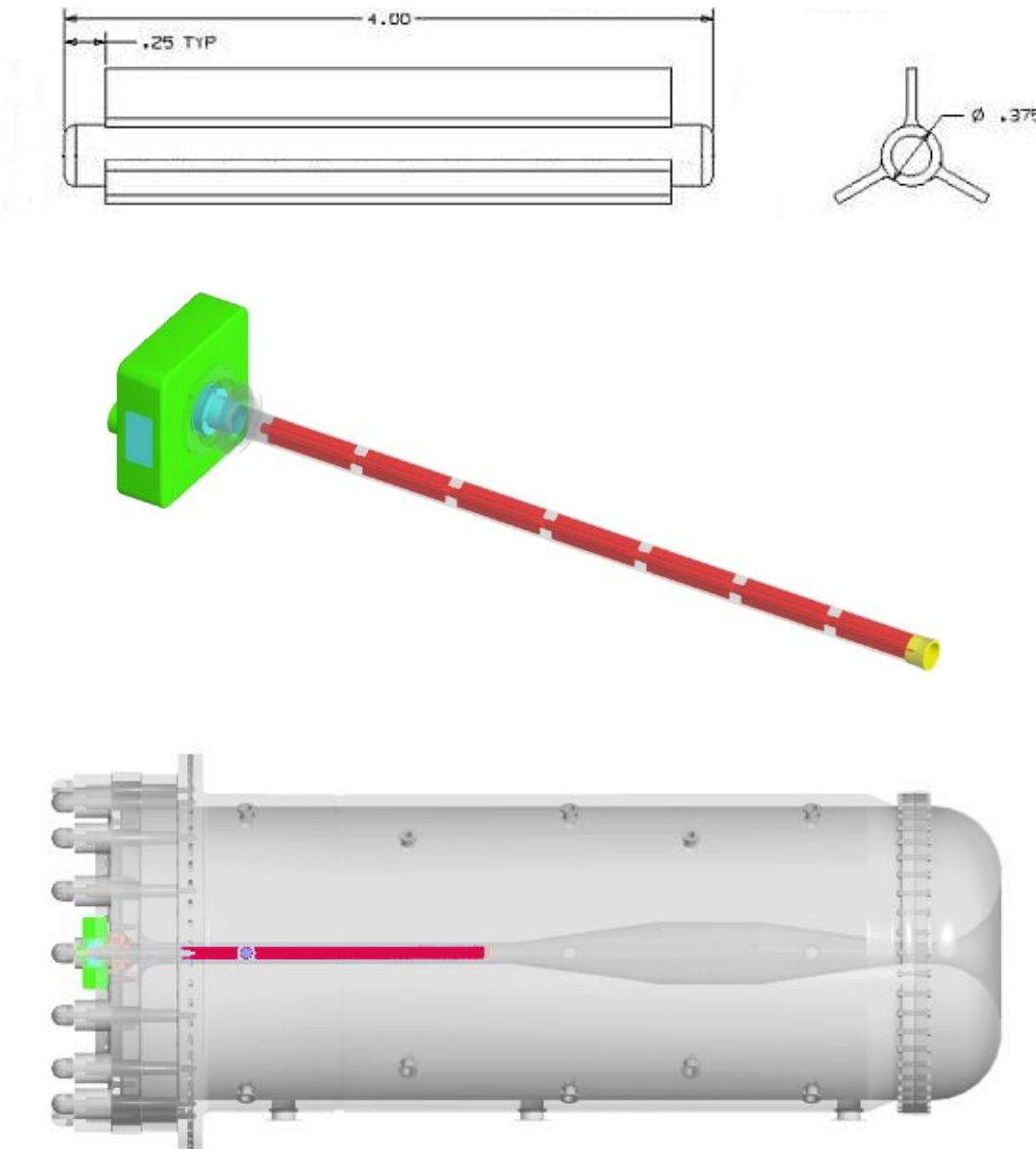
Figure 5.8: The Booster Neutrino Beamline beryllium target. The top images show the dimensions of the individual target sections (in inches). The middle drawing shows how the seven sections are assembled to make the full target [138], and the lower drawing shows how the target assembly is mounted inside the upstream half of the inner conductor [138].
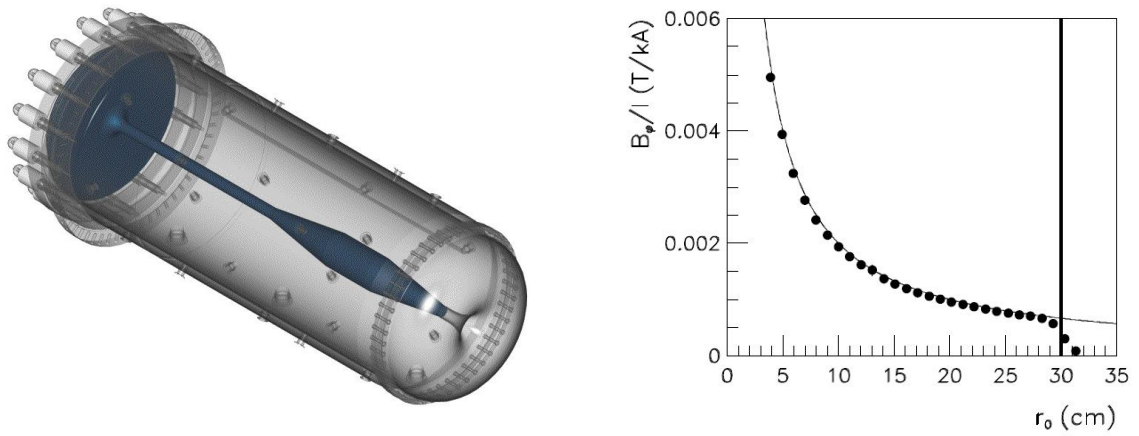
Figure 5.9: Focusing horn magnetic field. The left panel shows the inner and outer conductor shapes; the outer conductor has been rendered transparent, the inner conductor is in blue [138]. The right shows the azimuthal component of the magnetic field, B_ϕ, as measured (points) and according to Eq. 2.1, $B_\phi(r) = \mu_0 I/2\pi r$ (solid curve). The vertical line marks the inside edge of the outer conductor. Plot taken from [94].
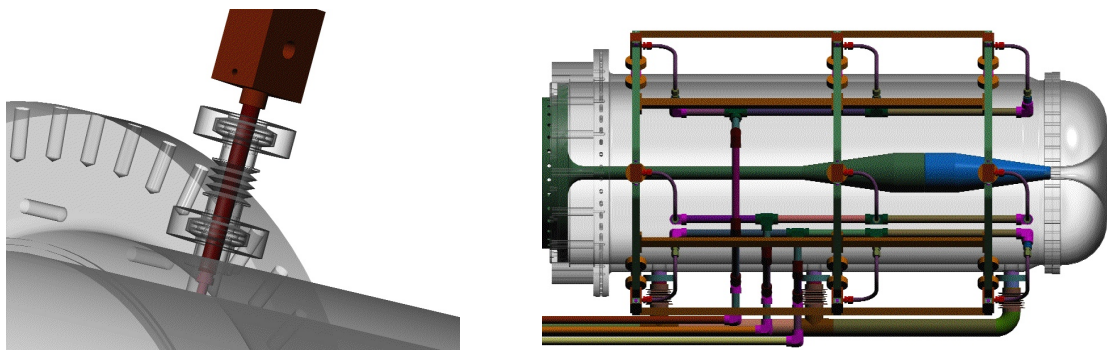
Figure 5.10: The magnetic focusing horn water cooling system [138].

5.3.4   Meson decay region

Immediately downstream of the horn/target assembly is a concrete collimator. The collimator, beginning 259 cm downstream of the forward face of the target, is 214 cm long with an upstream and downstream aperture diameter of 60 cm and 71 cm, respectively. The collimator opens into the meson decay region which is a 45 m long tunnel ~ 183 cm in diameter filled with air at standard atmospheric pressure. The walls of the decay region are made of a corrugated steel pipe surrounded by dolomite ($CaMg(CO_2)_3$, $\rho = 2.24 \mathrm{g/cm^3}$).

At the end of the decay pipe is a steel and concrete beam dump to absorb any undecayed leptons and hadrons in the beam. One could increase the ν_μ flux by lengthening the decay region and allowing more charged pions to decay ($\beta c \cdot \gamma \tau = 112$ m for a $2\,\mathrm{GeV}/c\,\pi^\pm$ implying that only 36% decay in 50 m), but a sharp increase in the ν_e background arising from μ decays offsets the gain in ν_μ flux for a $\nu_\mu \rightarrow \nu_e$ oscillation search. This explains why the NuMI decay region is significantly longer (675 m); MINOS is a ν_μ disappearance experiment and is less concerned with ν_e backgrounds than with ν_μ statistics.

Included in the beamline design is the ability to install a steel beam absorber at 25 m, thus systematically altering the normalization and energy spectrum of the beam components - in particular the ν_e from μ decay component. Ten steel plates are suspended above the decay pipe by chains and could be lowered into the beam path. The 25 m absorber was not deployed, however, during the taking of the data used in the $\nu_\mu \rightarrow \nu_e$ oscillation search.

5.4   The MiniBooNE detector

The main physics goals driving the design of the MiniBooNE detector were the need to discriminate between ν_μ and ν_e induced events and to reconstruct the neutrino's energy with sufficient resolution. The final design, shown in Figure 5.11, is a 610 cm radius carbon steel sphere filled with 818 tons of mineral oil. Event classification is achieved using the large amounts of Cherenkov light and lesser amounts of scintillation light generated by charged particles in the tank. An opaque PMT support structure is constructed
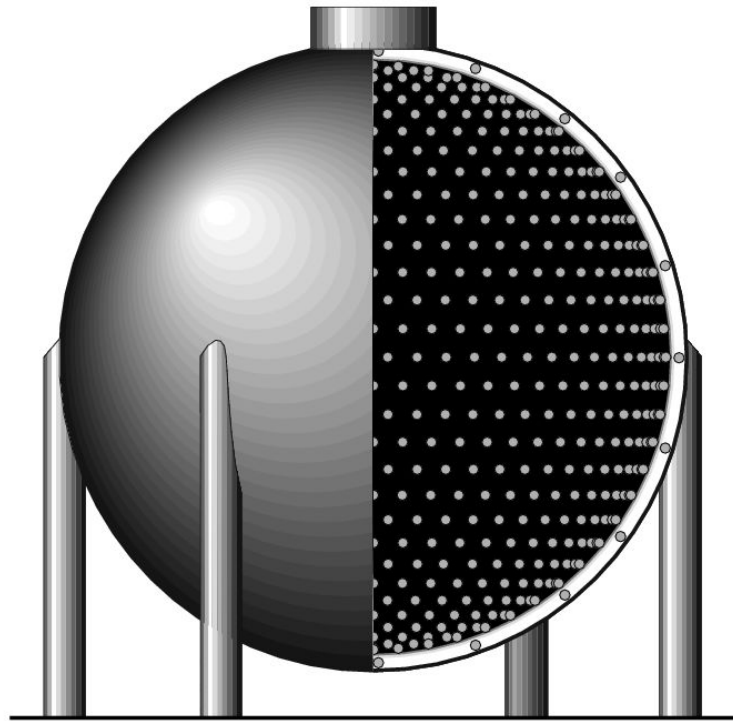
Figure 5.11: Schematic drawing of the MiniBooNE detector with a quarter sphere section cut away. The white band near the edge is the 35 cm wide veto region. The PMT distributions in the main detector region and the veto region are shown. Image taken from [72].

at a radius of 574.6 cm which separates an inner main detector region from an outer veto region. Mounted to the inside of this shell pointed toward the center of the tank are 1280 8-inch Hamamatsu photomultiplier tubes which provide an 11.3% photocathode coverage of the main detector region. The outer 35 cm thick veto shell is instrumented with 240 8-inch PMTs used to detect entering and exiting charged particles, particularly cosmic rays. Figure 5.12 shows a schematic diagram and photograph of the main detector/veto region boundary. Surfaces in the main detector have been painted black to minimize reflections. Reflected Cherenkov light can appear delayed and isotropic causing it to look like scintillation light and degrade the particle identification. In contrast, in the veto region one wants only to ensure the maximum efficiency for recording PMT signals after the passage of a charged particle, thus the surfaces have been painted white to increase
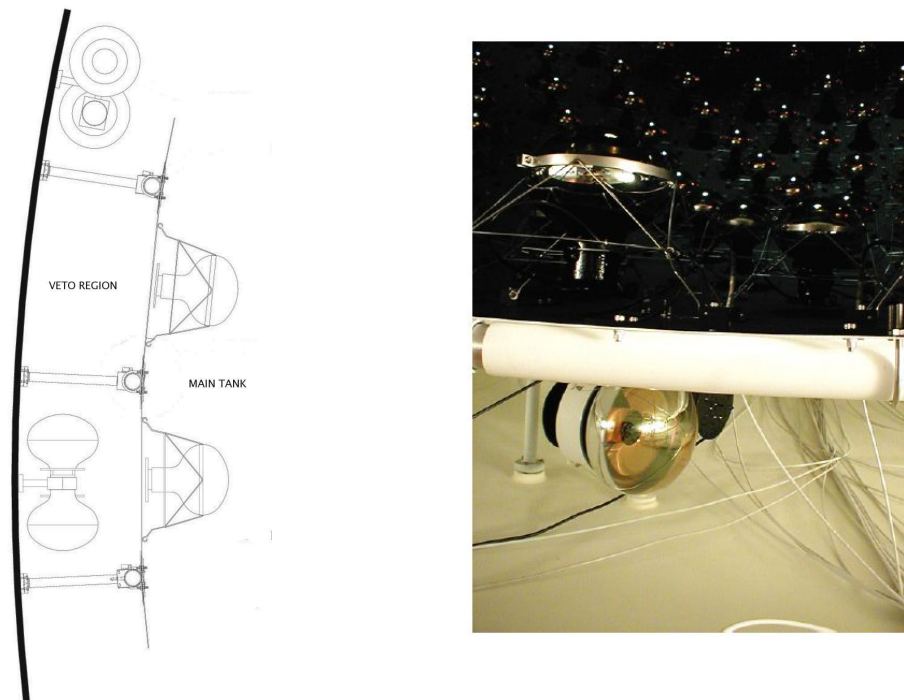
Figure 5.12: Engineering drawing [72] and photograph showing the PMT support structure which acts as the boundary between the main detector region (black) and the veto region (white).

reflections.

The detector tank sits below ground level inside a 13.7 m diameter cylindrical vault which acts as a secondary containment for the oil. Above the vault is a room which houses the detector's electronics and utilities. An earth overburden covers the MiniBooNE detector building such that the minimum earth equivalent that a cosmic ray must traverse to reach the detector is ∼3 m reducing the cosmic trigger rate to below 10 kHz. Figure 5.13 shows the detector inside its enclosure and the surface building above. Also visible is the 2500 gallon capacity overflow tank which allows for thermal expansion of the oil and provides a means by which the oil can be recirculated.
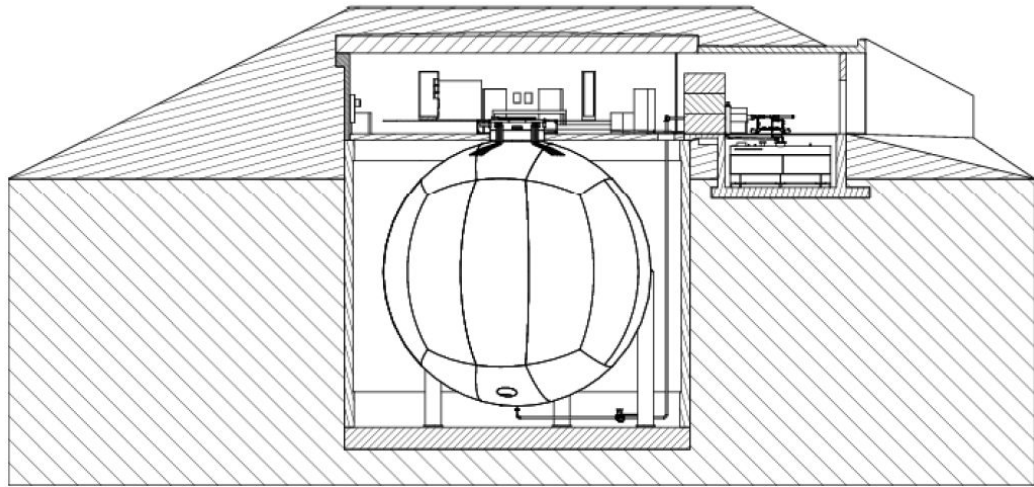
Figure 5.13: MiniBooNE detector containment plant. Image taken from [72].

5.4.1 Oil

The MiniBooNE detector volume is filled with Exxon/Mobil Marcol 7 mineral oil manufactured by Penreco. It was chosen from ten commercially available products based on its matching to a set of criteria including high index of refraction, a small dispersion and long attenuation length in the wavelength range 320 to 600 nm, low reactivity with the materials in the detector, and a small amount of scintillation light. A more detailed description of these qualities is important for an accurate simulation of the detector so this will be saved for Chapter 7.

Mineral oil was chosen to fill the detector volume instead of water for several reasons. The higher index of refraction of mineral oil ($n_{oil} = 1.47^4$, $n_{water} = 1.33$) together with the lower density ($\rho_{oil} = 0.86 \text{ g/cm}^3$, $\rho_{water} = 1.00 \text{ g/cm}^3$) results in considerably more Cherenkov light being produced by electrons in oil. The higher index of refraction also means a lower velocity of light in oil which improves the event vertex resolution (reconstructed from PMT time information) and lowers the threshold for Cherenkov production of muons, pions and protons. Table 5.2 lists the thresholds for the most important particles in the detector in both oil and water for comparison. Also, since the μ^- capture rate

---

[4]At $\lambda = 589.3$ nm and T = 20.0°

Particle	Cherenkov Threshold	
	oil, n = 1.47	water, n = 1.33
electron	0.7 MeV/c	0.8 MeV/c
muon	144 MeV/c	160 MeV/c
pion	190 MeV/c	212 MeV/c
proton	1280 MeV/c	1423 MeV/c

Table 5.2: Energy threshold for production of Cherenkov radiation for four important particle types in mineral oil and water.

is lower at 8% in oil compared to 20% in water, more muon events can be rejected simply by the presence of the decay electron.

5.4.2   Photomultiplier tubes

Two types of PMTs are used in the MiniBooNE detector; 1198 Hamamatsu [139] R1408 8-inch tubes inherited from the LSND detector and 322 newer model Hamamatsu R5912 8-inch tubes purchased specifically for MiniBooNE. The charge and time resolutions, high voltage level required to achieve a gain of 1.6×10^7 electrons per photoelectron (PE), and dark noise rate were measured for each of the 1520 PMTs used in the detector. The average values for the two types of tubes, taken from [74], are compared in Table 5.3. Because of their better time and charge resolutions, all 322 new PMTs were used in the main tank. Of the old tubes, those determined to have low dark noise levels were used in the outer veto region.

5.4.3   PMT charge and time signals

A single coaxial cable carries high voltage to each photomultiplier and also any signals back from the PMT anode. For each recorded event, charge and timing information is needed for all 1520 PMT channels. The PMT signals are amplified about $20\times$ by preamps and passed on to the charge/time digitization boards (QT boards). Signals on the QT boards are sampled at 10 MHz and the charge and time information is determined as

	Hamamatsu R1408	**Hamamatsu R5912**
count	1198	322
dynode stages	9	10
charge resolution @ 1 PE	∼130%	∼40%
time resolution	∼1.7 ns	∼1.1 ns
operating voltage	∼1.9 kV	∼1.7 kV
gain	1.6×10^7 electrons/PE	1.6×10^7 electrons/PE

Table 5.3: Average properties of the two types of photomultiplier tubes used in the Mini-BooNE detector. Data from [74].

illustrated in Figure 5.14.

The amplified anode signal, V_{pmt}, feeds an integrating capacitor located in the QT board which generates the slow signal, V_q ($\tau \approx 1.2~\mu s$). If V_{pmt} passes the discriminator threshold (∼0.25 photoelectrons), the discriminator is fired starting the time ramp signal, V_t. This signal rises linearly for two 100 ns clock ticks before quickly returning to baseline. When a trigger condition is met, the detector data stream consists of the following for each PMT channel:

- PMT channel number

- the clock tick, from the start of the event, that *precedes* the discriminator firing

- the four digitized values of V_q recorded at $(t-1) - (t+2)$ in Figure 5.14. This is the so-called *charge quad*.

- the four digitized values of V_t recorded at $(t-1) - (t+2)$ in Figure 5.14. This is the so-called *time quad*.

The two ADC readings at t and $t+1$ are sufficient to extrapolate back to the baseline and determine the time relative to the preceding clock tick at $t-1$, t_{raw}. The raw charge, q_{raw}, is determined from the four digitized values of V_q and knowing the delay constant of the integrating capacitor.
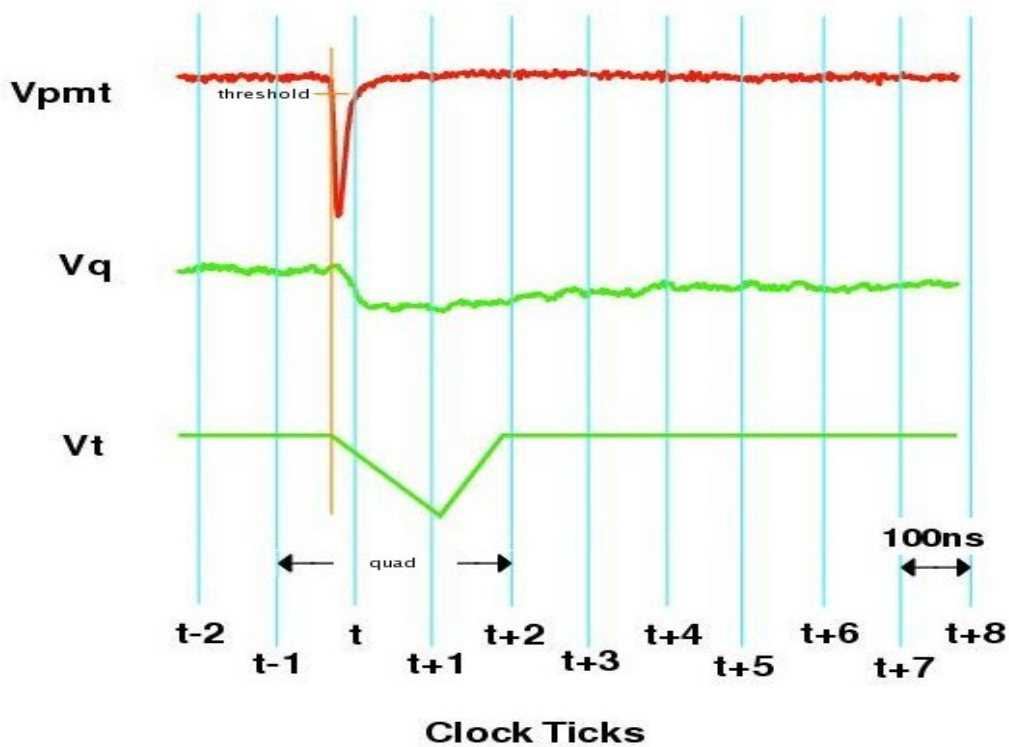
Figure 5.14: Charge and time signals for a single PMT. The amplified anode pulse, V_{pmt}, is integrated and convolved with a slow exponential to produce the analog signal, V_q. The vertical line marks when the anode signal crosses the discriminator threshold and starts the linear time ramp signal, V_t. V_q and V_t are digitized by FADCs every 100 ns. Image adapted from [72].

5.4.4   Calibration systems

Calibration systems are required to provide information on PMT charge and time re-
sponse and to tune and verify simulation and reconstruction algorithms. Two systems are
used: a laser calibration system, and a cosmic muon calibration system.

5.4.4.1   Laser calibration system

The MiniBooNE laser calibration system is comprised of a pulsed diode laser con-
nected via optical fibers to four dispersion flasks inside the detector volume. Each flask,
10 cm in diameter, is filled with a dispersive medium called $\text{Ludox}^{\textregistered}$. In addition to the
flasks there is a bare optical fiber near the top of the tank which emits light in a cone at
about $10°$. The laser system is continuously pulsed at 3.33 Hz (but vetoed by a beam trig-
ger) allowing the generation of calibration data on regular intervals (approximately every
four days). These data are used to generate several important calibrations for reconstruct-
ing PMT signal times and charge amplitudes from t_{raw} and q_{raw}.

- time offset correction, t_{offset}, due to the the dynode chain, cabling and electronics for
  each PMT channel

- time slewing correction, $t_{\mathrm{slew}}(q_{\mathrm{raw}})$, to account for the varying time taken to reach
  threshold depending on the raw charge amplitude

- PMT gain calibration for converting q_{raw} into a number of photoelectrons hitting the
  PMT surface

The reconstructed time (in nanoseconds) and PE (photoelectrons) for each PMT channel
are given by

$$
\begin{aligned}
t &= 100 \cdot (\mathrm{N}_{t-1}) + t_{\mathrm{raw}} + t_{\mathrm{offset}} + t_{\mathrm{slew}}(q_{\mathrm{raw}}) \\
\mathrm{PE} &= q_{\mathrm{raw}}/\mathrm{Gain}
\end{aligned}
\tag{5.2}
$$

where N_{t-1} is the number of 100 ns clock ticks from the beginning of the event to the tick
that precedes the discriminator firing for that channel, $(t-1)$ in Figure 5.14.
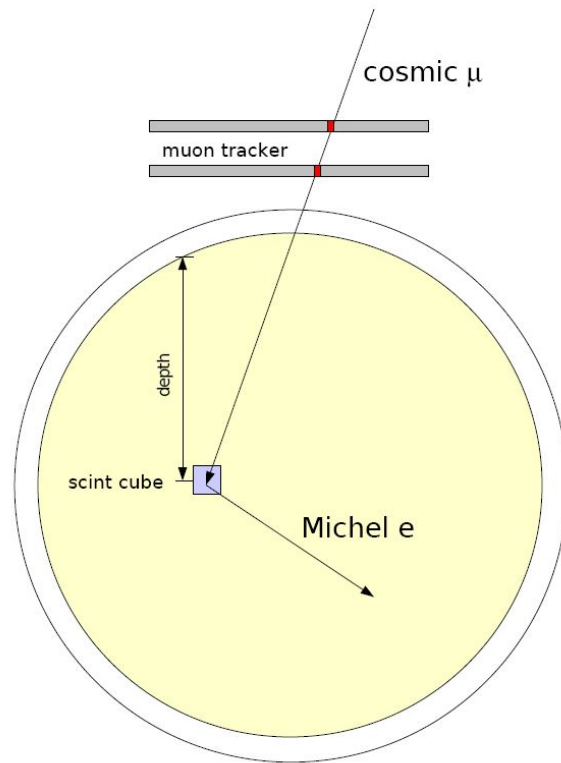
Figure 5.15: Schematic drawing of the muon tracker and cube calibration system. There are seven such cubes located throughout the detector. The drawing is not to scale.

5.4.4.2   Cosmic muon calibration system

The muon calibration system [81] consists of a scintillator hodoscope located above the detector and seven scintillator cubes located throughout the detector volume. The muon hodoscope is comprised of two horizontal planes separated vertically by 1.5 m. Each plane contains two orthogonal layers of Bicron BC-408 plastic scintillator strips instrumented with 2-inch PMTs such that the (x, y) position of a passing particle can be determined. The particle's path can then be extrapolated into the MiniBooNE detector below with directional resolution $\sigma_\theta \approx 2°$ and position resolution $\sigma_{x,y} \approx 10$ cm at the main tank boundary $(r = 575$ cm$)$.

Each cube is a 5 cm $\times$ 5 cm $\times$ 5 cm block of plastic scintillator housed in an aluminum casing with an optical fiber leading to a 1-inch PMT for readout. Cosmic muons which pass through the hodoscope, enter the tank from above, stop in one of the cubes and decay

Cube depth (cm)	$\langle \text{Range} \rangle$ (g/cm^2)	$\langle T_\mu \rangle$ MeV
31.3	28 ± 1	96 ± 2
60.3	54 ± 1	156 ± 2
100.5	89 ± 1	229 ± 3
200.8	174 ± 2	407 ± 4
298.1	256 ± 4	580 ± 8
401.9	344 ± 4	768 ± 9

Table 5.4: Position of scintillation cubes in the MiniBooNE detector. The depth is the vertical distance from the center of the cube to the optical barrier as shown in Figure 5.15. The average range and kinetic energy for muons stopping in each cube are given.

(see Figure 5.15) can be used to study the energy scale for muon track reconstruction. One knows the entry point and stopping point of the muon to ≤ 5 cm and thus can determine the amount of oil the muon traverses. Using ionization energy loss tables based on the Bethe-Bloch formula one can deduce the muon kinetic energy. Table 5.4 lists the depths and average muon kinetic energies for six of the scintillator cubes. Figure 5.16 shows the correlation between this expected muon energy and the reconstructed visible energy from PMT information for both data and simulation. Taking advantage of large available statistics the samples for each cube have been separated into two samples with slightly different average path lengths and muon kinetic energies.

5.4.5   Trigger conditions

The MiniBooNE trigger logic is constructed in software using external information from the Booster, the internal calibration systems and detector PMT multiplicities. PMT sum cards are used to total the PMTs in the main tank and veto region which fire the discriminator during a clock tick. Several trigger types are based on the totals N_{tank} and/or N_{veto}. For each triggered event, in addition to the digitized charge and time information for all PMT channels listed above, a global time stamp for the event, the type of trigger, and neutrino beam quality information from ACNET is recorded. There are several basic
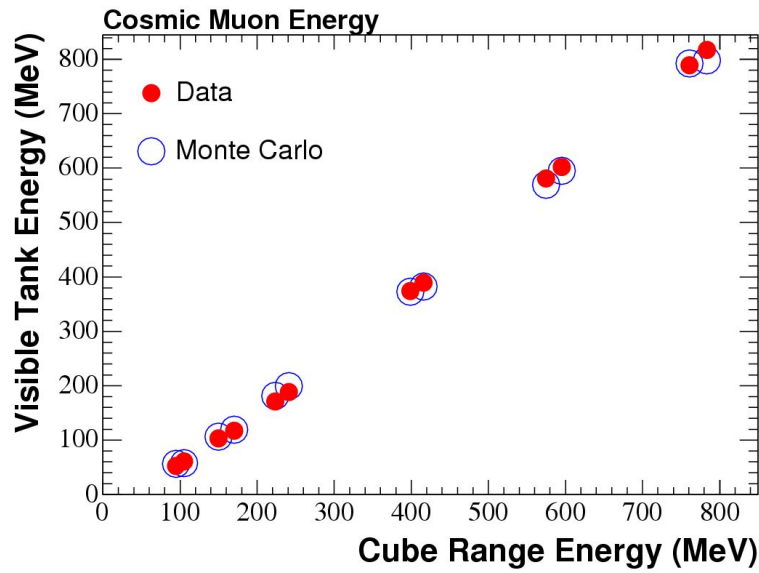
Figure 5.16: Energy reconstructed from PMT signals vs. the expected muon kinetic energy from the muon tracker and cube system geometry for both data (filled circles) and Monte Carlo (open circles). Plot taken from [81].

categories of trigger. The following is not an exhaustive list but describes the most relevant triggers for the oscillation search including detector calibration. A complete list of triggers can be found in [70].

- **Beam triggers -** The principle physics trigger is simply the arrival of proton beam from the Booster to the neutrino beamline target. All detector information is recorded for a 19.2 μs window (192 contiguous 100 ns clock ticks) surrounding the 1.6 μs wide proton pulse. The NuMI neutrino beamline also acts as a trigger as MiniBooNE can detect neutrinos from their beam [97, 86].

- **Random and calibration triggers -** Detector activity is randomly sampled outside of the beam window at 2.01 Hz and is referred to as the Strobe trigger. The firing of the calibration laser, scintillator cube activity, or a 4-fold coincidence in the muon tracker all trigger the recording of a calibration event.

- **Cosmic triggers -** Several triggers have been designed to record events from cosmic, non beam related, non neutrino related, activity. Large pre-scale factors are used

Trigger	Rate (Hz)	Pre-scale	Time Window (μs)
Booster beam	2–5	1	19.2
NuMI beam	0.5	1	19.2
Strobe	2.01	1	19.2
Laser	3.33	1	9.6
Cube	1.1	1	12.8
Tracker	0.7	170	12.8
Michel	1.2	600	19.2
Tank	0.4	90000	19.2
Veto	0.4	5000	19.2

Table 5.5: MiniBooNE detector trigger types and properties.

due to the high rate of such events. A Michel trigger happens when a low-energy tank event ($N_{tank} \geq 24$, $N_{veto} < 6$) occurs between 3 μs and 15 μs after a cosmic muon-like event ($N_{tank} \geq 100$, $N_{veto} \geq 6$). The Tank trigger is simply $N_{tank} \geq 10$ and the Veto trigger is $N_{veto} \geq 6$.

Table 5.5 lists the approximate rates and pre-scale factors of the triggers listed above as well as the length of the trigger window that is opened for each. The total trigger rate (including those not listed here) is ~26 Hz.

Chapter 6

Oscillation Analysis Overview

Before we proceed further toward our goal of presenting a search for $\nu_\mu \to \nu_e$ oscillations at MiniBooNE, it is instructive to give an overview of the analysis, identify the important backgrounds to a ν_e appearance search, and look at some basic properties of the data.

6.1 Overview

As stated in Section 5.2, the primary objective of MiniBooNE is to search for an excess of ν_e-induced events consistent with a $\nu_\mu \to \nu_e$ oscillation hypothesis. An oscillation consistent with that reported by LSND would imply an excess of roughly 0.3% of the ν_μ flux, or $\mathcal{O}(100)$ ν_e charged-current quasi-elastic events. The rejection efficiency for ν_μ-induced background events in the analysis must, therefore, be greater than 99% while maintaining a high efficiency for selecting ν_e-induced events.

Charged-current interactions are used because one can determine the neutrino's flavor by identifying the charged lepton produced in the event. Further, oscillations are an energy dependent phenomenon, and charged-current quasi-elastic (CCQE) scattering,

$$\nu_\ell + n \to p + \ell^+,$$

being a two-body interaction, allows one to reconstruct the incident neutrino's energy from the outgoing charged lepton's energy and angle. Therefore, it is in an energy distribution of candidate ν_e CCQE events where one looks for an excess above a background

of both intrinsic beam ν_e-induced and misidentified ν_μ-induced events.

In Section 6.2 we describe the neutrino interactions which make up the backgrounds and potential signal. In Section 6.3 we explain how a few simple cuts on basic event information can reject 99.99% of cosmic ray induced backgrounds and $\sim 80\%$ of beam related ν_μ charged-current events. The remaining needed background rejection will be achieved through a sophisticated particle identification algorithm to be presented in the next chapter.

A Monte Carlo simulation of the experiment will be used to predict the background rates and determine their uncertainties. However, several methods have been employed which use MiniBooNE data to directly constrain the most important physics models and background contributions to the ν_e appearance search. These are presented in detail in Chapters 7 and 8.

6.2   Neutrino events in the MiniBooNE detector

Figure 6.1 shows Feynman diagrams of the most relevant neutrino interactions within the MiniBooNE detector. In each diagram, the final state particles which produce Cherenkov light have been highlighted in red. In addition, any final state nucleons which are below Cherenkov threshold will produce a small amount of scintillation light. It is important to note that the MiniBooNE detector is incapable of distinguishing between an electromagnetic shower initiated by an electron and one initiated by gamma conversion. The interactions shown in Figure 6.1 are:

a) ν_e charged-current quasi-elastic (CCQE) scattering. These events comprise a potential signal as well as an irreducible background of intrinsic ν_e that will need to be estimated with sufficient accuracy. The electron in the final state identifies the neutrino as ν_e and allows an estimation of the neutrino's energy.

b) ν_μ charged-current quasi-elastic scattering. Roughly 82% of these events can be tagged by the presence of the muon's Michel electron produced in stopped muon decay ($\mu \rightarrow e\nu\nu$); those without an associated Michel must be separated from electrons by their distinct Cherenkov light patterns (see next sections).
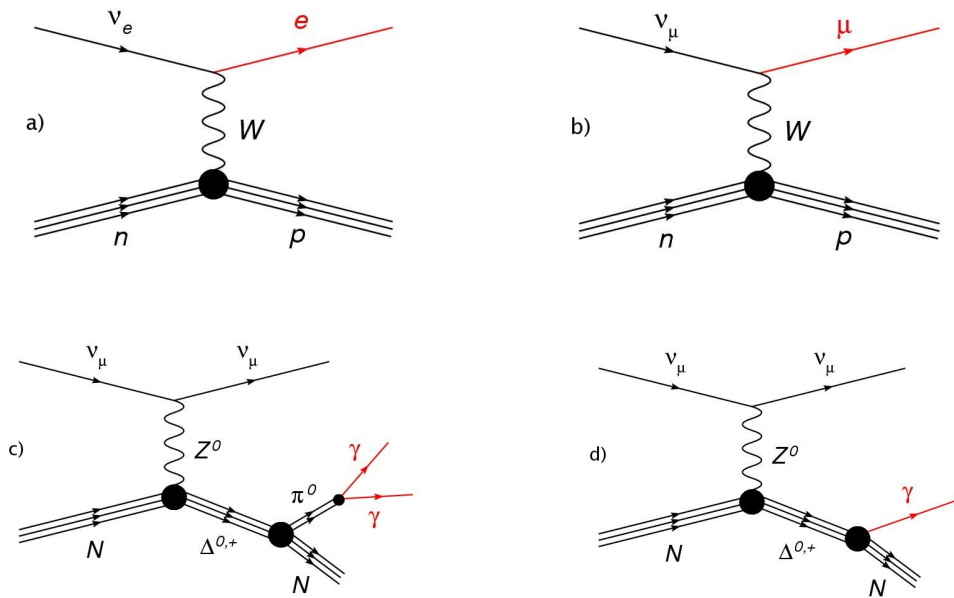
Figure 6.1: Feynman diagrams of four important neutrino interactions for the ν_e appearance search: *a)* ν_e charged-current quasi-elastic (CCQE) scattering *b)* ν_μ CCQE scattering *c)* ν_μ neutral-current (NC) resonant π^0 production and *d)* ν_μ NC Δ radiative decay. The final state particles which produce Cherenkov light in the detector have been highlighted in red.

c) ν_μ neutral-current interactions producing a neutral pion which decays to two photons. NC π^0 events can be identified by the presence of two electron-like showers pointing back to a common vertex; if either photon is lost, however, then these events become indistinguishable from ν_e CCQE events. The diagram shows resonant π^0 production (through a Δ resonance decay), but coherent production, where the target nucleus is left in the ground state, may also be possible.

d) ν_μ neutral-current interactions producing a Δ^0 or Δ^+ resonance which decays radiatively, producing a single photon. Events with a single photon final state cannot, in principle, be distinguished from a ν_e CCQE event.

The latter three event types constitute the majority of the ν_μ mis-ID backgrounds in the ν_e CCQE sample, and must be considered carefully. In Section 7.2, when discussing the MiniBooNE neutrino cross-section models, we will focus on these interactions. In Section

7.2.1, we describe how the high statistics ν_μ CCQE sample has been used to tune the charged-current quasi-elastic scattering model which applies to both ν_μ and ν_e. In Section 7.2.2, we present a procedure which uses the observed NC π^0 event rate at MiniBooNE to make an absolutely normalized prediction of the π^0 and $\Delta \rightarrow N\gamma$ backgrounds in the ν_e sample. In Chapter 8, we discuss a method for constraining the intrinsic beam ν_e background using the observed ν_μ CCQE sample.

6.3 Initial data reduction: subevents and N_{tank}, N_{veto}

Three basic pieces of information from an event are used in an initial reduction of the total MiniBooNE data sample toward isolating ν_e CCQE candidates. These include the number of time-separated clusters of PMT hits, known as "subevents", and the total number of tank and veto PMTs which have registered a hit in each subevent.

As described in Section 5.3.1, protons are delivered to the Booster Neutrino Beam in 1.6 μs long pulses at 15 Hz. The MiniBooNE detector DAQ records all detector activity within a 19.2 μs window beginning 4.6 μs before the start of each spill. Within this beam trigger window, clusters of PMT hits in time, corresponding to different particle tracks in the detector, are clearly visible. Figure 6.2 shows an example for a single beam trigger. The two distinct clusters are examples of subevents (SE) within a single trigger. Strictly, subevents are defined as ≥ 10 PMT hits separated by less than 10 ns. Figure 6.2 is an example of a ν_μ CC event; the primary μ is seen in the beam window and several microseconds later the Michel electron from its decay is clearly visible.

As mentioned above, $\sim 82\%$ of ν_μ CC events can be rejected by the presence of their Michel electrons as a second subevent. Of the remaining 18%, 8% of μ^- capture on carbon, 8% of muons decay too quickly for the electron to be separated from the primary μ event, and about 2% of Michel electrons are below threshold. The other interactions shown in Figure 6.1 (ν_e CCQE, NC π^0 and $\Delta \rightarrow N\gamma$), all of which do not contain a decaying muon, will create a single subevent only.

Figure 6.3 shows the time distribution of all such subevents (determined as the average calibrated time of the hits making up each subevent) for a set of beam triggers.
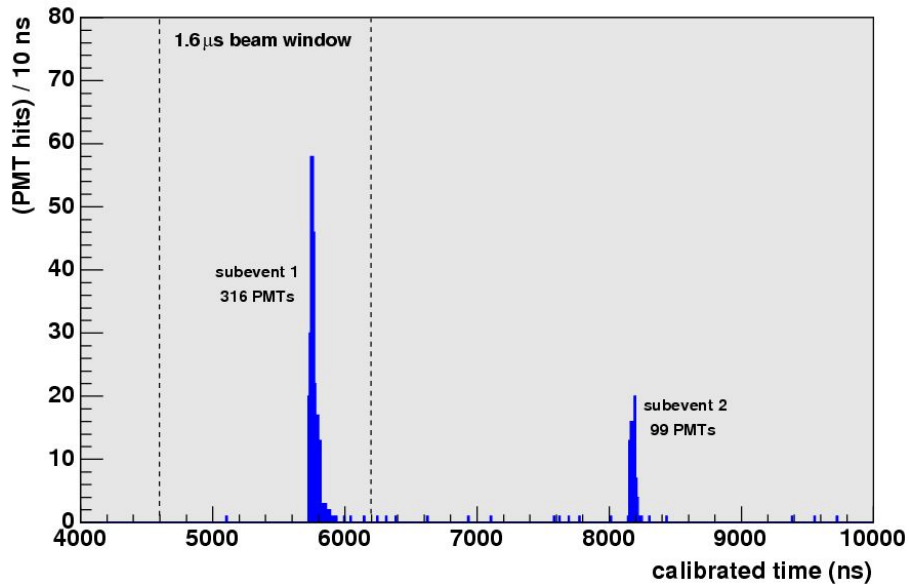
Figure 6.2: PMT hit time distribution for a single beam trigger with two clear subevents (SE). The event is a candidate ν_μ CCQE event where the first subevent is the muon and the second is the Michel electron from the muon's decay.

The low duty factor of the proton beam from the Booster makes the beam-on excess of events clearly visible. The flat background is due to cosmic muons ($\sim$10 kHz) and their decay electrons. The excess is due to beam neutrino interactions and the decays of muons created in those interactions. The Michel electrons from these decays account for the increase during the beam spill and the exponential fall-off following the spill. Two simple cuts reduce the cosmic background to less than 0.1%.

- $N_{tank} \geq$ **200:** The Michel endpoint at 52.8 MeV translates into a maximum number of PMT hits in the tank around N_{tank} = 180. Figure 6.4 shows the N_{tank} distribution for the 2nd subevent in a sample with exactly 2 subevents. The right panel shows the reconstructed energy for the 2nd subevent. The distribution is consistent with a Michel electron energy spectrum smeared by a resolution function. Figure 6.3 shows how the cut at N_{tank} > 200 removes the Michel electron features from the time distribution.

- N_{veto} < **6:** Figure 6.5 shows the distribution of N_{veto} for beam triggers. Two non-
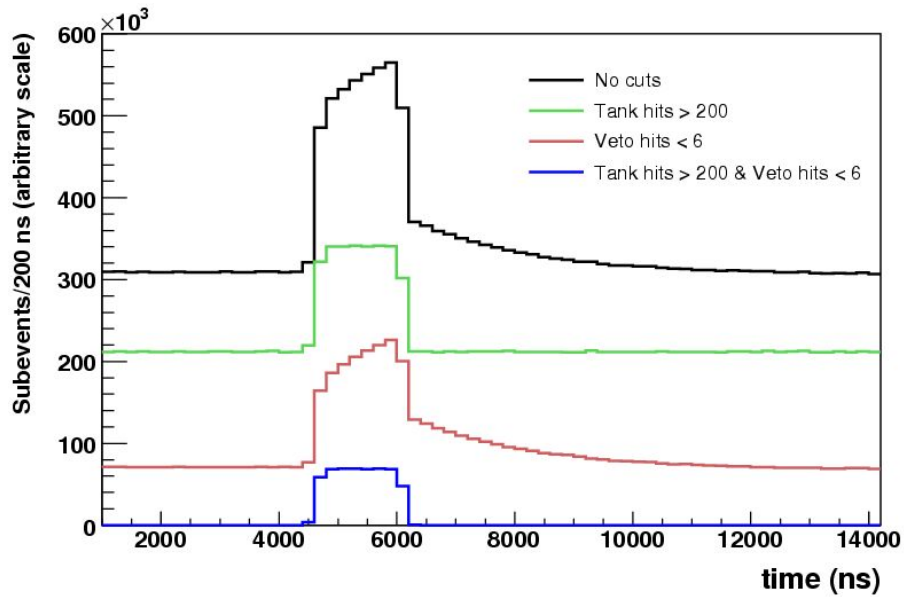
Figure 6.3: Time distribution for subevents (see text) in a sample of beam triggers. The excess of events in the beam spill is evident (black). A minimum requirement on number of tank PMTs above threshold, $N_{tank} \geq 200$, removes low energy Michel electrons produced in muon decays (green). A cut on veto activity, $N_{veto} < 6$, removes cosmic muons entering through the veto shell (red). Applying both cuts removes $> 99.99\%$ of non-beam-induced events (blue).
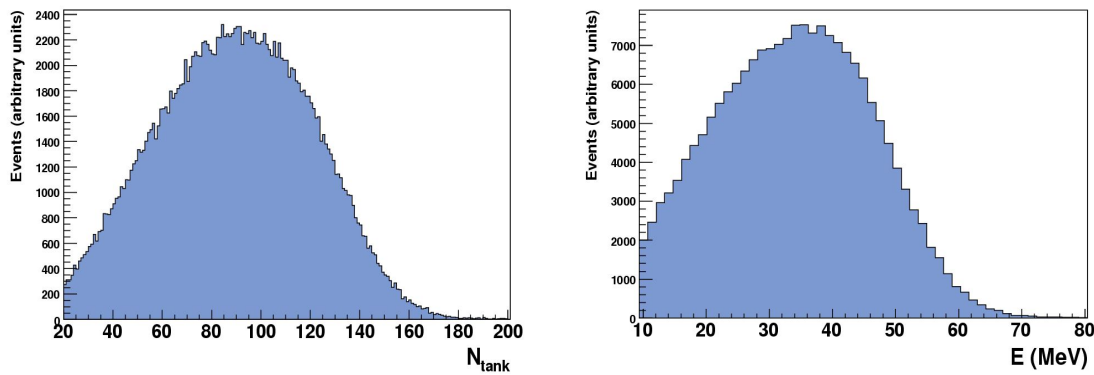
Figure 6.4: Number of tank PMT hits N_{tank} (left) for the second subevent in a SE == 2 sample. These are Michel electron candidates from stopped muon decays. The reconstructed energy (right) is consistent with the expected Michel electron spectrum convolved with an energy resolution function (14.8% at the Michel endpoint of 52.8 MeV).

zero peaks are visible. The first is from cosmic muons entering the veto and stopping in the detector (usually producing a Michel electron). The second is muons penetrating the entire detector and passing through the veto shell twice. This veto cut removes both types.

The application of the N_{tank} and N_{veto} cuts removes 99.99% of non beam-induced backgrounds as can be seen in Figure 6.3. An additional timing cut of 4600 ns $\leq t \leq$ 6200 ns removes the few out-of-beam-spill events which passed the N_{tank} and N_{veto} cuts.

6.4   Electron/muon Cherenkov light patterns

The ~18% of ν_μ CCQE events which cannot be rejected on the basis of having two distinct subevents from the muon and Michel electron must be rejected based on the different Cherenkov light patterns of a muon and an electron in the detector. For muons, the angular deflections caused by multiple Coulomb scattering are small, so the outside edge of the Cherenkov cone tends to be sharp. Also, the range in oil of an $\mathcal{O}(1 \text{ GeV})$ muon is several meters, so the ring will be partially or completely filled in as the muon approaches the walls of the tank. Electrons, on the other hand, will lose energy through
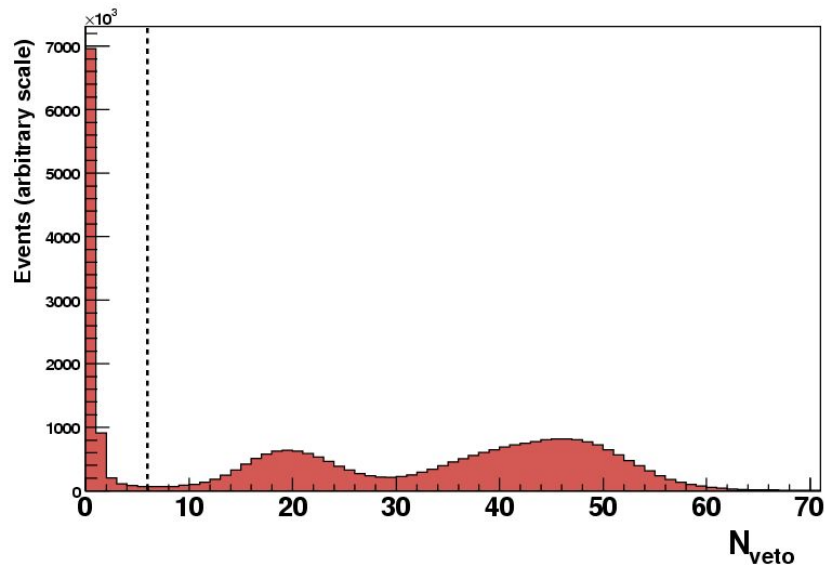
Figure 6.5: Number of veto PMT hits N_{veto} for beam trigger events. The two peaks from cosmic muons are clearly visible (see the text). The spike at $N_{veto} = 0$ are beam-induced neutrino events. The vertical line at $N_{veto} = 6$ marks the cut used to reject cosmic muon events.

bremsstrahlung and scatter to larger angles. The result is a diffuse ring of hit PMTs with a diameter defined by the Cherenkov angle and the distance of the electron from the tank wall.

Figure 6.6 illustrates the effect for electrons and muons. The right plots show the angular distribution of hits in the MiniBooNE detector. Using a 2 subevent sample (ν_μ CC events), each subevent has been further subdivided into prompt ($|t - \bar{t}_{SE}| < 5$ ns) Cherenkov radiation and delayed ($t - \bar{t}_{SE} > 5$ ns) isotropic scintillation light. The distinct profiles are evident. Note that Figure 6.6 compares data to the simulation and shows excellent agreement. Section 7.3 will discuss the simulation of light production and propagation in the MiniBooNE detector. Section 7.5 will describe how these differences in the light angular distributions shown in Figure 6.6 are used in the particle identification algorithm to separate ν_e and ν_μ charged-current quasi-elastic events.
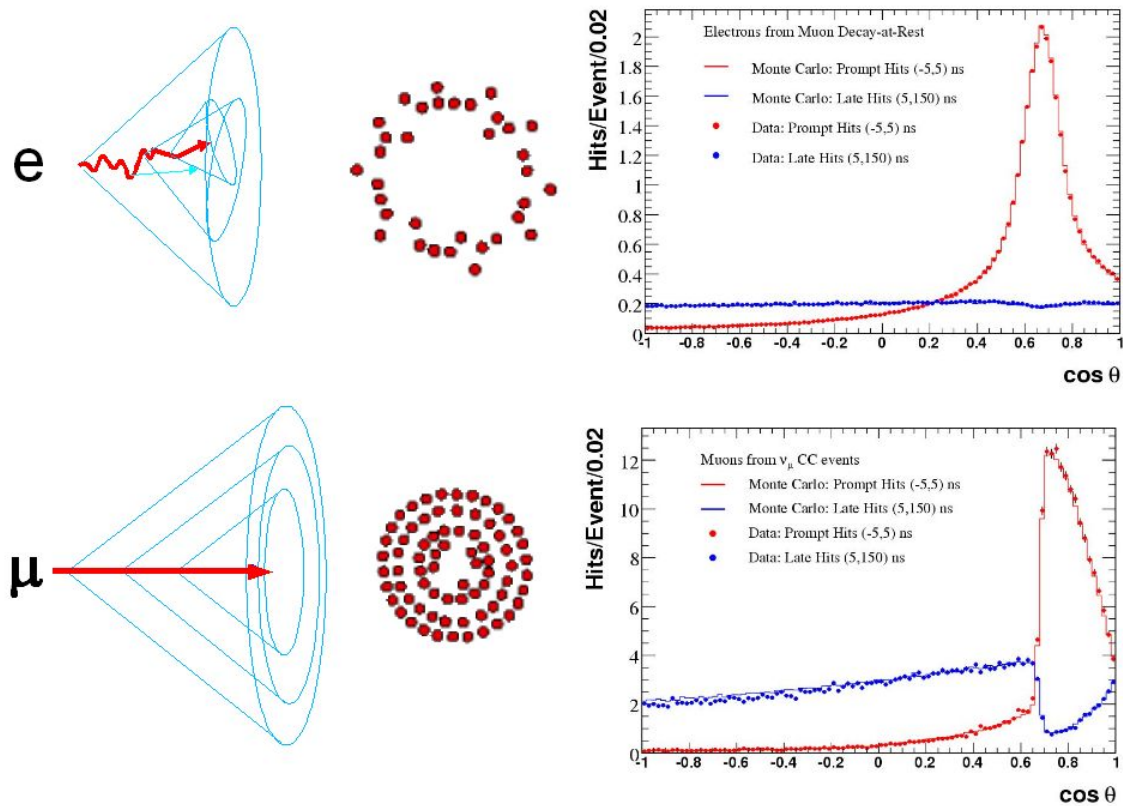
Figure 6.6: Cherenkov light patterns of electrons and muons in the MiniBooNE detector. The right plots show the angular distribution of PMT hits with respect to the electron or muon direction. Red points (data) and histograms (MC) are the prompt Cherenkov light. Blue points (data) and histograms (MC) are the contribution from more delayed scintillation light.

Chapter 7

MiniBooNE Simulation and Reconstruction Algorithms

A detailed and accurate simulation of the experiment is critical to the search for $\nu_\mu \to \nu_e$ oscillations at MiniBooNE. In this chapter, we describe the components of the simulation and the techniques used to constrain the charged-current quasi-elastic scattering model and the ν_μ mis-ID backgrounds introduced in Chapter 6. The MiniBooNE simulation is comprised of three separate Monte Carlo programs: the beam simulation, the neutrino interaction model and the MiniBooNE detector simulation.

7.1 Simulation of the Booster Neutrino Beam

A sophisticated Monte Carlo program has been developed to simulate the Booster Neutrino Beamline (BNB) in order to predict the neutrino fluxes (ν_μ, $\overline{\nu}_\mu$, ν_e, $\overline{\nu}_e$) as a function of neutrino energy (per proton on target per unit area) at a given detector location. To facilitate the ability to predict fluxes for different detectors and as a method for applying statistical enhancements to the neutrino flux predictions, two separate simulation codes are used. The first, a Geant4-based Monte Carlo, simulates all relevant processes from primary protons hitting the target to the point of decay of mesons which create neutrinos. The second program, a FORTRAN-based Monte Carlo code, uses the output of the

Geant4 simulation and generates the kinematics of the neutrino(s) produced in each meson decay and extrapolates the neutrino's path to determine if it crosses the location of a specified detector. The decay of each meson can be repeated many times to increase the statistical precision of the flux predictions at distant detectors. The most comprehensive descriptions of the BNB Monte Carlo can be found in [94] and [69].

7.1.1 Geant4-based Booster Neutrino Beamline Monte Carlo

Geant4 [125, 126, 127] is a C++ software toolkit for the simulation of the passage of particles through matter. The physics interface of Geant4 facilitates the use of a variety of built-in physics packages or the implementation of custom models by the user. The BNB Monte Carlo takes advantage of both of these possibilities. The BNB Monte Carlo can effectively be broken into five components:

- The definition of the beamline geometry, specified by the shape, location and material composition of the components of the BNB, through which all simulated particles must be tracked. This includes the simulation of the magnetic field within the horn volume.

- The generation of primary protons according to the expected beam optics properties.

- The simulation of inelastic interactions of primary protons with the beryllium target. Due to the importance of primary hadron production in the target, a custom model of the inclusive production of p, n, π^+, π^-, K^+, K^- and K^0 in p+Be interactions at 8.9 GeV/c has been implemented.

- The propagation of particles through the beamline geometry accounting for energy loss and electromagnetic and hadronic processes that can alter their kinematics or lead to the production of tertiary particles. The simulation of these interactions is based on a combination of built-in hadronic interaction models and custom built cross-section tables for interactions in the most important materials, beryllium and aluminum.

- The identification of decay processes that result in neutrinos.

Both hadronic and electromagnetic processes are considered for all particles tracked in the simulation. The most important electromagnetic processes, including particle trajectories through the horn magnetic field, multiple Coulomb scattering and energy loss by ionization, have been described and their simulations carefully validated in [94]. Here we will focus on the simulation of hadronic processes. Three forms are considered: elastic scattering, quasi-elastic scattering and inelastic interactions which produce final state particles different from those in the initial state. Elastic scattering refers to coherent scatters of hadrons off a nucleus as a whole. Quasi-elastic scattering involves the scattering of hadrons off nucleons *within* the nucleus in a manner analogous to elastic scattering of hadrons off free nucleons.

The simulation of each process is divided into two components. The first is the determination that an interaction has occurred based on the total cross-section (or rate) for that process. The total elastic cross-section, σ_{ELA}, total quasi-elastic cross-section, σ_{QEL}, and total inelastic production cross-section, σ_{PROD}, combine to give the total hadronic interaction cross-section, σ_{TOT}. The later two, σ_{QEL} and σ_{PROD}, combine to give the total inelastic cross-section, σ_{INE}.

$$\sigma_{\mathrm{TOT}} \;=\; \sigma_{\mathrm{ELA}} + (\sigma_{\mathrm{QEL}} + \sigma_{\mathrm{PROD}}) \;=\; \sigma_{\mathrm{ELA}} + \sigma_{\mathrm{INE}}. \tag{7.1}$$

The second component is the determination of the final state particles and their kinematics based on available models of differential cross-sections.[1] The BNB simulation requires a complete description of elastic, quasi-elastic and inelastic interactions for the most relevant hadrons (p, n, π^+, π^-, K^+, K^-, K^0) in the most relevant materials (Be, Al, Fe, concrete) in the most relevant energy ranges ($E_{\mathrm{p,n}} \leq 8\,\mathrm{GeV}$, $E_{\pi^\pm,\mathrm{K}} \leq 6\,\mathrm{GeV}$).

A combination of custom-built and built-in Geant4 models have been used in the BNB Monte Carlo. Relevant data is used to tune the cross-section tables wherever possible, particularly for the critical inelastic interactions of primary protons with beryllium. Table 7.1 summarizes the sources of the models for the most relevant hadronic interaction cross-sections in the default configuration of the BNB Geant4 Monte Carlo. The custom

---

[1] The three built-in physics models introduced in Section 2.2, the "Low Energy Parameterization Driven Model", the "Bertini Intranuclear Cascade Model" and the "Binary Cascade Model", are examples of differential cross-section models for determining final states.

Interaction	σ_{TOT}	σ_{QEL}	σ_{INE}	final state kinematics
p+Be ($K_p \geq 7.5$ GeV)			Data	Data/MARS
p+Be ($K_p \geq 7.5$ GeV)	Glauber	Shadow		G4 LHEP
p+Be ($K_p < 7.5$ GeV)	Glauber	Shadow	Data	G4 LHEP
p+Al	Glauber	Shadow	Data	G4 LHEP
n+Be	Data/Glauber	Shadow	same as p+Be	G4 LHEP
n+Al	Data/Glauber	Shadow	same as p+Al	G4 LHEP
$\pi^{\pm}$ +Be	Data/Glauber	Data/Shadow	Data	G4 LHEP
$\pi^{\pm}$ +Al	Data/Glauber	Data/Shadow	Data	G4 LHEP
$K^{\pm}$ +Be, K^0 +Be	G4 default	G4 default	G4 default	G4 LHEP
$K^{\pm}$ +Al, K^0 +Al	G4 default	G4 default	G4 default	G4 LHEP
X+other	G4 default	G4 default	G4 default	G4 LHEP

Table 7.1: Summary of the sources of the models for the most relevant hadronic interaction cross-sections in the BNB simulation. σ_{INE} is the total inelastic cross-section. σ_{PROD} can be determined from $\sigma_{\text{PROD}} = \sigma_{\text{INE}} - \sigma_{\text{QEL}}$. σ_{ELA} is determined from $\sigma_{\text{ELA}} = \sigma_{\text{TOT}} - \sigma_{\text{INE}}$. "Data", "Shadow" and "Glauber" all refer to custom-built models implemented specifically for the BNB Monte Carlo (see the text). "G4 LHEP" refers to the *Low Energy Parameterization Driven Model* [124], a built-in Geant4 model. "G4 default" refers to cross-section tables available in Geant4 for hadronic processes.

model for p+Be inelastic interactions at $K_p \geq 7.5$ GeV is described below, followed by an overview of the models developed for (p/n/π/K)+(Be/Al) total cross-sections.

7.1.1.1   Simulation of the beamline geometry

A basic feature of the Geant4 simulation toolkit is the ability to define geometric volumes and their material compositions. A careful definition of the relevant objects in the BNB has been created which includes the aluminum horn, beryllium target, both concrete and iron shielding, the dolomite surrounding the decay region and the 25 m and 50 m
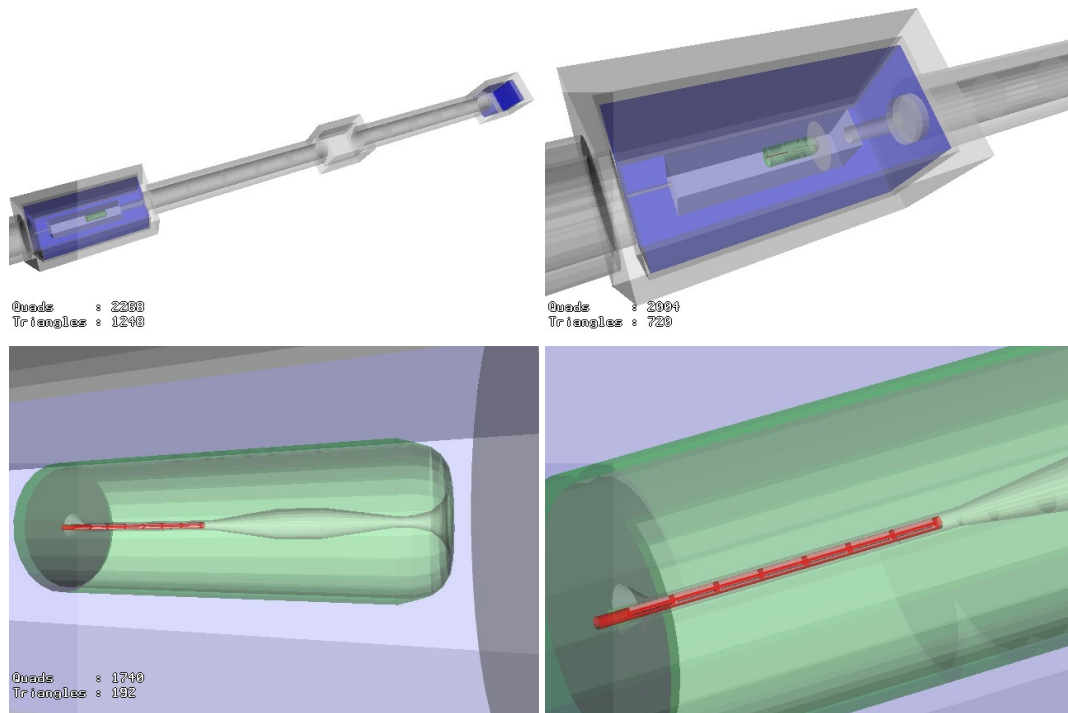
Figure 7.1: The Booster Neutrino Beamline geometry as defined in the Geant4 Monte Carlo. The images show the full 50 m decay region (top left), the target hall (top right), horn (bottom left) and target (bottom right). Images taken from [94].

beam absorbers.

Figure 7.1, taken from Ref. [94], shows the beamline geometry at four different zoom levels as implemented in the Geant4 simulation using a VRML [137] viewer. Beryllium, aluminum and iron are rendered in red, green and blue, respectively.

7.1.1.2 Simulation of the primary proton beam

Each Monte Carlo event begins with the generation of a single 8 GeV kinetic energy primary proton directed at the upstream face of the beryllium target. This approach is sufficient (and even preferred) since no correlated effects between protons in a bunch are expected.

The beam optics of the 8 GeV beamline are accurately simulated in order to account for its effect on the neutrino flux prediction. The coordinate system used has the z-axis along

the beam direction and the y-axis upward. In this frame, the initial position (x_0, y_0, z_0) and 3-momentum $(p_{x_0}, p_{y_0}, p_{z_0})$ are randomly generated from specified beam optics parameters:

$$
\begin{aligned}
x_0 &= \overline{x} + R_1 \sigma_x & p_{x_0} &= \sqrt{E_p^2 - m_p^2}(\overline{\theta_x} + R_3 \sigma_{\theta_x}) \\
y_0 &= \overline{y} + R_2 \sigma_y & p_{y_0} &= \sqrt{E_p^2 - m_p^2}(\overline{\theta_y} + R_4 \sigma_{\theta_y}) \\
z_0 &= z & p_{z_0} &= \sqrt{E_p^2 - m_p^2 - p_{x_0}^2 - p_{y_0}^2}
\end{aligned}
\tag{7.2}
$$

where $R_1 - R_4$ are independent random numbers drawn from a standard normal distribution (mean $= 0$, variance $= 1$), $E_p = 8$ GeV is the proton kinetic energy, m_p is the proton mass and $(\overline{x}, \overline{y}, \overline{\theta_x}, \overline{\theta_y}, \sigma_x, \sigma_y, \sigma_{\theta_x}, \sigma_{\theta_y})$ are the parameters describing the proton beam profile. In the default configuration, primary protons are generated 1 cm upstream of the target face ($z = $ -1.0 cm) and using the values listed in Table 5.1 to describe the beam optics.

7.1.1.3   Simulation of hadronic cross-sections in the beamline

Table 7.1 lists the models used for the most relevant hadronic interactions within the BNB and indicates where data have been used to constrain or check the models. The most important secondary interactions occur in the beryllium target or the aluminum horn and particular attention has been given to these interactions. Data has been used whenever available to constrain or check the models. The total hadronic cross-sections for protons and neutrons were calculated using the Glauber model [113] as described in [114]. The few data available have been used as a cross-check on the theoretical calculation. The inelastic cross-section model takes advantage of a large set of experimental data and fits these to parameterizations sufficiently sophisticated to reproduce the features of the data (particularly resonances in the $\pi^\pm$ inelastic cross-sections). The measurements of quasi-elastic scattering are again sparse, so a theoretical model has been used; σ_{QEL} is calculated as the incoherent sum of the cross-sections for scatters off the nucleons within the nucleus using the shadowed multiple scattering expansion [113]. σ_{PROD} and σ_{ELA} are determined from these calculations via $\sigma_{\mathrm{PROD}} = \sigma_{\mathrm{INE}} - \sigma_{\mathrm{QEL}}$ and $\sigma_{\mathrm{ELA}} = \sigma_{\mathrm{TOT}} - \sigma_{\mathrm{INE}}$. A very complete description is provided in [69] and the reader is referred there for details of the models and data used.

Each theoretical calculation of the cross-section or sample of data (where available) are fit to smooth parameterizations across the relevant momentum ranges for use in the simulation. Figures 7.2, 7.3 and 7.4 show the hadronic cross-section models used for p, n, π^+ and π^- in beryllium and aluminum. These total cross-sections, plus the differential cross-sections for primary hadron production at $p_B = 8.9$ GeV/c discussed in the next section, constitute the custom parts of the BNB Monte Carlo. All other interactions, accounting for $< 1\%$ of the neutrino flux prediction, use default Geant4 models.

7.1.1.4   Simulation of primary p+Be inelastic interactions in the target

In Chapter 2 we explored the relative impact of primary and secondary hadronic interactions for the MiniBooNE neutrino flux where 'primary' was defined as the interaction of beam protons with the beryllium target at 8.9 GeV/c.[2] Those studies not only revealed that primary interactions are significantly more important for an accurate flux prediction, but also that the variation in available Geant4 models is of order 50–100%. For this reason, we use a custom-built physics model for the simulation of inelastic production of the most important secondaries (π^+, π^-, K^+, K^-, K^0, p, n) in proton+beryllium interactions at 8.9 GeV/c.

The simulation proceeds in the following steps:

1. For each secondary considered, a table of double-differential inclusive production cross-sections is built in bins of longitudinal and transverse momentum of the secondary hadron, p_z and p_T:

$$
\frac{d^2\sigma^{\mathrm{p+Be}\rightarrow h+X}}{dp_z dp_T} = \begin{bmatrix} \left(\frac{d^2\sigma}{dp_z dp_T}\right)_{00} & \left(\frac{d^2\sigma}{dp_z dp_T}\right)_{01} & \cdots \\ \left(\frac{d^2\sigma}{dp_z dp_T}\right)_{10} & \cdots & \\ \cdots & & \end{bmatrix}
$$

Each table is defined in the range $0\,\mathrm{GeV}/c < p_z < 10\,\mathrm{GeV}/c$ (50 bins 200 MeV/c wide) and $0\,\mathrm{GeV}/c < p_T < 1\,\mathrm{GeV}/c$ (100 bins 10 MeV/c wide).

---

[2]In practice, beam protons may lose a small amount of energy before an inelastic collision occurs, so interactions are considered 'primary' in the Monte Carlo if the proton kinetic energy is greater than 7.5 GeV.
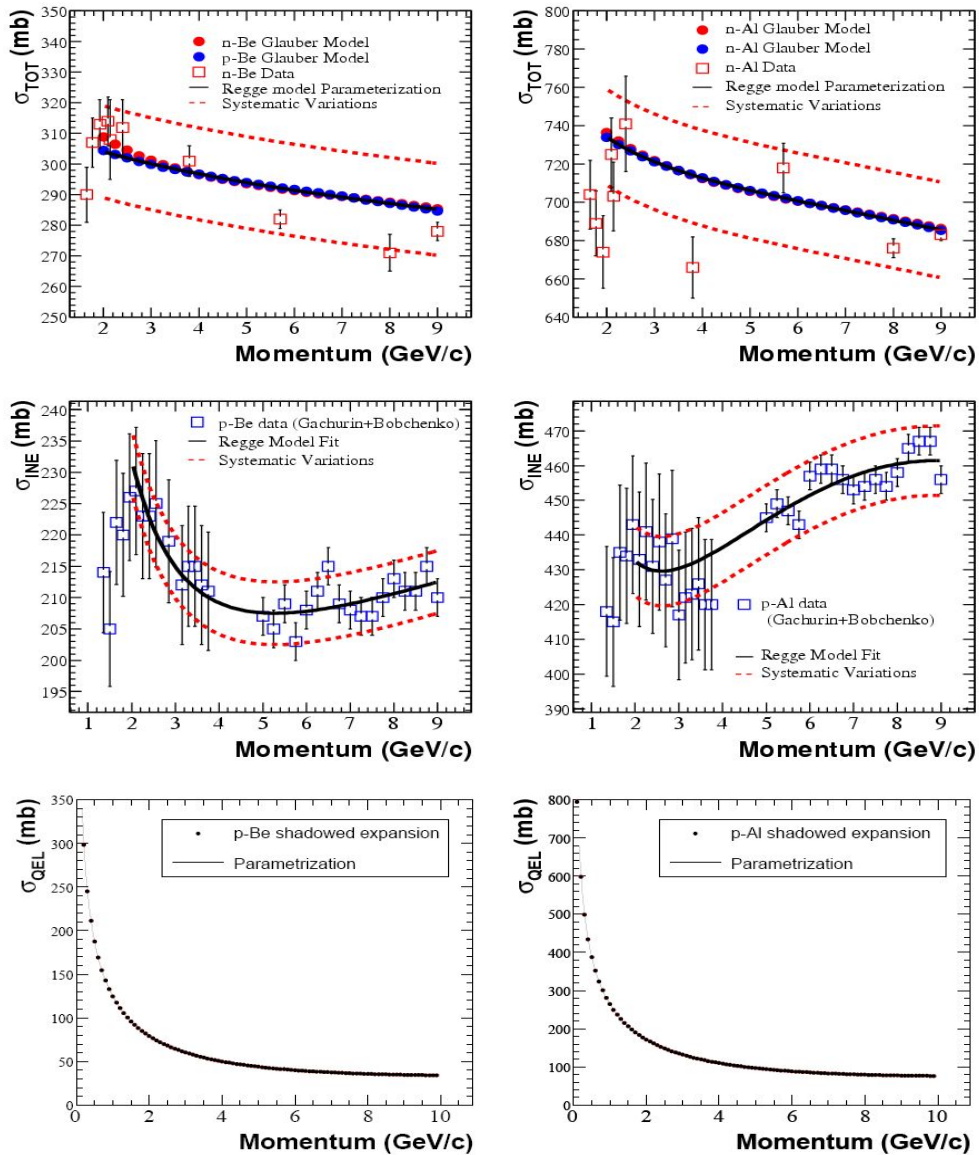
Figure 7.2: (p/n)+Be (left) and (p/n)+Al (right) hadronic cross-section models used in the BNB Geant4 simulation. The total hadronic (top), inelastic (middle) and quasi-elastic (bottom) cross-section models are shown in the relevant momentum ranges. The available data are plotted with the models for comparison. Plots taken from [69].

Figure 7.3: π^+ +Be (left) and π^- +Be (right) hadronic cross-section models used in the BNB Geant4 simulation. The total hadronic (top), inelastic (middle) and quasi-elastic (bottom) cross-section models are shown in the relevant momentum ranges. The available data are plotted with the models for comparison. Plots taken from [69].
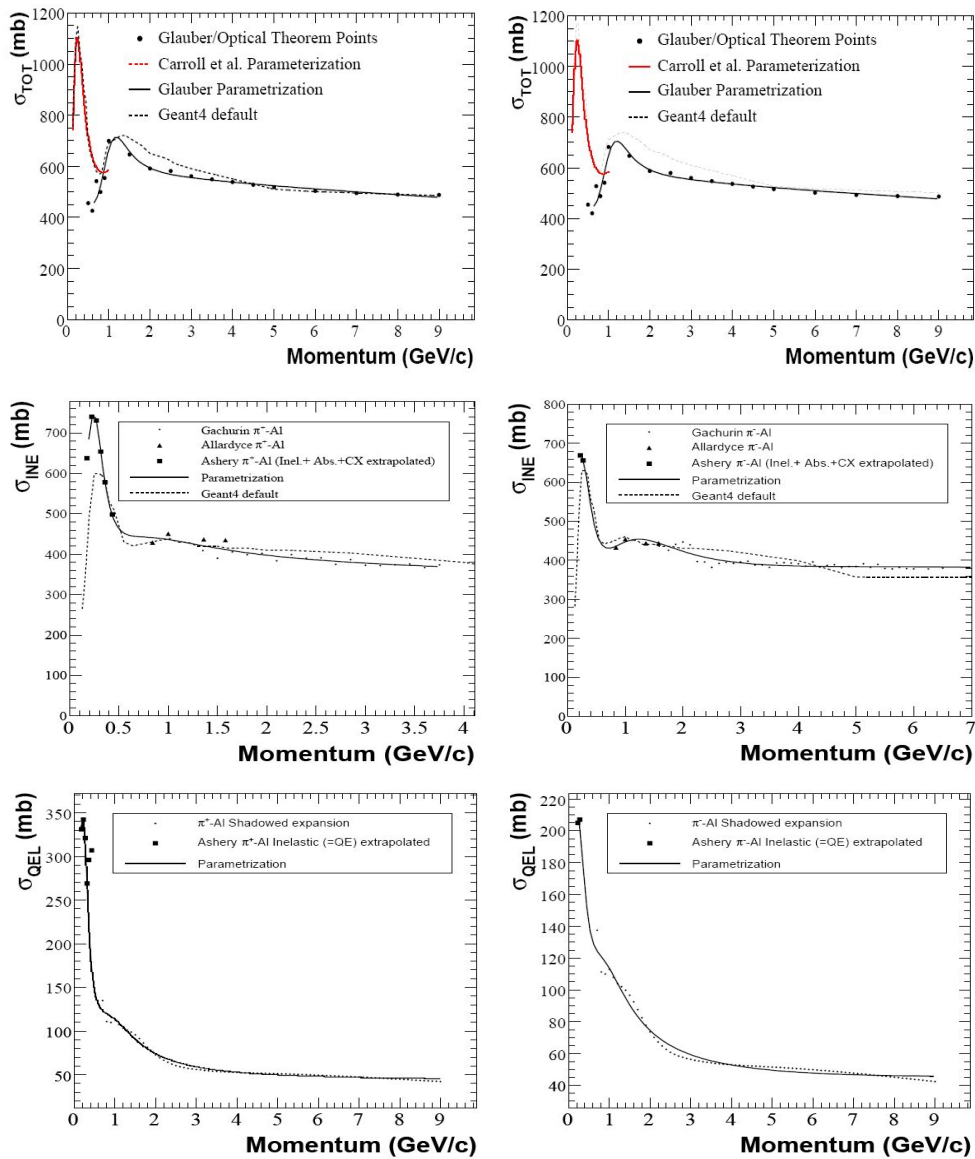
Figure 7.4: π^+ +Al (left) and π^- +Al (right) hadronic cross-section models used in the BNB Geant4 simulation. The total hadronic (top), inelastic (middle) and quasi-elastic (bottom) cross-section models are shown in the relevant momentum ranges. The available data are plotted with the models for comparison. Plots taken from [69].

2. Determine the average multiplicity per inelastic interaction for each secondary by integrating over the differential cross-section and normalizing to the total inelastic production cross-section

$$\langle N^h \rangle = \frac{\sum_{p_z, p_T} (d^2\sigma^h / dp_z dp_T) * (dp_z dp_T)}{\sigma_{PROD}} \tag{7.3}$$

3. The total production cross-section, σ_{PROD}, at 8.9 GeV/c determines the rate of inelastic interactions within the target. Once an inelastic interaction occurs the number of each secondary produced is drawn from a Poisson distribution with mean $\langle N^h \rangle$.

4. The kinematics (p_z, p_T) for each secondary in the event are randomly determined from the weighted elements in the cross-section tables from step 1.

Once generated, secondary hadrons are propagated through the geometry by Geant4 and subsequent hadronic interactions are controlled by cross-section tables and final state models described in Section 7.1.1.3.

Filling the inclusive cross-section tables   The inclusive double-differential production cross-section tables for π^+, π^-, K^+ and K^0 are filled from smooth parameterizations of available production data. The tables for K^-, p and n production are filled using cross-sections extracted from the MARS15 [121] Monte Carlo program.

Two different parameterizations have been used and are described in Appendix B. They are the 9 parameter model of Sanford and Wang (SW) given in Eq. B.1 and used to describe π^+, π^- and K^0 production, and a 7 parameter model based on Feynman scaling (FS) given in Eq. B.7 and used to describe K^+ production. The pion models are determined using data from the E910 [101] and HARP experiments, the latter being the data described previously in this dissertation. The K^+ model is based on data from 8 kaon production experiments and the K^0 model is based on E910 data and those of Abe *et al* [106]. The details of the fitting procedure, the results, the quality of the fits and errors on the parameters are described in detail in [69] and summarized in Appendix B.

Parent	Lifetime (ns)	Decay mode (positives)	Branching ratio (%)
π^+/π^-	26.03	$\mu^+\,\nu_\mu$	99.9877
		$e^+\,\nu_e$	0.0123
K^+/K^-	12.385	$\mu^+\,\nu_\mu$	63.44
		$\pi^0\,e^+\,\nu_e$	4.98
		$\pi^0\,\mu^+\,\nu_\mu$	3.32
K_L^0	51.6	$\pi^-\,e^+\,\nu_e$	20.333
		$\pi^+\,e^-\,\overline{\nu}_e$	20.197
		$\pi^-\,\mu^+\,\nu_\mu$	13.551
		$\pi^+\,\mu^-\,\overline{\nu}_\mu$	13.469
μ^+/μ^-	2197.03	$e^+\,\nu_e\,\overline{\nu}_\mu$	100.0

Table 7.2: Lifetimes and branching ratios of particle decays which produce neutrinos in the BNB simulation. The decays listed are for the positive parent. The negative parent decay is the charge conjugate of that listed.

7.1.2   FORTRAN-based meson/lepton decay simulation

The Geant4 simulation tracks all particles until they are absorbed or decay. Those decays producing neutrinos are recorded in output ntuples for propagation to the next stage of the simulation. The lifetimes and branching ratios of the neutrino-producing decays are given in Table 7.2. Each parent meson or lepton's position, 4-momentum and polarization at decay are stored. The next stage, a FORTRAN-based code, then simulates details of the decays [69, 94] as well as provides important statistical enhancements for the flux predictions. Each neutrino produced is propagated in space to determine if it intersects the cross-sectional area of the detector defined (a disc 610 cm in diameter, 541 m from the target and 1.89 m above the beam direction in the case of MiniBooNE). Statistical enhancements in the predicted neutrino flux at a distant detector are achieved by decaying each parent multiple times (N = 1000 in standard running mode) earning this Monte Carlo program its name, "re-decay".
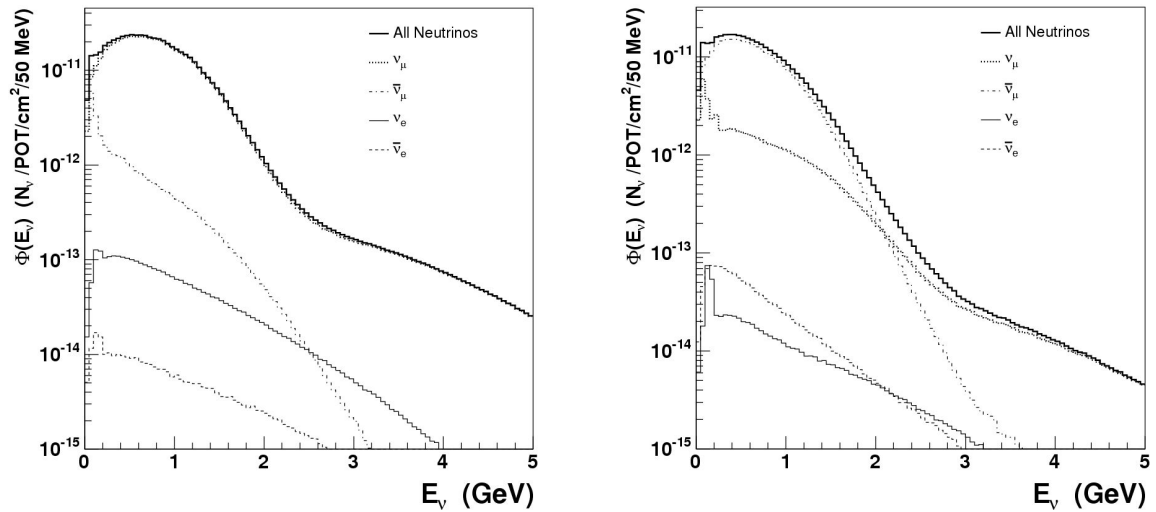
Figure 7.5: Neutrino flux predictions for neutrino mode (left) and antineutrino mode (right). The total fluxes are shown for ν_μ, $\overline{\nu}_\mu$, ν_e and $\overline{\nu}_e$ for both configurations.

7.1.3 Neutrino flux prediction at the MiniBooNE detector

The neutrino flux prediction at the MiniBooNE detector location according to the BNB Monte Carlo is shown in Figures 7.5 through 7.7. In Figure 7.5 the total flux of the four neutrino flavors (ν_μ, $\overline{\nu}_\mu$, ν_e, $\overline{\nu}_e$) are shown as a function of neutrino energy, E_ν, for both neutrino mode (horn I = +174 kA) and antineutrino mode (horn I = -174 kA) running of the Booster Neutrino Beamline.

In Figure 7.6, the neutrino mode fluxes have been further broken down according to the chain of hadronic processes which created the neutrino. In particular, they are separated by the primary hadron produced in a p+Be interaction. These plots provide important information about the history of each neutrino species and the hadronic processes that are most relevant to predicting their fluxes. In Appendix C we take it one step further still and look at the fraction of each neutrino's flux which has been directly constrained by the HARP cross-section measurements presented in Chapter 4. Figure 7.7 shows the same breakdown, but for antineutrino running of the BNB.

These figures contain a lot of complicated, energy dependent information. We have attempted to summarize this information in Table 7.3 which gives the fractional contribu-
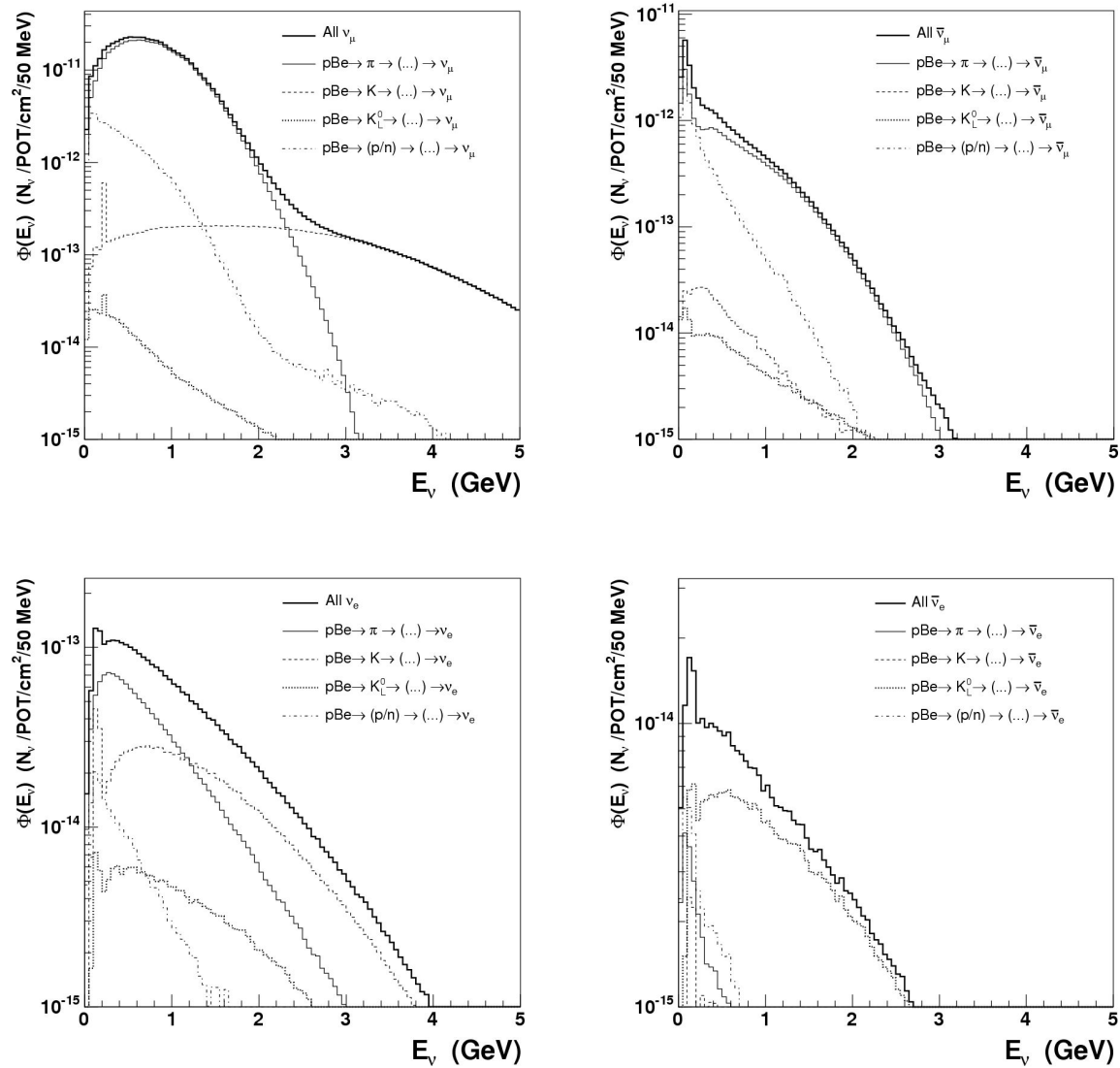
Figure 7.6: Neutrino flux predictions for neutrino mode for each of the four flavors broken into components based on the chain of hadronic processes which produced the neutrino. The four panels are ν_μ (top left), $\overline{\nu}_\mu$ (top right), ν_e (bottom left) and $\overline{\nu}_e$ (bottom right).
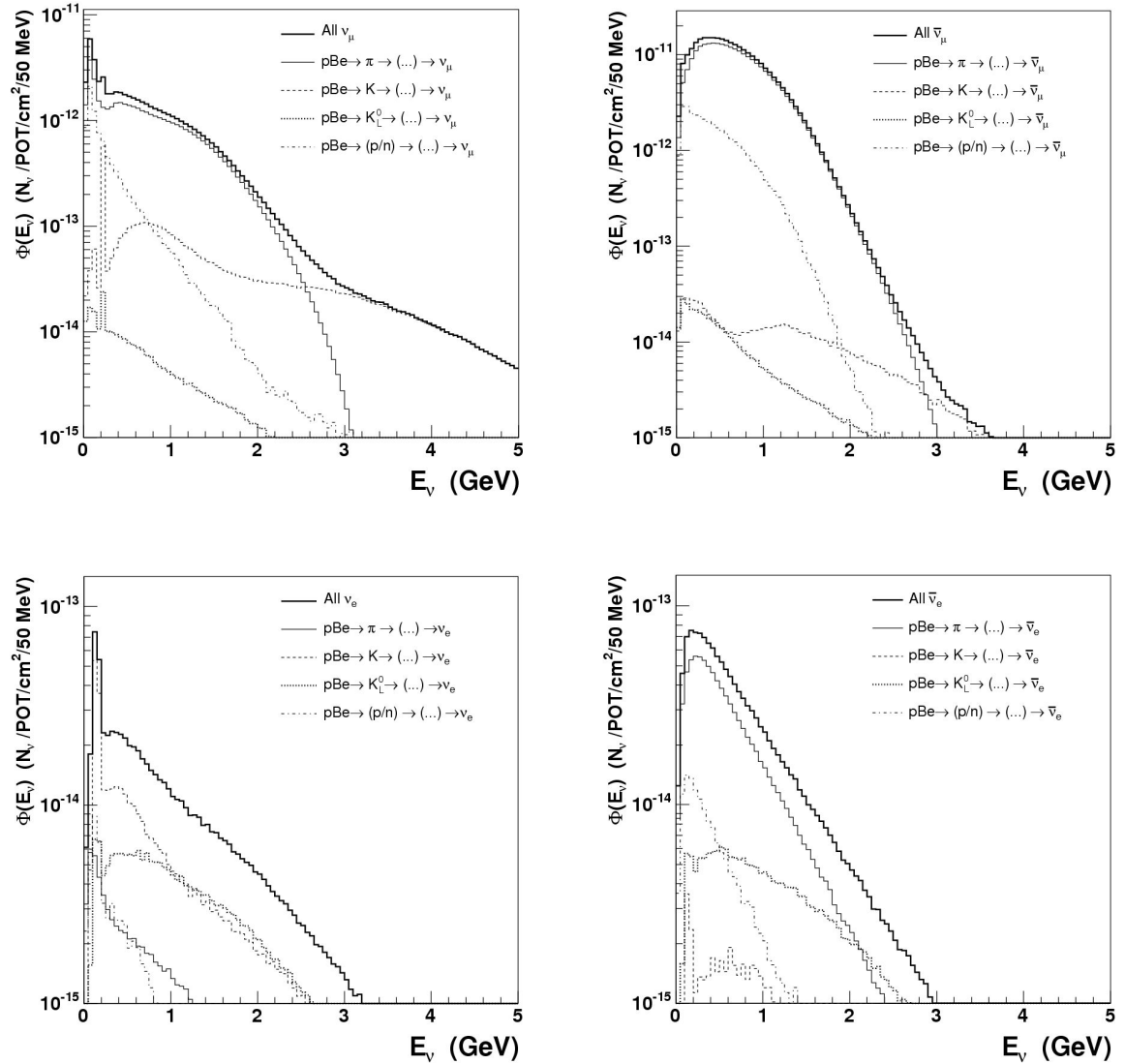
Figure 7.7: Neutrino flux predictions for antineutrino mode for each of the four flavors broken into components based on the chain of hadronic processes which produced the neutrino. The four panels are ν_μ (top left), $\overline{\nu}_\mu$ (top right), ν_e (bottom left) and $\overline{\nu}_e$ (bottom right).

Neutrino flavor		Process	Contribution	
ν mode	$\bar{\nu}$ mode		ν mode	$\bar{\nu}$ mode
ν_μ (93.5%)	ν_μ (15.7%)	p+Be $\to \pi^\pm \to (\dots) \to \nu_\mu$	89.5 %	75.5 %
		p+Be $\to K^\pm \to (\dots) \to \nu_\mu$	2.8%	7.4 %
		p+Be $\to K_L^0 \to (\dots) \to \nu_\mu$	<0.1 %	<0.5 %
		p+Be $\to$ p/n$\to (\dots) \to \nu_\mu$	7.7 %	16.4 %
ν_e (0.5%)	ν_e (0.2%)	p+Be $\to \pi^\pm \to (\dots) \to \nu_e$	48.8 %	11.2 %
		p+Be $\to K^\pm \to (\dots) \to \nu_e$	36.8 %	49.9 %
		p+Be $\to K_L^0 \to (\dots) \to \nu_e$	7.0 %	29.6 %
		p+Be $\to$ p/n$\to (\dots) \to \nu_e$	7.4 %	9.2 %
$\bar{\nu}_\mu$ (5.9%)	$\bar{\nu}_\mu$ (83.7%)	p+Be $\to \pi^\pm \to (\dots) \to \bar{\nu}_\mu$	66.5 %	87.4 %
		p+Be $\to K^\pm \to (\dots) \to \bar{\nu}_\mu$	1.3 %	0.2 %
		p+Be $\to K_L^0 \to (\dots) \to \bar{\nu}_\mu$	0.7 %	0.1 %
		p+Be $\to$ p/n$\to (\dots) \to \bar{\nu}_\mu$	31.0 %	12.1 %
		p+Be $\to$ other $\to (\dots) \to \bar{\nu}_\mu$	0.5 %	0.0 %
$\bar{\nu}_e$ (0.1%)	$\bar{\nu}_e$ (0.4%)	p+Be $\to \pi^\pm \to (\dots) \to \bar{\nu}_e$	12.9 %	68.8 %
		p+Be $\to K^\pm \to (\dots) \to \bar{\nu}_e$	6.3 %	3.4 %
		p+Be $\to K_L^0 \to (\dots) \to \bar{\nu}_e$	65.2 %	15.6 %
		p+Be $\to$ p/n$\to (\dots) \to \bar{\nu}_e$	15.4 %	12.2 %
		p+Be $\to$ other $\to (\dots) \to \bar{\nu}_e$	0.2 %	0.1 %

Table 7.3: Neutrino flux prediction broken down by neutrino type and hadronic process for neutrino and antineutrino running modes. The first two columns give the fraction of each neutrino type which make up the total flux and, therefore, each column adds to 100%. The last two columns give the fraction of that neutrino type which came from the listed chain of hadronic processes, so each block should add to $\sim$ 100%.

tions of each process represented in the figures integrated over all neutrino energies.

7.2 Neutrino cross-section model

MiniBooNE makes use of the NUANCE [128] neutrino event generator code to simulate neutrino interactions and nuclear effects in the detector volume. NUANCE is a comprehensive neutrino cross-section simulator which models virtually all relevant processes over a broad energy range from $E_\nu \sim 100\,\text{MeV} - 1\,\text{TeV}$. Ninety-nine exclusive reactions are modeled separately and the total cross-section is determined by summing the contribution from each. As discussed in Section 6.2, the most important of these for the MiniBooNE oscillation search are charged-current quasi-elastic scattering (CCQE), neutral-current (NC) π^0 production, and the NC production of resonances which decay radiatively, $\nu N \to \Delta^{0,+} \to N\gamma$.

Figures 7.8 and 7.9 give an idea of the current knowledge of these cross-sections. Figure 7.8 compares the NUANCE predictions for several charged-current cross-sections to available measurements of the CCQE, CC single pion, deep inelastic scattering, and inclusive CC interactions. Many data sets are available to constrain the models, but become noticeably more sparse in the relevant region below 1 GeV. Comparing the models, the CCQE interaction clearly becomes the dominant reaction below 1 GeV.

Figure 7.9 exhibits the relative lack of knowledge about NC π^0 production. The left panel compares the NUANCE prediction for resonant production to two available data points, both in the multi-GeV region. The right panel compares four different models to two data points for coherent π^0 production and demonstrates wide disagreement among theories. Note the scale of the right panel is two orders of magnitude smaller than the left. Also, the coherent measurements are reported per carbon atom since it is a coherent effect, while the resonant cross-sections are per nucleon.

MiniBooNE, which has collected the largest neutrino data set in the world at 1 GeV, is well positioned to make many relevant and interesting contributions to the physics of both charged-current and neutral-current interactions. For the purpose of the oscillation analysis, however, we specifically require the following:
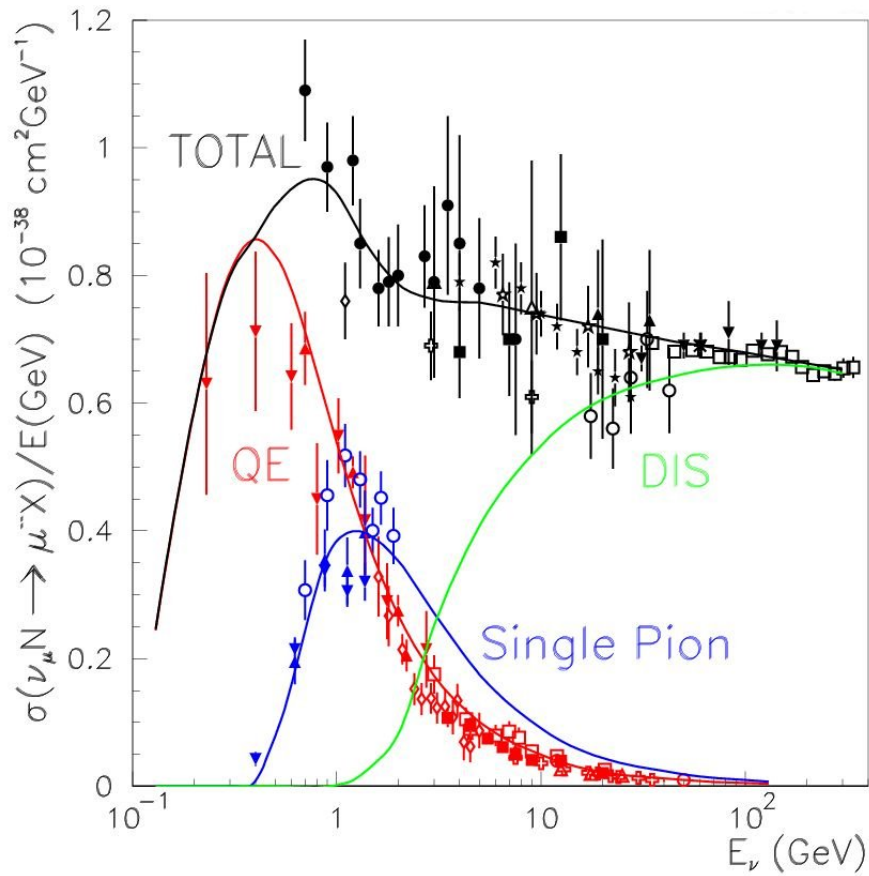
Figure 7.8: Contributing charged-current neutrino cross-sections vs. energy in the range $E_\nu \sim 100\,\mathrm{MeV} - 400\,\mathrm{GeV}$. The total cross-section (black), charged-current quasi-elastic (red), single pion production (blue) and deep-inelastic scattering (green) cross-sections are shown. Plot from G.P. Zeller [].
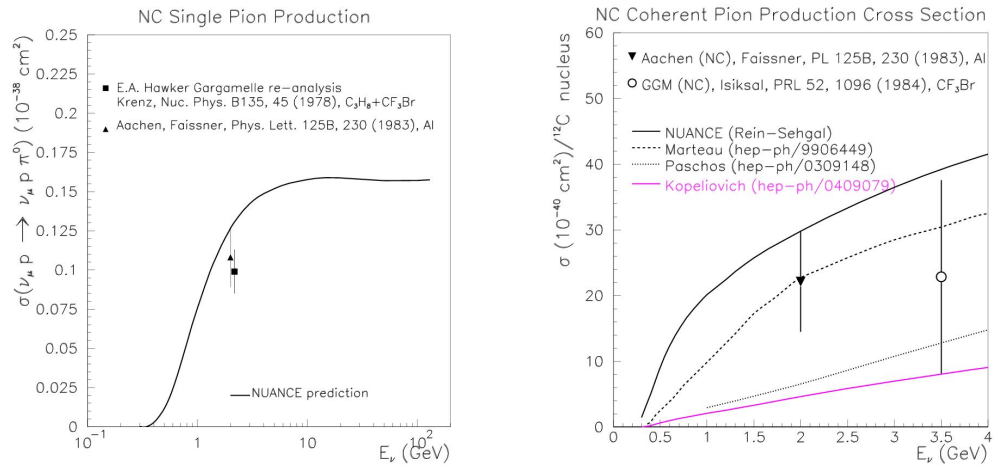
Figure 7.9: Neutral-current single pion production cross-sections vs. neutrino energy. The left panel shows the NUANCE prediction for NC resonant pion production off a bare proton target. Only two data points are available for comparison. The right panel compares four models of coherent π^0 production off carbon to the two available measurements of coherent production.

- A charged-current quasi-elastic model which accurately reproduces the data. CCQE events are used to form the energy distribution where we will search for oscillations. The cross-section shape as a function of energy and momentum transfer, Q^2, must be well understood. The rate can be further complicated by nuclear effects due to the target neutrons residing in carbon. As described in Section 7.2.1, the high statistics sample of ν_μ CCQE events will be used to extensively study the CCQE interaction and make corrections to the model as implemented in NUANCE.

- An absolute prediction of the rate of π^0 and $\Delta \to N\gamma$ events in MiniBooNE. The underlying physics model is much less relevant for neutral-current events. Instead we require a "dead-reckoning" of the rate at which π^0's and γ's are produced in the tank. The probability that a π^0 is misidentified as an electron depends directly on the kinematics of the photons created in its decay which in turn depends on the momentum of the decaying π^0. It is important, therefore, to study π^0 production as a function of momentum. This is described in Section 7.2.2.

7.2.1   The charged-current quasi-elastic scattering model

The overall basis for the CCQE cross-section model in NUANCE is the formalism of Llewellyn Smith [116] in which the differential cross-section on a bare nucleon is given by [115]

$$\frac{d\sigma}{dQ^2} = \frac{G_F^2 M}{8\pi E_\nu^2}\left[A \mp \frac{(s-u)}{M^2}B + \frac{(s-u)^2}{M^4}C\right] \tag{7.4}$$

where $(+)-$ refers to (anti)neutrino scattering, Q^2 is the squared 4-momentum transfer, G_F is the Fermi constant, M is the nucleon mass, E_ν is the incident neutrino energy, and $(s-u) = 4ME_\nu - Q^2 - m_\ell^2$ with m_ℓ the mass of the charged lepton produced in the interaction. The Q^2 dependence is explicit in the three parameters, A, B and C

$$A = \frac{(m_\ell^2 + Q^2)}{M^2}\left[(1+\tau)F_A^2 - (1-\tau)F_1^2 + \tau(1-\tau)F_2^2 + 4\tau F_1 F_2 - m_\ell^2\right.$$
$$\left. - \frac{m_\ell^2}{4M^2}\left[(F_1 + F_2)^2 + (F_A + 2F_P)^2 - 4(1+\tau)F_P^2\right]\right] \tag{7.5}$$

$$B = \frac{Q^2}{M^2}F_A(F_1 + F_2) \tag{7.6}$$

$$C = \frac{1}{4}(F_A^2 + F_1^2 + \tau F_2^2) \tag{7.7}$$

where $\tau = Q^2/4M$. The two vector form factors, F_1 and F_2, are given by

$$F_1 = \frac{1 + \tau(1 + \mu_p - \mu_n)}{(1+\tau)(1+Q^2/m_V^2)^2}, \qquad F_2 = \frac{(\mu_p - \mu_n)}{(1+\tau)(1+Q^2/m_V^2)^2} \tag{7.8}$$

the axial vector form factor is

$$F_A = \frac{g_A}{\left(1 + \frac{Q^2}{m_A^2}\right)^2} \tag{7.9}$$

and the pseudo-scalar form factor is

$$F_P = \frac{2M^2}{m_\pi^2 + Q^2}F_A \tag{7.10}$$

where m_π is the pion mass, μ_p and μ_n are the proton and neutron anomalous magnetic moments and m_V, g_A and m_A are empirical parameters. High statistics electron scattering
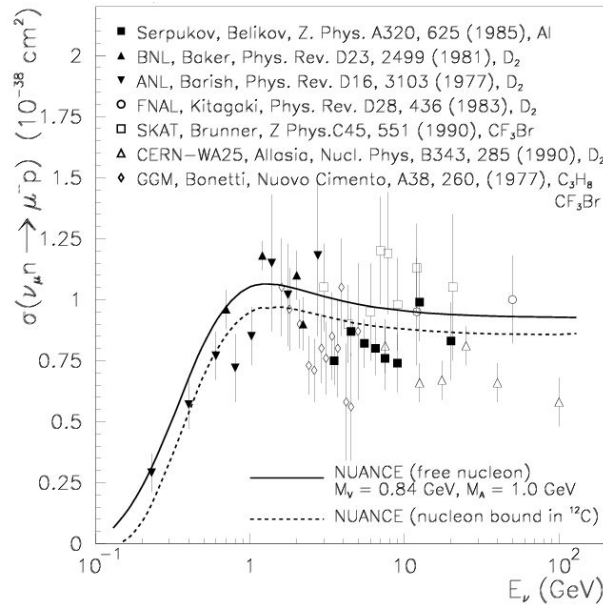
Figure 7.10: Existing ν_μ CCQE cross-section measurements (not MiniBooNE) on a variety of targets vs. E_ν compared to the Llewellyn Smith [116] prediction from NUANCE with $m_V = 0.84\,\mathrm{GeV}$, $m_A = 1.0\,\mathrm{GeV}$ and $g_A = $ -1.26 (solid). Also shown is the cross-section prediction on carbon from the Smith-Moniz RFG model described in the text (dashed).

data is used to inform our choice for the Q^2 dependence of the vector form factors, F_1 and F_2. Historically, the value of the vector mass parameter is taken to be $m_V = 0.84\,\mathrm{GeV}$. In our simulation, however, empirical fits from [119] are used to determine F_1 and F_2. The axial coupling parameter, $g_A = $ -1.267, is well determined from neutron beta decay experiments [135]. m_A must be determined from neutrino scattering data and the weighted average from available measurements is $m_A = 1.03\,\mathrm{GeV}$ [117]. Figure 7.10 compares this model using the parameter values given to existing CCQE cross-section measurements. The agreement is good, but the experimental uncertainties are large.

While Eq. 7.4 describes the cross-section on a bare nucleon target, the MiniBooNE target is $^{12}\mathrm{C}$ and hence nuclear corrections must be made. To model scattering off bound nucleons, NUANCE uses the Smith-Moniz relativistic Fermi gas (RFG) model [118]. The model assumes a flat nucleon momentum distribution out to some maximum value, the Fermi momentum, p_F ($p_F = 220\,\mathrm{MeV}/c$ for carbon [67]) with a binding energy $\mathrm{E_B} = $

34 MeV. In the RFG model, "Pauli-blocking" causes a suppression in the cross-section for low values of the momentum transfer, Q^2. This arises because, as fermions, the struck nucleon is forbidden from entering a state already occupied by one of the spectator nucleons in the interaction. The dashed curve in Figure 7.10 shows the CCQE cross-section prediction on neutrons bound in carbon using this model.

The cross-section formalism presented applies both to ν_e and ν_μ interactions with the appropriate change in m_ℓ. This allows us to use the high statistics observed ν_μ CCQE event sample to finely tune the cross-section model to accurately reproduce quasi-elastic interactions in the MiniBooNE detector. Figure 7.11 shows a comparison of the NUANCE prediction of the quasi-elastic event rate as a function of Q^2 (dashed) compared to the ν_μ CCQE data sample at MiniBooNE (points). The data and Monte Carlo have been relatively normalized and, therefore, illustrate the discrepancy in the *shape* of the Q^2 dependence of the cross-section between data and the model.

It was found that the adjustment of two parameters in the model greatly improved agreement with the data. First, the value of the axial mass parameter, m_A, has a significant effect on the distribution at high Q^2, so adjusting its value may improve the disagreement seen at $Q^2 > 0.2\,\mathrm{GeV}^2$. The low Q^2 region, recall, is strongly affected by the Pauli-blocking phenomenon mentioned above. The addition of a parameter, κ, as described in [67], provides control over the amount of Pauli-blocking in the model and thus has particularly strong effects in the low Q^2 region. The values of these parameters, m_A and κ, were determined in a fit to MiniBooNE ν_μ CCQE data with the result $m_A = 1.23 \pm 0.20$ and $\kappa = 1.019 \pm 0.011$ [67]. Using these effective parameter values, the predicted ν_μ CCQE distribution is shown in Figure 7.11 by the solid line with systematic errors given by the gray band. The agreement with data is excellent.

This tuning of these parameters accounts for any inadequacies in our axial form factor assumptions and the RFG-based nuclear model. Also, since these new parameter values result from relatively normalized fits to the MiniBooNE ν_μ CCQE data, they do not adjust for any observed normalization differences between data and the prediction[3].

Finally, as mentioned several times, charged-current quasi-elastic scattering is impor-

---

[3]The combined effect of the m_A, κ change is a 5.6% changed in the total predicted rate of CCQE events.
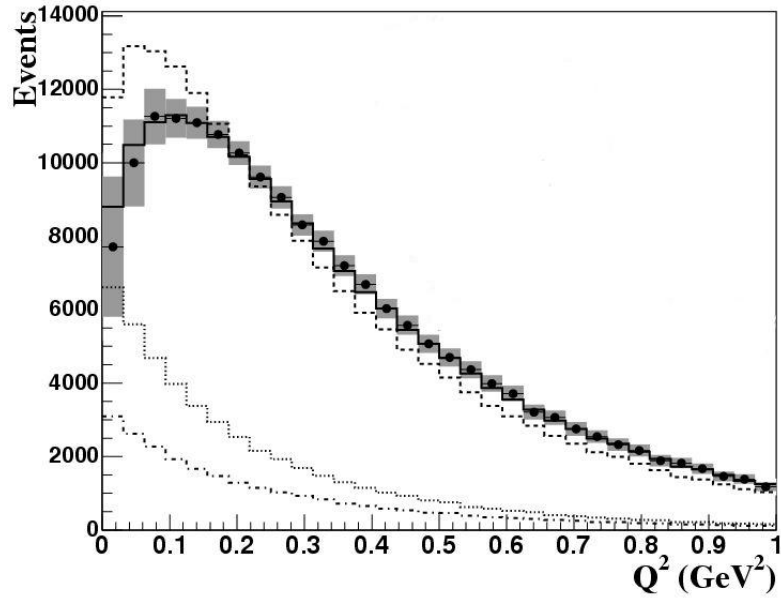
Figure 7.11: MiniBooNE ν_μ CCQE data (points) compared to the default NUANCE model with $m_A = 1.03$ GeV and $\kappa = 1.0$ (dotted) and to the fitted result with $m_A = 1.23$ GeV and $\kappa = 1.019$ (solid). The Monte Carlo curves have been relatively normalized to the data. Plot taken from [67].

tant to oscillation experiments because it allows the determination of the neutrino's energy from the reconstructed kinematics of the outgoing charged lepton[4]:

$$E_{\nu_\ell}^{\mathrm{QE}} = \frac{2(\mathrm{M_n} - \mathrm{E_B})E_\ell - (\mathrm{E_B^2} - 2\mathrm{M_n E_B} + m_\ell^2 + \Delta\mathrm{M}^2)}{2[(\mathrm{M_n} - \mathrm{E_B}) - E_\ell + p_\ell \cos\theta_\ell]} \tag{7.11}$$

where $\mathrm{M_n} = 938.7$ MeV is the neutron mass, $\mathrm{E_B} = 34$ MeV is the binding energy in carbon [67], m_ℓ is the lepton mass, $\Delta\mathrm{M}^2 = \mathrm{M_n^2} - \mathrm{M_p^2}$, and E_ℓ, p_ℓ and θ_ℓ are the reconstructed energy, momentum and scattering angle of the final state lepton, respectively.

7.2.2 NC π^0 and single γ production

The largest ν_μ-induced background in the $\nu_\mu \rightarrow \nu_e$ oscillation search is the neutral-current production of π^0's. Most (>90%) π^0 events can be identified by the presence of two Cherenkov rings created by the electromagnetic showers initiated by the photons in

---

[4]This is true if one ignores the Fermi motion of the target neutron (maximum $p_F = 220$ MeV/c). A calibration has been performed to account for this simplification and is detailed in Appendix A of [97]
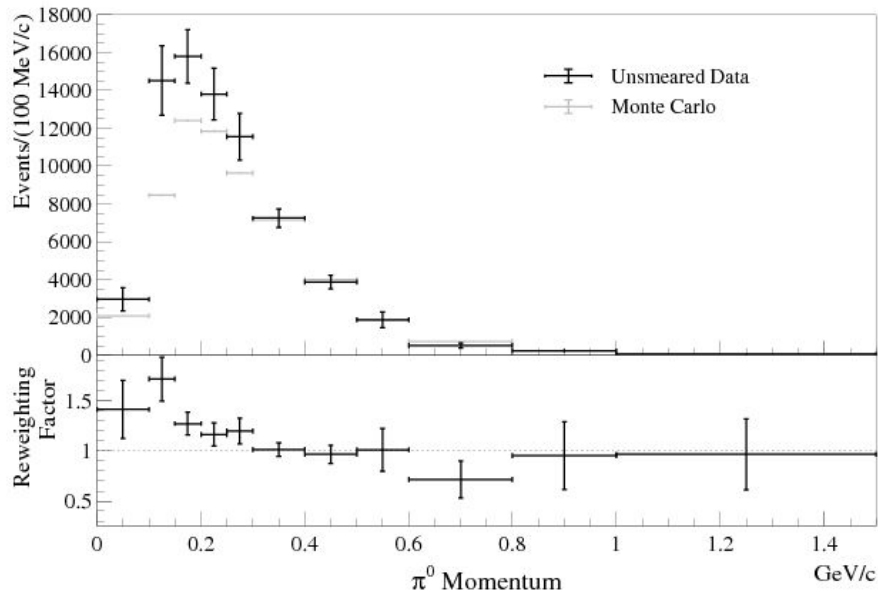
Figure 7.12: Absolutely normalized π^0 momentum distributions for data (dark points) and the default Monte Carlo (light points). The ratio $N^{\mathrm{data}}/N^{\mathrm{mc}}$ is shown below. Plot taken from [68].

$\pi^0 \to \gamma\gamma$ decay. However, a background to the ν_e appearance search arises when either of the photons is not reconstructed. This is most common in asymmetric decays with one very low energy photon or when one photon exits out the side of the detector.

The NUANCE model of NC π^0 production is based on the formalism of Rein and Sehgal [120] and includes both resonant and coherent π^0 production processes. In resonant production, the pion is produced in the decay of an excited nucleon state such as the $\Delta(1232)$. In the case of coherent scattering, the neutrino interacts with the nucleus as a whole leaving it in the ground state. The absolute rate of π^0 production in the detector is further complicated by nuclear effects as pions propagate in a carbon nucleus. A π^0 can be absorbed, change its identity through charge exchange, or have its kinematics altered, all effects with a strong dependence on the pion momentum. Given the large inherent uncertainties in the production of Δ resonances in CH_2 and the coherent π^0 production cross-section, as well as in pion propagation through the nucleus, we opt to measure the overall rate of π^0 production from MiniBooNE data and use it to constrain the Monte

Carlo prediction [68].

First, a very pure (97%) sample of 28,000 NC π^0 events is selected and the Monte Carlo is used to make corrections for efficiency and momentum smearing. Figure 7.12 compares the total number of events as a function of π^0 momentum for data and the default Monte Carlo. The Monte Carlo prediction differs from the data both in shape and overall normalization. A correction, N^{data}/N^{MC}, is shown at the bottom of Figure 7.12 which can then be used to reweight the π^0 true momentum distribution in the Monte Carlo, thereby correcting for any inadequacies in our π^0 production model as a function of π^0 momentum.

Figure 7.13 shows the reconstructed invariant mass distributions for π^0 candidate events in bins of π^0 momentum. The data with statistical errors are shown as black points. The default NUANCE Monte Carlo prediction is shown by the black dashed histogram. The corrected Monte Carlo with systematic errors is shown by the red boxes in Figure 7.13 and shows good agreement with the data.

Figure 7.14 compares other important kinematic quantities in the data and simulation both before and after applying the π^0 momentum-based correction to the Monte Carlo prediction. Panels a), b) and c) show the recontructed opening angle and energies of the two photons produced in the π^0 decay. These distributions are critical in determining the rate of mis-identification of NC π^0 events as CC ν_e events. The clear improvement in the photon kinematic distributions shows that the data-MC differences can largely be attributed to the disagreement seen in the π^0 rate as a function of momentum.

It is important to note that the described method measures the absolute rate of π^0's in the MiniBooNE data and adjusts the Monte Carlo to reproduce it. The effects of neutrino flux, π^0 resonant and coherent production cross-sections, as well as absorption, charge exchange and scattering in the nucleus are all folded together. Internally, we refer to any event where a π^0 escapes the nucleus and decays in the detector as an "effective π^0" event. What is important for the ν_e appearance search is the absolute rate for effective π^0 events as a function of π^0 momentum, and it is this rate that we have directly constrained with this procedure. The uncertainty on the absolute rate of effective π^0 events is reduced from $\sim 25\%$ using the Monte Carlo prediction to 5% [68]. The dominant uncertainty on the π^0-
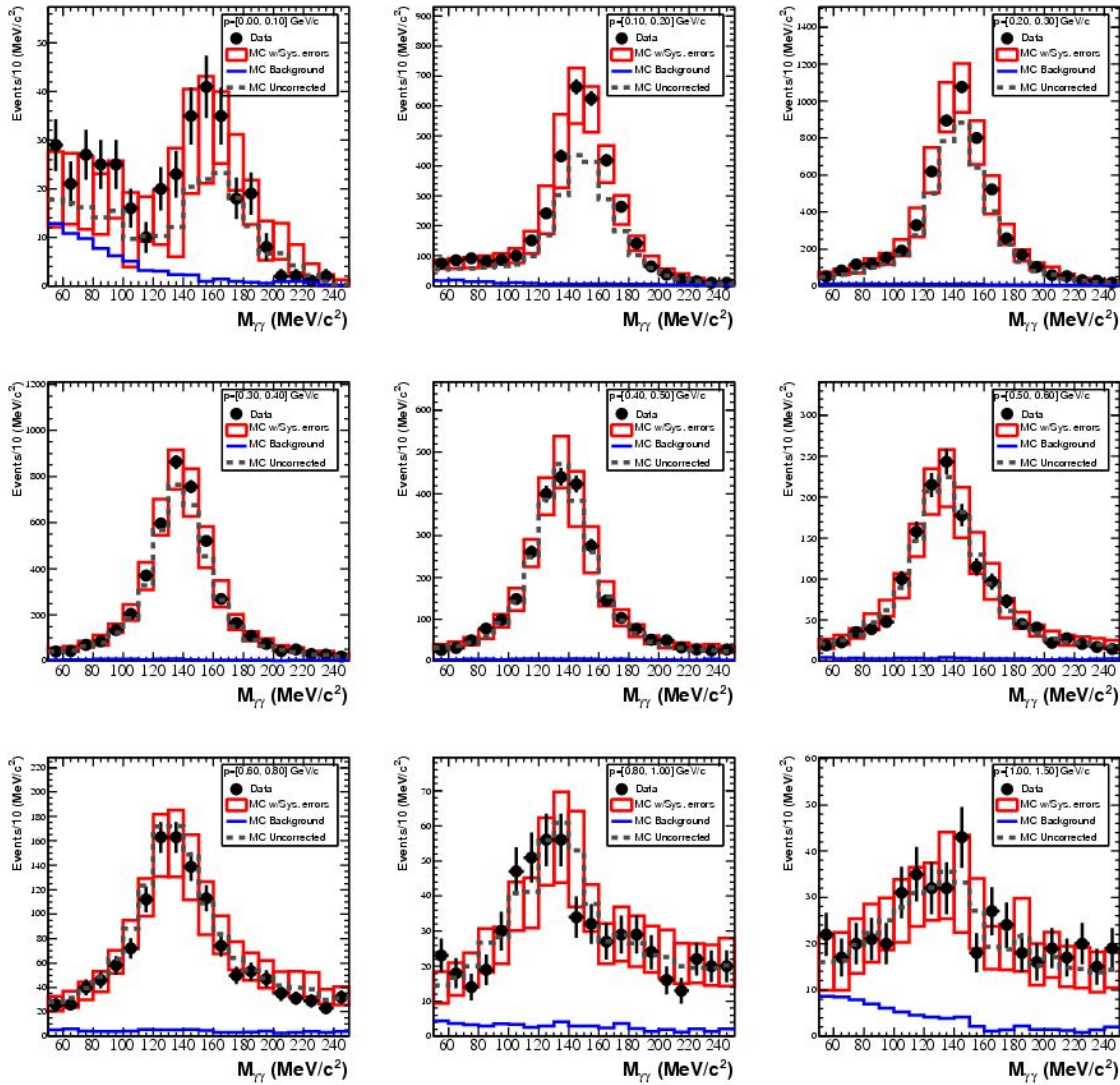
Figure 7.13: Reconstructed invariant mass distributions for NC π^0 candidate events in bins of π^0 momentum. The data are shown by the black points with statistical errors. The default NUANCE prediction is the black dashed histogram and the corrected Monte Carlo with systematic errors is shown by the red boxes. The data and Monte Carlo have been absolutely normalized.

induced background prediction will, therefore, come from the uncertainty of the rejection power of the particle identification algorithm.

Radiative Δ decay Using only the shapes of the pion kinematic distributions, the analysis described above was able to extract the fractions of π^0's which are produced through resonant production and through coherent production. The result is that 80.5% are produced through a resonance [68]. A related background arises from the radiative decay of baryonic resonances, $\Delta \rightarrow N\gamma$. Single photon events cannot be isolated in MiniBooNE data, but these decays (BR = 0.56%) have the same source (baryonic resonances) as 80% of the NC π^0 background that we have constrained with data. Therefore, the radiative Δ event rate predicted by NUANCE is scaled by the same correction factor (see Figure 7.12) as the NC π^0 sample.

7.3 MiniBooNE detector simulation

Final state particles emerging from the target nucleus in the NUANCE event generator are next passed to a Geant3 [129] simulation of the MiniBooNE detector which propagates them through the oil. Photons are generated through Cherenkov radiation and scintillation and propagated until they are absorbed or hit a PMT photocathode where they may produce a photoelectron. The PMT and DAQ electronics are simulated separately.

Similar to the Geant4-based BNB Monte Carlo, some custom additions to the base Geant3 simulation have been made. In particular two decays, $\pi^0 \rightarrow \gamma e^+ e^-$ and $\mu \rightarrow e\nu\bar{\nu}$, are controlled by a dedicated routine using matrix elements. Also, 8% of μ^- in the detector will capture on carbon before they can decay. Geant3 simply removes the muon, so a model to simulate the possible low energy final state neutrons and photons was developed [82]. Rarely, however, are these final state particles above detection threshold.

The default Geant3 hadronic model, GFLUKA [131], has been replaced by the GCALOR [130] package which better models pion absorptions and charge exchange processes. The two codes can be interchanged for performing systematics studies.

Finally, a sophisticated model of the propagation of photons through the oil has been
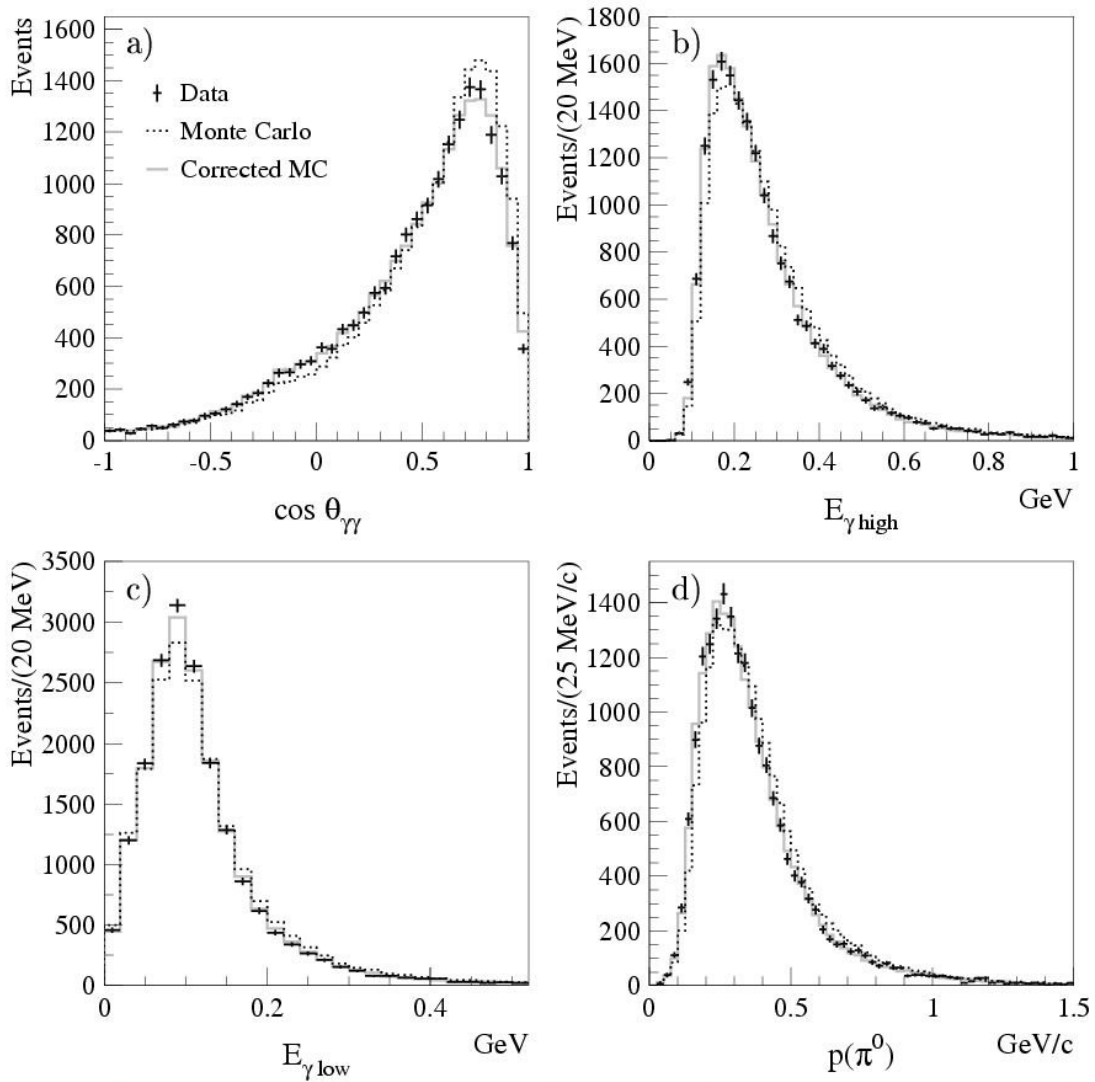
Figure 7.14: Relatively normalized π^0 event kinematic distributions: a) the opening angle between the two photons from the π^0 decay, b) energy of the more energetic photon, c) energy of the less energetic photon, and d) the π^0 momentum. The data are shown by the black points with statistical errors. The default NUANCE prediction is the black dashed histogram and the prediction after applying the momentum-based correction of Figure 7.12 is shown by the solid histogram. Plot taken from [68].

Property	# par.	Property	# par.
Cherenkov scale factor	1	index of refraction	3
fluor scintillation yield	4	extinction length	5
fluor fluorescence yield	4	scattering	3
fluor UV fluorescence yield	4	reflections	2
fluor time constant	4	PMT angular efficiency	2
Birks' law coefficients	2	old/new PMT relative efficiency	1

Table 7.4: Number of parameters used to model various aspects of the custom built model of the optical properties of the Marcol 7 oil and the PMTs used in the MiniBooNE detector. There are 35 total parameters.

developed. This model contains 35 adjustable parameters which have been tuned using a combination of external measurements and calibration data. Table 7.4 lists the various components of the detector optical model and the number of parameters associated with each.

Here we provide a very broad overview of the detector simulation highlighting only the components needed for understanding neutrino event reconstruction and identification. A detailed account of the detector simulation and a description of the tuning of the 35 optical model parameters is available in [96].

7.3.1   Cherenkov radiation

Charged particles traveling through a material medium with index of refraction $n(\omega)$ faster than the speed of light in that material, $c/n(\omega)$, will emit a coherent wavefront of electromagnetic radiation known as Cherenkov radiation [133]. The photons are emitted at a characteristic angle relative to the particle's path, θ_{C}, given by

$$\cos \theta_{\mathrm{C}} = \frac{1}{\beta \cdot n(\omega)} \tag{7.12}$$

λ_D	589.3 nm
T_0	20.0 °C
n_D	1.4684 ± 0.0002
B	(4240 ± 157) nm^2
β	$(3.66 \pm 0.04) \times 10^4$ (°C)$^{-1}$

Table 7.5: Parameter values in index of refraction model for Marcol 7 oil Eq. 7.14.

where $\beta \equiv v/c = p/E$ is the velocity of the particle. The number of photons generated per unit wavelength, $\lambda = 2\pi c/\omega$, per unit length, x, is [134]

$$\frac{d^2 \mathrm{N_{Ch}}}{d\lambda dx} = \frac{2\pi\alpha}{\lambda^2} \left(1 - \frac{1}{\beta^2 n^2(\lambda)}\right) \tag{7.13}$$

where α is the fine structure constant. An overall scale factor is used in the simulation and calibration samples prefer a value of $f_{\mathrm{Ch}} = 1.106$ - the first detector optical model parameter.

A careful measurement of the wavelength and temperature dependence of the index of refraction in Marcol 7 oil was made by H.O. Meyer in [80]. The measurements are well described by

$$n(\lambda, \mathrm{T}) = \left[n_D + \mathrm{B}\left(\frac{1}{\lambda^2} - \frac{1}{\lambda_D^2}\right)\right] \cdot [1 - \beta(\mathrm{T} - \mathrm{T_0})] \tag{7.14}$$

with the wavelength in nanometers, the temperature in degrees Celsius and the parameter values given in Table 7.5. These are 3 more of the 35 parameters of the detector optical model.

7.3.2 Scintillation and fluorescence

Ionizing particles traversing the MiniBooNE detector oil produce excitations of organic molecules which emit isotropic light upon de-excitation known as scintillation. When the excitation is produced by photons the emitted radiation is known as fluorescence. In either case, the emission is delayed according to the time constant of the particular fluorophore producing the radiation, typically 10's of nanoseconds. Four fluorophores

were detected in the MiniBooNE oil [89] and their individual time constants represent 4 more parameters of the optical model. Their scintillation, fluorescence and UV fluorescence[5] photon yields are 12 more. However, data rich in scintillation light (NC elastic scattering events) used to calibrate the model prefer the use of a single fluorophore with a time constant τ = 34 ns. The other three are used to assess systematic errors. The number of scintillation photons produced per unit deposited energy is simulated according to

$$\frac{dN_{Sci}}{dE} = \frac{31.64 \text{ MeV}^{-1}}{1 + B_1 \left(\frac{1}{\rho_{oil}} \frac{dE}{dx} \right) + B_2 \left(\frac{1}{\rho_{oil}} \frac{dE}{dx} \right)^2} \tag{7.15}$$

with $B_1 = 0.014 \text{ g}/(\text{MeV} \cdot \text{cm}^2)$ and $B_2 = 0.0 \text{ g}^2/(\text{MeV}^2 \cdot \text{cm}^4)$. B_2 is included only for the purposes of assessing systematic errors. This is known as Birks' Law and constitutes 2 of the 35 parameters of the detector optical model.

7.3.3   Photon propagation and detection

Photon propagation, including absorption, scattering and reflection, is described by 10 more parameters of the detector optical model. Both Rayleigh scattering and Raman scattering are considered with the latter contributing about 5% of the total effect. The amount of reflection from the tank walls in both the main tank and veto regions can also be controlled in the simulation. Figure 7.15 shows the rates for several of these processes as a function of wavelength. The level of absorption is determined by the difference between the measured total extinction and the other processes including scattering and fluorescence.

Figure 7.16 clearly demonstrates the importance of the reflection and scattering models. The figures show the PMT hit time distribution for a set of calibration laser triggers. The data are compared to the full simulation as well as a simulation with no reflection and no reflection or scattering.

The final 3 parameters of the detector optical model deal with the detection efficiency of the photomultipliers. Figure 7.17 shows the quantum efficiency (QE) in oil for the 322 new R5912 tubes as a function of the incident photon wavelength. The efficiency peaks at

---

[5]UV fluorescence refers to photons below 250 nm which are not propagated in the simulation fluorescing photons at higher wavelengths ($\lambda \geq 250$ nm) which could be seen by the PMTs
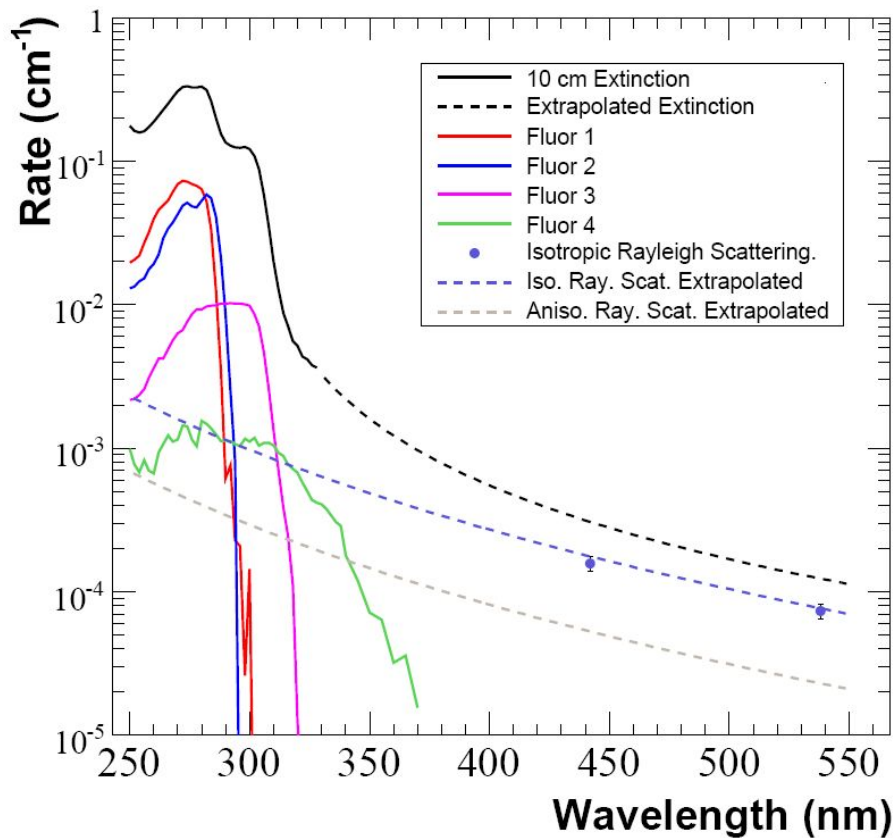
Figure 7.15: Optical photon extinction rates in the Marcol 7 oil used in MiniBooNE. Extinction refers to any process altering the path of the photon. The total extinction was measured in a 10 cm cell at FNAL and is shown by the solid black histogram. The extrapolation curve (black dashed) was determined using laser and Michel data. The rates of the four fluorophores mentioned in the text are shown; number 4 is the one preferred by data. Two Rayleigh scattering measurements and an extrapolation are shown. Plot taken from [96].
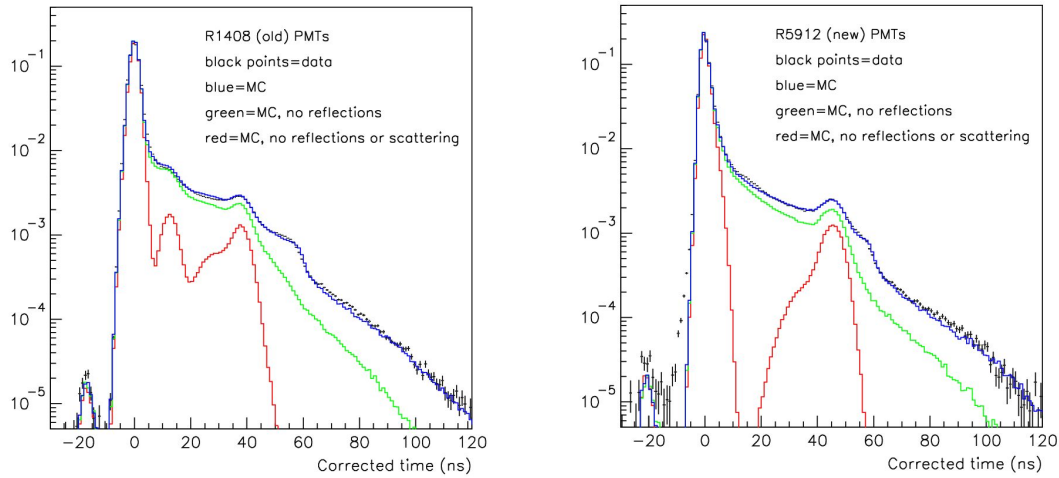
Figure 7.16: PMT hit times in a set of calibration laser triggers (see Section 5.4.4.1). Data are shown by the black crosses with statistical errors only, the total Monte Carlo by the blue histogram. The simulation with no reflections is shown in green. The simulation with no reflections and no scattering (Rayleigh or Raman), leaving only the simulated PMT responses, is shown in red.

about 22% near 400 nm for these tubes. Once a photon is absorbed by a PMT photocathode and produces a photoelectron a careful simulation of the PMT dynode chains and DAQ electronics converts the signal into a charge and time signal which can be used in the reconstruction algorithms. For a description of the electronics simulation see [96].

7.4   Event reconstruction

For each event in the MiniBooNE detector a set of raw charges and times are recorded for each PMT as described in Section 5.4.3 and corrected quantities are calculated using PMT calibration information as in Eq. 5.2. From these charge and time data one must reconstruct the full set of physical parameters (particle positions, directions and energies) describing the event with the goal of identifying different varieties of neutrino interactions.

As indicated in several places above, the neutrino interactions important for the oscillation search will produce electrons, muons, single photons or π^0's (2 photons) in the
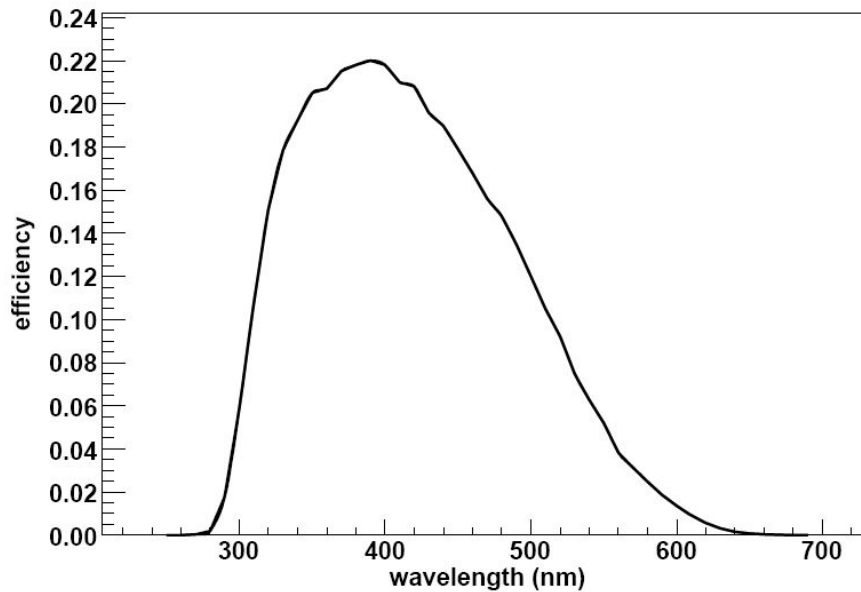
Figure 7.17: Quantum efficiency of the new (R5912) PMTs in oil. Plot taken from [96].

detector. The reconstruction should be robust for these types of events. Further, each event type will produce both Cherenkov and scintillation light and determining the contributions from each should be part of the reconstruction.

Multiple reconstruction algorithms have been developed for the experiment [79, 96] with the latter building from and improving upon the former. Both are based on maximizing the likelihood that a set of measured charges and times correspond to a given event hypothesis. A single track can be described by seven parameters defining its position, time, direction and energy

$$\vec{\alpha} = (x, y, z, t, \theta, \phi, E) \,. \tag{7.16}$$

and the likelihood that a set of measured charges q_i and times t_i correspond to an event defined by $\vec{\alpha}$ is given by

$$\mathcal{L}(\vec{\alpha}) = \prod_{i=1}^{1280} P(q_i|\vec{\alpha}) \cdot P(t_i|\vec{\alpha}) \tag{7.17}$$

where $P(q_i|\vec{\alpha})$ is the probability to measure charge q_i in PMT i for an event with parameters $\vec{\alpha}$, $P(t_i|\vec{\alpha})$ is the same for the measured time, and we have multiplied the probabilities

for all 1280 main tank PMTs.[6] In writing Eq. 7.17 we have assumed that the measurements in each PMT are independent and that the measurements of charge and time in a single PMT are independent. The parameter set is determined by minimizing the negative log of the likelihood function

$$-\log(\mathcal{L}(\vec{\alpha})) = -\sum_{i=1}^{1280} \log(P(q_i|\vec{\alpha})) - \sum_{i=1}^{1280} \log(P(t_i|\vec{\alpha})) \tag{7.18}$$

with respect to $\vec{\alpha}$.

The reconstruction algorithm used in the ν_e event selection described below (Ref. [79], colloquially referred to as the *S-Fitter*) proceeds in a series of steps designed to increase the level of sophistication of the fit at each step and use the results of the previous step as a seed for the current one. Detailed descriptions are available in many places, notably [93] and [97], and will not be reproduced here.

The detailed and accurate construction of the charge and time probability functions $P(q_i|\vec{\alpha})$ and $P(t_i|\vec{\alpha})$ is, of course, the entire game in producing a precise and accurate reconstruction algorithm. These must include effects of the emission spectra of Cherenkov and scintillation light from charged particles in the tank, the absorption and scattering of photons in their propagation toward the PMT surfaces as well as the quantum efficiency and gains of the individual PMTs.

A major advantage of the second reconstruction algorithm mentioned above (Ref. [96], and often referred to as, what else, the *P-Fitter*) is its modeling of subtleties in the photon emission spectra due to extended tracks in the detector. This is particularly important for muons which have path lengths of several meters at the relevant energies. The S-Fitter, in contrast, makes a point-source approximation; Cherenkov and scintillation light in an event are assumed to both be produced from a single point in the tank. The 3-vertex found in the minimization is, therefore, the mean photon emission point and not the neutrino interaction vertex. For events being fit under an electron hypothesis, an energy dependent correction, extracted from Michel electron data, is used to estimate the event vertex with a resolution ~ 30 cm. When fitting for a muon, the central light

---

[6]Both the charge and time likelihoods include the possibility of measuring 0, or no hit above threshold in that channel

source is divided into two equal sources which are moved out symmetrically from the mean emission point until a new minimum of the log likelihood function is found. The reconstructed distance between the two sources is not the full track length, but will be significantly longer for true muons than for electron tracks.

Finally, a word about reconstructing NC $\pi^0 \rightarrow \gamma\gamma$ events. Each photon initiated shower is indistinguishable from an electron. It is the presence of two tracks and their combined energy near the pion mass that identifies them as a NC π^0 event.[7] π^0 candidate events are fit to a 14 parameter model

$$\vec{\alpha}_{\pi^0} = (x, y, z, t, s_1, \theta_1, \phi_1, \rho_1, \Phi_1, s_2, \theta_2, \phi_2, \rho_2, \Phi_2) \tag{7.19}$$

where (x, y, z, t) is the 4-vertex of the π^0, (s_i, θ_i, Φ_i) are the conversion distance and direction of the two photons, and (ρ_i, Φ_i) are the Cherenkov and scintillation strengths of the two EM showers and are proportional to the energy of that photon. From these results the invariant mass can be reconstructed via

$$m_{\pi^0}^2 = 2E_1 E_2 (1 - \cos\theta_{\gamma\gamma}) \tag{7.20}$$

where E_1 and E_2 are the reconstructed energies of the two photons and $\theta_{\gamma\gamma}$ is the angle between the two photon directions. Figure 7.18 shows the reconstructed mass for two ring events with the expected peak near the pion mass.[8]

Due to the large number of parameters, the fitting procedure proceeds in multiple stages where at each step a minimal number of parameters are allowed to float and the others are held fixed. The 0th step is that the event has already been fit to the electron hypothesis as described above and the results are considered a starting point for the more energetic photon. Detailed descriptions of the π^0 fitting algorithm used in this analysis are available in [78] and [93].

One can compare the maximum likelihood values for fits to the electron, muon and pion hypothesis and already have a decent discriminator between event types. The next

---

[7]Note that π^0's can also be created in charged-current (CC) events, $\nu_\mu n \rightarrow \mu^- p \pi^0$, but the presence of the muon makes these events easily separated from ν_e CCQE events.

[8]Figure 7.13 showed the mass distributions used in the effective π^0 constraint analysis, which was performed using the P-Fitter, not the S-Fitter. The measurement as a constraint on the effective π^0 rate in MiniBooNE is, however, universal and still an important part of the oscillation analysis.
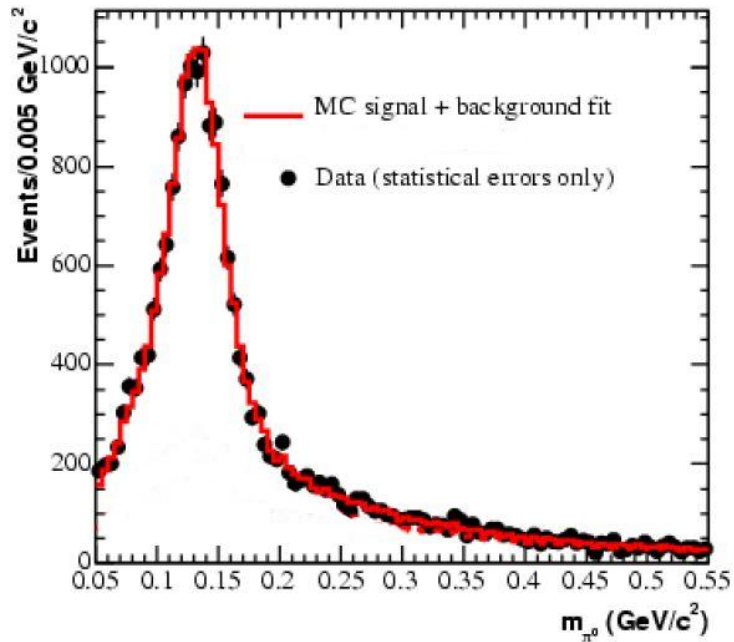
Figure 7.18: Reconstructed π^0 mass using the S-Fitter. Data (black points) is compared to the Monte Carlo (red histogram). Plot taken from [93].

section, however, describes a much more sophisticated and powerful algorithm for the isolation of ν_e (electron) events.

7.5   The BDT ν_e CCQE event selection algorithm

The boosting machine learning algorithm is a process by which many weak classifiers are combined into a single powerful discriminating variable. In the case of MiniBooNE, the boosting technique has been applied to decision trees and is known as the Boosted Decision Tree (BDT) algorithm [90].

The BDT algorithm is trained using Monte Carlo samples of signal (ν_e CCQE events) and single subevent (see section 6.3) backgrounds (including ν_μ CCQE with no Michel electron, NC π^0, $\Delta \rightarrow N\gamma$, etc.). 172 reconstructed variables from the S-Fitter provide the input to the decision trees. We leave a description of the details of the BDT algorithm itself to the many references available [90, 91, 92], but a brief discussion of the nature of the 172
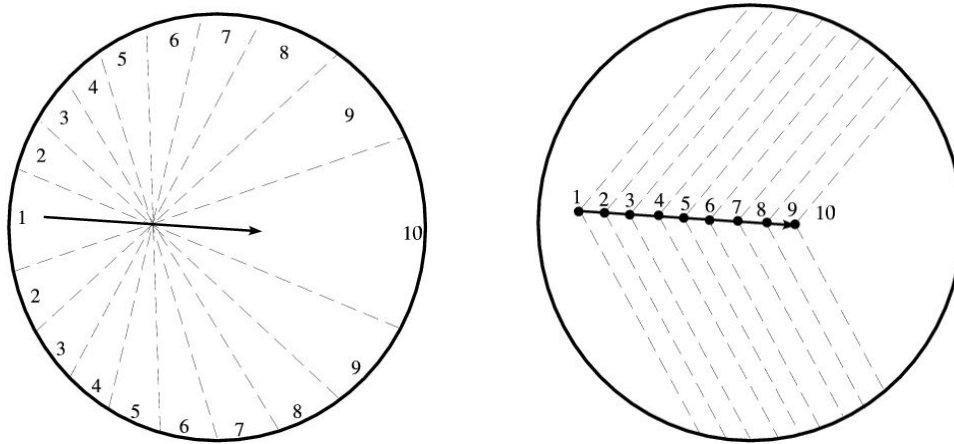
Figure 7.19: Schematic diagrams of the $\cos\theta$ (left) and ring sharpness (right) bin definitions mentioned in the text. Figures taken from [97].

input variables used may prove enlightening.

The 172 variables used were chosen from a pool of near 1000 output variables from the reconstruction. It seems slightly implausible at first that a detector with only 1280 PMT charge and time readouts per event could have such a large number of reconstructed quantities. A large multiplication of basic tank hit information is found, for example, by dividing the tank into 10 equal $\Delta\cos\theta$ bins around the reconstructed track position. In another example, the reconstructed track length is divided into 10 equal segments to form 10 rings with the expected Cherenkov angle from each segment. The ratio of hit to unhit PMTs in each successive sub-ring is a measure of the total ring's sharpness. The $\Delta\cos\theta$ and ring sharpness bins are shown schematically in Figure 7.19. The BDT input variables can be broken into five categories [97]:

- **Physical or geometric observables:** reconstructed quantities like the π^0 mass, track length and angle, radial position of the mean photon emission point, etc.

- **Time related variables:** time likelihood values for the μ, e and π^0 hypotheses for all PMTs or in separate $\cos\theta$ or ring sharpness bins. Also likelihood ratios and products between different $\cos\theta$ and sharpness bins are calculated.

- **Charge related variables:** charge likelihood values for the μ, e and π^0 hypothesis.

Also the ratios of hit to unhit PMTs in $\cos\theta$ and ring sharpness bins as mentioned above.

- **Combinations of charge and time information:** charge likelihoods in corrected time bins, fractions of prompt and delayed PMT hits, etc.

- **Auxiliary variables from minimizations:** minimum negative log likelihood values and ratios from fits to the μ, e and π^0 hypotheses.

Each of the 172 input variables chosen for the algorithm were rigorously checked for data/Monte Carlo agreement using full systematic errors in five different MiniBooNE data samples [88] including:

- ν_μ CCQE (1st subevent - the μ)

- NC π^0 events with reconstructed $m_{\pi^0} > 50\,\mathrm{MeV}/c^2$

- NC elastic scatters

- Michel electron sample (2nd subevent in cosmic μ events)

- 10% of 1 subevent sample (a low statistics signal sample)

Figure 7.20 demonstrates the separation power of the BDT algorithm using these 172 inputs. In all plots ν_e CCQE events (the signal) are compared to important ν_μ-induced backgrounds: ν_μ CCQE events with one subevent, NC π^0 events and radiative Δ decay events. The separation between ν_e and ν_μ CCQE events is very powerful due to the markedly different light patterns produced by electrons and muons in the detector. The separation improves at higher energies. Both NC π^0 and radiative Δ backgrounds increase at low reconstructed energy (note all events have been reconstructed assuming they are a ν_e CCQE event using Eq. 7.11). The separation from radiative Δ events is particularly poor because of the fact that showers initiated by electrons and photons look the same in the detector.

Using this particle identification algorithm, in Chapter 8 we will assess systematic errors and explore optimizations of event selection for performing the $\nu_\mu \to \nu_e$ oscillation search.
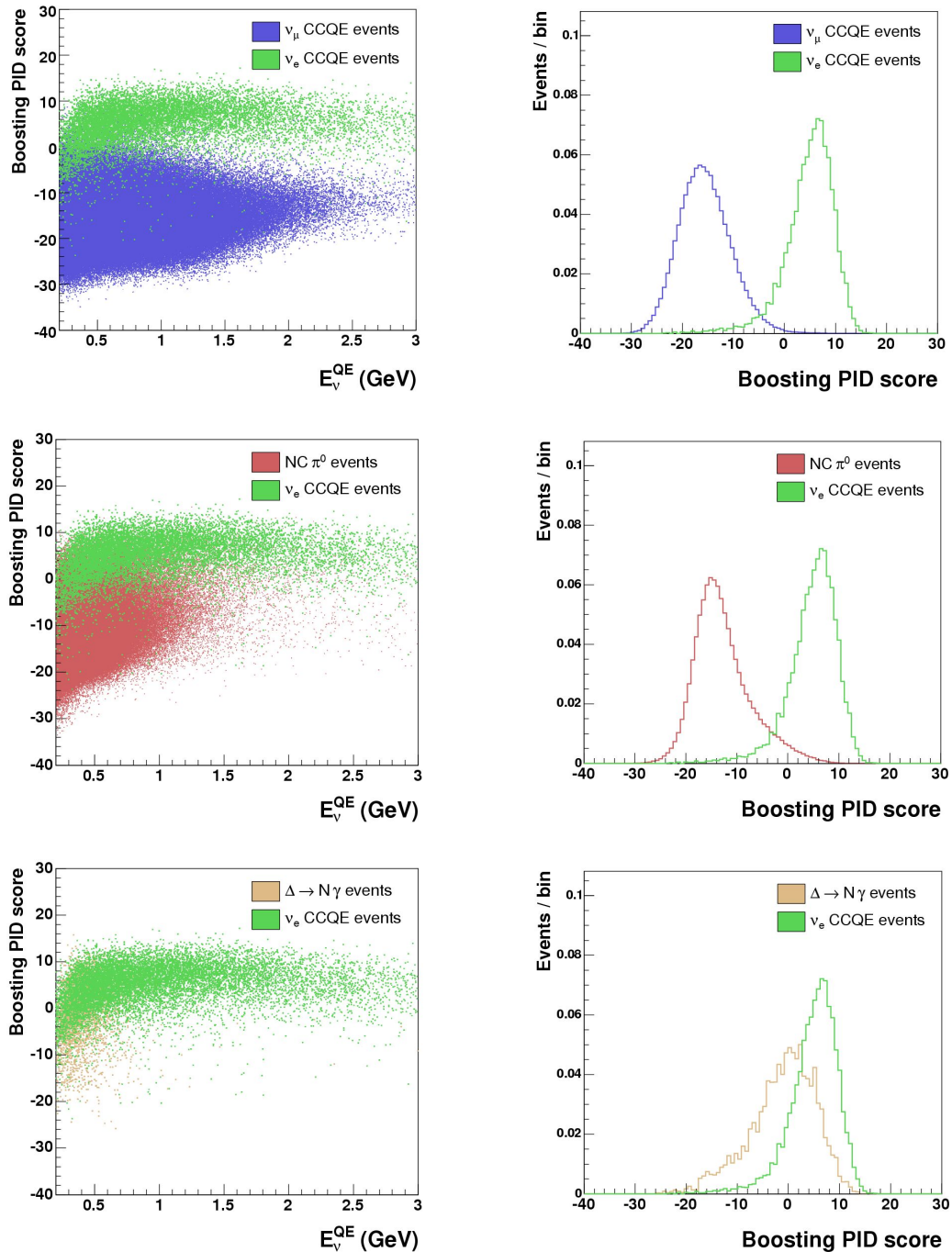
Figure 7.20: Monte Carlo distributions of the BDT PID score for important backgrounds compared to ν_e CCQE events as a function of reconstructed (CCQE) energy and integrated over energy from 0.2–3.0 GeV. The backgrounds shown are ν_μ CCQE (top), NC π^0's (middle) and radiative delta decays (bottom). All distributions have been normalized to have unit area.

Chapter 8

A Search for $\nu_\mu \to \nu_e$ Oscillations at MiniBooNE

In this final chapter we present a search for $\nu_\mu \to \nu_e$ oscillations using the MiniBooNE data. A χ^2 fitting procedure is developed to test for evidence of oscillations in the ν_e candidate sample which also incorporates a constraint on ν_e backgrounds enabled by the ν_μ CCQE data. An overview of the experimental uncertainties affecting the analysis is presented culminating in a final sensitivity to the oscillation parameters $(\Delta m^2, \sin^2(2\theta))$. Finally, we apply the fitting procedure to neutrino mode data from MiniBooNE corresponding to 5.58×10^{20} protons on target (POT) collected between 2002 and 2006.

8.1 Introduction

The observed distribution of ν_e events at MiniBooNE will be used to set limits on possible values of the oscillation parameters, Δm^2 and $\sin^2(2\theta)$. To do so, a fitting procedure must be developed to compare simulated background and signal predictions with the measured data. Experimental uncertainties must be carefully considered in order to quantify the level at which the data are consistent with a given oscillation hypothesis. We will consider both data and Monte Carlo statistical uncertainties as well as systematic uncertainties arising from our modeling of the neutrino fluxes, neutrino interaction

cross-sections, and the detector simulation. Many of these uncertainties will introduce correlations among different energy regions in the predicted spectrum. Because neutrino oscillations are an energy dependent phenomenon, the fitting algorithm should include these correlations. In Section 8.2 we introduce such an algorithm which also incorporates an experimental constraint on the oscillation background provided by the observed ν_μ data. In Section 8.3 we detail the experimental errors considered in the analysis. Section 8.4 presents the ν_μ CCQE selection and data/Monte Carlo comparisons. Section 8.5 discusses two possible selections of ν_e candidate events and compares their sensitivities to oscillation parameters. Finally, in Section 8.7, we apply these ν_e selections to MiniBooNE data and present the result of a fit for oscillations.

8.2 The $\nu_\mu - \nu_e$ combined fitting technique

In the previous chapter we discussed important misidentification backgrounds and how their absolute rates have been directly constrained using non-ν_e CCQE data samples. In this section, we present a technique by which we use the observed high statistics ν_μ CCQE event sample to constrain the absolute rate of intrinsic ν_e-induced backgrounds. The approach used incorporates this constraint as part of the fitting procedure used to search for an excess of ν_e events consistent with the $\nu_\mu \rightarrow \nu_e$ expectation.

8.2.1 Correlations between observed ν_μ and ν_e events

The details of the method will be described, but first we outline some key elements of the experiment which create this important correlation between the observed ν_μ CCQE events and the expected ν_e CCQE event distribution. It is helpful to note that the observed rate of each is just the product of a flux, interaction cross-section, and event selection efficiency:

$$N_{\nu_\mu} = \Phi_{\nu_\mu} \times \sigma_{\nu_\mu} \times \varepsilon_{\nu_\mu} \qquad\qquad N_{\nu_e} = \Phi_{\nu_e} \times \sigma_{\nu_e} \times \varepsilon_{\nu_e}$$

1. The ν_μ flux from π^+ decay (90% of the total ν_μ flux) is correlated with the ν_e flux
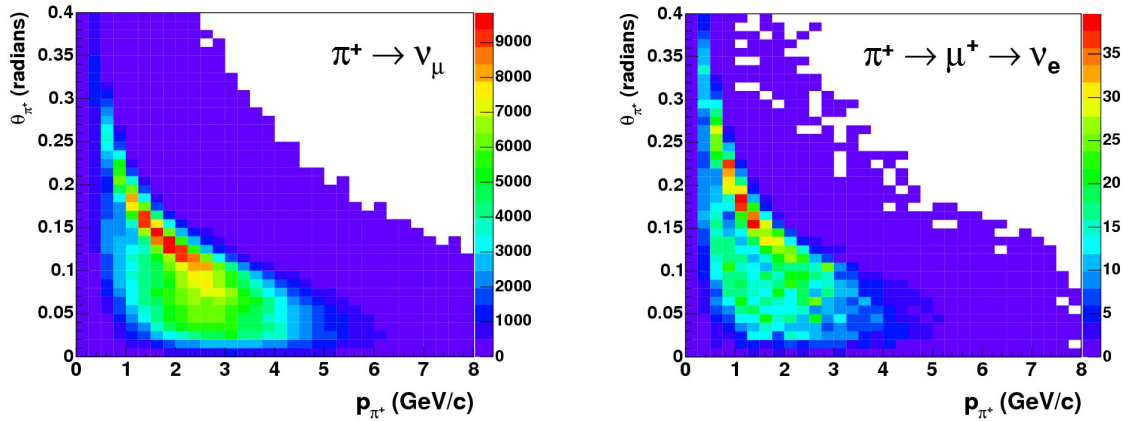
Figure 8.1: Kinematic distributions of π^+ which contribute to the ν_μ flux through $\pi^+ \rightarrow \mu^+ \nu_\mu$ decays (left) and which contribute to the ν_e flux through $\pi^+ \rightarrow \mu^+ \rightarrow e^+ \overline{\nu}_\mu \nu_e$ decays (right). The absolute scales are arbitrary, but the relative scales are those predicted by the BNB Monte Carlo.

from μ^+ decay (49% of the total ν_e flux) through the decay chain:

$$\pi^+ \rightarrow \mu^+ + \nu_\mu$$

$$\downarrow$$

$$\mu^+ \rightarrow e^+ + \overline{\nu}_\mu + \nu_e$$
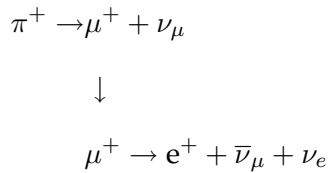
A measurement of the high statistics ν_μ CCQE event rate, therefore, provides a constraint on the ν_e CCQE rate coming from muon decays. Two facts make this constraint possible. First, the muons creating the ν_e flux are produced in decays of the same π^+ that produce the ν_μ flux. This is demonstrated in Figure 8.1 showing the kinematic distributions of the parent π^+ for ν_μ's crossing the MiniBooNE detector and the grandparent π^+ for ν_e from μ^+ decay which cross the detector. There is a large overlap in pion phase space in the two distributions. Second, due to the small solid angle which the MiniBooNE detector subtends (10 m/541 m $\approx$ 0.02 rad), the muon neutrino energy is strongly correlated with the energy of its parent pion. Only the most forward decays can contribute to the flux and in the limit of perfectly forward decays $E_\nu \approx (1 - m_\mu^2/m_\pi^2)E_\pi = 0.43 E_\pi$. Figure 8.2 shows the actual correlation according to the BNB simulation. The peak near the small angle approximation
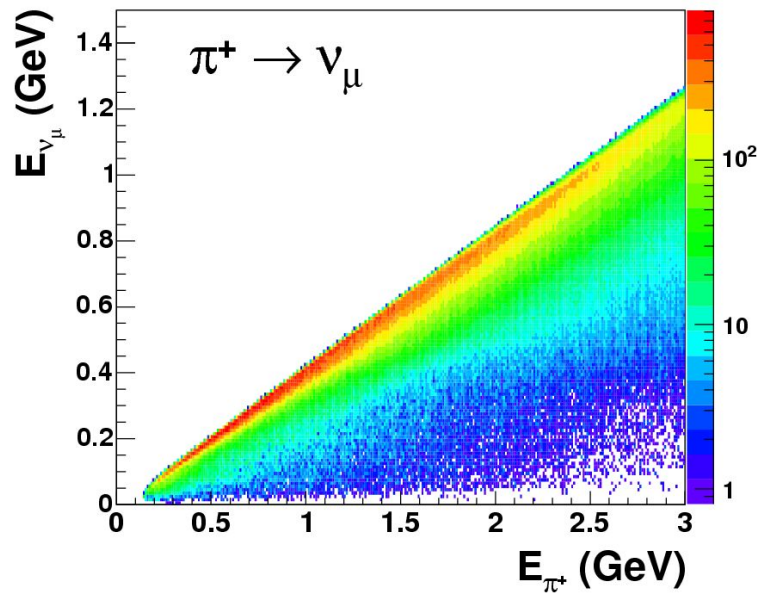
Figure 8.2: Correlation between the muon neutrino energy (ordinate axis) and its parent pion energy (abscissa axis) for neutrinos passing through the MiniBooNE detector. The peak near the physical cutoff at $E_\nu = 0.43E_\pi$ is clearly visible.

$0.43E_\pi$ is clear.

2. The ν_μ CCQE event rate, modulated by allowed combinations of $(\Delta m^2, \sin^2(2\theta))$, constrains the possible signal shapes and magnitudes from $\nu_\mu \to \nu_e$ oscillations. Figure 8.3 shows possible distributions of signal events passing ν_e selection pre-cuts given the predicted ν_μ flux shape. The black histogram represents a flux of electron neutrinos with exactly the shape and magnitude (when properly normalized, which Figure 8.3 is not) of the predicted ν_μ flux. Typically, such a fully $\nu_\mu \to \nu_e$ transmutated Monte Carlo sample is referred to as a "full-osc" sample and we will use this nomenclature where convenient. The colored histograms in Figure 8.3 show the fully oscillated sample modulated by $\sin^2(1.267 \, \Delta m^2 \, 0.541 \text{ km}/E_\nu)$ for three values of Δm^2.

3. Muon and electron neutrinos share the same CCQE cross-section; the constraint on the model described in Section 7.2.1 from observed ν_μ events applies equally to ν_e. The difference comes only from lepton mass effects, so the correlation between the
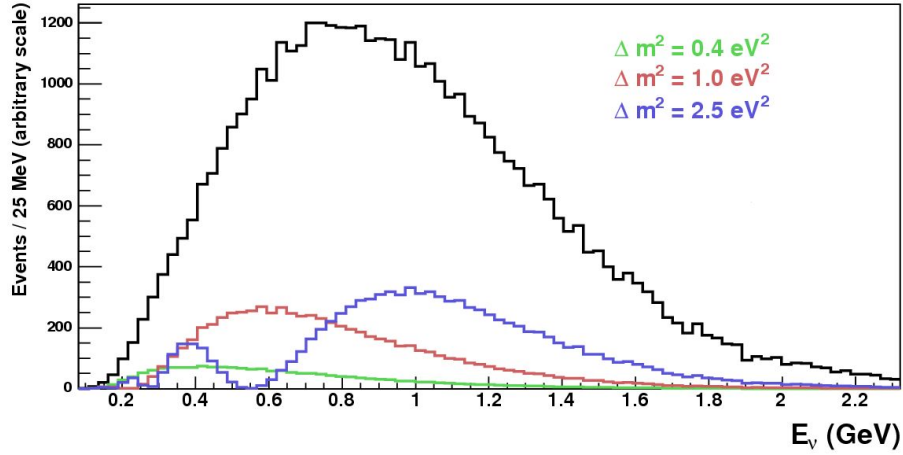
Figure 8.3: Examples of possible oscillation signal shapes for different values of Δm^2. The black histogram shows the distribution of events passing ν_e pre-cuts (SE $= 1, \mathrm{N_{tank}} >$ $200, \mathrm{N_{veto}} < 6$) for a fully transmutated ν_μ flux (that is, a flux of electron neutrinos with exactly the ν_μ flux shape). The colored histograms demonstrate how the signal is modulated for different possible values of Δm^2.

two cross-section is large.

4. The detection efficiency for electron events, as we will see, is strongly dependent upon the MiniBooNE detector model which has large uncertainties. Unfortunately, these effects are only marginally correlated with the ν_μ efficiencies.

8.2.2   Definition of the χ^2 statistic

In order to test for evidence of an oscillation signal in MiniBooNE data we will determine the minimum value of a χ^2 statistic that depends simultaneously upon the observed and predicted spectra of ν_μ events, ν_e background events, and ν_e signal events:

$$\chi^2(\Delta m^2, \sin^2(2\theta)) =$$
$$\sum_{i,j}^{n_{\nu_e}+n_{\nu_\mu}} \left[\mathrm{N}_i^{\mathrm{obs}} - \mathrm{N}_i^{\mathrm{pred}}(\Delta m^2, \sin^2(2\theta)) \right] E_{ij}^{-1} \left[\mathrm{N}_j^{\mathrm{obs}} - \mathrm{N}_j^{\mathrm{pred}}(\Delta m^2, \sin^2(2\theta)) \right] \tag{8.1}$$

where the sum runs over the total number of energy bins in *both* the ν_e and ν_μ distributions, $n_{\nu_e} + n_{\nu_\mu}$. The observed and predicted numbers of events in reconstructed energy

bin i are given by N_i^{obs} and N_i^{pred}, respectively. The ν_e prediction is built from the set of considered backgrounds and a signal component:

$$N_i^{pred} = N_i^{bkgd} + P(\Delta m^2, \sin^2(2\theta), L_\nu, E_\nu) \times N_i^{full-osc} \qquad (\nu_e \text{ energy bins}) \quad (8.2)$$

where the background, $N_i^{bkgd} = N_i^{\nu_\mu-misID} + N_i^{\nu_e-int}$, includes the number of both ν_μ-induced and intrinsic ν_e-induced events expected to pass a given set of ν_e selection cuts and $N_i^{full-osc}$ is the number of events passing these cuts from a fully oscillated $\nu_\mu \to \nu_e$ sample. The oscillation probability, P, is calculated using the two neutrino appearance equation, Eq. 1.20, and is a function of the *true* travel distance, L_ν, and neutrino energy, E_ν, which are obtained from the Monte Carlo. The predicted ν_μ distribution is just the number of events expected to pass ν_μ CCQE selection cuts:

$$N_i^{pred} = N_i^{\nu_\mu-CCQE} \qquad (\nu_\mu \text{ energy bins}) \quad (8.3)$$

Strictly, the ν_μ prediction should include a term accounting for the probability of ν_μ disappearance, $-P(\Delta m^2, \sin^2(2\theta), L_\nu, E_\nu) \times N_i^{\nu_\mu-CCQE}$. However, for an expected oscillation probability of $\sim 0.3\%$, the term is negligible in the fit compared to the systematic uncertainties and can be neglected.

Finally, E_{ij} is the $(i, j)^{th}$ element of a correlated error matrix which includes all statistical and systematic uncertainties considered in the analysis:

$$E = \begin{pmatrix} N_1 + \sigma_1^2 & \rho_{21}\sigma_2\sigma_1 & \cdots & \rho_{n1}\sigma_n\sigma_1 \\ \rho_{12}\sigma_1\sigma_2 & N_2 + \sigma_2^2 & \cdots & \rho_{n2}\sigma_n\sigma_2 \\ \vdots & \vdots & \ddots & \vdots \\ \rho_{1n}\sigma_1\sigma_n & \rho_{2n}\sigma_2\sigma_n & \cdots & N_n + \sigma_n^2 \end{pmatrix} \qquad (8.4)$$

where N_i is the number of events in the ith bin (or the statistical error squared) and ρ_{ij} is the correlation coefficient between the systematic error in those bins, σ_i and σ_j.

8.2.3   The error matrix

To facilitate the simultaneous fitting of ν_μ and ν_e events, we must construct a single covariance matrix describing the uncertainties for both the ν_μ and ν_e energy distributions.

In doing so, the off-diagonal terms will describe the correlations *among energy bins within a distribution* as well as the correlations *between the ν_μ and ν_e energy spectra*. It is these correlation terms which will provide the constraint on the ν_e prediction provided by the high statistics ν_μ sample.

The calculation of the systematic error matrices follows closely the methods used in the analysis of the HARP cross-section data as described in Section 4.6. Briefly, a Monte Carlo technique is employed to translate the uncertainty on underlying parameters to an uncertainty on a final output quantity. For HARP this was the differential production cross-section. In the case of MiniBooNE, the output quantity is a reconstructed energy distribution of charged-current quasi-elastic candidate events. To continue the analogy, the matrix we will build for MiniBooNE data would be equivalent to building a correlation matrix between the π^+ and proton cross-sections at HARP. One can imagine that the measured cross-sections are highly correlated (same reconstruction efficiencies, anti-correlated PID efficiencies, etc.).

Each systematic error matrix will be calculated analogously to Eq. 4.13,

$$E_{ij}^m = \frac{1}{\mathcal{N}} \sum_{n=1}^{\mathcal{N}} [\mathrm{N_{CV}} - \mathrm{N}_{m,n}]_i \times [\mathrm{N_{CV}} - \mathrm{N}_{m,n}]_j \tag{8.5}$$

where i and j label bins of E_ν^{QE}, E_{ij}^m is the $(i,j)^{th}$ element of the error matrix being considered (labeled m), $\mathrm{N_{CV}}$ is the central value for the predicted number of either ν_μ or ν_e candidate events and $\mathrm{N}_{m,n}$ is the prediction from the nth variation of the mth systematic error source.

Figure 8.4 shows a schematic diagram of the covariance matrix to be built. The correlations with the ν_e signal and background components are generated separately. The energy binning chosen for the two samples must have bin boundaries in common to allow their combination in future steps. If one chooses the same binning for the ν_e background and signal components, then the final error matrix will contain $(2n_{\nu_e} + n_{\nu_\mu}) \times (2n_{\nu_e} + n_{\nu_\mu})$ elements. For the matrices generated for this analysis $n_{\nu_e} = 18$ and $n_{\nu_\mu} = 17$ with bin boundaries:

- $E_{\nu_e}^{\mathrm{QE}} = [0.2, 0.3, 0.4, 0.5, 0.6, 0.7, 0.8, 0.9, 1.0, 1.1, 1.2, 1.3, 1.4, 1.5, 1.6, 1.7, 1.8, 1.9, 3.0]$ GeV
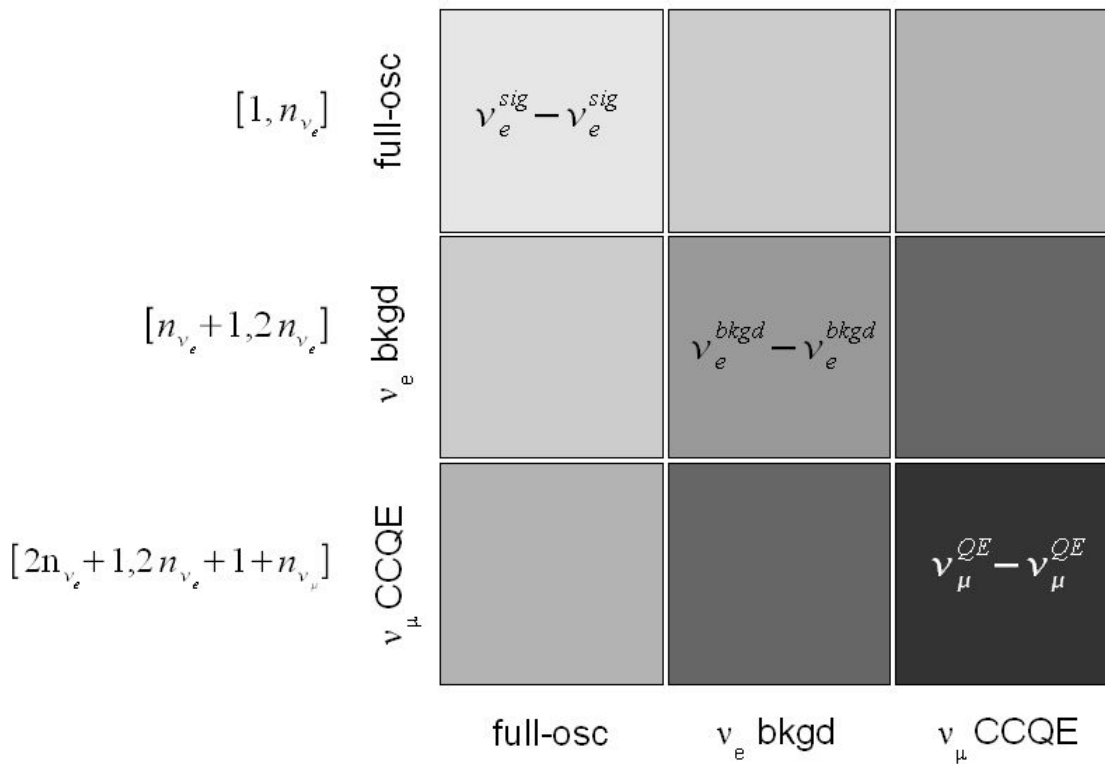
Figure 8.4: Schematic diagram of the covariance matrix built to describe the correlations within the MiniBooNE muon and electron neutrino data. Separate blocks exist for the ν_e signal (upper left), ν_e background (middle) and ν_μ CCQE (lower right) predictions. In addition, each of these distributions may be correlated with each other and are described by the off-diagonal blocks. The total error matrix contains $(2n_{\nu_e} + n_{\nu_\mu}) \times (2n_{\nu_e} + n_{\nu_\mu})$ elements.

- $E_{\nu_\mu}^{\mathrm{QE}} = [0.0, 0.4, 0.5, 0.6, 0.7, 0.8, 0.9, 1.0, 1.1, 1.2, 1.3, 1.4, 1.5, 1.6, 1.7, 1.8, 1.9, 3.0]$ GeV

so that the error matrix contains 53×53 elements. The fitting software allows combinations of the events in neighboring bins, but the bin boundaries used in the matrix must be respected.

Finally, it is the *fractional* variations which are input to the fitting algorithm:

$$E_{ij}^{\mathrm{frac}} = \frac{E_{ij}}{\mathrm{N}_i^{\mathrm{pred}} \mathrm{N}_j^{\mathrm{pred}}} \tag{8.6}$$

This separation of ν_e background and signal components in the fractional error matrix allows us to construct a total error matrix corresponding to a particular signal hypothesis within the mechanics of the fitting procedure.

8.2.4 Oscillation fit mechanics

The goal of the fit is to determine the values of Δm^2 and $\sin^2(2\theta)$ for which the χ^2 statistic of Eq. 8.1 is minimized. We discovered in the previous section that the error matrix itself contains a signal component and, therefore, is also a function of the oscillation parameters, $E \equiv E(\Delta m^2, \sin^2(2\theta))$. In the data, of course, it is not possible to separate the background and signal components of the events for comparison[1]. Therefore, the ν_e background and signal components of the error matrix must be combined just as the predicted number of events are combined in Eq. 8.2. First, the fractional errors must be multiplied by the number of predicted events in each bin ($\mathrm{N}_i^{\mathrm{pred}} \times \mathrm{N}_j^{\mathrm{pred}}$) to convert the input fractional error matrix into a total error matrix in units of $(\mathrm{events})^2$. The matrix elements corresponding to the same E_ν^{QE} bin can then simply be summed to collapse the 3×3 block error matrix into the 2×2 block format that we need in order to compare to data (a total ν_e block and a ν_μ block). This procedure is depicted in Figure 8.5 showing how the elements are added when considering one ν_e energy bin.

Allowing the error in a χ^2 minimization to vary with the parameters is, in general, a dangerous strategy. In our χ^2 definition as a matrix equation with correlations, multiplying by the matrix inverse corresponds to division by the uncorrelated error in the

---

[1]Wouldn't it be nice if it were!
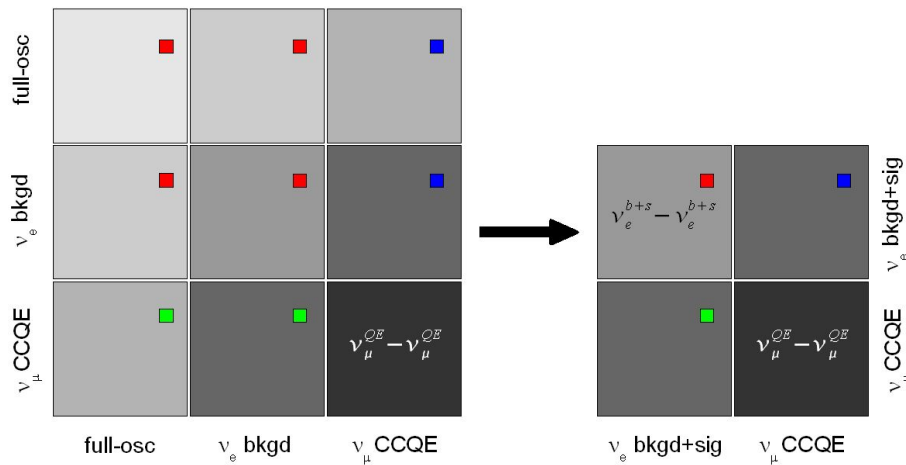
Figure 8.5: Schematic diagram showing the collapse of the covariance matrix to combine the ν_e background and signal error elements. The four red bins on the left are added to give the value in the red bin in the collapsed matrix on the right. Similarly for the blue and green bins.

traditional χ^2 definition, $E^{-1} \Leftrightarrow 1/\sigma^2$. Mathematically, therefore, it would be possible to minimize the function by taking the errors to infinity, $\sigma^2 \to \infty$. In our case, the error matrix can be increased by increasing $\mathrm{N}^{\mathrm{pred}}$, or adding signal! While we desire to carefully account for the systematics on the signal prediction as well as take advantage of the constraint provided by the observed ν_μ data, we clearly wish to avoid this artificial minimizing of the χ^2 statistic.

To minimize the function in a controlled way we adopt an iterative approach to updating the error matrix. We begin with an error matrix built assuming no signal, which we refer to as the null hypothesis matrix, $E_{\mathrm{null}} \equiv E(0,0)$. Keeping the matrix fixed, we step through the 2-dimensional $(\Delta m^2, \sin^2(2\theta))$ parameter space with sufficiently small steps, update the ν_e event prediction, $\mathrm{N}^{\mathrm{pred}}$, at each grid point according to Eq. 8.2 and calculate the value of χ^2 using Eq. 8.1. In this manner, we map out a smooth surface of χ^2 values across the relevant regions of oscillation parameter space upon which the minimum point can easily be determined $[\Delta m^2, \sin^2(2\theta)]_{\mathrm{min}}$. This minimum set is used to build a new error matrix $E([\Delta m^2, \sin^2(2\theta)]_{\mathrm{min}})$ and the process is repeated until the fit result converges.

Numerous tests performed using fake data samples verified that the iterative method is stable, and showed that the fit nearly always converged in a single iteration.

8.2.5   Understanding the ν_μ constraint on the ν_e prediction : The 2 bin example

We use a simple example to give an idea how the ν_μ events are able to constrain the ν_e background prediction and produce a smaller error on the extracted number of signal events. We assume each distribution is made up of only a single energy bin. We define the difference between the number of predicted and observed events in the single ν_e and single ν_μ bin as:

$$
\begin{aligned}
\Delta_{\nu_e} &= N_{\nu_e}^{\text{obs}} - N_{\nu_e}^{\text{bkgd}} \\
\Delta_{\nu_\mu} &= N_{\nu_\mu}^{\text{obs}} - N_{\nu_\mu}^{\text{pred}}
\end{aligned}
\tag{8.7}
$$

The covariance matrix in this case is reduced to a 2×2 matrix with only a single correlation coefficient $\rho_{\nu_e\nu_\mu} = \rho_{\nu_\mu\nu_e} \equiv \rho$. We explicitly separate the statistical uncertainties, $s = \sqrt{N}$, from the systematic uncertainties, σ, such that the total diagonal error in a bin is given by $s^2 + \sigma^2$ and only the systematic errors are potentially correlated:

$$
E = \begin{pmatrix} s_{\nu_e}^2 + \sigma_{\nu_e}^2 & \rho\sigma_{\nu_e}\sigma_{\nu_\mu} \\ \rho\sigma_{\nu_e}\sigma_{\nu_\mu} & s_{\nu_\mu}^2 + \sigma_{\nu_\mu}^2 \end{pmatrix}
\tag{8.8}
$$

which has the trivial inverse

$$
E^{-1} = \frac{1}{|E|} \begin{pmatrix} s_{\nu_\mu}^2 + \sigma_{\nu_\mu}^2 & -\rho\sigma_{\nu_e}\sigma_{\nu_\mu} \\ -\rho\sigma_{\nu_e}\sigma_{\nu_\mu} & s_{\nu_e}^2 + \sigma_{\nu_e}^2 \end{pmatrix}
\tag{8.9}
$$

where $|E| = (s_{\nu_e}^2 + \sigma_{\nu_e}^2)(s_{\nu_\mu}^2 + \sigma_{\nu_\mu}^2) - (\rho\sigma_{\nu_e}\sigma_{\nu_\mu})^2$ is the matrix determinant. Writing out the χ^2 expression as a matrix equation and including potential signal events, $\mathcal{S}$, in the ν_e block yields:

$$
\chi^2 = \begin{pmatrix} \Delta_{\nu_e} - \mathcal{S} & \Delta_{\nu_\mu} \end{pmatrix} \frac{1}{|E|} \begin{pmatrix} s_{\nu_\mu}^2 + \sigma_{\nu_\mu}^2 & -\rho\sigma_{\nu_e}\sigma_{\nu_\mu} \\ -\rho\sigma_{\nu_e}\sigma_{\nu_\mu} & s_{\nu_e}^2 + \sigma_{\nu_e}^2 \end{pmatrix} \begin{pmatrix} \Delta_{\nu_e} - \mathcal{S} \\ \Delta_{\nu_\mu} \end{pmatrix}
\tag{8.10}
$$

$$
= \frac{1}{|E|} \left[\left(s_{\nu_\mu}^2 + \sigma_{\nu_\mu}^2\right)(\Delta_{\nu_e} - \mathcal{S})^2 - 2\rho\sigma_{\nu_e}\sigma_{\nu_\mu}\Delta_{\nu_\mu}(\Delta_{\nu_e} - \mathcal{S}) + \left(s_{\nu_e}^2 + \sigma_{\nu_e}^2\right)\Delta_{\nu_\mu}^2 \right]
$$

which is just a quadratic equation in $(\Delta_{\nu_e} - \mathcal{S})$. Setting the first derivative equal to zero, $\partial\chi^2/\partial\mathcal{S} = 0$, produces the best fit number of signal events:

$$\mathcal{S} = \Delta_{\nu_e} - \left[\frac{\sigma_{\nu_e}\sigma_{\nu_\mu}}{s_{\nu_\mu}^2 + \sigma_{\nu_\mu}^2} \right] \rho\Delta_{\nu_\mu} \tag{8.11}$$

and twice the inverse of the second derivative yields the uncertainty on the number of signal events:

$$\sigma_{\mathcal{S}}^2 = s_{\nu_e}^2 + \left[1 - \frac{\rho^2}{\left(\frac{s_{\nu_\mu}^2}{\sigma_{\nu_\mu}^2} + 1 \right)} \right] \sigma_{\nu_e}^2 \tag{8.12}$$

Below we make several observations from Eq. 8.11 and 8.12 about the nature of the ν_μ constraint on the ν_e's and potential signal:

- Eq. 8.11 shows how the best fit number of signal events are affected by any discrepancy observed between the measured and predicted number of ν_μ's.

  1. If the ν_μ data agree perfectly with the prediction such that $\Delta_{\nu_\mu} = 0$, or if there is no correlation between the ν_μ and ν_e samples so $\rho = 0$, then Eq. 8.11 reduces to $\mathcal{S} = \Delta_{\nu_e}$ and the ν_e candidates attributed to signal become just the excess of observed ν_e events over the prediction.

  2. If the two samples are correlated and the agreement is not exact, then a correction is made. For example, assume the two samples are positively correlated with a coefficient $\rho > 0$. Further, assume there are an excess of ν_μ events in data over the prediction, such that $\Delta_{\nu_\mu} > 0$. The ν_e background prediction is pulled up by the positive correlation and the data excess observed in the ν_μ's. In Eq. 8.11 the sign of the second term remains negative, thus reducing the number of signal events observed, exactly as one expects given an increase in the background estimate.

- Eq. 8.12 shows how the uncertainty on the extracted signal is constrained by the high statistics ν_μ sample. Note that the uncertainty constraint is dependent upon the level of correlation with the ν_e background and the statistical precision of the ν_μ sample, but not on the data/Monte Carlo agreement in the ν_μ's.

1. If the ν_μ and ν_e backgrounds are completely uncorrelated such that $\rho = 0$, then the uncertainty on the signal is just the quadrature sum of the statistical and systematic uncertainties on the predicted background $\sigma_\mathcal{S}^2 = s_{\nu_e}^2 + \sigma_{\nu_e}^2$.

2. In the opposite limit, if the ν_μ and ν_e backgrounds are fully correlated such that $\rho = 1$, and the ν_μ statistical errors are negligible compared to the systematic uncertainty so that $s_{\nu_\mu}^2/\sigma_{\nu_\mu}^2 \to 0$, then Eq. 8.12 reduces to just the statistical errors on the background prediction. The fully correlated, infinite statistics sample has been used to eliminate the systematic errors on the low statistics sample.

3. In practice, we have a moderately correlated sample with semi-infinite statistics, so we get a reduction, but not an elimination of the systematic uncertainties on the ν_e backgrounds.

8.3 Estimation of systematic errors

For the $\nu_\mu \to \nu_e$ oscillation search, the error matrix in Eq. 8.1 is a combination of both data and Monte Carlo statistical errors and 10 sources of systematic uncertainty on the predicted ν_μ and ν_e CCQE distributions. A full covariance matrix is constructed for each systematic according to Eq. 8.5. The statistical error matrix is a purely diagonal matrix with the uncorrelated statistical errors for each bin. The total error matrix is just the sum of the 11 matrices:

$$E = E^{\pi^+} + E^{\pi^-} + E^{K^+} + E^{K^0} + E^{\text{beam}} + E^\sigma + E^{\pi^0} + E^{\text{dirt}} + E^{\text{det}} + E^{\text{DAQ}} + E^{\text{stat}} \quad (8.13)$$

Below we briefly describe each source of error considered and the methods used to propagate them to the final output quantity, E_ν^{QE}.

8.3.1 Neutrino flux uncertainties

Flux related uncertainties are considered for a variety of sources associated with the simulation of the Booster Neutrino Beamline described in Section 7.1. The dominant uncertainty in the neutrino flux arises from the modeling of primary particle production

in the beryllium target and these are considered separately for π^+, π^-, K^+ and K^0. The production of each secondary meson is modeled by a parameterization of the double-differential production cross-section based on available production data as described in Appendix B:

$$\frac{d^2\sigma}{dpd\Omega}(p,\theta) \;\equiv\; f(p,\theta,c_1 \ldots c_k) \tag{8.14}$$

where p and θ are the secondary meson kinematics and c_1 through c_k are the k parameters of the model. For each set of parameters, a $k \times k$ covariance matrix is also generated in the fit to data. Using the Cholesky decomposition method [136], allowed variations in the model parameters can be drawn. The resulting variation in the double-differential production cross-section at any point (p,θ) can be determined by comparison to the default parameterization value. Since we know the kinematics of the parent meson which produced each neutrino in the simulation, the variation in the meson cross-sections can be propagated to the neutrino flux by assigning a weight to each neutrino event equal to the ratio of the double-differential production cross-section of its parent given by the varied and default parameter sets:

$$w \;=\; \frac{f(p,\theta,c_1^n \ldots c_k^n)}{f(p,\theta,c_1 \ldots c_k)} \tag{8.15}$$

where $c_1^n \ldots c_k^n$ are the nth variation of the set of model parameters. In this way, $\mathcal{N}$ total variations of the parameters ($\mathcal{N} \sim \mathcal{O}(1000)$) are used to build $\mathcal{N}$ neutrino flux distributions for each neutrino type from which the error matrices E^{π^+}, E^{π^-}, E^{K^+} and E^{K^0} can be constructed from Eq. 8.5.

The remaining beam related error matrix, E^{beam}, is built from variations due to uncertainties in the hadronic cross-section model (see Section 7.1.1.3) and properties of the horn magnetic field. Table 8.1 lists the variations that are made in the underlying models. Two neutrino flux variations are generated by varying the horn current ± 1 kA from the nominal value. The "skin depth" effect allows for the magnetic field to penetrate into the inner conductor of the horn, thus increasing the amount of field seen by particles entering the horn volume. The default model is an exponential decay of the field with decay length 1.4 mm. A model with the magnetic field located completely within the horn volume (no

BNB MC parameter	nominal value	excursion	
horn current	174 kA	± 1 kA	
skin depth	exponential	surface	
(p/n)-(Be/Al)		Be	Al
σ_{TOT}	Fig. 7.2	± 15.0 mb	± 25.0 mb
σ_{INE}	Fig. 7.2	± 5.0 mb	± 10.0 mb
σ_{QEL}	Fig. 7.2	± 20.0 mb	± 45.0 mb
(π^+/π^-)-(Be/Al)		Be	Al
σ_{TOT}	Fig. 7.3,7.4	± 11.9 mb	± 28.7 mb
σ_{INE}	Fig. 7.3,7.4	± 10.0 mb	± 20.0 mb
σ_{QEL}	Fig. 7.3,7.4	± 11.2 mb	± 25.9 mb

Table 8.1: Variations in BNB Monte Carlo parameter values used to build the beam systematic error matrix E^{beam}. For each hadron-nucleus cross-section, the momentum dependent cross-section is offset by the listed amount.

inner conductor penetration) is used as an excursion. Finally, each hadronic cross-section is individually raised and lowered by the amount listed in Table 8.1 to create twelve more neutrino flux variations. These 15 variations of the neutrino fluxes are used to build the beam covariance matrix, E^{beam}.

8.3.2 Neutrino cross-section uncertainties

Neutrino interactions are modeled using the NUANCE event generator code as described in Section 7.2. Within this model, there are many parameters which control the shape and rate of the various interactions. To estimate the uncertainty on the ν_μ and ν_e charged-current quasi-elastic candidate distributions a weighting method similar to that used for the primary meson production uncertainties in the beam is employed. A covariance matrix from which allowed values of the parameters can be drawn has been generated for NUANCE parameters which affect the rate of CCQE interactions or their backgrounds. Table 8.2 lists the cross-section model parameters considered and their uncertainties. Only a few pairs of parameters are correlated and their coefficients are given in the table. The other off-diagonal elements of the error matrix are zero.

The quasi-elastic axial mass, m_A^{QE}, κ, E_{B} and p_{F} are the parameters introduced in Section 7.2.1 which described the charged-current quasi-elastic interaction model. The first two have been measured using the MiniBooNE ν_μ CCQE data sample [67]. The errors listed in the table do not include contributions from the flux or detector model to avoid double counting of these uncertainties. The other mass parameters listed have effects on the background rates in the ν_μ CCQE sample, 75% of which are charged-current single π^+ events.

The total rate of π^0 events in MiniBooNE has been constrained to $\sim 5\%$ and that measurement has its own uncertainties which will be addressed in the next section. The fraction of π^0's which are produced coherently, however, affects the electron misidentification rate of π^0 events because of the different kinematics of coherent and resonant events (coherent events are more forward). Therefore, the uncertainty on the coherent fraction is included in the cross-section model errors. The varying of the coherent cross-section is fully correlated with the resonant cross-section in order to maintain a total consistent

cross-section model par.	nominal value	error	correlation
m_A^{QE}, quasi-elastic axial mass	1.23 GeV	$\pm$ 0.077 GeV	$\rho(m_A^{\mathrm{QE}}, \kappa) = $ -0.875
$m_A^{1\pi}$, single pion axial mass	1.1 GeV	$\pm$ 0.28 GeV	none
$m_A^{\mathrm{coh}\pi}$, coherent axial mass	1.03 GeV	$\pm$ 0.28 GeV	none
$m_A^{\mathrm{N}\pi}$, multi pion axial mass	1.3 GeV	$\pm$ 0.52 GeV	none
κ, Pauli-blocking correction	1.02	$\pm$ 0.02	$\rho(\kappa, m_A^{\mathrm{QE}}) = $ -0.875
E_B, binding energy in ^{12}C	34 MeV	$\pm$ 9 MeV	none
p_F, Fermi momentum in ^{12}C	220 MeV/c	$\pm$ 30 MeV/c	none
resonant π^0 fraction	19.5%	$\pm$ 2.5%	$\rho(\mathrm{Res}, \mathrm{Coh}) = $ -1
coherent π^0 fraction	80.5%	$\pm$ 2.5%	$\rho(\mathrm{Coh}, \mathrm{Res}) = $ -1
$\Delta \to \mathrm{N}\gamma$ decay BR	0.56%	$\pm$ 0.04%	none
π escape probability in ^{12}C	62.5%	$\pm$ 7.5%	none
π charge exchange in ^{12}C	energy dependent	50%	none
π absorption in ^{12}C	energy dependent	35%	none

Table 8.2: NUANCE cross-section model parameter values and errors.

with the measured rate. This measurement was used to constrain the rate of radiative delta decays as well, but the uncertainty on the branching ratio for the $\Delta \to \mathrm{N}\gamma$ decay must be considered.

Pion charge exchange and absorption within the nucleus affect the ν_μ CCQE backgrounds. When pions created in a charged-current reaction are absorbed by final state interactions within the target nucleus, the only final state particle is the muon, making the event indistinguishable from a ν_μ CCQE event. Therefore, the uncertainty on the pion charge exchange and absorption rates are included.

W^{π^0}	1.4477	1.4794	1.1301	1.0414	0.9515	1.0241	0.7071	0.9638	0.9684
$\mathcal{M}_{ij}^{\pi^0}$	0.0–0.1	0.1–0.2	0.2–0.3	0.3–0.4	0.4–0.5	0.5–0.6	0.6–0.8	0.8–1.0	1.0–1.5
0.0–0.1	0.1203	0.0401	0.0015	-0.0079	-0.0182	-0.0455	-0.0345	-0.0672	-0.0898
0.1–0.2	0.0401	0.0195	0.0008	-0.0027	-0.0074	-0.0165	-0.0161	-0.0240	-0.0392
0.2–0.3	0.0015	0.0008	0.0016	0.0001	0.0001	-0.0003	-0.0010	-0.0024	-0.0024
0.3–0.4	-0.0079	-0.0027	0.0001	0.0019	0.0009	0.0037	0.0024	0.0035	0.0063
0.4–0.5	-0.0182	-0.0074	0.0001	0.0009	0.0054	0.0043	0.0076	0.0081	0.0170
0.5–0.6	-0.0455	-0.0165	-0.0003	0.0037	0.0043	0.0314	0.0104	0.0317	0.0412
0.6–0.8	-0.0345	-0.0161	-0.0010	0.0024	0.0076	0.0104	0.0198	0.0203	0.0400
0.8–1.0	-0.0672	-0.0240	-0.0024	0.0035	0.0081	0.0317	0.0203	0.0777	0.0540
1.0–1.5	-0.0898	-0.0392	-0.0024	0.0063	0.0170	0.0412	0.0400	0.0540	0.1274

Table 8.3: Correction factors applied to the predicted π^0 and $\Delta \to N\gamma$ event rates to match that seen in data. The top row gives the scaling factors to be applied in bins of true π^0 or γ momentum given in the second row (in GeV/c). The matrix below describes the errors and correlations for the 9 scaling factors.

8.3.3 π^0 and $\Delta \to N\gamma$ event rate uncertainties

The rate of effective π^0 events in the MiniBooNE detector has been measured as described in Section 7.2.2. This measurement was used to generate a set of correction factors used to scale Monte Carlo π^0 and Δ radiative decay events as a function of the true momentum of the final state π^0 or γ. The scaling factors are listed in the top row of Table 8.3 along with a covariance matrix describing the systematic errors and bin correlations for these weights. A weighting technique is again used to propagate the uncertainty on the Monte Carlo correction factors to the predicted CCQE distributions.

Note that the uncertainty on the π^0 and $\Delta \to N\gamma$ event rates affect only the ν_e candidate prediction and is negligible for the ν_μ's which do not have a π^0 or single photon background component. This complete lack of correlation with the ν_μ CCQE sample made the *in situ* measurement of the π^0 event rate a critical component of the ν_e appearance search.

8.3.4 Dirt event rate uncertainties

Another background in the ν_e CCQE sample comes from neutrinos interacting in the dirt surrounding the detector. If a single photon, mostly from π^0 decays, penetrates the veto and converts in the fiducial volume, then it can mimic a signal event. Dirt events were studied in the data by isolating a sample of events reconstructed at large radius and moving towards the center of the tank. It was found that the Monte Carlo accurately predicted the rate of dirt events, so no additional correction factor was required. A flat 15% uncertainty on the dirt event rate as a function of reconstructed neutrino energy was estimated from these studies.

8.3.5 Detector model uncertainties

The detector simulation and optical photon model are described in Section 7.3. The 35 parameters of the optical model and their covariance matrix comprise another multi-variate normal distribution of underlying parameters whose uncertainties must be propagated to the ν_μ and ν_e CCQE candidate distributions. The parameter values and covariance matrix have been generated as described in [96] using MiniBooNE Michel electron data to constrain the parameters.

The detector model effects, however, cannot be propagated to the reconstructed E_ν^{QE} distribution by the weighting techniques used for flux and cross-section errors. Changes in the optical photon model have subtle effects on the reconstruction of different event types rather than pure normalization effects on the total number of events. For example, the scattering of photons in the oil could affect the sharpness of Cherenkov rings, or photon extinction and reflections from the tank walls can affect the energy scale of the reconstruction.

Unable to employ weighting techniques, the full Monte Carlo simulation, reconstruction and particle identification algorithms must be run for each variation of the detector model parameters starting from a statistically independent sample of events generated by NUANCE. The weighting approach allowed one to use a single high statistics sample of events and quickly generate many systematic variations in order to build the systematic

error matrix. The significant computational requirements of running the full simulation, however, makes the generation of many large samples with negligible statistical fluctuations impractical. This introduces the additional complication that the $\mathcal{N}$ resulting event distributions will contain statistical variations in addition to the systematic ones caused by the detector model uncertainties. To account for this, the following modification is made when building the detector error matrix E^{det}. First, we rewrite Eq. 8.5 as

$$E_{ij}^{\text{det}} = \frac{1}{\mathcal{N}} \sum_{n=1}^{\mathcal{N}} \left[\text{N}_{\text{CV}} - \left| \frac{\text{N}_{n,\text{det}}}{\text{N}_{\text{CV}}} \right| \cdot \text{N}_{\text{CV}} \right]_i \times \left[\text{N}_{\text{CV}} - \left| \frac{\text{N}_{n,\text{det}}}{\text{N}_{\text{CV}}} \right| \cdot \text{N}_{\text{CV}} \right]_j \tag{8.16}$$

where the ratio $\left| \frac{\text{N}_{n,\text{det}}}{\text{N}_{\text{CV}}} \right|$ will differ from 1.0 according to the statistical and systematic fluctuations in the event distributions of the nth Monte Carlo generation. This ratio is fit to a polynomial as a function of reconstructed energy separately for the full-osc, ν_e candidate and ν_μ CCQE distributions. The order of the polynomial is chosen such that it is large enough to track the systematic variations, but sufficiently below the number of bins in each distribution, so that the bin-to-bin statistical fluctuations are smoothed out in the ratio. It is the value from this polynomial function in energy bin i and j that is used in the generation of E^{det} in Eq. 8.16.

For this analysis, $\mathcal{N} = 66$ detector model variations were generated. The finite number of detector model variation samples has an important consequence for the analysis. The covariance matrix is intended to contain information about the systematic correlations between all pairs of bins in the ν_μ and ν_e energy distributions. For the ν_μ and ν_e background blocks this could be as many as $(17 + 18) \times (17 + 18) = 35 \times 35$ matrix elements that must be calculated with only 66 variations. Tests performed with samples of generated fake data revealed that statistical fluctuations in off-diagonal elements could produce unreliable behavior in fits. We have settled on a convention with 8 ν_μ and 8 ν_e bins:

- $E_{\nu_e}^{\text{QE}} = [0.2, 0.4, 0.6, 0.8, 1.0, 1.2, 1.4, 1.6, 3.0]$ GeV

- $E_{\nu_\mu}^{\text{QE}} = [0.0, 0.5, 0.7, 0.9, 1.1, 1.3, 1.5, 1.7, 1.9]$ GeV

This binning structure was well behaved in tests performed using Monte Carlo samples with no signal and a variety of generated fake signals.

It will be seen that the effect of the optical model variations on the ν_e background rejection efficiency is substantial, making the detector model a dominant source of uncertainty in the ν_e appearance search. Therefore, methods to reduce the effect of detector uncertainties and maximize the sensitivity of the analysis to oscillations will be explored in Section 8.5.

8.3.6   DAQ uncertainties

The final systematic error matrix in Eq. 8.13, E^{DAQ}, is constructed from excursions in two data acquisition system related quantities whose implementations do not lend themselves to being incorporated into the detector variations above. The first is the threshold of the discriminator on the PMT electronics which determines when a hit is recorded. The second is the correlation between the charge amplitude and hit time for the PMT electronics mentioned in Section 5.4.4.1. A new Monte Carlo sample is generated for a conservative variation in the discriminator threshold and another in the charge-time correlation model. These two variations are combined to form E^{DAQ}. It is necessary to employ the smoothing procedure used to build the detector model error matrix for the DAQ matrix as well, as the variations also contain non-negligible statistical fluctuations.

8.3.7   Data and Monte Carlo statistical uncertainties

Data and Monte Carlo statistical error matrices are built within the fitting software. Data statistical errors can be set using the data, $\sqrt{\mathrm{N}_i^{\mathrm{obs}}}$, or estimated from the Monte Carlo when properly scaled to data statistics. Monte Carlo statistical errors are included, but are small. The predicted ν_e and ν_μ distributions are generated from a sample 7.9 times larger than data (4.4×10^{21} POT). The dirt event background is estimated from a sample 4.1 times larger than data (2.3×10^{21} POT). The full-osc sample used to generate possible signal distributions in the fit corresponds to a ν_μ flux from 7.1×10^{19} POT. This is 49 times larger than a signal from $P(\nu_\mu \to \nu_e) \approx 0.26\%$ would be in the data.

8.4 ν_μ CCQE sample

The following selection cuts are used to isolate a ν_μ CCQE candidate sample. According to Monte Carlo, the selection is 35% efficient at selecting quasi-elastic events with 74% purity [67].

- Exactly 2 subevents (corresponding to the muon and its Michel electron)

- 1st subevent in the beam window ($4400 < t < 6400$ ns)

- $N_{tank} > 200$ (1st subevent), $N_{tank} < 200$ (2nd subevent)

- $N_{veto} < 6$ (both subevents)

- Radius < 500 cm (1st subevent)

- $\Delta R < 100$ cm (ΔR is the distance between the Michel vertex and the muon end-point)

Figure 8.6 shows the events selected by these cuts in the data and the Monte Carlo as a function of reconstructed E_ν^{QE} (Eq. 7.11). The Monte Carlo has been normalized to 5.58×10^{20} POT to match the data. The error bars on the data are statistical only and no systematic errors are shown. In the left panel, the Monte Carlo has been separated into signal (CCQE) and background (non-CCQE) components. On the right, the predicted events are separated into those where the ν_μ was produced in $\pi^+ \rightarrow \mu^+ \nu_\mu$ decays and those with a non-π^+ parent.

A normalization difference clearly exists between the predicted and measured ν_μ CCQE events. Fortunately, we can use the fitting tools and systematic error propagation techniques introduced in the previous two sections to study the ν_μ CCQE sample alone without incorporating the ν_e's. The covariance matrix is reduced to the lower right block in Figure 8.4 where only the correlations within the ν_μ distribution are considered. The χ^2 expression becomes

$$\chi^2 = \sum_{i,j}^{n_{\nu_\mu}} \left[N_i^{obs} - N_i^{pred} \right] E_{ij}^{-1} \left[N_j^{obs} - N_j^{pred} \right] \tag{8.17}$$
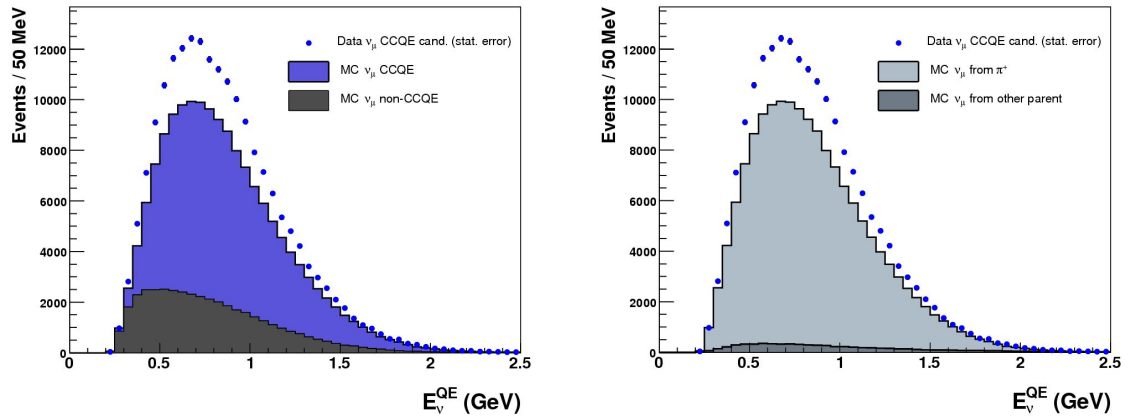
Figure 8.6: ν_μ charged-current quasi-elastic candidate events as a function of recon-structed E_ν^{QE}. Data and Monte Carlo are absolutely normalized to 5.58×10^{20} POT. Statistical errors are shown on the data but no systematic uncertainties are shown. The total Monte Carlo and the data are the same in both panels. The left panel separates Monte Carlo events into a signal (CCQE) and background (non-CCQE) component. The right panel divides the Monte Carlo into neutrinos with a π^+ parent and those with a different parent.

with no dependence on the oscillation parameters and the sums run only over ν_μ energy bins. Figure 8.7 shows the ν_μ distribution re-binned to the 8 E_ν^{QE} bins of the error matrix to be used in the oscillation fits. The systematic errors shown on the Monte Carlo are the square-root of the diagonal elements of the ν_μ covariance matrix. Using the full covariance matrix to compare absolutely normalized data and Monte Carlo, Eq. 8.17 yields a χ^2 per degree of freedom of $\chi^2/\mathrm{dof} = 6.8/8$, indicating good agreement within the estimated uncertainties.

Nonetheless, a systematic discrepancy between the observed and predicted ν_μ event rate is evident. We add a free parameter, f_π, to the χ^2 expression which scales only events where the ν_μ was created in $\pi^+ \to \mu^+ \nu_\mu$ decay (see Figure 8.6):

$$\chi^2(f_\pi) = \sum_{i,j}^{n_{\nu_\mu}} \left[\mathrm{N}_i^{\mathrm{obs}} - \left(f_\pi \cdot \mathrm{N}_i^{\mathrm{pred}}(\pi^+) + \mathrm{N}_i^{\mathrm{pred}}(\not\pi^+) \right) \right] E_{ij}^{-1} \left[\mathrm{N}_j^{\mathrm{obs}} - \left(f_\pi \cdot \mathrm{N}_j^{\mathrm{pred}}(\pi^+) + \mathrm{N}_j^{\mathrm{pred}}(\not\pi^+) \right) \right]$$

$$(8.18)$$
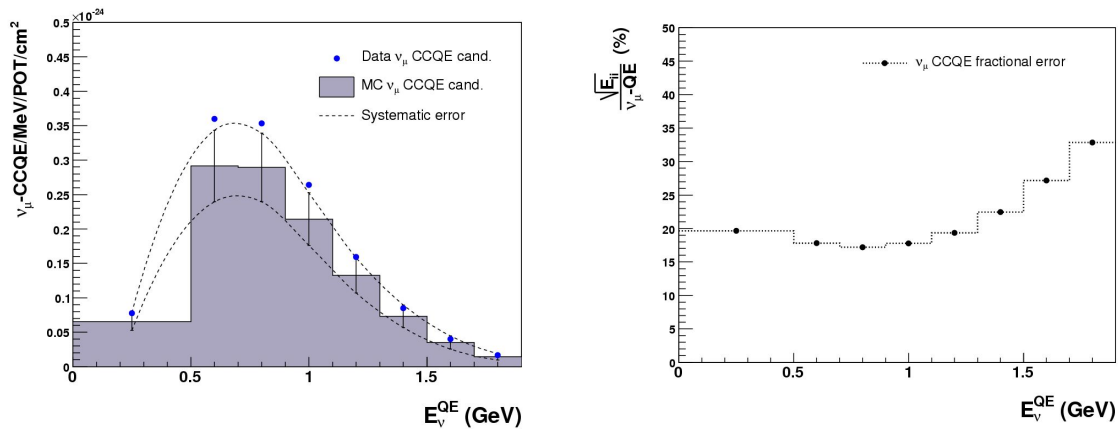
Figure 8.7: ν_μ charged-current quasi-elastic candidate events as a function of reconstructed E_ν^{QE} binned according to the error matrix to be used in the oscillation fit. Data and Monte Carlo are absolutely normalized to 5.58×10^{20} POT. Statistical errors are shown on the data but are smaller than the points. The systematic error band is generated from the square-root of the diagonal elements of the ν_μ CCQE total covariance matrix. The right panel shows these errors as a fraction of the total predicted number of events.

A fit is performed to minimize χ^2 with respect to f_π with the result shown in Figure 8.8. A value of $f_\pi = 1.19 \pm 0.21$ is preferred with a minimum $\chi^2/\mathrm{dof} = 4.6/7$. Note that we have lost a degree of freedom due to the new parameter f_π.

By including this new parameter we have, in effect, absorbed much of the data/Monte Carlo disagreement seen in the ν_μ CCQE events into the production of π^+ in the Booster Neutrino Beamline target. This is not necessarily a physics measurement - we do not purport to have measured π^+ production in beryllium using neutrino data - but rather a convenient way to handle a normalization discrepancy seen in ν_μ CCQE data. We will make the assumption, however, that the true cause(s) of the disagreement affect all events originating from π^+ in the beamline and will, therefore, scale all such events[2] by the same factor $f_\pi = 1.19$.

---

[2]This will not apply to event samples where the absolute rate has been measured in the data, namely the π^0, $\Delta \to N\gamma$ and dirt event rates.
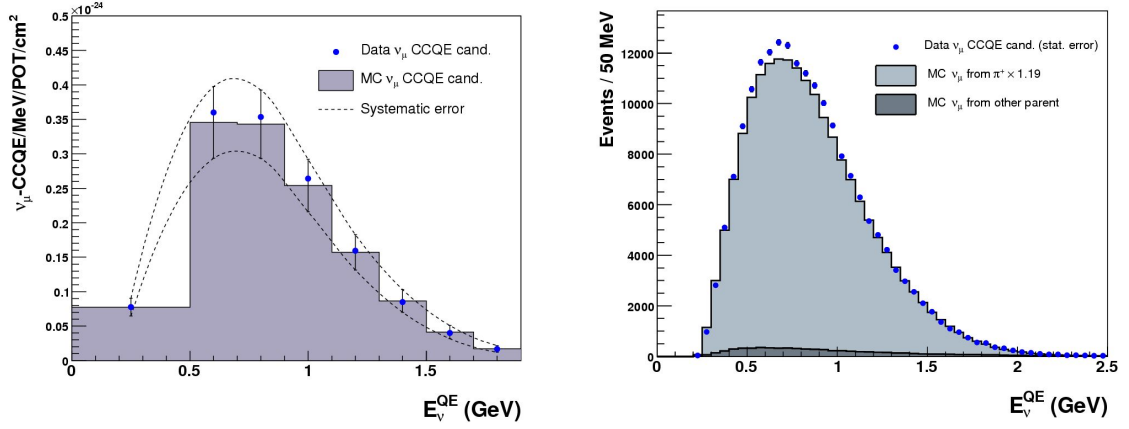
Figure 8.8: ν_μ charged-current quasi-elastic candidate events as a function of recon-structed E_ν^{QE} after fitting for the parameter f_π. Monte Carlo events where the neutrino parent is a π^+ have been scaled by $f_\pi = 1.19$.

8.5 ν_e CCQE sample and oscillation sensitivity - two possible selections

The following pre-cuts are used to begin to isolate a ν_e CCQE candidate sample in MiniBooNE data (see Section 6.3):

- Exactly 1 subevent (reject ν_μ CC events)

- $N_{\mathrm{tank}} > 200$ (reject Michel electrons)

- $N_{\mathrm{veto}} < 6$ (reject cosmics and out-of-tank events)

- Radius < 500 cm (fiducial volume)

- event in the beam window ($4400 < t < 6400$ ns)

In Section 7.5, we described a Boosted Decision Tree (BDT) algorithm developed to reject non-ν_e CCQE single subevent backgrounds, particularly ν_μ CCQE and NC π^0 events. Figure 8.9 shows the distribution of the BDT particle identification output score as a function of reconstructed[3] E_ν^{QE} for a sample of Monte Carlo ν_e charged-current quasi-elastic

---

[3]The neutrino energy has been reconstructed in all events using the quasi-elastic formula of Eq. 7.11 and assuming that the final state particle detected is an electron.
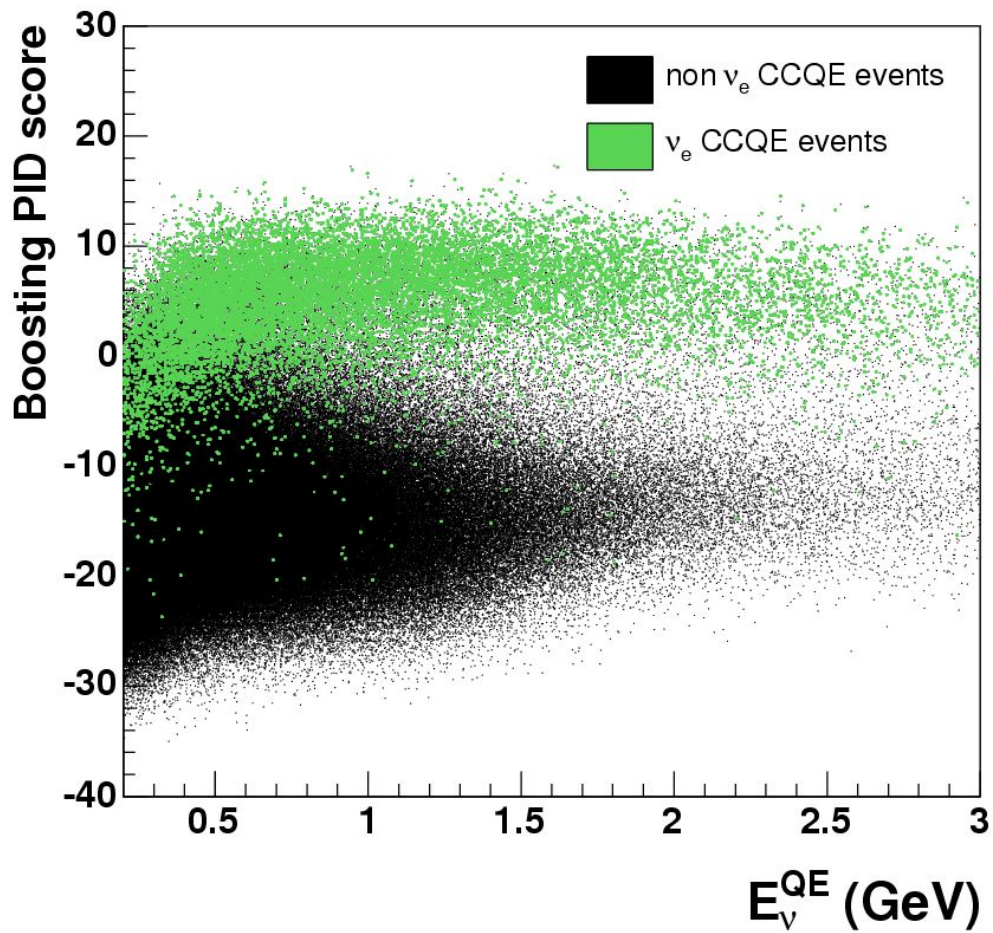
Figure 8.9: Distribution of the BDT PID score as a function of reconstructed E_ν^{QE} for ν_e CCQE events (green) and all other event types (black) in the ν_e pre-cuts sample. The two samples have been relatively normalized and the green has been plotted on top of the black, thus obscuring a portion of the background.

events (green) and all backgrounds (black) which have passed the ν_e pre-cuts above. We are now faced with the task of determining the cut positions in the BDT output variable as a function of reconstructed energy. Of the systematic uncertainties discussed in Section 8.3, only the detector model uncertainties have an effect on the signal efficiency or the background rejection rate of the algorithm. Therefore, it is with respect to the detector model uncertainties that we wish to optimize the cut positions in isolating ν_e quasi-elastic events.

Below we present two approaches to determining the BDT event selection. Both are based on Monte Carlo input only to avoid any bias introduced by using the data[4]. The intent in both approaches is to minimize the impact of the detector model systematic errors on the BDT selection efficiencies. They differ in the figure of merit (FOM) used to perform the optimization.

8.5.1   Optimization Strategy 1: Isolate intrinsic ν_e events

The first method treats each reconstructed E_ν^{QE} bin independently and determines the optimal BDT cut position for separating intrinsic ν_e events from non-ν_e backgrounds. The first E_ν^{QE} bin (0.2-0.4 GeV) used in the oscillation fits is divided into two 100 MeV bins when applying BDT selection cuts, making 9 total energy bins:

- $E_{\nu_e}^{\mathrm{QE}}(\mathrm{PID}) = [0.2, 0.3, 0.4, 0.6, 0.8, 1.0, 1.2, 1.4, 1.6, 3.0]$ GeV

Both the ν_μ mis-ID backgrounds and detector model uncertainties increase sharply at the lowest energies, so it was believed the extra freedom in the BDT cut at low energy would be beneficial.

---

[4]While we have blatantly ignored the interesting issue of "blindness" in this dissertation, the two methods of optimizing the ν_e event selection were both developed entirely using Monte Carlo before even looking at the ν_e data candidates. The blindness concept was used by MiniBooNE to eliminate any potential biasing of the ν_e appearance analysis. All event selections, background predictions, physics models, systematic errors and fitting routines were extensively studied and eventually fixed before we allowed ourselves to analyze the data ν_e candidates for evidence of oscillations. The official "unblinding" of the ν_e data was done using the analysis presented in this dissertation as well as another based on an independent event reconstruction, particle identification and ν_μ constraint/fitting algorithm [96] on March 26, 2007. Those initial results have been published in Physical Review Letters [66].

For each bin in E_ν^{QE}, our goal is to maximize the number of intrinsic ν_e CCQE events passing the selection, N_{ν_e}, relative to the systematic variation in the total number of events caused by the detector model uncertainties, $(\text{RMS})_{\text{All}}$:

$$\text{F.O.M.} = \frac{N_{\nu_e}}{(\text{RMS})_{\text{All}}} \tag{8.19}$$

Note there is no consideration of the particular signal we are looking for ($\nu_\mu \to \nu_e$ oscillation events) in this approach; we are simply maximizing the significance of the ν_e event selection by using the intrinsic ν_e background prediction. A significant excess of ν_e events in the data above this prediction would then be attributed to oscillations.

We can build our figure of merit of Eq. 8.19 by using the 66 Monte Carlo samples produced for constructing the detector model covariance matrix, E^{det}. By applying a given cut in the BDT output variable to each sample, we calculate the average number of intrinsic ν_e CCQE events that are selected, and also the RMS of *all* events passing the same cut from the spread in the 66 samples. The ratio of Eq. 8.19 can then be mapped as a function of the BDT variable cut position in each bin of E_ν^{QE}.

The result is shown in Figure 8.10. The nine panels correspond to the nine bins of reconstructed energy where we will select a unique cut position. In each panel, the black histogram shows how the FOM of Eq. 8.19 changes as a function of cut location. From the left axis labels one can read off the significance of the intrinsic ν_e selection in the bin for a given BDT cut. In each bin there is a clear peak in the distribution where we choose to set the BDT cut in order to maximize our figure of merit in that energy range. The other curves shown (which use the right axis labels) illustrate how the fractions of signal (red) and background (blue dashed) events which pass the selection changes with the cut position.

Figure 8.11 shows the set of cuts determined by this method plotted over the 2-dimensional (BDT vs. E_ν^{QE}) distribution of signal and background events. The efficiency of these cuts has been calculated as a function of E_ν^{QE} for signal (ν_e CCQE events) and two important backgrounds (NC π^0 and ν_μ CCQE events) and is shown in the right panel. At the lowest point, near 500 MeV, the BDT cut rejects 99.8% of NC π^0 events and 99.95% of ν_μ CCQE events which have passed ν_e pre-cuts while maintaining $\sim$ 30% efficiency for ν_e CCQE
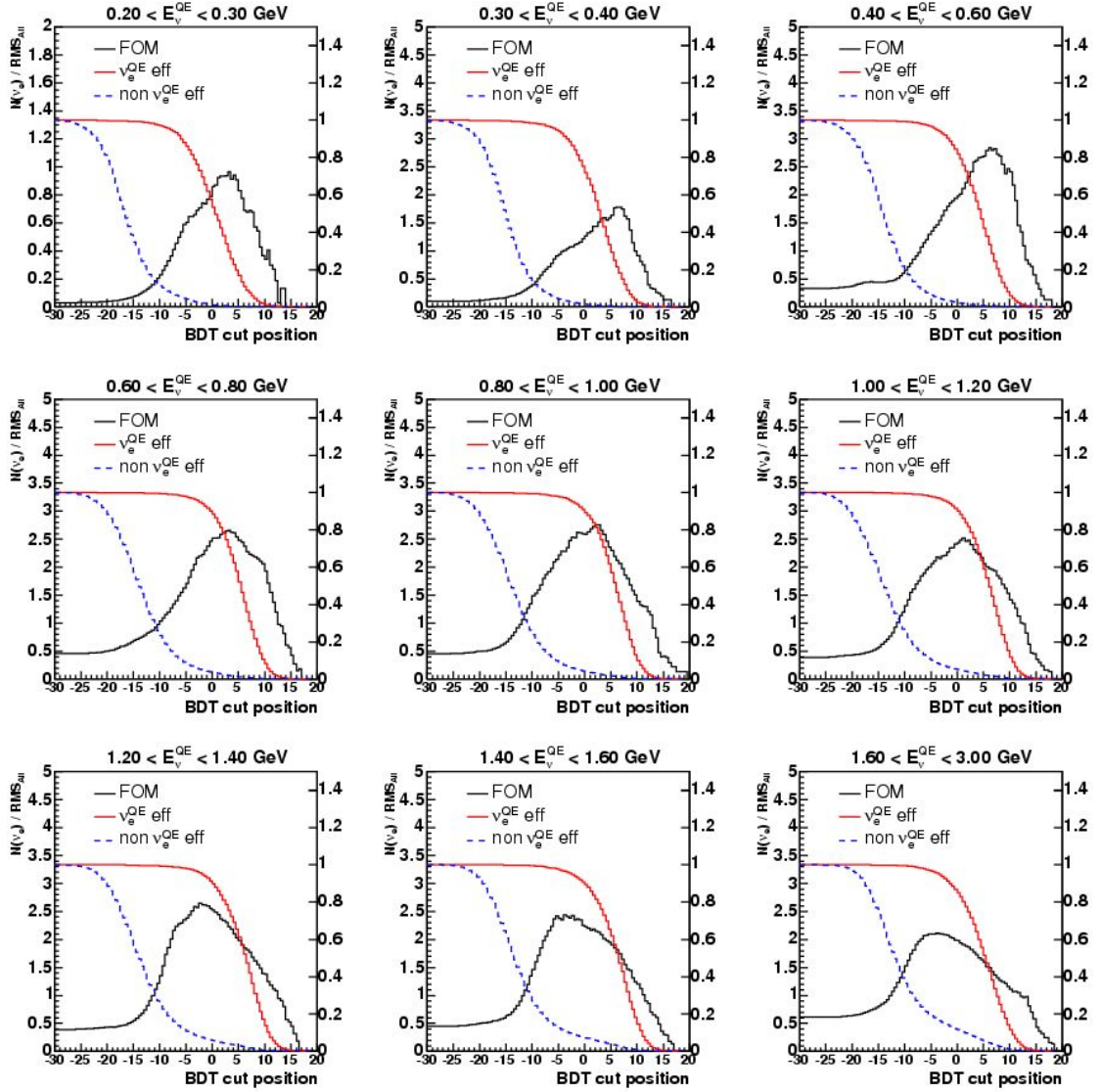
Figure 8.10: The figure of merit of Eq. 8.19 as a function of the BDT output score cut position (black histogram) in nine different bins of reconstructed E_ν^{QE}. Also shown (using the right axis labels) are the signal (red) and background (blue dashed) efficiency as a function of the cut value.
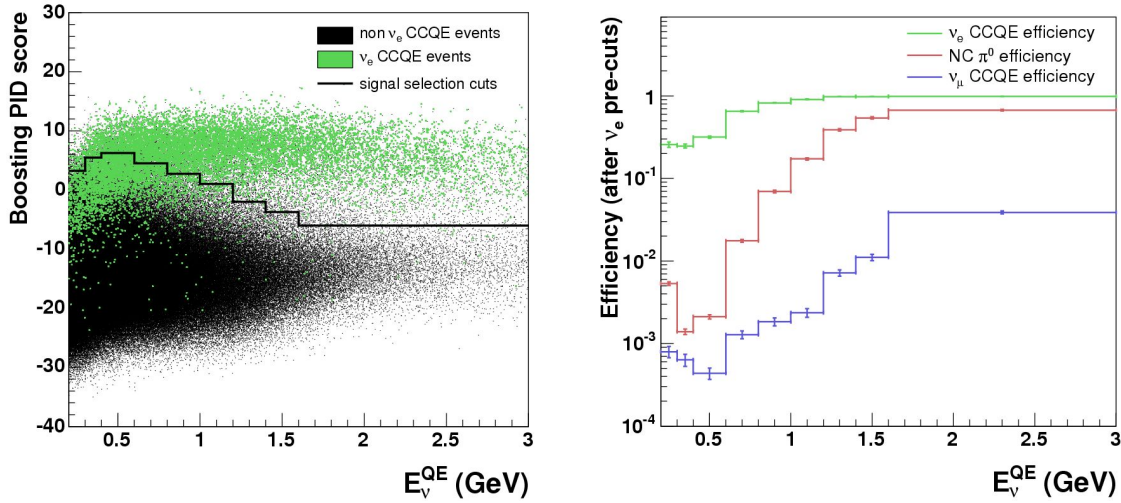
Figure 8.11: The left panel shows the BDT score cuts as a function of reconstructed E_ν^{QE} optimized for separating intrinsic ν_e events from non-ν_e backgrounds. The right is the corresponding efficiencies for three types of events: ν_e CCQE events, NC π^0 events, and ν_μ CCQE events.

events. The cuts loosen and the ν_e efficiency steadily rises to nearly 100% at high energy.

The predicted event distribution for this set of cuts is presented in Figure 8.12. The Monte Carlo has been normalized to 5.58×10^{20} POT, so the plot shows an absolute prediction. The error bars are the square-root of the diagonal elements of the total error matrix of Eq. 8.13 before applying the constraint from the high statistics ν_μ CCQE sample. The dashed curves show the effect of the ν_μ constraint for comparison. The ν_μ mostly provide a constraint on the rate of ν_e from muon decay since the correlation between these samples is strong.

Figure 8.13 presents the sensitivity of this event selection and analysis methods to $\nu_\mu \to \nu_e$ oscillations. All systematic and statistical errors as well as the constraint from the ν_μ CCQE sample are considered in the generation of the 90% C.L. sensitivy curve shown in the top figure. The bottom panel provides valuable information about the relative impact of the various systematic uncertainties. The sensitivity is shown for different subsets of the total error matrices of Eq. 8.13. The blue line shows the 90% C.L. sensitivity curve if only the statistical uncertainty of the data is considered and represents an absolute upper limit
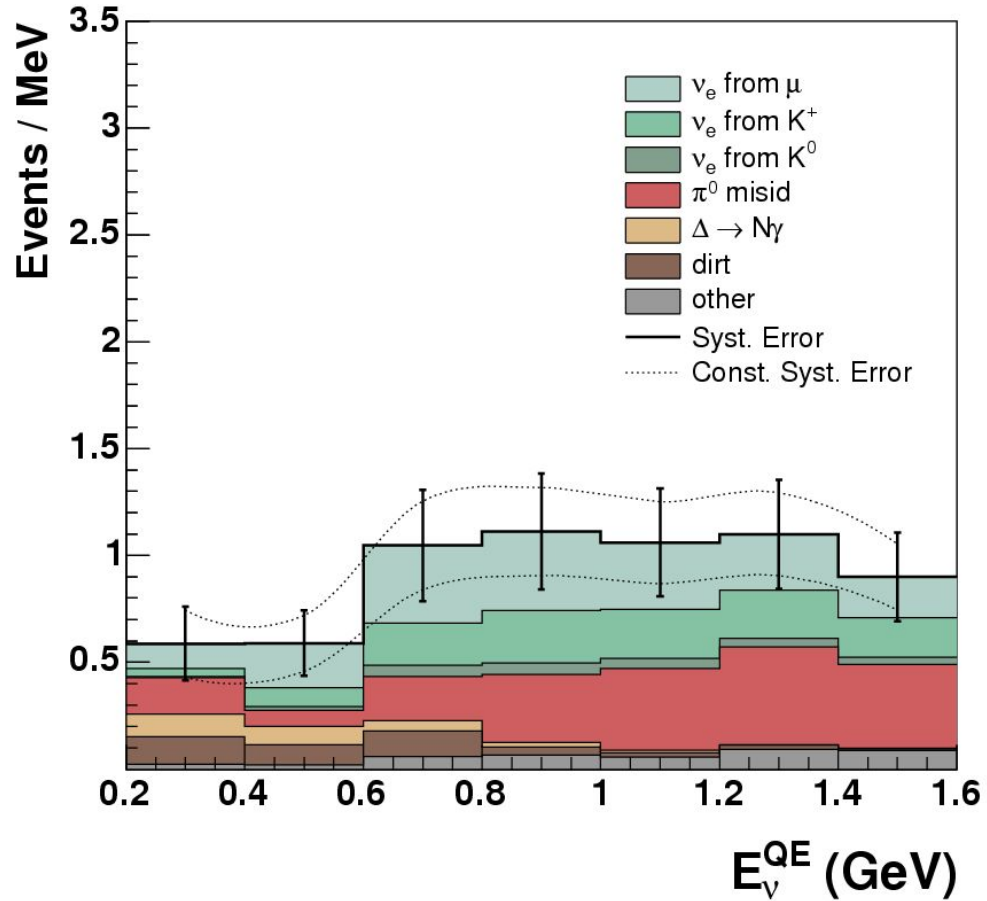
Figure 8.12: Monte Carlo prediction for events passing the ν_e BDT selection cuts optimized for separating intrinsic ν_e events from non-ν_e backgrounds. The prediction has been absolutely normalized to 5.58×10^{20} POT to match the neutrino data set. The error bars shown are the square-root of the diagonals of the total covariance matrix before any constraint from the ν_μ CCQE sample. The dashed curves are the errors after the ν_μ constraint is applied which mostly affects the intrinsic ν_e's from muons (top green band).
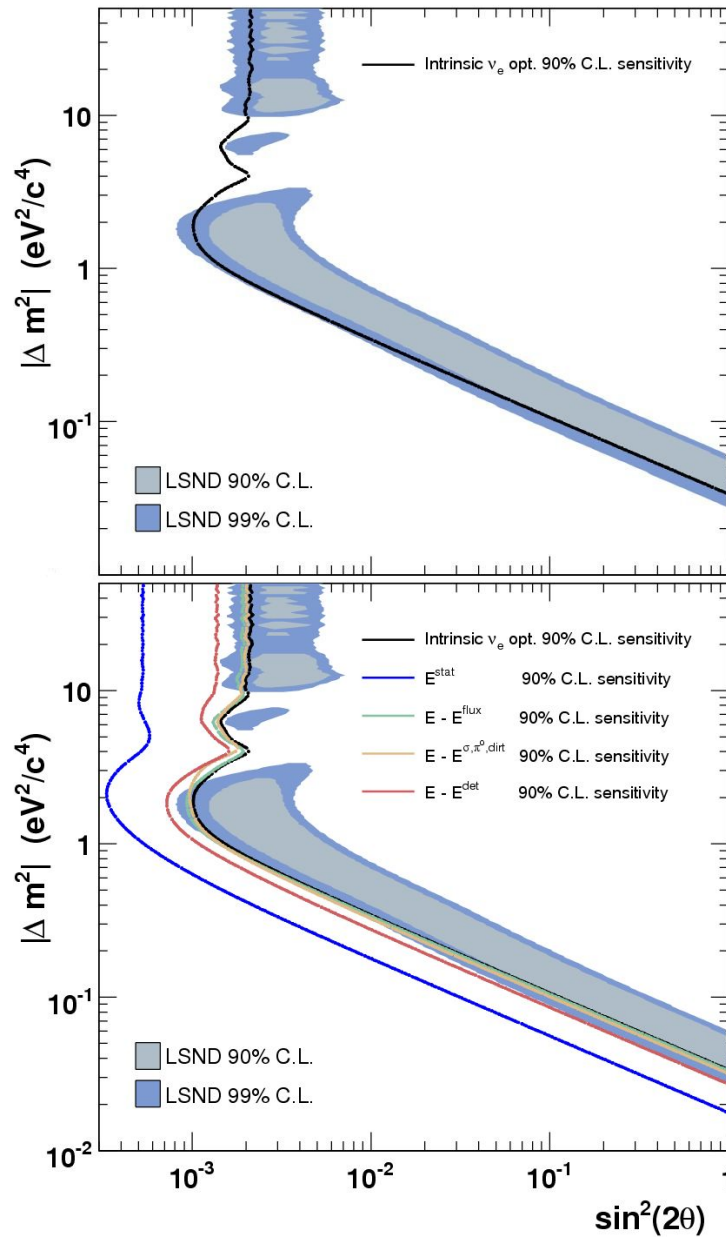
Figure 8.13: Sensitivity to $\nu_\mu \rightarrow \nu_e$ oscillation parameters $(\Delta m^2, \sin^2(2\theta))$ using the ν_e BDT selection cuts optimized for separating intrinsic ν_e events from non-ν_e backgrounds. The top plot shows the 90% C.L. sensitivty curve including all statistical and systematic uncertainties. The bottom plot shows the 90% C.L. sensitivity considering different subsets of the error matrices. The sensitivity with statistical errors only is shown by the blue curve. The green and orange curves show the result of removing all flux related errors and neutrino interaction errors, respectively. The red curve is for all errors except the detector optical model errors.

for the data available. The black curve is a reproduction of the full sensitivity from above. If all flux related errors ($E^{\pi^+}, E^{\pi^-}, E^{\mathrm{K}^+}, E^{\mathrm{K}^0}, E^{\mathrm{beam}}$) are ignored the sensitivity is given by the gold curve. If the neutrino cross-section model errors, the π^0 rate measurement errors and the error on the dirt event rate ($E^\sigma, E^{\pi^0}, E^{\mathrm{dirt}}$) are all ignored, then the resulting sensitivity is shown by the green line. Both curves are barely different from the final sensitivity.

The red sensitivity curve, however, is the result of removing only a single matrix, the detector optical model error matrix, E^{det}. Here we see a noticeable improvement in the oscillation sensitivity implying that the detector model errors have the single largest impact on the sensitivity of this analysis. While the simple optimization described here produces a decent coverage of the relevant oscillation parameter space, we nonetheless explore one more possibility at reducing the impact of the optical model variations on the analysis.

8.5.2   Optimization Strategy 2: Maximize sensitivity to $\nu_\mu \to \nu_e$ oscillations

The second method of determining the BDT ν_e selection cuts will not treat the E_ν^{QE} bins independently, but rather will compare the sensitivity to $\nu_\mu \to \nu_e$ oscillations of *sets of cuts* and seek to find the set with the maximum sensitivity. Again, we will consider only the detector optical model systematic uncertainty as it is the dominant effect in reducing the sensitivity of the analysis. While the strategy is rather straight forward, the process is quite involved. Below we provide a detailed description of the steps:

1. Randomly select a set of 9 BDT cut values for the 9 E_ν^{QE} (PID) bins listed in the previous section.

2. Apply this set of cuts to the high statistics (7.9× data POT) central value Monte Carlo which has already been filtered through ν_e pre-cuts to generate a ν_e CCQE candidate sample.

3. Apply the same cuts to the central value full-osc Monte Carlo which has been modulated by $\sin^2(1.267\,\Delta m^2\,0.541\,\mathrm{km}/E_\nu)$ for the value of $\Delta m^2 = (\Delta m^2)^{\mathrm{opt}}$ for which you wish to optimize the analysis.

4. Apply the same BDT cuts to the 66 Monte Carlo samples corresponding to the 66 detector model parameter variations.

5. Use the central value and 66 detector model variations of ν_e candidates along with the central value and detector model variations of the ν_μ CCQE sample to build the (ν_e, ν_μ) blocks of the covariance matrix, E^{det}, as in Eq. 8.16.

6. Calculate χ^2 using Eq. 8.1 and $((\Delta m^2)^{\mathrm{opt}}, 0)$ for oscillation parameters. This is the reference χ^2 value corresponding to no signal, χ^2_{null}.

7. Increase $\sin^2(2\theta)$ in steps, scale the full-osc sample accordingly to generate a test signal, and recalculate χ^2 until $\Delta\chi^2 = \chi^2 - \chi^2_{\mathrm{null}} \geq 9.0$. This is the value of $\sin^2(2\theta) \equiv (\sin^2(2\theta))^{3\sigma}$ that sits on the 3σ sensitivity curve for this set of BDT cuts at $(\Delta m^2)^{\mathrm{opt}}$.

8. Repeat steps 1–7 N times where $N \to \infty$ and compare the 3σ crossing points for all sets of cuts. Select the set with the smallest value of $\sin^2(2\theta)$ which sits on the 3σ sensitivity curve (furthest to the left on the oscillation parameter space plots).

We make two important modifications to the procedure outlined above:

- The problem described above is one of function minimization. The figure of merit we wish to minimize is the value of the mixing angle for which we have 3σ sensitivity, $(\sin^2(2\theta))^{3\sigma}$, and it depends (albeit, in a very complicated way) on the set of 9 BDT cut positions used to select the ν_e candidate sample. The "brute-force" approach of repeating the procedure N times with a new set of 9 random cut values is far from optimal. We, therefore, embed the calculation of steps 2–7 within the FCN routine of the MINUIT function minimization software package [132]. MINUIT is then used to explore the 9-dimensional parameter space and seek the set of cut positions which yields the minimum value of $(\sin^2(2\theta))^{3\sigma}$.

- We wish to optimize the analysis for detecting $\nu_\mu \to \nu_e$ oscillations, but not necessarily for a particular value of Δm^2. The range in Δm^2 allowed by the LSND data spans several orders of magnitude and we would like to avoid biasing the analysis to a precise value. To do this we define a new figure of merit which depends on the

sensitivity at multiple Δm^2 values:

$$\text{F.O.M.} = \sum_{\Delta m_i^2} \frac{(\sin^2(2\theta))^{3\sigma}}{W_{\Delta m_i^2}} . \tag{8.20}$$

Typically, 2–3 values of Δm^2 are used which are spaced appropriately through the allowed region. The weighting factors, $W_{\Delta m_i^2}$, are used to normalize the contributions from the different Δm^2 to the total figure of merit since the absolute value of $(\sin^2(2\theta))^{3\sigma}$ can vary widely at different values of Δm^2, as is obvious from Figure 8.13.

We have applied the above procedure combining the sensitivities at $\Delta m^2 = 0.4$ eV^2 and 1.8 eV^2 in the FOM of Eq. 8.20. The results are displayed in Figures 8.14 through 8.17.

The BDT cuts and selection efficiencies are shown in 8.14 and 8.15. The optimization has had two noticeable effects on the cut values relative to the optimization strategy of Section 8.5.1. First, the ν_e selection efficiency between 300–1400 MeV has become fairly flat in the 60–70% range. For our previous selection, the ν_e efficiency rose steadily from 25% to 95% in this same range. Second, the optimization has relaxed the cut in the 200-300 MeV energy bin to a BDT score of -10.8. This causes the first energy bin to be flooded with ν_μ-induced backgrounds as seen in the top panel of Figure 8.16.

This surprising result can be understood by comparing the left and right panels of Figure 8.14. These plots illustrate the change in our definition of "signal" in the two optimization strategies presented. The left plot shows the intrinsic ν_e CCQE events (green points) compared to all other predicted event types (black points), as before. In the right plot, the green points are ν_e CCQE events for ν_e's from a 1% (flat in energy) $\nu_\mu \to \nu_e$ oscillation. The black points are all backgrounds to the oscillation search including intrinsic ν_e-induced events. The two distributions are *absolutely* normalized to the same number of protons on target.

Note the clustering of signal events in the ~ 300–1400 MeV range in the right panel of Figure 8.14. Also, as mentioned previously, the ν_μ-induced backgrounds and, along with them, the systematic uncertainties increase sharply at low reconstructed E_ν^{QE}. But these backgrounds tend to be strongly correlated as a function of energy. Therefore, the loose

BDT cut in the 200-300 MeV E_ν^{QE} bin provides a high statistics constraint on the level of ν_μ-induced backgrounds (NC π^0, $\Delta \rightarrow \mathrm{N}\gamma$, and dirt events) in the same way that the high statistics ν_μ CCQE sample provides a constraint on the rate of intrinsic ν_e events from muon decays in the beam - through the covariance matrix used in the oscillation fit. The lack of oscillation signal events in this energy range means the benefit of this constraint far outweighs the damage done by reducing the likelihood of seeing a significant excess in the first energy bin.

Figure 8.16 shows the predicted distribution of ν_e candidate events for this set of BDT cuts. The bottom panel simply reduces the energy range shown in order to highlight the prediction in the region where we expect to look for oscillation events. The dotted histogram shows the expected excess of events for a possible set of oscillation parameters, $(\Delta m^2, \sin^2(2\theta)) = (1.2 \, \mathrm{eV}^2, 0.003)$, the LSND best-fit values.

The oscillation sensitivity curve for this selection, considering all sources of experimental uncertainty, is shown in Figure 8.17. The bottom panel of Figure 8.17 compares directly the 90% C.L. sensitivities of the two ν_e event selection strategies presented. This latter strategy creates a significant improvement in the oscillation sensitivity for $\Delta m^2 \leq 1 \, \mathrm{eV}^2$.

8.6   Verifying the simulation in a BDT sideband

In this section, we take our first look at the neutrino data for events having passed the ν_e pre-cuts listed at the start of Section 8.5. Rather than looking immediately in the ν_e candidate region as defined by the BDT cuts determined in the previous section, we choose to inspect first a "sideband" region just outside of these cuts. The intent is to verify the simulation and systematic error estimates as well as test the fitting algorithms using a sample of real data events.

To perform the test we define a new set of cut positions in the BDT score variable as shown by the blue line in the upper left panel of Figure 8.18. For the set of events which fall *between* the blue and black cut lines, we select events in the data and generate a central value Monte Carlo prediction. We also calculate the full set of systematic error matrices
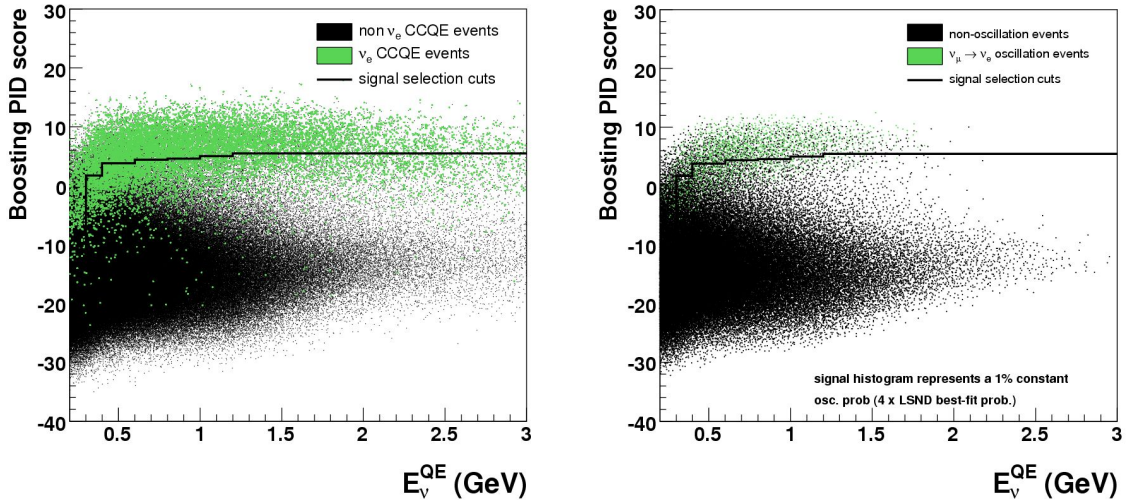
Figure 8.14: BDT score cuts as a function of reconstructed E_ν^{QE} optimized for sensitivity to oscillation signal events. The left panel compares the cuts to relatively normalized ν_e CCQE (green points) and non-ν_e backgrounds (black points) as before. In the right panel, the green points represent a 1% flat probability oscillation signal. The black points are all backgrounds to the oscillation search including intrinsic ν_e-induced events. The two distributions are *absolutely* normalized to the same POT.
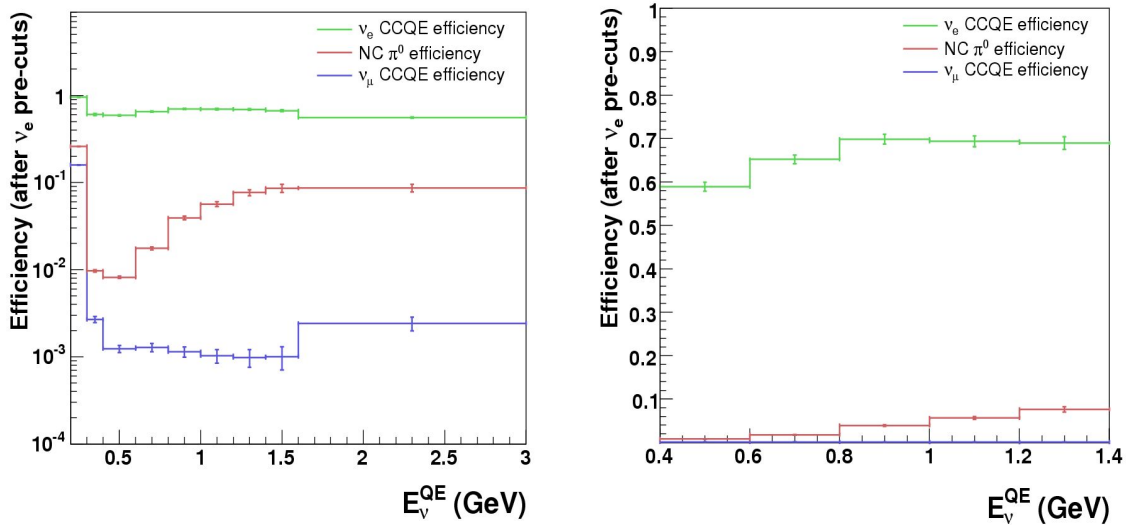
Figure 8.15: Selection efficiencies for three types of events: ν_e CCQE events, NC π^0 events, and ν_μ CCQE events for the BDT cuts optimized for sensitivity to oscillation signal events.
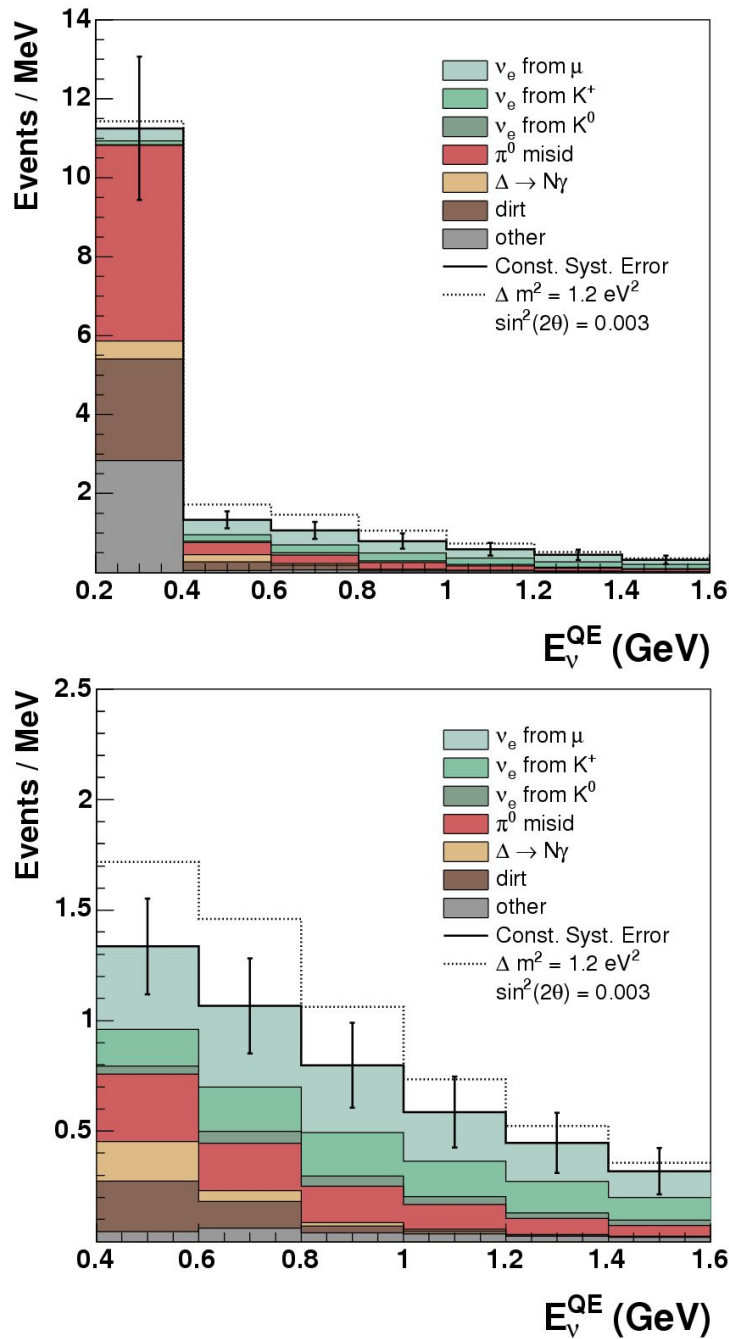
Figure 8.16: Monte Carlo prediction for events passing the ν_e BDT selection cuts optimized for sensitivity to oscillation signal events. The prediction has been absolutely normalized to 5.58×10^{20} POT to match the neutrino data set. The error bars shown are the square-root of the diagonals of the total covariance matrix after constraint by the ν_μ sample. The dotted histogram is the expected number of signal events for oscillation parameters $(\Delta m^2, \sin^2(2\theta)) = (1.2\,\mathrm{eV}^2, 0.003)$, the LSND best-fit point.
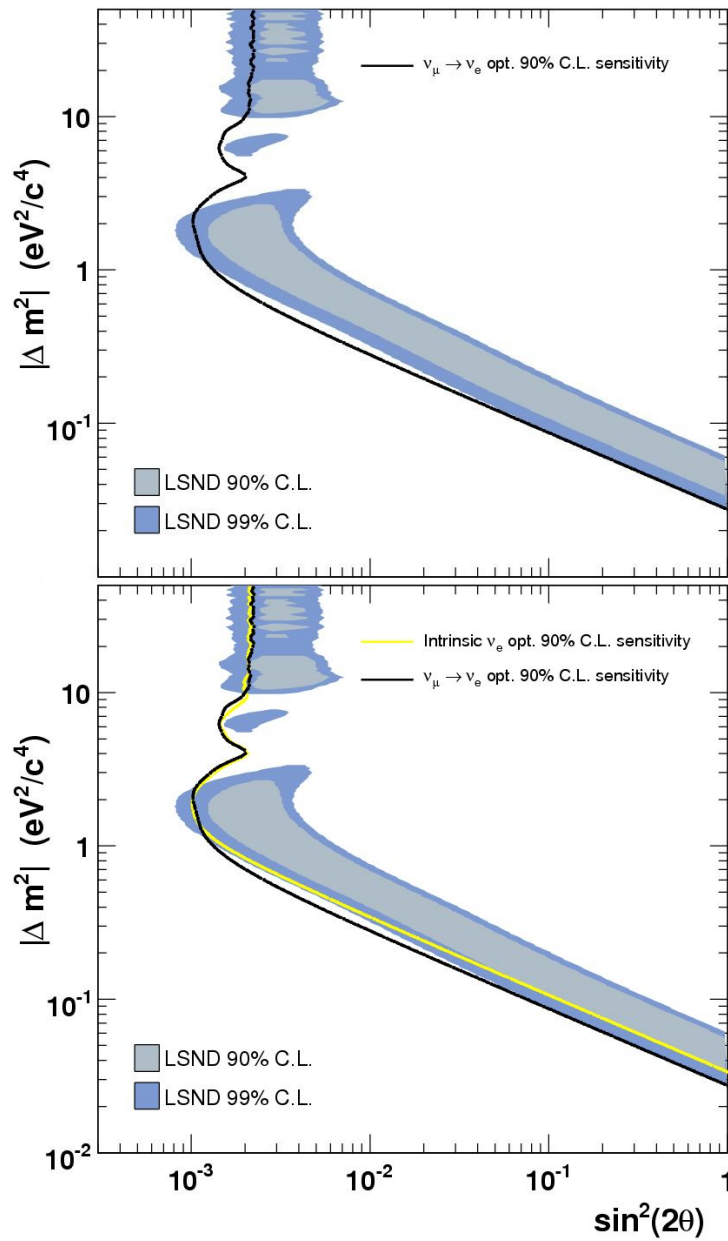
Figure 8.17: Sensitivity to $\nu_\mu \to \nu_e$ oscillation parameters $(\Delta m^2, \sin^2(2\theta))$ with the BDT selection cuts optimized for sensitivity to oscillation signal events. The top plot shows the 90% C.L. sensitivty curve including all statistical and systematic uncertainties. The bottom plot compares the sensitivity of this selection to that of the selection optimized using intrinsic ν_e events described in Section 8.5.1.

listed in Eq. 8.13 to enable a quantitative comparison of data and prediction.

The upper right panel of Figure 8.18 shows the absolutely normalized data and Monte Carlo prediction in the sideband region. The Monte Carlo prediction is dominated by NC π^0 events (red). The gray band, labeled "other" is mostly ν_μ quasi-elastic events. The figure also shows the effects of the high statistics ν_μ sample on the ν_e background prediction. In Figure 8.8 there is a residual discrepancy between the ν_μ data and Monte Carlo even after scaling the prediction by $f_\pi = 1.19$. In the peak of the distribution, the Monte Carlo sits a few percent below the data such that $\Delta_{\nu_\mu} = N_{\nu_\mu}^{\text{obs}} - N_{\nu_\mu}^{\text{pred}} < 0$. The positive correlation with both the ν_e from muon decay and, more importantly in the sideband, the ν_μ quasi-elastic background, will act to pull up the prediction a few percent. The colored stacked histograms are the absolute prediction before any adjustment based on the ν_μ's. The solid histogram with systematic error bars is the final Monte Carlo prediction after incorporating information from the ν_μ CCQE data/Monte Carlo disagreement.

The χ^2 statistic is calculated according to equation 8.1 to be $\chi^2/\text{dof} = 7.1/15$. The 15 degrees of freedom are calculated from +8 ν_μ bins (see Figure 8.7), +8 ν_e bins (the 1.6–3.0 GeV bin is not shown in Figure 8.18) and -1 for the parameter $f_\pi = 1.19$ which multiplies events with a π^+ parent.

Finally, the bottom panel in Figure 8.18 shows the projection onto the BDT score axis for events in the energy range 400–1400 MeV. The data and Monte Carlo are absolutely normalized to the data POT. ν_e events from muon decays and ν_μ quasi-elastic events have been scaled up by $f_\pi = 1.19$. The error bars shown are the data statistical errors only and no systematic errors are presented. Above the absolute distributions is the data/Monte Carlo ratio as a function of the BDT variable. A flat line fit to the ratio yields $R = 1.02 \pm 0.02$ considering only statistical uncertainties.

The plots of Figure 8.18 demonstrate a very successful test of the simulation and fitting methods in a sample of nearest-neighbors to the potential signal events. We now proceed to analyzing the ν_e candidate events and searching for evidence of $\nu_\mu \to \nu_e$ oscillations in the MiniBooNE data.
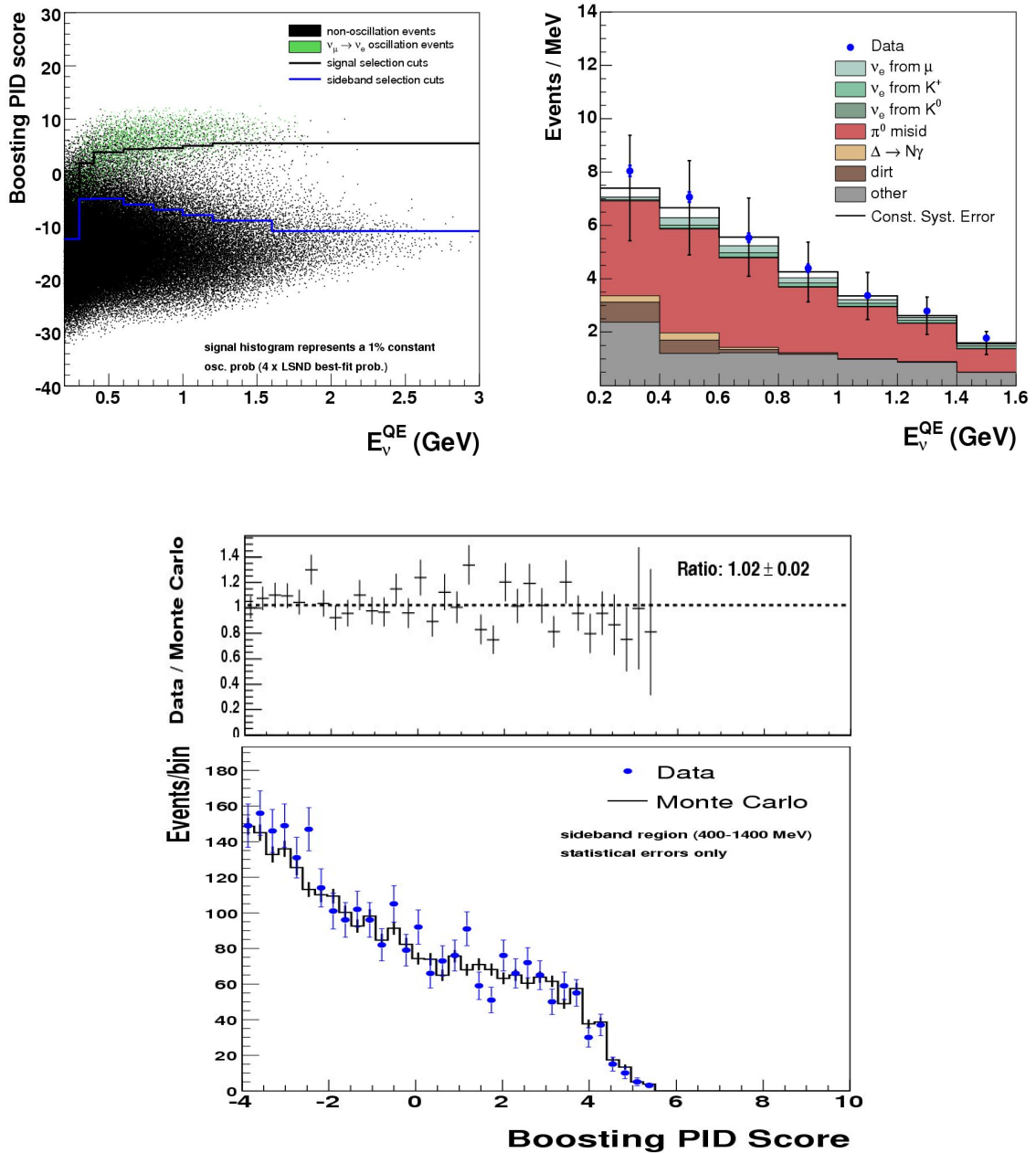
Figure 8.18: BDT "sideband" test. The sideband is defined in the upper left panel as the events between the blue and black curves. Absolutely normalized data and Monte Carlo are compared in the top right panel. Using the full covariance matrix and the ν_μ constraint the $\chi^2/\mathrm{dof} = 7.1/15$. The bottom panel shows a projection onto the BDT score axis for events in the energy range 400–1400 MeV and the Data/MC ratio. A flat line fit to the ratio yields $R = 1.02 \pm 0.02$ with statistical errors only.

8.7 Oscillation results

With the analysis tools vetted and all systematic uncertainties estimated, we turn to the ν_e candidate events in the MiniBooNE data. We present comparisons of data and Monte Carlo for both sets of BDT event selection cuts[5] presented in Section 8.5. It should be noted, however, that these are in no way independent samples. The events selected by one set of cuts are necessarily a sub-set of the other, depending on which has a tighter BDT cut in each energy bin. While the relative normalization and shape difference between the data and Monte Carlo in the two samples will have subtle impacts on the oscillation fit, the general conclusions, to be at all conclusive, must be the same.

Tables 8.4 and 8.5 report basic information from the oscillation fits performed for the two samples (BDT 1 = intrinsic ν_e optimization, BDT 2 = oscillation ν_e optimization). The total number of predicted and observed ν_e candidate events is given in the reconstructed energy range 200–1600 MeV. For the BDT 2 selection we separate these into a 200–400 MeV and a 400–1600 MeV region because of the loose cut in the low-energy bin. The total systematic uncertainty on the prediction is calculated by summing over the elements of the error matrix. The error on the number of observed events is just $\sqrt{N}$ of the data. The difference in the total number of events (Data - MC) is listed in the last column with total statistical and systematic uncertainties added in quadrature. This single number provides a first indication of whether there is evidence of neutrino oscillations in the MiniBooNE data. For both samples, the total numbers of predicted and observed events agree within the uncertainties.

Table 8.5 lists the relevant χ^2 values determined in the oscillation fit:

- χ^2_{null} – the value of the χ^2 statistic of Eq. 8.1 when comparing the data and Monte Carlo without adding any signal component to the prediction. The error matrix used also contains no signal component, $E_{\text{null}} \equiv E(0,0)$.

- $\chi^2_{\text{best-fit}}$ – the minimum value of the χ^2 statistic determined by fitting for oscillation parameters. The error matrix used is that from the last iteration of the fitting routine

---

[5]Originally, the ν_e data were unblinded in March, 2007 using cuts optimized by the 2nd method of Section 8.5.2 only and not by the cuts optimized to isolate intrinsic ν_e's.

ν_e **sample**	E_ν^{QE} (MeV)	**MC events**	**Data events**	**Data - MC**
BDT 1	200-1600	1372 ± 228	1192 ± 35	$-180 \pm 231 \, (0.78\sigma)$
BDT 2	400-1600	985 ± 198	788 ± 28	$-197 \pm 200 \, (0.98\sigma)$
BDT 2	200-400	2346 ± 364	2582 ± 51	$+236 \pm 368 \, (0.64\sigma)$

Table 8.4: Total numbers of predicted and observed events in the ν_e candidate samples in the range $200 \leq E_\nu^{\mathrm{QE}} \leq 1600$ MeV. BDT 1 = intrinsic ν_e optimized cuts presented in Section 8.5.1. BDT 2 = oscillation ν_e optimized cuts from Section 8.5.2.

ν_e **sample**	E_ν^{QE} (MeV)	$\chi^2_{\mathrm{null}}/\mathrm{dof}$ (Prob.)	$\chi^2_{\mathrm{best-fit}}/\mathrm{dof}$ (Prob.)	$(\Delta m^2, \sin^2(2\theta))_{\mathrm{best-fit}}$
BDT 1	200-3000	$10.17/15 \, (80.9\%)$	$10.16/13 \, (68.1\%)$	$0.01 \, \mathrm{eV}^2, 0.16$
BDT 2	200-3000	$11.90/15 \, (68.7\%)$	$10.81/13 \, (62.7\%)$	$7.56 \, \mathrm{eV}^2, 0.0014$

Table 8.5: χ^2 values from the oscillation fits. See the text for definitions of χ^2_{null}, $\chi^2_{\mathrm{best-fit}}$, and $(\Delta m^2, \sin^2(2\theta))_{\mathrm{best-fit}}$.

(see Section 8.2.4).

- $(\Delta m^2, \sin^2(2\theta))_{\mathrm{best-fit}}$ – the best-fit oscillation parameters corresponding to $\chi^2_{\mathrm{best-fit}}$.

In neither case is the best-fit χ^2 a significant improvement over the null hypothesis case.

The energy distributions of events are shown in Figures 8.19 and 8.20 for the BDT 1 and BDT 2 samples, respectively. No evidence of an excess of ν_e events is seen. For each, therefore, we calculate a limit on the $\nu_\mu \rightarrow \nu_e$ oscillation hypothesis as a function of Δm^2 at 90% C.L. The 90% C.L. contours shown in the right panels of the figures have been determined by calculating the value of $\sin^2(2\theta)$ at each Δm^2 for which the χ^2 increases by $\Delta\chi^2 = \chi^2 - \chi^2_{\mathrm{null}} = 1.64$ units.

One final way of expressing the level of data/Monte Carlo agreement in the Mini-BooNE data is shown in Figure 8.21. The plots show the data event excess over prediction in all ν_μ and ν_e CCQE candidate energy bins. For the majority of the ν_e energy bins, of course, we see a systematic deficit, but in almost every bin the data and prediction agree
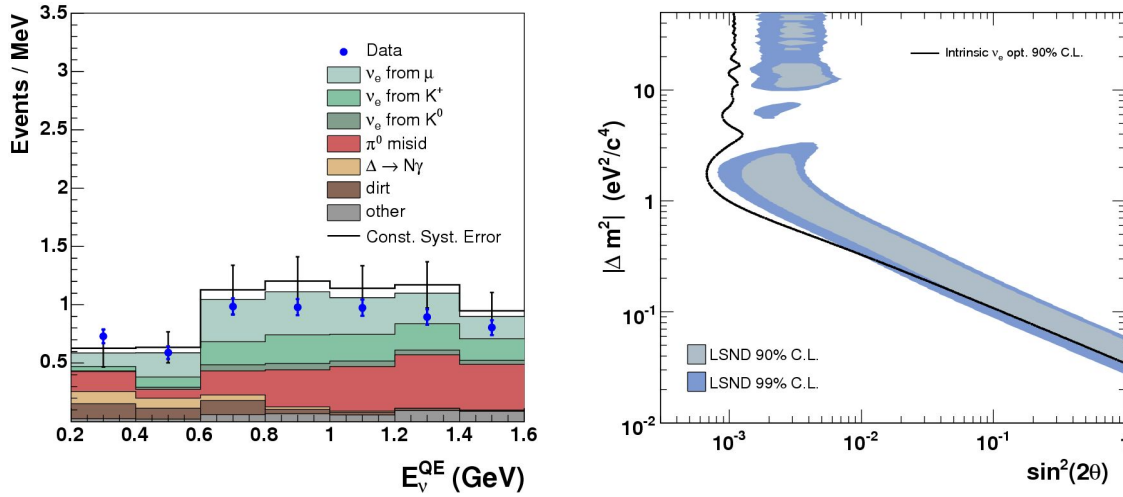
Figure 8.19: Comparison of observed and predicted event rates in the ν_e CCQE candidate region selected using the BDT cuts optimized for separating intrinsic ν_e from non-ν_e backgrounds (BDT 1). The right panel shows the resulting 90% C.L. limit on $\nu_\mu \to \nu_e$ oscillations set by these data.
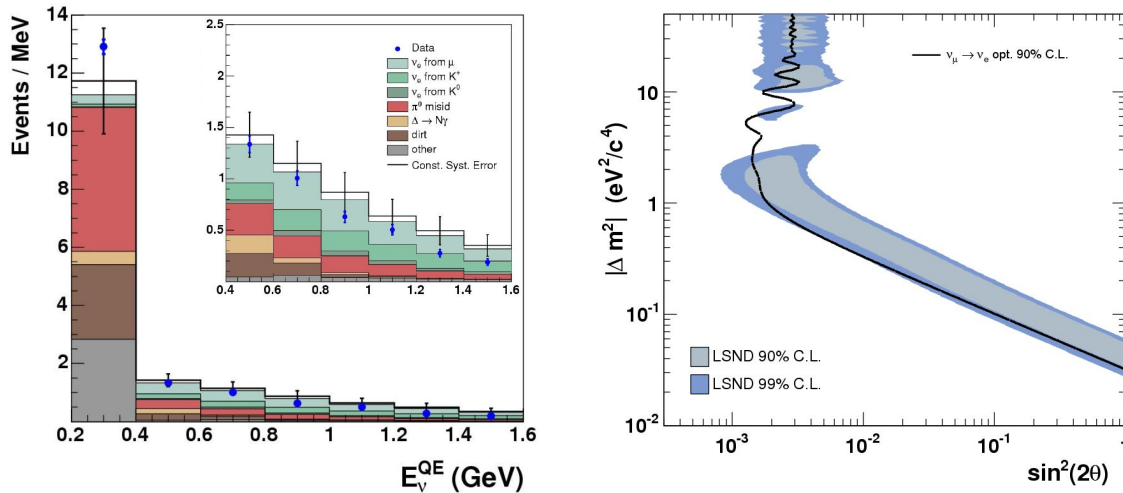
Figure 8.20: Comparison of observed and predicted event rates in the ν_e CCQE candidate region selected using the BDT cuts optimized for separating oscillation events from non-oscillation backgrounds (BDT 2). The right panel shows the resulting 90% C.L. limit on $\nu_\mu \to \nu_e$ oscillations set by these data.
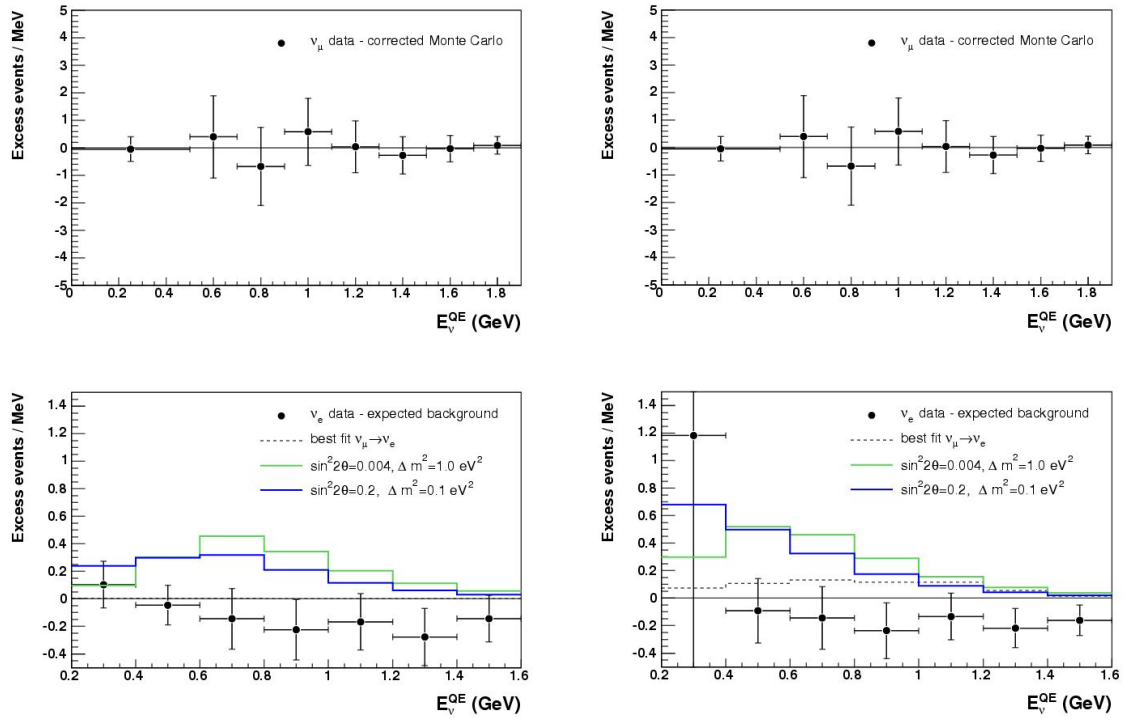
Figure 8.21: Data - MC event excesses for ν_μ (top) and ν_e (bottom) CCQE candidates selected using the BDT cuts optimized for separating intrinsic ν_e from non-ν_e backgrounds (left) and those optimized for separating oscillation events from non-oscillation backgrounds (right). The error bars shown are the square-root of the diagonals of the error matrix and include all statistical and systematic uncertainties. The green and blue histograms show the expectations for two different sets of oscillation parameters in the LSND allowed region.

within the estimated uncertainties.
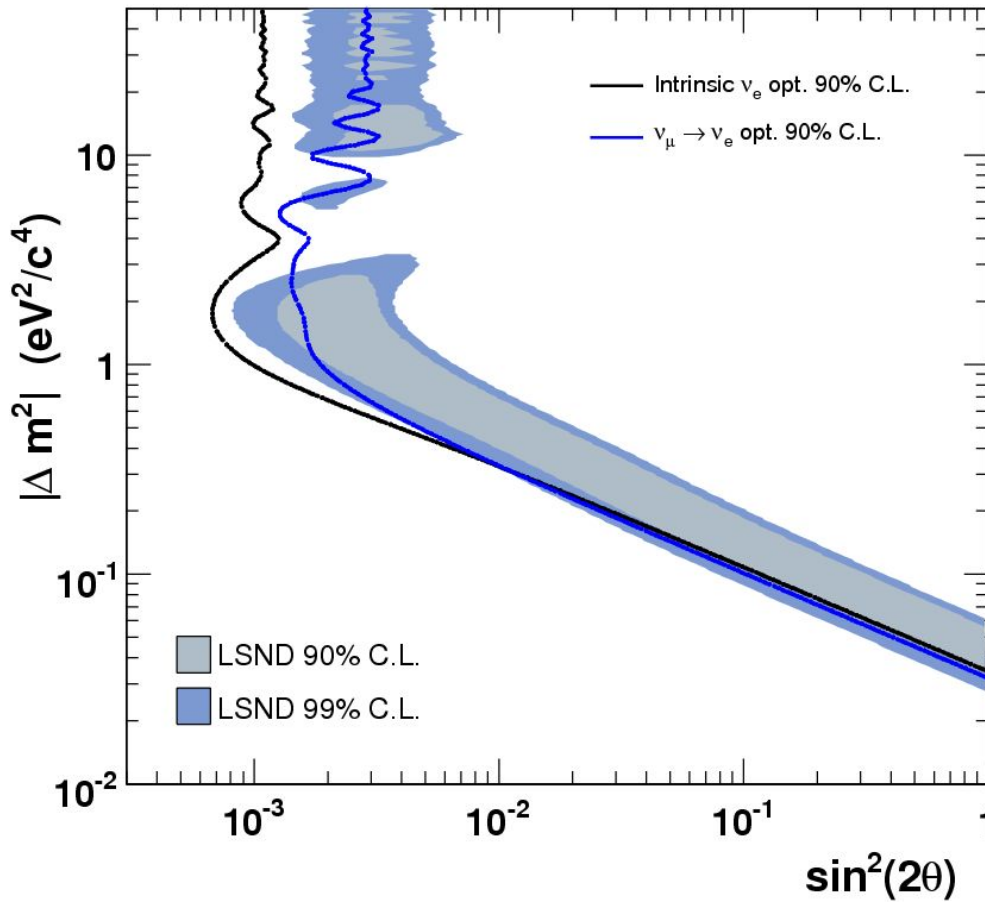
Figure 8.22: Summary of the search for $\nu_\mu \rightarrow \nu_e$ oscillations using MiniBooNE data. The 90% C.L. limits are shown for two (not independent) samples of ν_e candidate events selected using the BDT algorithm. Oscillations consistent with those reported by LSND are strongly excluded by these data.

Part IV

Appendices

Appendix A

HARP cross-section data

This appendix contains tables of double-differential production cross-section data measured at the HARP experiment at CERN. Proton, π^+ and π^- production from interactions of 8.9 GeV/c protons with beryllium and 12.9 GeV/c protons with aluminum are presented in bins of laboratory frame momentum, p, and polar angle with respect to the incident proton direction, θ, in the range 0.75 GeV/$c \le p \le 8.0$ GeV/c and 0.030 rad $\le \theta \le 0.210$ rad. For each kinematic bin the central value cross-section and the square-root of the corresponding diagonal element of the covariance matrix are listed. For the data and full 84×84 element error matrices in a readable ASCII format please see **http://home.fnal.gov/~dschmitz/thesis/harp_data/**.

					8.9 GeV/c proton + beryllium							
θ_{min} (mrad)	θ_{max} (mrad)	p_{min} (GeV/c)	$p$max (GeV/c)	$d^2\sigma^{\pi^+}/(dpd\Omega)$ (mb/(GeV/c sr))			$d^2\sigma^{\pi^-}/(dpd\Omega)$ (mb/(GeV/c sr))			$d^2\sigma^{\mathrm{p}}/(dpd\Omega)$ (mb/(GeV/c sr))		
30	60	0.75	1.00	176.5	$\pm$	22.7	122.9	$\pm$	15.3	72.0	$\pm$	12.3
		1.00	1.25	172.5	$\pm$	21.7	137.9	$\pm$	16.8	75.0	$\pm$	11.8
		1.25	1.50	187.7	$\pm$	21.0	130.7	$\pm$	13.0	69.3	$\pm$	10.3
		1.50	1.75	179.7	$\pm$	19.7	120.3	$\pm$	11.6	85.2	$\pm$	10.6
		1.75	2.00	197.5	$\pm$	17.8	106.6	$\pm$	9.4	83.5	$\pm$	9.9
		2.00	2.25	208.5	$\pm$	17.5	86.7	$\pm$	11.0	98.3	$\pm$	10.9
		2.25	2.50	188.9	$\pm$	14.6	86.9	$\pm$	8.9	122.3	$\pm$	12.6
		2.50	2.75	179.9	$\pm$	13.3	75.6	$\pm$	9.0	128.0	$\pm$	13.4
		2.75	3.00	168.7	$\pm$	12.8	66.2	$\pm$	7.9	146.3	$\pm$	12.9
		3.00	3.25	124.4	$\pm$	9.8	51.8	$\pm$	6.2	162.1	$\pm$	12.4
		3.25	4.00	97.8	$\pm$	7.7	40.9	$\pm$	4.1	184.3	$\pm$	15.3
		4.00	5.00	65.9	$\pm$	5.9	19.9	$\pm$	2.4	268.9	$\pm$	20.5
		5.00	6.50	29.5	$\pm$	5.0	7.1	$\pm$	1.0	413.1	$\pm$	25.7
		6.50	8.00	10.3	$\pm$	6.6	0.7	$\pm$	0.4	562.7	$\pm$	34.5
60	90	0.75	1.00	153.5	$\pm$	16.8	129.6	$\pm$	14.4	82.7	$\pm$	9.4
		1.00	1.25	160.1	$\pm$	15.0	120.9	$\pm$	11.9	68.3	$\pm$	7.7
		1.25	1.50	168.4	$\pm$	15.6	106.0	$\pm$	10.0	77.1	$\pm$	7.6
		1.50	1.75	176.8	$\pm$	15.2	108.5	$\pm$	10.0	79.4	$\pm$	7.9
		1.75	2.00	183.3	$\pm$	13.8	103.2	$\pm$	8.3	85.4	$\pm$	6.4
		2.00	2.25	185.7	$\pm$	11.4	91.9	$\pm$	8.1	81.6	$\pm$	7.7
		2.25	2.50	177.3	$\pm$	10.2	75.4	$\pm$	5.8	96.6	$\pm$	9.2
		2.50	2.75	151.9	$\pm$	8.6	64.5	$\pm$	5.4	106.0	$\pm$	9.8
		2.75	3.00	125.4	$\pm$	7.6	47.9	$\pm$	4.7	117.7	$\pm$	9.0
		3.00	3.25	92.1	$\pm$	7.6	34.9	$\pm$	4.5	130.4	$\pm$	8.9
		3.25	4.00	70.3	$\pm$	5.4	28.9	$\pm$	2.3	150.8	$\pm$	10.3
		4.00	5.00	44.7	$\pm$	3.2	14.2	$\pm$	1.3	183.3	$\pm$	8.5
		5.00	6.50	17.9	$\pm$	2.3	3.8	$\pm$	0.5	207.0	$\pm$	10.3
		6.50	8.00	4.7	$\pm$	2.4	0.2	$\pm$	0.1	226.2	$\pm$	13.8

θ_min (mrad)	θ_max (mrad)	p_min (GeV/c)	p_max (GeV/c)	$d^2\sigma^{\pi^+}/(dpd\Omega)$ (mb/(GeV/c sr))			$d^2\sigma^{\pi^-}/(dpd\Omega)$ (mb/(GeV/c sr))			$d^2\sigma^{p}/(dpd\Omega)$ (mb/(GeV/c sr))		
90	120	0.75	1.00	186.4	±	17.6	122.3	±	12.5	79.9	±	9.3
		1.00	1.25	179.7	±	16.9	112.3	±	13.1	67.4	±	7.5
		1.25	1.50	180.9	±	13.2	108.0	±	10.0	69.2	±	8.2
		1.50	1.75	146.5	±	11.9	99.0	±	8.1	80.0	±	5.9
		1.75	2.00	143.9	±	12.4	85.2	±	8.4	78.7	±	6.6
		2.00	2.25	127.2	±	8.5	69.5	±	7.3	72.0	±	6.8
		2.25	2.50	118.4	±	7.9	56.9	±	5.4	79.4	±	7.0
		2.50	2.75	94.9	±	6.7	45.4	±	4.0	78.4	±	6.9
		2.75	3.00	75.0	±	7.0	37.4	±	4.2	86.7	±	7.6
		3.00	3.25	58.4	±	5.1	24.9	±	3.3	89.9	±	7.1
		3.25	4.00	45.0	±	3.1	19.7	±	1.9	100.1	±	5.9
		4.00	5.00	24.1	±	2.7	7.6	±	1.1	110.2	±	5.2
		5.00	6.50	8.7	±	1.4	1.4	±	0.4	97.1	±	5.4
		6.50	8.00	1.3	±	0.9	0.1	±	0.1	67.8	±	4.9
120	150	0.75	1.00	175.0	±	17.5	104.1	±	13.9	71.7	±	10.4
		1.00	1.25	158.7	±	15.1	116.0	±	13.7	71.4	±	8.2
		1.25	1.50	156.0	±	13.2	103.1	±	8.8	74.1	±	6.9
		1.50	1.75	143.2	±	11.2	82.8	±	8.7	77.5	±	6.6
		1.75	2.00	119.9	±	8.7	71.6	±	7.4	76.8	±	6.1
		2.00	2.25	97.1	±	7.7	53.4	±	5.8	71.7	±	8.2
		2.25	2.50	85.7	±	6.0	45.9	±	4.1	78.7	±	5.9
		2.50	2.75	66.8	±	5.7	33.8	±	3.0	83.3	±	5.8
		2.75	3.00	55.8	±	4.3	25.9	±	2.3	76.0	±	5.8
		3.00	3.25	45.2	±	3.9	18.1	±	2.2	75.0	±	5.6
		3.25	4.00	28.4	±	3.0	14.6	±	1.1	81.3	±	4.5
		4.00	5.00	15.1	±	1.7	6.1	±	0.7	74.9	±	4.1
		5.00	6.50	5.2	±	0.7	0.9	±	0.2	48.9	±	3.3
		6.50	8.00	0.4	±	0.4	0.0	±	0.1	19.5	±	2.9

8.9 GeV/c proton + beryllium

				$d^2\sigma^{\pi^+}/(dpd\Omega)$			$d^2\sigma^{\pi^-}/(dpd\Omega)$			$d^2\sigma^{\mathrm{p}}/(dpd\Omega)$		
$\theta_{\min}$	$\theta_{\max}$	$p_{\min}$	$p\max$									
(mrad)	(mrad)	(GeV/c)	(GeV/c)	(mb/(GeV/c sr))			(mb/(GeV/c sr))			(mb/(GeV/c sr))		
150	180	0.75	1.00	172.5	±	20.2	134.7	±	19.3	71.6	±	9.3
		1.00	1.25	180.1	±	16.9	99.9	±	13.5	63.5	±	7.5
		1.25	1.50	147.5	±	13.7	95.9	±	10.6	59.8	±	6.5
		1.50	1.75	119.0	±	9.8	73.6	±	8.5	57.0	±	6.5
		1.75	2.00	98.4	±	7.1	55.5	±	6.8	58.4	±	6.2
		2.00	2.25	69.5	±	5.4	35.7	±	5.7	54.2	±	5.9
		2.25	2.50	52.6	±	5.2	26.0	±	4.7	59.7	±	5.4
		2.50	2.75	41.8	±	3.7	25.0	±	3.1	53.2	±	5.2
		2.75	3.00	35.7	±	3.5	21.1	±	2.7	52.2	±	4.9
		3.00	3.25	24.9	±	2.9	13.9	±	2.3	54.2	±	4.2
		3.25	4.00	17.4	±	2.1	7.1	±	1.4	51.0	±	3.6
		4.00	5.00	7.5	±	1.2	2.2	±	0.6	39.4	±	2.7
		5.00	6.50	2.7	±	0.3	0.4	±	0.1	21.7	±	2.0
		6.50	8.00	0.2	±	0.1	0.0	±	0.1	4.9	±	1.2
180	210	0.75	1.00	177.5	±	24.8	121.8	±	21.5	65.3	±	10.5
		1.00	1.25	139.3	±	16.5	94.1	±	13.7	66.9	±	7.1
		1.25	1.50	103.8	±	11.3	82.6	±	9.3	55.9	±	6.2
		1.50	1.75	66.9	±	7.5	55.8	±	7.0	56.3	±	5.3
		1.75	2.00	49.7	±	6.0	37.0	±	5.8	46.8	±	4.7
		2.00	2.25	39.9	±	4.8	31.9	±	4.0	40.0	±	4.6
		2.25	2.50	28.7	±	4.1	25.3	±	2.7	34.2	±	3.6
		2.50	2.75	21.8	±	2.7	14.7	±	3.1	32.1	±	3.0
		2.75	3.00	15.9	±	2.2	9.7	±	3.1	26.6	±	3.0
		3.00	3.25	13.3	±	1.7	8.1	±	2.2	22.1	±	2.9
		3.25	4.00	10.0	±	1.0	4.3	±	1.2	20.0	±	2.5
		4.00	5.00	5.5	±	0.8	1.3	±	1.2	16.0	±	1.6
		5.00	6.50	1.7	±	0.4	0.1	±	0.1	8.4	±	1.3
		6.50	8.00	0.0	±	0.1	0.0	±	0.1	0.7	±	0.3

8.9 GeV/c proton + beryllium

				12.9 GeV/c proton + aluminum								
θ_{min} (mrad)	θ_{max} (mrad)	p_{min} (GeV/c)	$p$max (GeV/c)	$d^2\sigma^{\pi^+}/(dpd\Omega)$ (mb/(GeV/c sr))			$d^2\sigma^{\pi^-}/(dpd\Omega)$ (mb/(GeV/c sr))			$d^2\sigma^{p}/(dpd\Omega)$ (mb/(GeV/c sr))		
30	60	0.75	1.00	442.2	±	54.5	389.4	±	48.3	207.6	±	23.2
		1.00	1.25	484.6	±	54.1	417.9	±	45.7	186.4	±	19.2
		1.25	1.50	469.2	±	47.6	372.2	±	41.7	177.4	±	17.5
		1.50	1.75	463.5	±	46.8	362.6	±	38.2	170.1	±	16.9
		1.75	2.00	461.0	±	41.3	293.8	±	31.3	201.8	±	16.6
		2.00	2.25	461.1	±	35.4	284.5	±	27.6	214.9	±	16.3
		2.25	2.50	487.9	±	40.7	283.8	±	26.4	205.1	±	17.6
		2.50	2.75	474.9	±	35.6	241.4	±	23.5	219.8	±	18.7
		2.75	3.00	450.5	±	32.2	210.5	±	21.6	233.6	±	18.0
		3.00	3.25	418.5	±	28.1	160.0	±	16.3	264.4	±	21.0
		3.25	4.00	387.6	±	22.9	165.7	±	14.5	300.6	±	17.1
		4.00	5.00	283.5	±	16.8	103.9	±	8.7	360.2	±	20.3
		5.00	6.50	169.7	±	10.6	58.8	±	5.4	496.7	±	26.2
		6.50	8.00	89.6	±	7.1	16.7	±	2.8	570.9	±	27.5
60	90	0.75	1.00	443.8	±	49.3	363.4	±	43.2	208.0	±	18.8
		1.00	1.25	418.0	±	45.0	359.3	±	39.4	177.3	±	15.2
		1.25	1.50	421.7	±	40.4	363.1	±	35.2	171.7	±	14.7
		1.50	1.75	463.3	±	39.9	320.3	±	30.8	171.4	±	13.9
		1.75	2.00	453.3	±	34.8	280.3	±	26.6	185.6	±	16.7
		2.00	2.25	465.4	±	32.3	253.8	±	22.6	185.9	±	13.3
		2.25	2.50	414.0	±	28.5	264.2	±	22.4	186.5	±	13.9
		2.50	2.75	421.8	±	27.8	236.3	±	18.3	216.3	±	15.2
		2.75	3.00	372.3	±	23.2	188.8	±	16.8	221.9	±	14.6
		3.00	3.25	315.1	±	21.6	147.6	±	13.0	227.5	±	15.1
		3.25	4.00	269.0	±	16.0	127.9	±	9.8	251.1	±	13.9
		4.00	5.00	172.1	±	10.4	73.1	±	5.9	284.6	±	14.8
		5.00	6.50	86.8	±	5.6	30.4	±	3.1	296.4	±	13.9
		6.50	8.00	29.8	±	2.5	6.7	±	1.1	212.9	±	13.2

				12.9 GeV/c proton + aluminum								
$\theta_{\min}$	$\theta_{\max}$	$p_{\min}$	$p$max	$d^2\sigma^{\pi^+}/(dpd\Omega)$			$d^2\sigma^{\pi^-}/(dpd\Omega)$			$d^2\sigma^{\mathrm{p}}/(dpd\Omega)$		
(mrad)	(mrad)	(GeV/c)	(GeV/c)	(mb/(GeV/c sr))			(mb/(GeV/c sr))			(mb/(GeV/c sr))		
90	120	0.75	1.00	450.1	$\pm$	56.7	351.8	$\pm$	44.9	217.1	$\pm$	19.8
		1.00	1.25	445.2	$\pm$	47.6	343.9	$\pm$	39.6	187.2	$\pm$	15.6
		1.25	1.50	454.8	$\pm$	41.3	322.5	$\pm$	31.7	170.5	$\pm$	14.4
		1.50	1.75	425.8	$\pm$	35.3	306.1	$\pm$	28.2	183.0	$\pm$	16.5
		1.75	2.00	395.2	$\pm$	30.8	263.1	$\pm$	23.0	189.2	$\pm$	14.6
		2.00	2.25	356.4	$\pm$	26.7	220.0	$\pm$	19.4	190.6	$\pm$	13.3
		2.25	2.50	329.4	$\pm$	23.4	210.4	$\pm$	18.0	152.8	$\pm$	14.2
		2.50	2.75	295.8	$\pm$	20.2	191.6	$\pm$	16.0	169.2	$\pm$	13.0
		2.75	3.00	268.1	$\pm$	17.8	145.5	$\pm$	12.6	172.4	$\pm$	12.8
		3.00	3.25	224.0	$\pm$	15.7	104.4	$\pm$	12.1	188.5	$\pm$	12.8
		3.25	4.00	188.0	$\pm$	11.5	77.1	$\pm$	6.9	181.7	$\pm$	11.2
		4.00	5.00	111.5	$\pm$	6.8	49.8	$\pm$	4.2	178.7	$\pm$	10.2
		5.00	6.50	47.3	$\pm$	3.1	16.2	$\pm$	2.0	149.9	$\pm$	9.1
		6.50	8.00	14.9	$\pm$	1.4	2.4	$\pm$	0.4	95.5	$\pm$	6.9
120	150	0.75	1.00	462.4	$\pm$	62.5	342.4	$\pm$	44.9	182.5	$\pm$	19.7
		1.00	1.25	446.1	$\pm$	50.4	318.1	$\pm$	36.3	178.5	$\pm$	15.7
		1.25	1.50	395.3	$\pm$	41.8	289.3	$\pm$	29.4	182.3	$\pm$	16.4
		1.50	1.75	357.8	$\pm$	32.3	261.3	$\pm$	25.8	170.0	$\pm$	14.9
		1.75	2.00	307.7	$\pm$	25.6	245.7	$\pm$	20.1	149.9	$\pm$	13.0
		2.00	2.25	265.3	$\pm$	20.4	193.8	$\pm$	16.7	141.6	$\pm$	12.4
		2.25	2.50	237.8	$\pm$	19.0	171.8	$\pm$	15.1	137.8	$\pm$	12.5
		2.50	2.75	219.8	$\pm$	16.6	127.6	$\pm$	12.0	142.7	$\pm$	12.2
		2.75	3.00	190.9	$\pm$	14.0	111.8	$\pm$	11.3	150.0	$\pm$	11.5
		3.00	3.25	160.9	$\pm$	11.8	89.5	$\pm$	7.9	159.1	$\pm$	11.9
		3.25	4.00	125.8	$\pm$	9.0	73.7	$\pm$	5.7	144.3	$\pm$	9.5
		4.00	5.00	65.4	$\pm$	4.8	30.9	$\pm$	3.3	122.5	$\pm$	8.4
		5.00	6.50	23.9	$\pm$	1.9	7.8	$\pm$	1.4	79.7	$\pm$	5.9
		6.50	8.00	7.6	$\pm$	1.0	0.7	$\pm$	0.3	45.9	$\pm$	3.8

				12.9 GeV/c proton + aluminum								
θ_{min}	θ_{max}	p_{min}	$p$max	$d^2\sigma^{\pi^+}/(dpd\Omega)$			$d^2\sigma^{\pi^-}/(dpd\Omega)$			$d^2\sigma^{p}/(dpd\Omega)$		
(mrad)	(mrad)	(GeV/c)	(GeV/c)	(mb/(GeV/c sr))			(mb/(GeV/c sr))			(mb/(GeV/c sr))		
150	180	0.75	1.00	457.6	$\pm$	71.6	350.5	$\pm$	55.3	202.6	$\pm$	23.4
		1.00	1.25	407.0	$\pm$	54.8	360.6	$\pm$	48.2	197.7	$\pm$	17.9
		1.25	1.50	376.4	$\pm$	44.2	299.1	$\pm$	36.2	185.2	$\pm$	17.2
		1.50	1.75	277.8	$\pm$	28.6	212.5	$\pm$	22.9	135.8	$\pm$	13.6
		1.75	2.00	256.1	$\pm$	24.1	191.8	$\pm$	19.0	114.1	$\pm$	13.1
		2.00	2.25	204.6	$\pm$	20.8	149.1	$\pm$	14.2	127.0	$\pm$	12.0
		2.25	2.50	168.5	$\pm$	17.1	127.6	$\pm$	12.7	140.5	$\pm$	13.1
		2.50	2.75	135.0	$\pm$	12.3	104.0	$\pm$	10.1	124.5	$\pm$	10.4
		2.75	3.00	125.4	$\pm$	10.7	86.6	$\pm$	8.7	117.2	$\pm$	9.9
		3.00	3.25	102.2	$\pm$	9.9	61.8	$\pm$	7.2	117.2	$\pm$	9.6
		3.25	4.00	63.6	$\pm$	5.3	38.6	$\pm$	4.0	89.0	$\pm$	6.9
		4.00	5.00	34.4	$\pm$	3.4	15.5	$\pm$	2.2	64.8	$\pm$	5.6
		5.00	6.50	11.2	$\pm$	1.3	3.2	$\pm$	0.8	38.7	$\pm$	3.6
		6.50	8.00	3.0	$\pm$	0.8	0.1	$\pm$	0.1	19.4	$\pm$	2.0
180	210	0.75	1.00	432.0	$\pm$	104.1	377.9	$\pm$	83.7	202.3	$\pm$	35.7
		1.00	1.25	341.4	$\pm$	54.3	338.5	$\pm$	46.8	170.5	$\pm$	19.1
		1.25	1.50	252.3	$\pm$	34.3	255.4	$\pm$	29.8	139.5	$\pm$	15.5
		1.50	1.75	183.9	$\pm$	21.8	188.7	$\pm$	21.8	116.6	$\pm$	11.8
		1.75	2.00	144.6	$\pm$	15.3	143.1	$\pm$	17.2	109.4	$\pm$	10.3
		2.00	2.25	115.3	$\pm$	12.3	103.6	$\pm$	11.5	88.9	$\pm$	9.5
		2.25	2.50	80.8	$\pm$	9.4	90.4	$\pm$	10.0	67.8	$\pm$	8.4
		2.50	2.75	68.5	$\pm$	8.4	66.0	$\pm$	8.6	64.6	$\pm$	6.9
		2.75	3.00	52.8	$\pm$	6.3	44.4	$\pm$	8.1	57.8	$\pm$	5.8
		3.00	3.25	39.9	$\pm$	4.9	30.6	$\pm$	6.5	52.6	$\pm$	5.1
		3.25	4.00	31.3	$\pm$	3.7	16.3	$\pm$	3.3	45.6	$\pm$	4.7
		4.00	5.00	15.0	$\pm$	2.0	5.0	$\pm$	2.4	27.2	$\pm$	3.5
		5.00	6.50	6.6	$\pm$	0.9	1.1	$\pm$	0.4	17.1	$\pm$	1.9
		6.50	8.00	2.8	$\pm$	0.6	0.0	$\pm$	0.1	9.9	$\pm$	1.4

Appendix B

Meson Production Cross-Section Models for the BNB

This appendix provides details on the models used to describe pion and kaon production in the Booster Neutrino Beamline beryllium target.

B.1 A note on cross-section parameterizations

The inclusion of hadron production cross-section data in Monte Carlo simulations typically requires the use of some form of parameterization for one or more of the following reasons:

- to scale available production data to the primary proton beam momentum or target nucleus of the experimental configuration being simulated

- to facilitate the combination of multiple hadron production data sets

- to interpolate between data points and provide a smooth description of the differential cross-section in secondary phase space

- to extrapolate the differential cross-section into regions of secondary phase space where production data are not available

Many scaling laws and parameterizations have been explored by different authors ([107, 108, 109, 110, 111, 112] among others) which are based on various amounts of em-

pirical, phenomenological and theoretical arguments. Unfortunately, no parameterization will reproduce the data exactly and often a systematic uncertainty is included to cover the discrepancy between data and the model. Additionally, one must be cautious regarding extrapolations into regions of phase space not covered by data where there is no constraint on the function and the result is particularly sensitive to the accuracy of scaling laws and other assumptions used in the development of a parameterization's functional form.

B.1.1 The Sanford-Wang Parameterization

The parameterization of Sanford and Wang [107] has been used by both the K2K and MiniBooNE experiments to model pion production in their targets. It is an empirical formula originally developed to describe charged pion production in proton-beryllium collisions. The functional form was developed by inspection of data from four early production papers published before 1967 for incident proton momenta between 10 and 34 GeV/c [102, 103, 104, 105].

The Sanford-Wang (SW) formula describes the double-differential production cross-section of secondary pions in terms of the incident proton momentum, p_{B}, the secondary pion total momentum in the laboratory frame, p, the pion production angle w.r.t to the incoming proton direction, θ, and 8 free parameters, c_i,

$$\frac{d^2\sigma}{dpd\Omega}(p,\theta) \;=\; c_1 \cdot p^{c_2}\left(1 - \frac{p}{p_{\mathrm{B}} - c_9}\right)e^{-g(p,\theta)} \tag{B.1}$$

with

$$g(p,\theta) \;=\; c_3 \cdot \frac{p^{c_4}}{p_{\mathrm{B}}^{c_5}} + c_6\theta\left(p - c_7 \cdot p_{\mathrm{B}} \cdot \cos^{c_8}\theta\right). \tag{B.2}$$

The parameter c_1 is an overall normalization factor, c_2, c_3, c_4, c_5 describe the momentum dependence of the cross-section in the forward direction and c_6, c_7, c_8 make adjustments to the momentum distribution at larger production angles. c_9 is related with the threshold for producing a given secondary, and for pions is usually fixed at 0 or 1. The parameters $c_1, ..., c_9$ can be determined by a least-squares or χ^2 fit to available production data.[1]

---

[1] In its original form the function included an exponent on θ as an additional parameter, $c_6\theta^m$, but the fit favored a value consistent with 1.0, so the authors removed m as a free parameter [107].

Due to the p_B dependence in the formula it is possible to combine data sets with different proton momenta (but same nuclear target) into a single fit. The general χ^2 expression is then given by

$$\chi^2(c_1, ..., c_8) = \sum_k \left[\sum_{i,j} (D_{i,k} - N_k \cdot SW_i) E_{ij,k}^{-1} (D_{j,k} - N_k \cdot SW_j) + \frac{(N_k - 1)^2}{\sigma_k^2} \right] \quad (B.3)$$

where i and j label bins of (p, θ), $D_{i,k}$ is the ith data point in the kth data set, SW_i is the value of the Sanford-Wang function in the ith bin for the current set of parameter values, $E_{ij,k}$ is the $(i,j)^{th}$ element of the correlated error matrix for the kth data set (such as the HARP data error matrix from Eq. 4.14), N_k is a normalization fit parameter for each data set and σ_k is the experiment's quoted normalization error. Using a function minimizing software such as MINUIT [132] one can determine a set of parameters with errors and correlations by minimizing Eq. B.3.

Hadron production experiments report the average cross-section values over 2D bins of phase space, typically of size $\Delta p \times \Delta \theta$. However, the average cross-section is, in general, not equal to the cross-section at the center of the bin, $(p_{min} + \Delta p/2,\ \theta_{min} + \Delta \theta/2)$, particularly for larger bins or for bins in which the cross-section is changing rapidly. Therefore, when minimizing the χ^2, it is the average cross-section across the kinematic bin $(p_{max} - p_{min}, \theta_{max} - \theta_{min})$

$$\overline{SW_i} = \frac{1}{\Delta p \Delta \Omega} \int_{p_{min}}^{p_{max}} \int_{\theta_{min}}^{\theta_{max}} SW(p, \theta) \cdot 2\pi \sin \theta\, dp\, d\theta\,, \quad (B.4)$$

which is compared to the data value.

B.1.2   A parameterization based on Feynman scaling

A second example is a parameterization developed by Shaevitz [84] to describe K$^+$ production off beryllium based on the Feynman scaling hypothesis [108]. The fit proceeds in two steps. First, the scaling hypothesis is used to translate all available production data to the production at the proton beam momentum needed. The hypothesis states that the invariant cross-section is only a function of two variables, the transverse momentum, p_T, and the ratio of the longitudinal momentum to the maximum longitudinal momentum in

the center-of-mass frame, known as the Feynman scaling variable, x_F,

$$x_F = \frac{p_L^{cm}}{\left(p_L^{cm}\right)^{max}} .$$ (B.5)

Once scaled to a single proton momentum, the data can be simultaneously fit without explicit dependence on the beam momentum in the parameterization. The functional form is also motivated by Feynman's idea that the invariant cross-section depends only on p_T and x_F

$$\mathrm{E}\frac{d^3\sigma}{dp^3} = A \cdot F(p_T, x_F)$$ (B.6)

A seven parameter model has been developed, given by

$$\mathrm{E}\frac{d^3\sigma}{dp^3} = \frac{\mathrm{E}}{p^2}\left(\frac{d^2\sigma}{dp d\Omega}\right) = c_1 \cdot (1 - |x_F|) \, e^{-c_2 p_T - c_3 |x_F|^{c_4} - c_5 p_T^2 - c_7 |p_T \cdot x_F|^{c_6}}$$ (B.7)

Again a minimization program is used to determine the parameter values by minimizing a χ^2 between the model and available production data. In Chapter 7 this model was used to predict K^+ production in the BNB.

B.2   BNB π^+ π^- production models

The production models for secondary π^+ and π^- in the BNB target are based on fits of the SW parameterization (Eq. B.1) to data sets from two different experiments, E910 at Brookhaven National Laboratory and HARP at CERN. Table B.1 gives the best fit parameters and covariance matrix for the π^+ SW model. Table B.2 gives the same for π^-. Figures B.1 and B.2 show the fit results compared to the production data for π^+ and π^-, respectively.

B.3   BNB K^+ K^0 production models

The production model for secondary K^+ in the BNB target is based on a fit of the FS parameterization (Eq. B.7) to data sets from eight different experiments which have all been scaled to $p_B = 8.89\,\mathrm{GeV}/c$. The K^0 model is a fit of SW to data from E910 and Abe *et al* [106]. Table B.3 gives the best fit parameters and covariance matrix for the K^+ FS
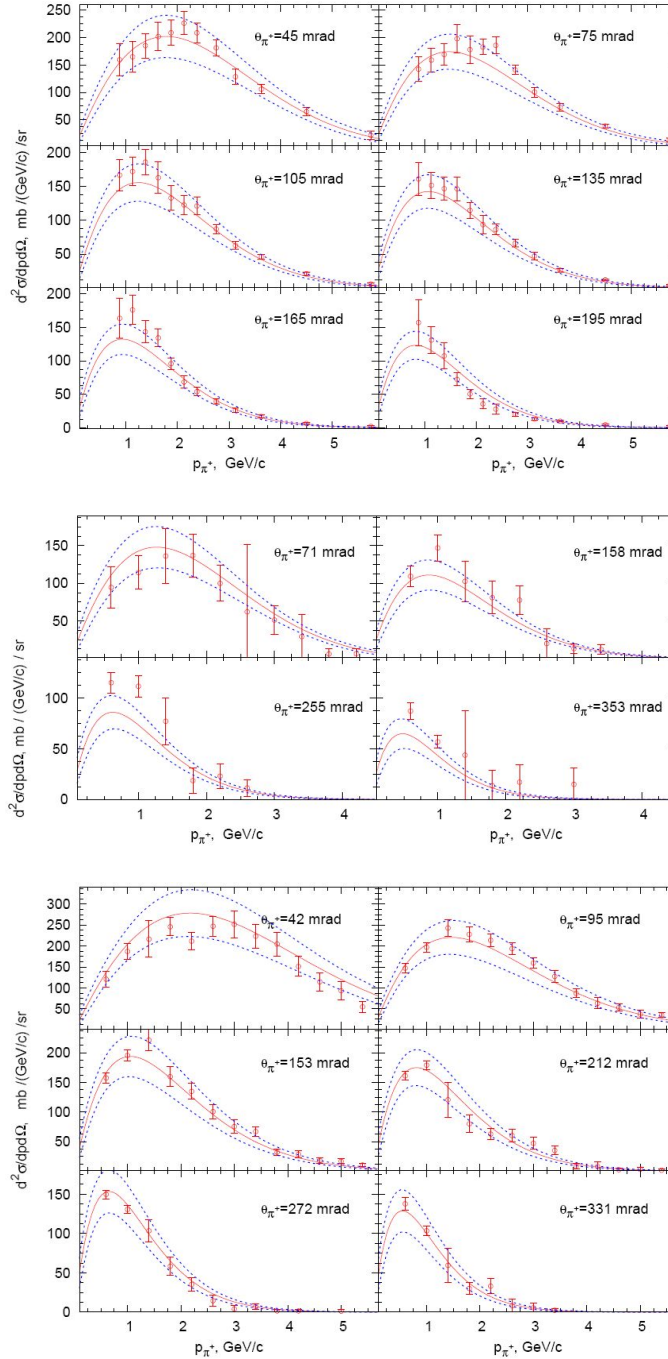
Figure B.1: π^+ production data from HARP at $p_B = 8.9 \, \text{GeV}/c$ (top), E910 at $p_B = 6.4 \, \text{GeV}/c$ (middle) and E910 at $p_B = 12.3 \, \text{GeV}/c$ (top). The global SW fit (solid red line) and 1σ (68%) band (dashed blue lines) determined from the covariance matrix of Table B.1 are shown.

Figure B.2: π^- production data from HARP at $p_B = 8.9\,\text{GeV}/c$ (top), E910 at $p_B = 6.4\,\text{GeV}/c$ (middle) and E910 at $p_B = 12.3\,\text{GeV}/c$ (top). The global SW fit (solid red line) and 1σ (68%) band (dashed blue lines) determined from the covariance matrix of Table B.1 are shown.
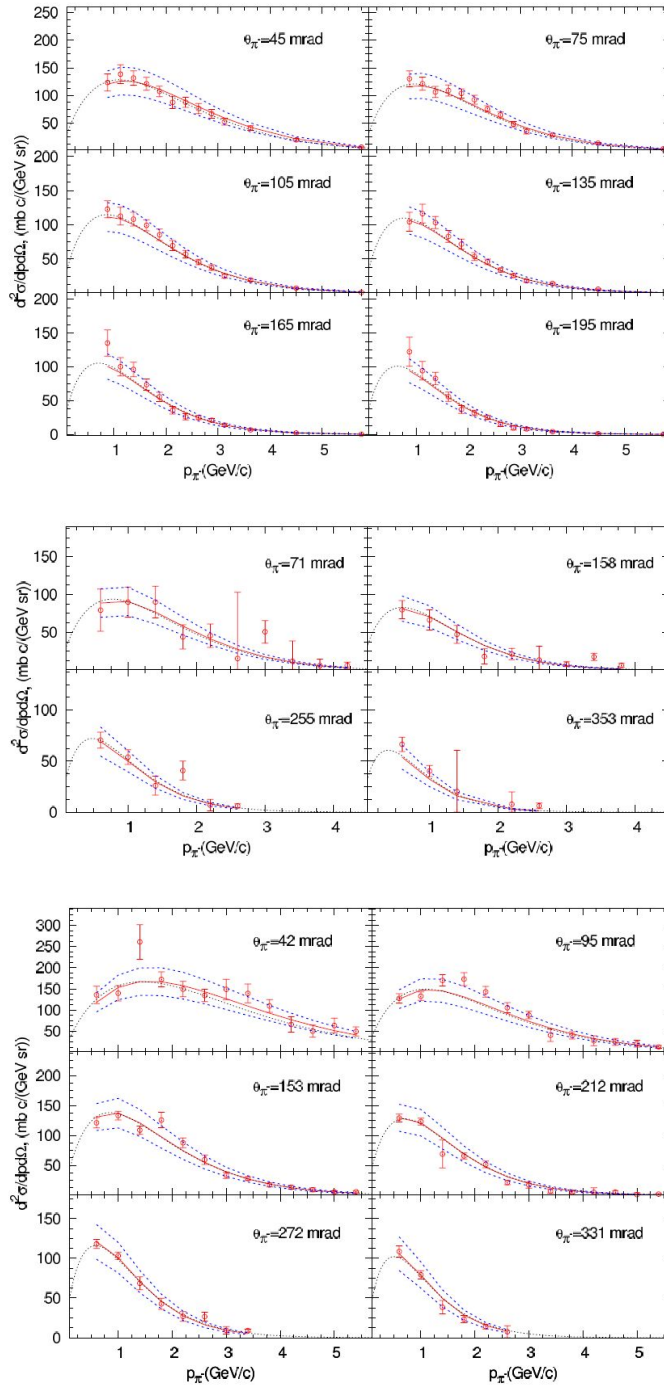
SW$^{\pi^+}$	220.7	1.080	1.978	1.320	5.572	0.08678	9.686
$\mathcal{M}_{ij}^{\pi^+}$	c_1	c_2	c_4	c_5	c_6	c_7	c_8
c_1	1707.22	1.14601	-17.6455	-15.9683	-8.80997	-0.73472	-60.8160
c_2	1.14601	0.03963	-0.10719	-0.09928	0.03249	0.00069	-0.07772
c_4	-17.6455	-0.10719	0.59447	0.50491	0.06546	0.00251	0.19795
c_5	-15.9683	-0.09928	0.50491	0.44109	0.05684	0.00250	0.22709
c_6	-8.80997	0.03249	0.06546	0.05684	0.20664	0.00466	0.10310
c_7	-0.73472	0.00069	0.00251	0.00250	0.00466	0.00049	0.06405
c_8	-60.8160	-0.07772	0.19795	0.22709	0.10310	0.06405	16.01887

Table B.1: The best fit and covariance matrix of SW parameters describing π^+ production in the BNB determined from fits to HARP and E910 [101] π^+ production data. Parameters c_3 and c_9 have been fixed ($\mathbf{c_3 = 1.0, c_9 = 1.0}$) and therefore do not have entries in the covariance matrix.

SW$^{\pi^-}$	213.7	0.9379	1.210	1.284	4.781	0.07338	8.329
$\mathcal{M}_{ij}^{\pi^-}$	c_1	c_2	c_4	c_5	c_6	c_7	c_8
c_1	3688.9	7.6100	-15.666	-17.480	-11.329	-0.9925	-91.400
c_2	7.6100	0.0388	-0.0437	-0.0509	0.0102	-0.0009	-0.1957
c_4	-15.666	-0.0437	0.0841	0.0895	0.0301	0.0029	0.2588
c_5	-17.480	-0.0509	0.0895	0.0986	0.0375	0.0033	0.3141
c_6	-11.329	0.0102	0.0301	0.0375	0.1595	0.0051	0.1933
c_7	-0.9925	-0.0009	0.0029	0.0033	0.0051	0.0005	0.0640
c_8	-91.400	-0.1957	0.2588	0.3141	0.1933	0.0640	17.242

Table B.2: The best fit and covariance matrix of SW parameters describing π^- production in the BNB determined from fits to HARP and E910 [101] π^- production data. Parameters c_3 and c_9 have been fixed ($\mathbf{c_3 = 5.454, c_9 = 1.0}$) and therefore do not have entries in the covariance matrix.
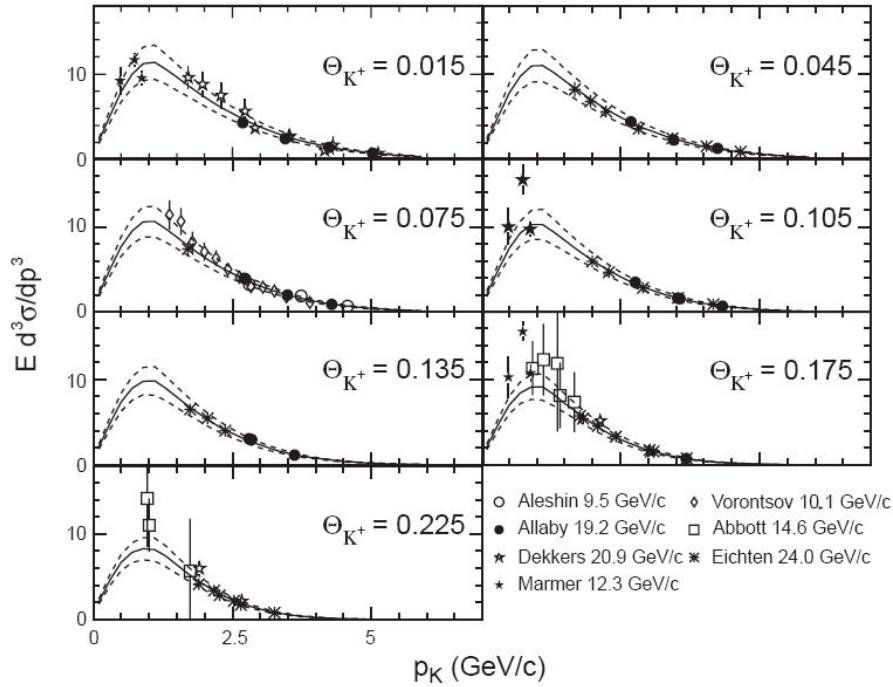
Figure B.3: K^+ production data scaled to $p_B = 8.89\,\text{GeV}/c$. The global FS fit (solid line) and 1σ (68%) band (dashed lines) determined from the covariance matrix of Table B.3 are shown.

model. Table B.4 gives the same for the K^0 SW fit. Figures B.3 and B.4 show the fit results compared to the production data for K^+ and K^0, respectively.

Figure B.4: K^0 production data from E910 at $p_B = 17.6\,\text{GeV}/c$ and $p_B = 12.3\,\text{GeV}/c$ and Abe *et al* at $p_B = 12.0\,\text{GeV}/c$. The global SW fit is shown. Plot taken from [83].

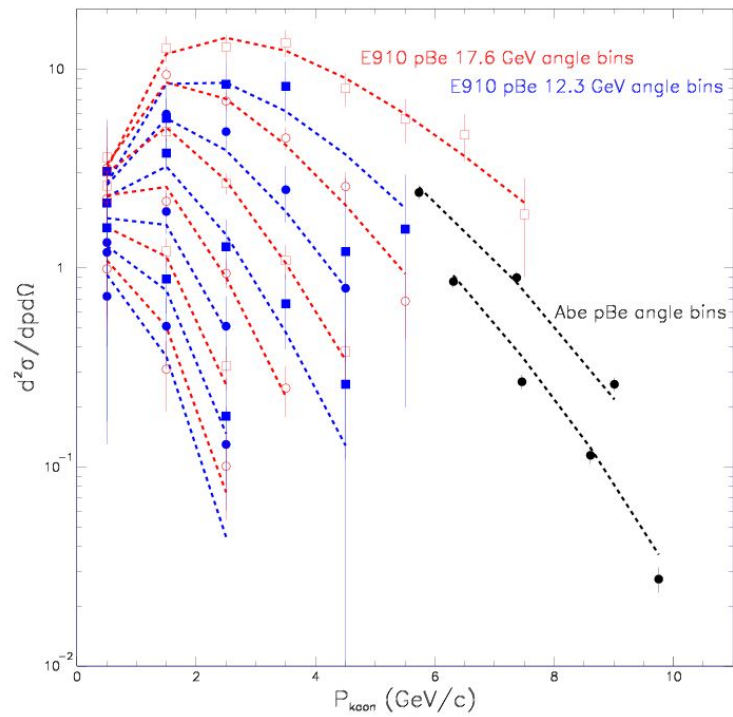| FS^{K^+}	11.70	0.88	4.77	1.51	2.21	2.17	1.51
$\mathcal{M}_{ij}^{K^+}$	c_1	c_2	c_3	c_4	c_5	c_6	c_7
c_1	1.094046	0.05017	2.99E-03	-0.03316	-0.03745	0.125194	0.074319
c_2	0.05017	0.016104	1.39E-03	-1.44E-03	-0.01264	0.032194	0.021996
c_3	2.99E-03	1.39E-03	7.47E-03	2.06E-03	1.93E-03	0.013534	-3.34E-03
c_4	-0.03316	-1.44E-03	2.06E-03	3.46E-03	2.03E-03	-4.11E-03	-6.28E-03
c_5	-0.03745	-0.01264	1.93E-03	2.03E-03	0.014637	-0.01544	-0.02444
c_6	0.125194	0.032194	0.013534	-4.11E-03	-0.01544	0.181522	0.126181
c_7	0.074319	0.021996	-3.34E-03	-6.28E-03	-0.02444	0.126181	0.159265

Table B.3: The best fit and covariance matrix of FS parameters describing K^+ production in the BNB determined from fits to K^+ production data scaled to $p_B = 8.89$ GeV/c using the Feynman scaling hypothesis [84].

SW^{K^0}	15.13	1.975	4.084	0.9277	0.7306	4.362	4.79E-02	13.3	1.278
$\mathcal{M}_{ij}^{K^0}$	c_1	c_2	c_3	c_4	c_5	c_6	c_7	c_8	c_9
c_1	32.302	-0.0969	0.8215	-0.1018	-0.2124	-0.8902	-0.1333	16.552	-1.7893
c_2	-0.0969	0.0957	0.0325	0.0013	-0.0130	0.0884	-0.0003	-1.5364	-0.2156
c_3	0.8215	0.0325	0.5283	-0.0192	0.0227	-0.0033	-0.0024	0.0391	-0.0802
c_4	-0.1018	0.0013	-0.0192	0.0084	0.0040	0.0007	-0.0004	-0.0144	-0.0730
c_5	-0.2124	-0.0130	0.0227	0.0040	0.0098	0.0029	0.0003	-0.0578	0.0297
c_6	-0.8902	0.0884	-0.0033	0.0007	0.0029	0.3599	0.0038	-4.7514	-0.1577
c_7	-0.1333	-0.0003	-0.0024	-0.0004	0.0003	0.0038	0.0010	0.0581	0.0069
c_8	16.552	-1.5364	0.0391	-0.0144	-0.0578	-4.7514	0.0581	130.201	1.2222
c_9	-1.7893	-0.2156	-0.0802	-0.0730	0.0297	-0.1577	0.0069	1.2222	2.9480

Table B.4: The best fit and covariance matrix of SW parameters describing K^0 production in the BNB determined from fits to K^0 production data [83].

Appendix C

Relevance of HARP Production Data for Neutrino Experiments

The hadron production cross-section data measured in Part II and tabulated in Appendix A were chosen for their particular relevance to two accelerator neutrino beams: the KEK 12.9 GeV/c proton synchrotron neutrino beam and the FNAL 8.9 GeV/c Booster neutrino beam, and three neutrino experiments: K2K, MiniBooNE and SciBooNE. This appendix is intended to give an idea how these data are used by these experiments and to illustrate the impact on the neutrino measurements made by them.

C.1   Significance of HARP data for K2K

Pion production data from HARP have also been used by the K2K long baseline oscillation experiment in Japan. The original analysis of the K2K oscillation data [30] used the Sanford-Wang fit of the so-called "Cho-CERN compilation" which was based largely on the production data of Cho et al. [100]. The Cho data is from proton collisions with beryllium at 12.4 GeV/c necessitating a scaling in proton momentum *and* target atomic mass before being used to simulate the KEK beamline. The measurement of π^+ production in proton+aluminum interactions at exactly 12.9 GeV/c done at HARP [57] was used by the K2K experiment in an updated publication in 2006 [31]. The HARP results published in
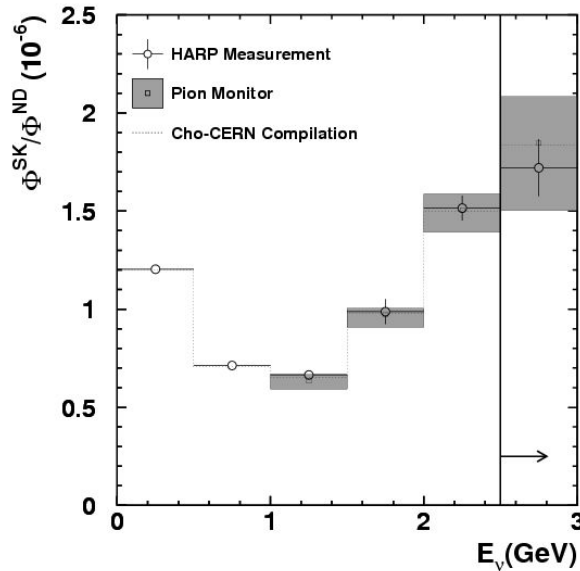
Figure C.1: The predicted ratio of the ν_μ fluxes in Super Kamiokande and the K2K near detector in the absence of oscillations. The empty circles with error bars show the central values and systematic errors on the ratio using the HARP π^+ production data [57]. The shaded regions show the ratio using the pion monitor measurement in the K2K beamline and the dotted histogram is the ratio based on the previous pion production model using the Cho-CERN compilation. Plot taken from Ref. [31].

[57] used an earlier version (2005) of the same analysis described in this dissertation.

K2K measures neutrino oscillations through the disappearance of ν_μ created mostly in the chain $p + Al \rightarrow \pi^+ \rightarrow \nu_\mu$. The neutrino beam simulation is used to calculate the "far-to-near ratio" for extrapolating the near detector event rate into an expected event rate at Super-Kamiokande. Figure C.1 has been reproduced from [31] and shows the calculated far-to-near ratio using the original model based on Cho and that using the HARP aluminum data. The agreement is excellent, but the systematic uncertainties on the HARP data are significantly smaller and allow a more precise prediction of the neutrino flux in the far detector.

Most of the significance of the K2K oscillation result comes from an observed normal-ization difference (3.4σ) with less coming from distortions in the neutrino energy spec-

trum (2.9σ) [31]. The introduction of the HARP production data between [30](2005) and [31](2006) was particularly beneficial in reducing the systematic uncertainty on the total number of ν_μ events expected (normalization). The far-to-near ratio contribution to this uncertainty was reduced from 5.1% to 2.9% between the two publications.

C.2 Significance of HARP data for MiniBooNE

Early versions of the MiniBooNE flux predictions were based upon the SW model of Eq. B.1 fit to the $\pi^\pm$ production cross-sections at $p_B = 6.4$ GeV/c and 12.3 GeV/c measured by the E910 experiment at Brookhaven National Laboratory [101]. A model such as SW was absolutely necessary for interpolating the differential cross-sections to $p_B = 8.9$ GeV/c, but model uncertainties are large and difficult to quantify. The minimum χ^2 in a fit to the E910 data sets, which is quite good at 83 for 91 degrees of freedom, unfortunately tells us nothing about how to estimate the model uncertainty at 8.9 GeV/c. In the words of Sanford and Wang, "except for kinematical constraints, the approach is purely algebraic rather than physical."

The HARP data, therefore, being at exactly the Booster momentum, are a critical addition to the development of the pion production model, reducing the model uncertainties from extrapolation to 8.9 GeV/c. The E910 data sets continue to be used, however, in a simultaneous fit to all three data sets in order to provide an additional constraint at angles larger than 210 mrad. Figure C.2 compares the kinematic coverage of the HARP data set and the two E910 data sets. The left panel compares the binning of the data sets in laboratory variables p and θ with no attempt to normalize to a common beam momentum. The right panel compares the data coverage using the Feynman scaling hypothesis introduced above. The figure clearly shows the added coverage that the E910 data provides at high p_T and values of x_F near 0.

A preliminary version of the HARP π^+ production data available in early 2006 were incorporated into a SW fit to be used in the MiniBooNE neutrino flux simulations. The minimum χ^2 in a fit to the three data sets was degraded to 302 for 168 degrees of freedom, indicating that the functional form of the SW model in Eq. B.1 is insufficient to accurately
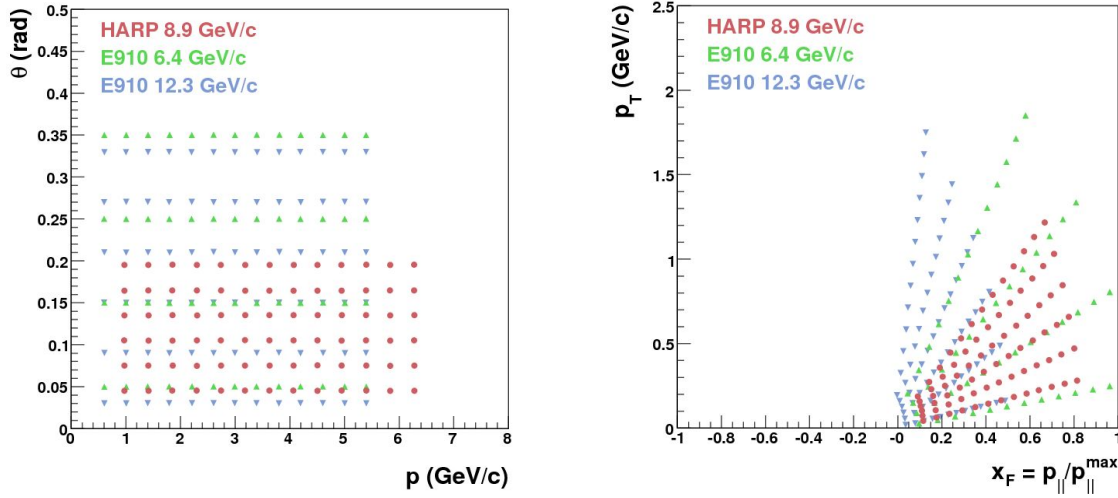
Figure C.2: Comparison of the kinematic coverage of the HARP pion data sets at 8.9 GeV/c to the E910 data at 6.4 GeV/c and 12.3 GeV/c. The left panel is binned in laboratory variables p and θ. These have been converted into the invariant quantities p_T and x_F in the right panel.

describe π^+ production at these momenta - a fact that was previously hidden by the larger experimental errors of the available data. The updated HARP cross-sections presented in this thesis, which represent a further reduction in uncertainties since the preliminary result, further reveal the inadequacies of the SW model by a continued degradation of the minimum χ^2 to 413 for 168 degrees of freedom.

This incompatibility of the SW model with data results in the inflation of uncertainties on the parameters determined in the fitting procedure, in particular the normalization parameter, c_1. The parameterized curve used in the MiniBooNE neutrino flux predictions at the time of the first oscillation analysis [66] is compared to the final HARP π^+ production cross-sections in Figure C.3. Due to the relative timing of the first HARP and MiniBooNE results the SW parameterization shown is that based on the preliminary HARP results mentioned above. The error band on the parameterized curve represents the uncorrelated error on the parameter c_1 (18.2%) and shows complete coverage of the data within this overall normalization error.

The result is an absolute neutrino flux prediction with uncertainties larger than those
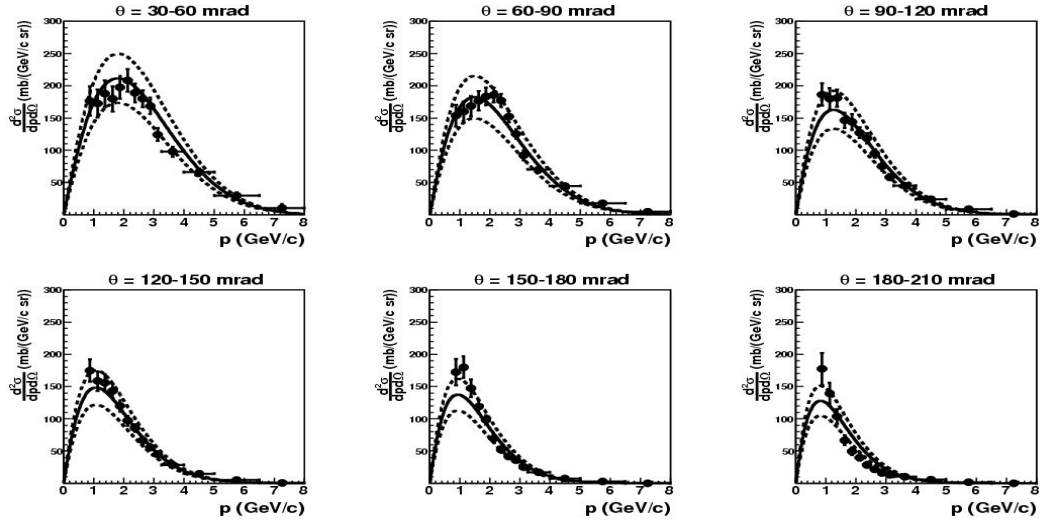
Figure C.3: Sanford-Wang parameterization used in the MiniBooNE flux prediction compared to the π^+ production data presented in this dissertation.

of the underlying hadron production data used to predict it. Figure C.4 shows the number of events reconstructed as ν_μ charged-current quasi-elastic (CCQE) events according to simulation. The distribution is, therefore, a product of the predicted ν_μ flux, the CCQE cross-section on carbon and detector effects. The errors shown ($\sim$16%) are those attributed to the π^+ production model only, yet in Table 4.2 we see that the average uncertainty on the π^+ cross-section is <10%. Recently a method has been proposed [87] by a member of the MiniBooNE collaboration for developing a production model using 2D spline fits instead of a global function which should better reflect the uncertainty in the production data. Preliminary results indicate the flux systematic on CCQE events will improve from the 16% shown in Figure C.4 to 5–10%.

For now, however, it is critical to note that the analysis methods used in the ν_e appearance search make it largely insensitive to normalization errors on pion production as was demonstrated in Chapter 8. It is for absolute neutrino cross-section measurements and ν_μ disappearance searches to be made at MiniBooNE in the future that the flux errors from pion production have the greatest impact. Using the spline method, absolute flux predictions to better than 10% should be achievable where the flux is directly constrained
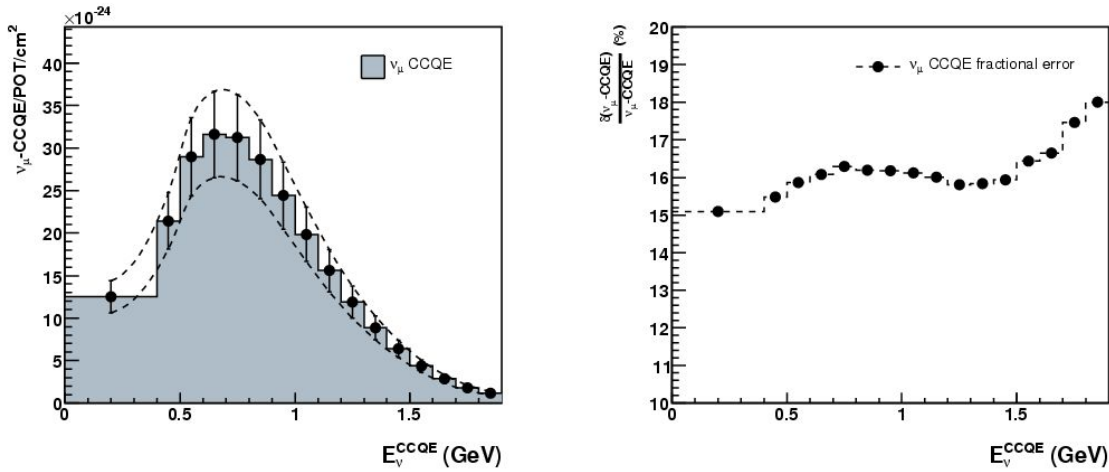
Figure C.4: ν_μ CCQE event rate prediction as a function of reconstructed energy at Mini-BooNE running in neutrino mode. The errors shown come from the current π^+ production model only. The right panel shows the fractional error.

by production data at 8.9 GeV/c from HARP.

Figures C.5 and C.6 illustrate the regions of muon and electron neutrino flux that are directly constrained by the HARP cross-section data for neutrino and antineutrino modes, respectively. It is worth noting that any tests one can perform to quantify the coverage are slightly circular - data is used to generate a model which is used in a simulation of the beamline which is, in turn, used to quantify the impact of the data. Despite small model dependencies, however, such an exercise remains important for defining the regions of meson production which are shown to be important to the flux prediction yet remain unconstrained by data.

In each panel of Figures C.5 and C.6 the total ν_μ or ν_e flux prediction is given by the solid black histogram on the right plot. The other curves and the left panel illustrate the direct impact of the HARP data on the MiniBooNE flux prediction. For example, in the top panel of Figure C.5 the blue curve on the right shows the high fraction (90.3%) of total ν_μ which come from the decays of π^+ which were created in primary interactions in the target. The kinematic distribution of these π^+ are shown by the black histogram in the 2D panel on the left. The red box marks the boundary of the HARP measurement and thus

the region of the π^+ parameterization that is directly constrained by data. Moving back to the right panel, the dashed black curve, labeled $p + Be \rightarrow \pi^+_{HARP} \rightarrow \nu_\mu$, shows the ν_μ whose parent π^+ is directly constrained by the HARP data (originates from inside the red box). Almost 80% of the π^+ which contribute to the ν_μ flux are being directly constrained by the measurement.

The remaining three curves (red, green, magenta) show the flux contributions from primary π^+ which are not being directly constrained by HARP data. The red curve represents ν_μ coming from all pions at small angles ($\theta < 30$ mrad), the green curve is ν_μ from large angle pions ($\theta > 210$ mrad) and the magenta represents ν_μ created by all pions with momentum below 750 MeV. The low momentum and high-angle pions contribute mostly to the lowest energy neutrino fluxes. As mentioned above the inclusion of the E910 production data are important to constraining pion production outside of the range of the HARP measurements.

The bottom panel of Figure C.5 shows the coverage for $\pi^+ \rightarrow \mu^+ \rightarrow \nu_e$ events in neutrino mode. Primary pion production accounts for 49% of the total intrinsic ν_e flux. The other half is split between K^+ and K^0 decays.

Figure C.6 shows the equivalent distributions for antineutrino running mode fluxes. For $\bar\nu_\mu$ and $\bar\nu_e$ from muon decay it is the measurements of π^- production which are relevant. Also shown in the bottom two rows are the ν_μ and ν_e flux predictions since the so-called "wrong sign" component is significant in antineutrino mode. The conclusion concerning the lowest energy fluxes is similar for antineutrinos. The "wrong sign" neutrino fluxes are largely unconstrained at 31% and 23% coverage of the π^+ producing the ν_μ and ν_e fluxes, respectively. It is the most forward π^+ which tend to generate the neutrino background since they miss the field region of the horn and are, therefore, not defocused.
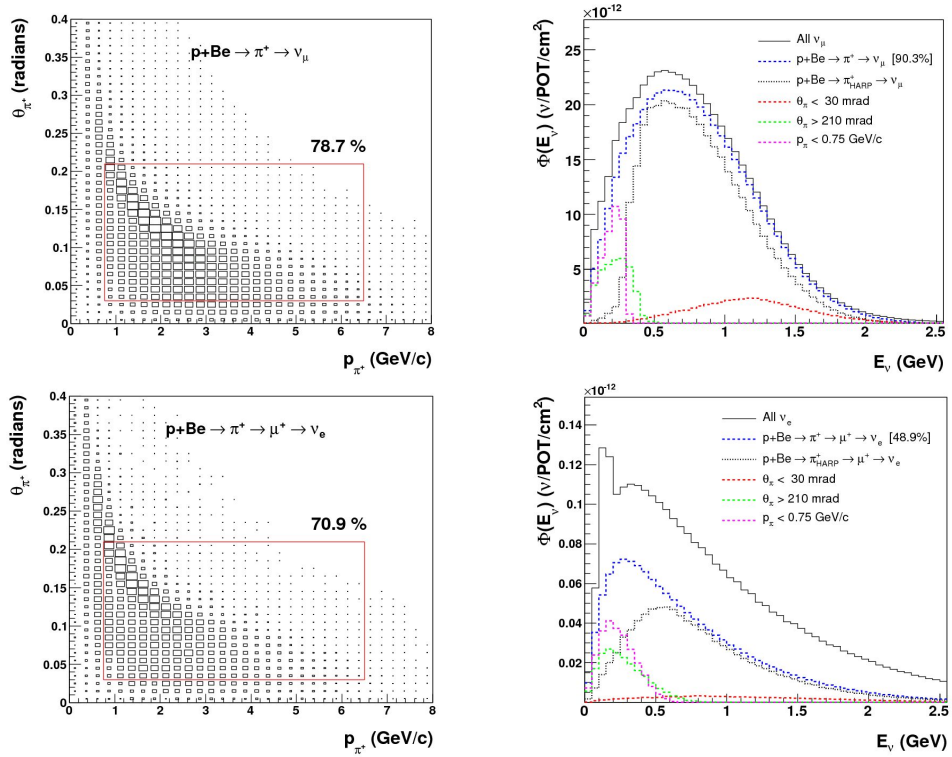
Figure C.5: Relevance of the HARP forward production data for the MiniBooNE ν_μ and ν_e flux predictions in neutrino mode. See the text for details.
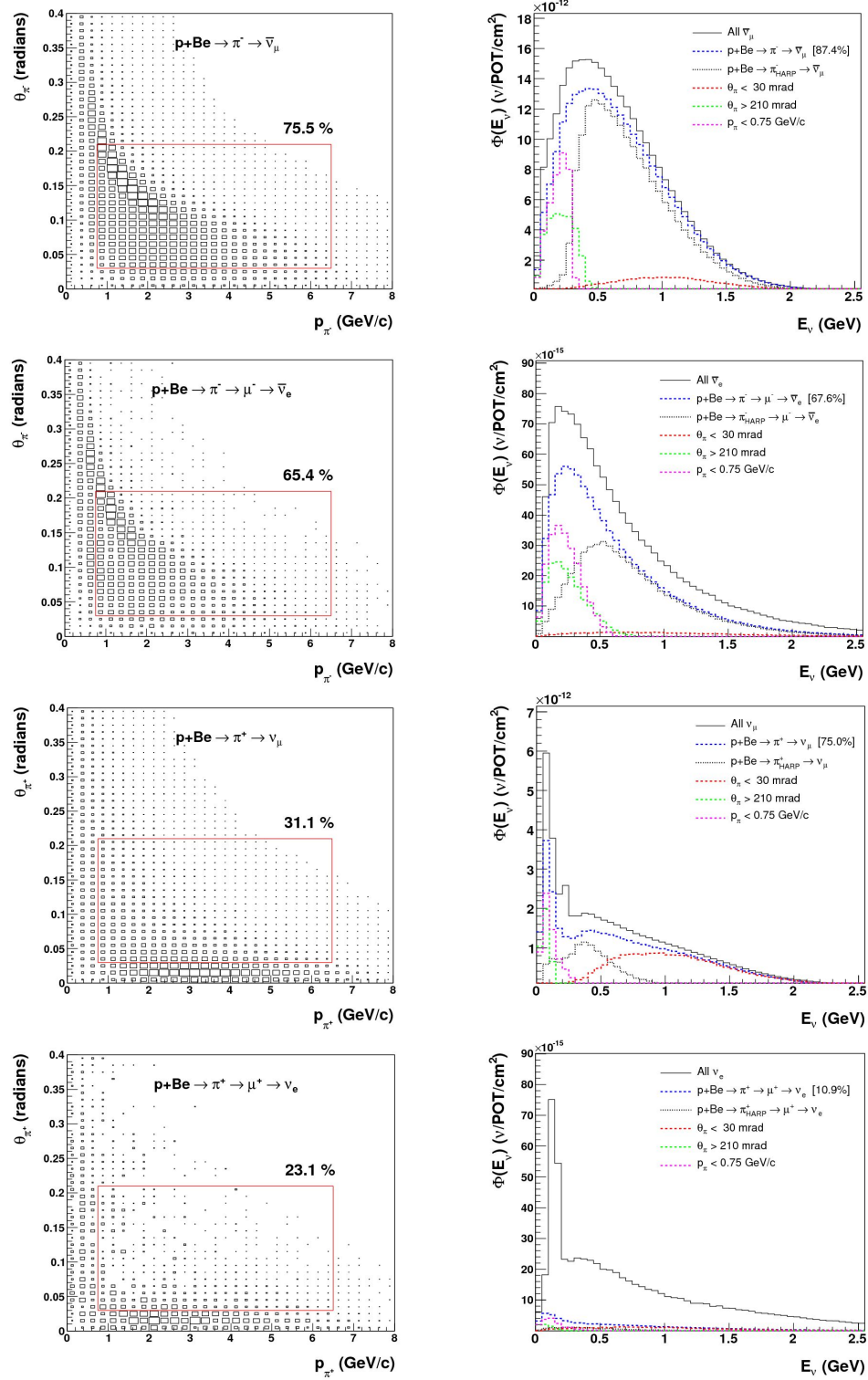
Figure C.6: Relevance of the HARP forward production data for the MiniBooNE $\overline{\nu}_\mu$, $\overline{\nu}_e$. ν_μ and ν_e flux predictions in antineutrino mode. See the text for details.

Bibliography

[1] E. Fermi, "An attempt of a theory of beta radiation. 1," Z. Phys. **88**, 161 (1934).

[2] H. Bethe and R. Peierls, "The 'neutrino'," Nature **133**, 532 (1934).

[3] F. Reines and C. L. Cowan, "A Proposed Experiment To Detect The Free Neutrino," Phys. Rev. **90**, 492 (1953).

F. Reines and C. L. Cowan, "Free anti-neutrino absorption cross-section. 1: Measurement of the free anti-neutrino absorption cross-section by protons," Phys. Rev. **113**, 273 (1959).

[4] T. D. Lee and C. N. Yang, "Question Of Parity Conservation In Weak Interactions," Phys. Rev. **104**, 254 (1956).

[5] C. S. Wu, E. Ambler, R. W. Hayward, D. D. Hoppes and R. P. Hudson, "EXPERIMENTAL TEST OF PARITY CONSERVATION IN BETA DECAY," Phys. Rev. **105**, 1413 (1957).

[6] R. P. Feynman and M. Gell-Mann, "Theory of the Fermi interaction," Phys. Rev. **109**, 193 (1958).

E. C. G. Sudarshan and R. E. Marshak, "Chirality invariance and the universal Fermi interaction," Phys. Rev. **109**, 1860 (1958).

[7] D. Griffiths, "Introduction to Elementary Particles," John Wiley and Sons, Inc. (1987).

[8] S. Weinberg, "A Model Of Leptons," Phys. Rev. Lett. **19**, 1264 (1967).

[9] A. Salam, "Weak And Electromagnetic Interactions," *Originally printed in *Svartholm: Elementary Particle Theory, Proceedings Of The Nobel Symposium Held 1968 At Lerum, Sweden*, Stockholm 1968, 367-377*

[10] P. W. Higgs, "Broken Symmetries And the Masses of Gauge Bosons," Phys. Rev. Lett. **13**, 508 (1964).

[11] C. Quigg, "Gauge Theories of the Strong, Weak and Electromagnetic Interactions," Addison Wesley Longman, Inc. (1997).

[12] B. Kayser, "Neutrino mass, mixing, and flavor change," [arXiv:hep-ph/0211134].

[13] B. Kayser, "Neutrino physics," *In the Proceedings of 32nd SLAC Summer Institute on Particle Physics (SSI 2004): Natures Greatest Puzzles, Menlo Park, California, 2-13 Aug 2004, pp L004* [arXiv:hep-ph/0506165].

[14] M. Kobayashi and T. Maskawa, "CP Violation In The Renormalizable Theory Of Weak Interaction," Prog. Theor. Phys. **49**, 652 (1973).

[15] R. J. Davis, D. S. Harmer and K. C. Hoffman, "Search for neutrinos from the sun," Phys. Rev. Lett. **20**, 1205 (1968).

[16] B. T. Cleveland *et al.*, "Measurement of the solar electron neutrino flux with the Homestake chlorine detector," Astrophys. J. **496**, 505 (1998).

[17] J. N. Bahcall, S. Basu and M. H. Pinsonneault, "How uncertain are solar neutrino predictions?," Phys. Lett. B **433**, 1 (1998) [arXiv:astro-ph/9805135].

[18] J. N. Abdurashitov *et al.* [SAGE Collaboration], "Measurement of the solar neutrino capture rate by the Russian-American gallium solar neutrino experiment during one half of the 22-year cycle of solar activity," J. Exp. Theor. Phys. **95**, 181 (2002) [Zh. Eksp. Teor. Fiz. **122**, 211 (2002)] [arXiv:astro-ph/0204245].

[19] W. Hampel *et al.* [GALLEX Collaboration], "GALLEX solar neutrino observations: Results for GALLEX IV," Phys. Lett. B **447**, 127 (1999).

[20] M. Altmann *et al.* [GNO COLLABORATION Collaboration], "Complete results for five years of GNO solar neutrino observations," Phys. Lett. B **616**, 174 (2005) [arXiv:hep-ex/0504037].

[21] Y. Fukuda *et al.* [Super-Kamiokande Collaboration], "Measurement of the solar neutrino energy spectrum using neutrino electron scattering," Phys. Rev. Lett. **82**, 2430 (1999) [arXiv:hep-ex/9812011].

[22] M. B. Smy *et al.* [Super-Kamiokande Collaboration], "Precise measurement of the solar neutrino day/night and seasonal variation in Super-Kamiokande-I," Phys. Rev. D **69**, 011104 (2004) [arXiv:hep-ex/0309011].

[23] L. Wolfenstein, "Neutrino oscillations in matter," Phys. Rev. D **17**, 2369 (1978).

S. P. Mikheev and A. Y. Smirnov, "Resonance enhancement of oscillations in matter and solar neutrino spectroscopy," Sov. J. Nucl. Phys. **42**, 913 (1985) [Yad. Fiz. **42**, 1441 (1985)].

[24] B. Aharmim *et al.* [SNO Collaboration], "Electron energy spectra, fluxes, and day-night asymmetries of B-8 solar neutrinos from the 391-day salt phase SNO data set," Phys. Rev. C **72**, 055502 (2005) [arXiv:nucl-ex/0502021].

[25] T. Araki *et al.* [KamLAND Collaboration], "Measurement of neutrino oscillation with KamLAND: Evidence of spectral distortion," Phys. Rev. Lett. **94**, 081801 (2005) [arXiv:hep-ex/0406035].

[26] Y. Fukuda *et al.* [Kamiokande Collaboration], "Atmospheric muon-neutrino / electron-neutrino ratio in the multiGeV energy range," Phys. Lett. B **335**, 237 (1994).

[27] R. Becker-Szendy *et al.*, "The Electron-neutrino and muon-neutrino content of the atmospheric flux," Phys. Rev. D **46**, 3720 (1992).

[28] Y. Ashie *et al.* [Super-Kamiokande Collaboration], "A measurement of atmospheric neutrino oscillation parameters by Super-Kamiokande I", Phys. Rev. D **71** (2005) 112005 [arXiv:hep-ex/0501064].

[29] Y. Ashie *et al.* [Super-Kamiokande Collaboration], "Evidence for an oscillatory signature in atmospheric neutrino oscillation," Phys. Rev. Lett. **93**, 101801 (2004) [arXiv:hep-ex/0404034].

[30] E. Aliu *et al.* [K2K Collaboration], "Evidence for muon neutrino oscillation in an accelerator-based experiment," Phys. Rev. Lett. **94**, 081802 (2005) [arXiv:hep-ex/0411038].

[31] M. H. Ahn *et al.* [K2K Collaboration], "Measurement of neutrino oscillation by the K2K experiment", Phys. Rev. D **74** (2006) 072003 [arXiv:hep-ex/0606032].

[32] D. G. Michael *et al.* [MINOS Collaboration], "Observation of muon neutrino disappearance with the MINOS detectors and the NuMI neutrino beam," Phys. Rev. Lett. **97**, 191801 (2006) [arXiv:hep-ex/0607088].

[33] M. Sanchez, "MINOS Status and Prospects," Fermilab PAC presentation (2008).

[34] M. Apollonio *et al.* [CHOOZ Collaboration], "Limits on neutrino oscillations from the CHOOZ experiment," Phys. Lett. B **466**, 415 (1999) [arXiv:hep-ex/9907037].

[35] M. Apollonio *et al.* [CHOOZ Collaboration], "Search for neutrino oscillations on a long base-line at the CHOOZ nuclear power station," Eur. Phys. J. C **27**, 331 (2003) [arXiv:hep-ex/0301017].

[36] F. Ardellier *et al.* [Double Chooz Collaboration], "Double Chooz: A search for the neutrino mixing angle theta(13)," [arXiv:hep-ex/0606025].

[37] X. Guo *et al.* [Daya Bay Collaboration], "A precision measurement of the neutrino mixing angle theta(13) using reactor antineutrinos at Daya Bay," [arXiv:hep-ex/0701029].

[38] Y. Itow *et al.* [T2K Collaboration] "The JHF-Kamioka Neutrino Project", [arXiv:hep-ex/0106019v1].

[39] D. S. Ayres *et al.* [NOvA Collaboration], "NOvA proposal to build a 30-kiloton off-axis detector to study neutrino oscillations in the Fermilab NuMI beamline," [arXiv:hep-ex/0503053].

[40] M.C. Gonzalez-Garcia and M. Maltoni, "Phenomenology of Massive Neutrinos", [arXiv:hep-ph/0704.1800v2].

[41] T. Schwetz, "Neutrino oscillations: present status and outlook," AIP Conf. Proc. **981**, 8 (2008) [arXiv:0710.5027 [hep-ph]].

[42] M. Maltoni, T. Schwetz, M. Tortola and J.W.F. Valle, "Status of Global Fits to Neutrino Oscillations", [arXiv:hep-ph/0405172v6].

[43] C. Athanassopoulos *et al.* [LSND Collaboration], "The Liquid Scintillator Neutrino Detector and LAMPF Neutrino Source," Nucl. Instrum. Meth. A **388**, 149 (1997) [arXiv:nucl-ex/9605002].

[44] A. Aguilar *et al.* [LSND Collaboration], "Evidence for neutrino oscillations from the observation of $\bar{\nu}_e$ appearance in a $\bar{\nu}_\mu$ beam", Phys. Rev. D **64** (2001) 112007 [arXiv:hep-ex/0104049].

[45] [ALEPH Collaboration], "Precision electroweak measurements on the Z resonance," Phys. Rept. **427**, 257 (2006) [arXiv:hep-ex/0509008].

[46] M. Sorel, J. M. Conrad and M. Shaevitz, "A combined analysis of short-baseline neutrino experiments in the (3+1) and (3+2) sterile neutrino oscillation hypotheses," Phys. Rev. D **70**, 073004 (2004) [arXiv:hep-ph/0305255].

[47] G. Karagiorgi, A. Aguilar-Arevalo, J. M. Conrad, M. H. Shaevitz, K. Whisnant, M. Sorel and V. Barger, "Leptonic CP violation studies at MiniBooNE in the (3+2) sterile neutrino oscillation hypothesis," Phys. Rev. D **75**, 013011 (2007) [arXiv:hep-ph/0609177].

[48] A. A. Aguilar-Arevalo *et al.* [SciBooNE Collaboration], "Bringing the SciBar detector to the Booster neutrino beam", [arXiv:hep-ex/0601022].

[49] A. . (. Blondel *et al.*, "ECFA/CERN studies of a European neutrino factory complex," CERN-2004-002, ECFA-04-230 (2004)

[50] J. Altegoer *et al.* [NOMAD Collaboration], "The NOMAD experiment at the CERN SPS," Nucl. Instrum. Meth. A **404**, 96 (1998).

[51] G. Danby, J. M. Gaillard, K. Goulianos, L. M. Lederman, N. B. Mistry, M. Schwartz and J. Steinberger, "Observation of high-energy neutrino reactions and the existence of two kinds of neutrinos," Phys. Rev. Lett. **9**, 36 (1962).

[52] K. Kodama *et al.* [DONUT Collaboration], "Observation of tau-neutrino interactions," Phys. Lett. B **504**, 218 (2001) [arXiv:hep-ex/0012035].

[53] S. E. Kopp, "Accelerator neutrino beams," Phys. Rept. **439**, 101 (2007) [arXiv:physics/0609129].

[54] M. G. Catanesi *et al.* [HARP Collaboration], "Proposal to study hadron production for the neutrino factory and for the atmospheric neutrino flux" CERN-SPSC/99-35 SPCS/P315 (1999).

[55] M. G. Catanesi *et al.* [HARP Collaboration], "The Harp Detector At The Cern PS", Nucl. Instrum. Meth. A **571**, 527 (2007).

[56] M. Anfreville *et al.*, "The drift chambers of the NOMAD experiment", Nucl. Instrum. Meth. A **481** 339 (2002). [arXiv:hep-ex/0104012].

[57] M. G. Catanesi *et al.* [HARP Collaboration], "Measurement of the production cross-section of positive pions in p Al collisions at 12.9-GeV/c," Nucl. Phys. B **732**, 1 (2006) [arXiv:hep-ex/0510039].

[58] M. G. Catanesi *et al.* [HARP Collaboration], "Measurement of the production cross-section of positive pions in the collision of 8.9 GeV/c protons on beryllium," Eur. Phys. J. C **52**, 29 (2007) [arXiv:hep-ex/0702024].

[59] M. G. Catanesi *et al.* [HARP Collaboration], "Measurement of the production of charged pions by protons on a tantalum target," [arXiv:hep-ex/0706.1600].

[60] M. G. Catanesi *et al.* [HARP Collaboration], "Large-angle production of charged pions by 3 GeV/c - 12.9 GeV/c protons on beryllium, aluminium and lead targets," Eur. Phys. J. C **54**, 37 (2008) [arXiv:hep-ex/0709.3458].

[61] M. G. Catanesi *et al.* [HARP Collaboration], "Particle identification algorithms for the HARP forward spectrometer," Nucl. Instrum. Meth. A **572**, 899 (2007).

[62] M. Baldo-Ceolin *et al.*, "The Time-Of-Flight TOFW Detector Of The HARP Experiment: Construction And Performance", Nucl. Instrum. Meth. A **532** 548 (2004).

[63] A. Cervera, J.J. Gomez-Cadenas and J.A. Hernando, Nucl. Instrum. Meth. A **534**, 180 (2004).

[64] P. Billoir, "Track Fitting With Multiple Scattering: A New Method," Nucl. Instrum. Meth. A **225**, 352 (1984).

[65] E. Church *et al.* [BooNe Collaboration], "A proposal for an experiment to measure muon-neutrino → electron-neutrino oscillations and muon-neutrino disappearance at the Fermilab Booster: BooNE", FERMILAB-PROPOSAL-0898.

[66] A. A. Aguilar-Arevalo *et al.* [The MiniBooNE Collaboration], "A Search for Electron Neutrino Appearance at the Delta m**2 1 eV**2 Scale," Phys. Rev. Lett. **98**, 231801 (2007) [arXiv:hep-ex/0704.1500].

[67] A. A. Aguilar-Arevalo *et al.* [The MiniBooNE Collaboration], "Measurement of Muon Neutrino Quasi-Elastic Scattering on Carbon", Phys. Rev. Lett. **100**, 032301 (2008) [arXiv:hep-ex/0706.0926].

[68] A. A. Aguilar-Arevalo *et al.* [The MiniBooNE Collaboration], "First Observation of Coherent π^0 Production in Neutrino Nucleus Interactions with $E_\nu < 2$ GeV," [arXiv:hep-ex/0803.3423].

[69] A. A. Aguilar-Arevalo *et al.* [The MiniBooNE Collaboration], "The Monte Carlo-based Neutrino Flux Prediction at MiniBooNE," *in preparation*.

[70] A. A. Aguilar-Arevalo *et al.* [The MiniBooNE Collaboration], "The MiniBooNE Detector," *in preparation*.

[71] I. Stancu *et al.* [The MiniBooNE Collaboration], "Technical Design Report for the 8 GeV Beam," http://www-boone.fnal.gov/about_boone.

[72] I. Stancu *et al.* [The MiniBooNE Collaboration], "The MiniBooNE Detector Technical Design Report," http://www-boone.fnal.gov/about_boone.

[73] C. Moore, J. Anderson Jr., R. Ducar, R. Ford, T. Kobilarcik, E. Prebys, A. Russell, R. Stenfanski, J. Monroe, "Initial operation of the Fermilab MiniBooNE beamline," Proceedings of the 2003 Particle Accelerator Conference, 1652- 1654 vol.3 (2003).

[74] S. J. Brice *et al.*, "Photomultiplier tubes in the MiniBooNE experiment," Nucl. Instrum. Meth. A **562**, 97 (2006).

[75] I. Stancu "Maximum Likelihood Event Reconstruction for BooNE: Point-like Particles in a Perfect Detector," MiniBooNE Technical Note 6 (1998).

[76] I. Stancu "The High-Energy Electron Reconstruction in BooNE," MiniBooNE Technical Note 18 (1999).

[77] I. Stancu "The Muon Reconstruction in BooNE and Particle-ID via ANN," MiniBooNE Technical Note 19 (1999).

[78] I. Stancu "The Neutral Pion Reconstruction in BooNE and Particle-ID via ANN," MiniBooNE Technical Note 19 (1999).

[79] I. Stancu "An Introduction to the Maximum Likelihood Event Reconstruction in MiniBooNE," MiniBooNE Technical Note 19 (1999).

[80] H.O. Meyer, "Index of Refracion in Marcol 7" MiniBooNE Technical Note 90 (2003).

[81] R. Imlay, B. Metcalf, S. Ouedraogo, M. Sung, and M. Wascko, "Energy Calibration of Stopping Muons in MIniBooNE Using the Muon Tracker and Cubes", MiniBooNE Technical Note 106 (2003).

[82] P. Meyers, "A New μ^- Capture Model for the BooNE Detector Monte Carlo," Mini-BooNE Technical Note 135 (2004)

[83] M.H. Shaevitz, "Determination of the Neutral K Production Cross-Section at 8 GeV Using External Data" MiniBooNE Technical Note 188 (2006)

[84] M.H. Shaevitz, "Determination of the K^+ Production Cross-Section at 8 GeV Using External Data" MiniBooNE Technical Note 209 (2006)

[85] T. Katori *et al*, "Update on the MiniBooNE ν_μ QE Analysis," MiniBooNE Technical Note 219 (2006).

[86] Z. Djurcic, A. Aguilar-Arevalo, "Analysis of numu and nue events from NuMI beamline at MiniBooNE," MiniBooNE Technical Note 238 (2007).

[87] S. Brice "Better Propagation of Pion Production Uncertainties", http://www-boone.fnal.gov/software_and_analysis/meetings/03_07_08/PipProdErrors.pdf

[88] H. Ray *et al*, "MiniBooNE Algorithms Homepage" http://www-boone.fnal.gov/algorithms/

[89] D. Toptygin, JHU FLuoresence Reports 1-7.

[90] H. Yang, B. Roe, J. Zhu, "Studies of Stability and Robustness for Artificial Neural Networks and Boosted Decision Trees," Nucl. Instrum. Meth. A574, 342 (2007).
H. Yang, B. Roe, J. Zhu, "Studies of Boosted Decision Trees for MiniBooNE Particle Identification," Nucl. Instrum. Meth. A555, 370 (2005).
B. Roe *et al.*, "Boosted Decision Trees, an Alternative to Artificial Neural Networks", Nucl. Instrum. Meth. A543, 577 (2005).

[91] Y. Freund, and R.R. Schapire, "Experiments with a New Boosting Algorithm," Proc COLT, 209-217. ACM Press, New York (1996).

[92] J. Friedman, "Greedy Function Approximation: A Gradient Boosting Machine," Annals of Statistics, 29(5), 1189-1232 (2001).

J. Friedman, T. Hastie, R. Tibshirani, "Additive Logistic Regression: A Statistical View of Boosting," Annals of Statistics, 28(2), 337-07 (2000).

[93] J. L. Raaf, "A measurement of the neutrino neutral current pi0 cross section at Mini-BooNE," UMI-31-90981.

[94] M. Sorel, "Search for Sterile Neutrinos Using the MiniBooNE Beam," UMI-31-74896.

[95] J. R. Monroe, "A combined nu/mu and nu/e oscillation search at MiniBooNE," FERMILAB-THESIS-2006-44.

[96] R. B. Patterson, "A search for muon neutrino to electron neutrino oscillations at $\delta(m^2) > 0.1$ eV^2," FERMILAB-THESIS-2007-19.

[97] A. A. Aguilar-Arevalo, "An improved Neutrino Oscillations Analysis of the Mini-BooNE Data," FERMILAB-THESIS-2008-01.

[98] D. Isenhower *et al.* [MIPP Collaboration], "Proposal to upgrade the MIPP experiment," [arXiv:hep-ex/0609057].

[99] N. Antoniou *et al.* [NA49-future Collaboration], "Study of hadron production in hadron nucleus and nucleus nucleus collisions at the CERN SPS,"

[100] Y. Cho *et al.*, "Pion production in proton-beryllium collisions at 12.4 gev/c," Phys. Rev. D **4**, 1967 (1971).

[101] I. Chemakin *et al.* [E910 Collaboration], "Pion Production by Protons on a Thin Beryllium Target at 6.4, 12.3, and 17.5 GeV/c Incident Proton Momenta," *in preparation*.

[102] D. Dekkers *et al.*. Phys. Rev. B **137**, 962 (1965).

[103] R.A. Lundy *et al.*. Phys. Rev. Lett. **14**, 504 (1966).

[104] W.F. Baker *et al.*. Phys. Rev. Lett **7**, 101 (1961).

[105] V.L. Fitch *et al.*. Phys. Rev. **126**, 1849 (1962).

[106] F. Abe *et al*. Phys. Rev. D **36**, 1302 (1987).

[107] J. R. Sanford and C. L. Wang, "Empirical formulas for particle production in p-Be collisions between 10 and 35 BeV/c", Brookhaven National Laboratory, AGS internal report, (1967) (*unpublished*).

[108] R. P. Feynman, "Very high-energy collisions of hadrons," Phys. Rev. Lett. **23**, 1415 (1969).

[109] C. L. Wang, "Pion, kaon, and anti-proton production between 10 and 70 bev," Phys. Rev. Lett. **25**, 1068 (1970).

[110] M. M. Sternheim and R. R. Silbar, "Model for production of pi+ and pi- by protons from nuclei," Phys. Rev. D **6**, 3117 (1972).

[111] L. C. Tan and L. K. Ng, "Parametrization Of Hadron Inclusive Cross-Sections In P P Collisions Extended To Very Low-Energies," J. Phys. G **9**, 1289 (1983).

[112] L. C. Tan and L. K. Ng, "Estimation Of Average Hadron Multiplicities In P P Collisions Extended To Very Low-Energies," J. Phys. G **9**, 1453 (1983).

[113] R.J. Glauber, in "Lectures in Theoretical Physics", edited by W.E. Britten *et al* (Interscience, New York, Volume I, (1959).

[114] V. Franco, "High-energy neutron-nuclei total cross-sections," Phys. Rev. C **6**, 748 (1972).

[115] G. P. Zeller, "Low energy neutrino cross sections: Comparison of various Monte Carlo predictions to experimental data," [arXiv:hep-ex/0312061].

[116] C. H. Llewellyn Smith, "Neutrino Reactions At Accelerator Energies," Phys. Rept. **3**, 261 (1972).

[117] V. Bernard, L. Elouadrhiri and U. G. Meissner, "Axial structure of the nucleon," J. Phys. G **28**, R1 (2002) [arXiv:hep-ph/0107088].

[118] R. A. Smith and E. J. Moniz, "Neutrino Reactions On Nuclear Targets," Nucl. Phys. B **43** (1972) 605 [Erratum-ibid. B **101** (1975) 547].

[119] R. Bradford, A. Bodek, H. Budd and J. Arrington, "A new parameterization of the nucleon elastic form factors," Nucl. Phys. Proc. Suppl. **159**, 127 (2006) [arXiv:hep-ex/0602017].

[120] D. Rein and L. M. Sehgal, "Neutrino Excitation Of Baryon Resonances And Single Pion Production," Annals Phys. **133**, 79 (1981).

[121] N. V. Mokhov and S. I. Striganov, "MARS15 overview," AIP Conf. Proc. **896**, 50 (2007).

[122] G. Folger, V. N. Ivanchenko, J. P. Wellisch, "The Binary cascade model", Eur. Phys. Jour. A21 (3) (2004) 407.

[123] A. Heikkinen, N. Stepanov and J. P. Wellisch, "Bertini intra-nuclear cascade implementation in Geant4," In the Proceedings of 2003 Conference for Computing in High-Energy and Nuclear Physics (CHEP 03), La Jolla, California, 24-28 Mar (2003), pp MOMT008 [arXiv:nucl-th/0306008].

[124] http://geant4.web.cern.ch/geant4/UserDocumentation/UsersGuides/ PhysicsReferenceManual/html/node110.html

[125] S. Agostinelli *et al.* [GEANT4 Collaboration], "GEANT4: A simulation toolkit", Nucl. Instrum. Meth. A **506** (2003) 250.

[126] J. Allison *et al.* [GEANT4 Collaboration], " Geant4 developments and applications", IEEE Transactions on Nuclear Science 53 No. 1 (2006) 270-278.

[127] http://geant4.web.cern.ch/geant4/

[128] D. Casper, "The nuance neutrino physics simulation, and the future," Nucl. Phys. Proc. Suppl. **112**, 161 (2002) [arXiv:hep-ph/0208030].

[129] R. Brun, F. Bruyant, M. Maire, A. C. McPherson and P. Zanarini, "GEANT3,"

[130] C. Zeitnitz and T. A. Gabriel, "The GEANT - CALOR interface and benchmark calculations of ZEUS test calorimeters," Nucl. Instrum. Meth. A **349**, 106 (1994).

[131] G. Battistoni *et al.*, "The FLUKA code: Description and benchmarking," AIP Conf. Proc. **896**, 31 (2007).

[132] F. James and M. Roos, "Minuit: A System For Function Minimization And Analysis Of The Parameter Errors And Correlations," Comput. Phys. Commun. **10**, 343 (1975).

[133] P.A. Cerenkov, "Visible Emission of Clean Liquids by Action of Radiation", Doklady Akad. Nauk SSSR 2 (1934) 451.

[134] W.R. Leo, "Techniques for Nuclear and Particle Physics Experiments," Springer-Verlag, 2nd Ed. (1994)

[135] W.-M.Yao et al. (Particle Data Group), J. Phys. G 33, 1 (2006) and 2007 partial update for the 2008 edition

[136] Wikipedia contributors, "Multivariate normal distribution," Wikipedia, http://en.wikipedia.org/w/index.php?title=Multivariate_normal_distribution&oldid=154677319 (accessed September 14, 2007).

[137] Wikipedia contributors, "VRML," Wikipedia, http://en.wikipedia.org/w/index.php?title=VRML&oldid=182930578 (accessed January 22, 2008).

[138] Bartoszek Engineering. http://www.bartoszekeng.com/mboone/mboone.htm

[139] Hamamatsu Photonics http://www.hamamatsu.com